KU LEUVEN

ARENBERG DOCTORAL SCHOOL
Faculty of Engineering Science

Semi-analytical methodologies for airfoil noise prediction

Leandro Dantas de Santana

Supervisor:
Prof. dr. ir. Wim Desmet
Prof. dr. ir. Christophe Schram

Dissertation presented in partial fulfillment of the requirements for the degree of Doctor in Engineering Science: Mechanical Engineering

September 2015

Semi-analytical methodologies for airfoil noise prediction

Leandro Dantas DE SANTANA

Examination committee:
Prof. dr. ir. Pierre Verbaeten, chair
Prof. dr. ir. Wim Desmet, supervisor
Prof. dr. ir. Christophe Schram, supervisor
dr. ir. Wim De Roeck
Prof. dr. ir. Paul Sas
Prof. dr. ir. Johan Meyers
Prof. dr. ir. William J. Devenport
(Virginia Polytechnic Institute and State University)
Prof. dr. ir. Michel Roger
(École Centrale de Lyon)
Prof. dr. ir. Stéphane Moreau
(Université de Sherbrooke)

Dissertation presented in partial
fulfillment of the requirements for
the degree of Doctor
in Engineering Science: Mechanical Engineering

September 2015

Uitgegeven in eigen beheer, Leandro Dantas de Santana, Celestijnenlaan 300B box 2420, B-3001 Heverlee (Belgium)

ISBN XXX-XX-XXXX-XXX-X

D/XXXX/XXXX/XX

Acknowledgments

This work has been mainly founded by the Brazilian Coordination for Improvement of Higher Education Personnel – CAPES – process number BEX-0520-10-1. The European Commission is gratefully acknowledged for their support of the FP7 project IDEALVENT (Grant Agreement no 314066). The Fund for Scientific Research – Flanders (F.W.O.) is gratefully acknowledged for its support.

In this thesis, I wrote about the most relevant research results in aeroacoustics that I obtained along my PhD trajectory. I am not afraid to say that I did my best effort to present complete developments, however, I found that important lessons learned during the track are still missing in this manuscript. This omission is not related with limitations of maximum number of pages or time to complete the manuscript. The absent part is linked with experiences that I lived along this journey, which I found impossible to be converted into words. Therefore, I wish to acknowledge the people who contributed with those lessons, making this PhD training a life experience and a joyful educational process.

Firstly, I wish to express my special gratitude to prof. Christophe Schram for the daily guidance, motivation and for showing me when I had to stop with the experiments and start to write my thesis. More than a thesis supervisor, I found in Christophe a good friend and an exemplar person who, by the example, taught me important research and life lessons.

I also want to thank prof. Wim Desmet for accepting me as a PhD candidate at KU Leuven. His example of organization and leadership over a solid research group and cooperation with industrial and academic partners inspired me to pursue the academic career. Furthermore, in Leuven, I lived some of the most memorable moments of my stay in Belgium and I will keep good memories of this city for the rest of my life.

I want, as well, to acknowledge my jury for the nice discussion performed during the private thesis defense. Each point of view contributed to elevate my

understanding about the topic and the quality of this manuscript.

It is important also to recognize the contribution of my colleagues from the VKI and KU Leuven aeroacoustic research group. All the research discussions, social events, beer meetings, lunches, dinners, barbecues, parties, etc... made me feel like I was at home.

Some people who helped me build the blocks of my career, up to this point, also deserve my appreciation. Firstly, I wish to thank prof. Mico Hirschberg for presenting me to prof. Christophe Schram, his prompt and sincere advices were (and will be) very valuable to my career. I wish also to acknowledge prof. Leandro Franco de Souza and prof. Fernando Martini Catalano for introducing me to the aeroacoustics research world. Finally, I wish to express my very sincere gratitude to prof. Gunar Wilhelm Koelle for believing in my potential and giving me a scholarship to study in the Colégio Koelle. This was the first and most important positive turning point in my trajectory.

I wish to thank my parents and brother for taking, some years ago, the decision to invest in education. Now, we can see that this correct choice is the most effective way to build a solid, happy and safe future. Your great effort and devotion gave me the strength to face the challenge of moving to Belgium to pursue a PhD and this force will support me to overcome any difficult that life may one day present. Muito obrigado pela educação e pelo exemplo de vida que vocês são.

Finally, my special thanks to somebody who appeared in the middle of this PhD track and suddenly became the love of my life and my wife. Diana, without your effort, patience and compromise with our objectives I would never reach the end of this thesis. Muchas gracias mi vida y te amo muchísimo!

Abstract

The noise generated aerodynamically by airfoil-shaped parts is a major issue in applications of large societal interest, such as office and home appliances, wind power generation, air and ground transportation vehicles, etc. At early design stages, semi-analytical noise prediction methodologies are preferred over more CPU-intensive methods, and have recently gained considerable accuracy through advanced physical modeling. This thesis work aims to push further the accuracy and reliability of state-of-the-art semi-analytical techniques for the prediction of incoming-turbulence airfoil noise. To validate the proposed techniques, a novel experimental rig was developed and used to collect detailed databases for rod-airfoil and turbulence-airfoil interaction cases. The new facility was characterized from aerodynamic and acoustic viewpoints, and physical aspects relevant to semi-analytical noise prediction were quantified. The semi-analytical methodologies proposed in this thesis are meant to address specific frequency ranges, determined by the airfoil acoustical compactness. For the frequency range where the acoustic wavelength is larger than the airfoil chord. i.e. when the airfoil is acoustically compact, this work proposes an extension to the Amiet theory, proposing two extra applications of the Schwarzschild theorem to improve the convergence and, consequently, increase the noise prediction accuracy. Results show that the computation of two extra iterations impacts significantly the predicted noise spectrum in the frequency range of interest, and are verified against the experimental results developed in this thesis showing improved agreement. To address geometrical effects, this work develops a technique which applies the Boundary Element Methodology (BEM) to solve the linearized flow equations. This procedure is verified against analytical results, given by the Amiet technique to a flat-plate geometry, and applied to noise computations of generic geometry airfoils. This approach is validated against the experimental database developed in this work with results showing that the airfoil shape impacts the acoustic prediction.

Beknopte samenvatting

Aerodynamische geluidsopwekking is vaak een de oorzaak van geluidshinder en vindt zijn toepassing in onder andere huishoudtoestellen, windturbines en voertuigen. Gevanaceerde simulatietechnieken bieden de mogelijkheid om, reeds in het begin van de ontwerpcyclus, de geluidsopwekking en uiteindelijke afstraling te voorspellen en kunnen zo helpen tot het reduceren van de aeroakoestische geluidsopwekking. In deze context zijn semi-analytische methodes optimaal vanwege de korte rekentijden en de steeds hoger wordende nauwkeurigheid. Het onderzoek, beschreven in dit doctoraat heeft als doel de huidige semi-analytische methodes verder te ontwikkelen, om zo het gehele aerodynamisch opgewekte geluidsspectrum rond vleugelprofielen te kunnen berekenen binnen enkele uren met standaard PC's. De ontwikkelde methode is gevalideerd aan de hand van experimentele resultaten bekomen uit windtunneltesten. De aeroakoestische eigenschappen van deze windtunnel zijn volledig gekarakteriseerd en verschillende parameters, die van belang zijn voor de semi-analytische methodes, zijn gekwantificeerd. De ontwikkelde methodologie is toepasbaar voor een specifiek frequentiebereik, afhankelijk van de compactheid van het vleugelprofiel. Voor dit frequentiegebied, waar de akoestische golflengte groter is dan de koordlengte van het profiel, is een uitbreiding van Amiet's theorie voorgesteld. Een dubbele toepassing van het Schwarzschild theorema worden gebuikt om het iteratieve process, de convergentie en bijgevolg eveneens de nauwkeurigheid van de geluidsvoorspelling te vergroten. Er is aangetoond dat het uitvoeren van twee extra iteraties een significante invloed heeft op het gesimuleerde geluidsspectrum in het frequentiebereik waar de geluidsopwekking dominant is voor het grootste deel van de aeroakoestische toepassingen. Uit een vergelijking met de experimele data kan een duidelijke verbetering van de voorspelling van de uiteindelijke geluidsafstraling in vergelijking met de originele theorie van Amiet vastgesteld worden. Om geometrische aspecten in detail te bestuderen is er een techniek ontwikkeld die gebasseerd is op de randelementen methode om de gelineariseerde stromingsvergelijkingen op te lossen. Deze procedure is gevalideerd met analytische resultaten, bekomen met

Amiet's theorie voor een vlakke plaat en vervolgens toegpast voor de berekening van de aerodynamische geluidsopwekking van vleugelprofielen met een meer realistische en complexere geometrie. Deze resultaten zijn gevalideerd met de resultaten van de uitgevoerde experimenten en laten zien dat de vorm van het profiel een grote invloed heeft op de uiteindelijke geluidsafstraling.

Contents

List of Symbols and Abbreviations

a	Typical body dimension (RDT context)
b	Airfoil semi-chord
β	Compressibility factor $\beta = \sqrt{1 - M^2}$
c	Airfoil chord ($c = 2b$)
c_0	Sound speed
d	Airfoil half-span
E	Fresnel integral ($\mathrm{E}(x) = \int_0^x \frac{e^{\mathrm{i}t}}{\sqrt{2\pi t}} \mathrm{d}t$)
f_s	Sampling frequency
He	Helmholtz number ($He = kc$)
i	Imaginary unit ($\mathrm{i} = \sqrt{-1}$)
k	Wave-number ($k = \omega / c_0$)
kc	Helmholtz number
k_e	average wavenumber of the energy-containing eddies
K_x	chordwise specifc wavenumber
k_x	chordwise wavenumber
$\bar{k}_x$	Normalized wavenumber ($\bar{k}_x = k_x b$)
$\bar{k}_x^*$	Normalized wavenumber considering Mach ($\bar{k}_x^* = \bar{k}_x M / \beta^2$)

K_y	spanwise specifc wavenumber ($K_y = y/\sigma_0 k$)
k_y	spanwise wavenumber
λ	Gust or acoustic wavelength
$\mu = \bar{k}_x^* M$	Compressibility parameter
Λ_f	Longitudinal turbulence integral correlation length
Λ_g	Traverse turbulence integral correlation length
Λ_h	Normal turbulence integral correlation length
M	Flow Mach number
M_x	Flow Mach number at the x direction
M_y	Flow Mach number at the y direction
M_z	Flow Mach number at the z direction
ω	Angular frequency
Φ	Flow velocity potential
ϕ	Flow velocity potential Fourier transformed in time
PIV	Particle Image Velocimetry
PSD	Power Spectral Density
RDT	Rapid Distortion Theory
Re	Reynolds number
Re_c	Reynolds number based on the airfoil chord
Re_d	Reynolds number based on the rod diameter
ρ	Flow density
Sr	Strouhal number
U_0	Mean longitudinal flow velocity
u'	Velocity fluctuation root-mean-square
U_{ref}	Reference velocity - jet center line velocity
φ	Flow velocity potential Fourier transformed in time and space coordinates

w^I	Incident normal perturbation velocity
w^S	Scattered normal perturbation velocity

Chapter 1

Introduction

1.1 Noise reduction challenges

The noise generated aerodynamically is a recurrent critical issue in applications of large societal interest. In developed societies, people are constantly interacting with machines in places such as their houses, work and city environment. This large exposition to machines may lead to excessive exposition to noise, which is known as an important threat to the physical and psychological health. Among the noise generation mechanisms, the aerodynamic production is daily present in applications such as cooling and refrigeration systems, wind-farms, automobiles and airplanes.

The study of the noise generated aerodynamically, from the basic principles to technological applications, is a science field named aeroacoustics. Aeroacoustic studies started around the 50's, highly motivated by the unbearable – to the general society – noise level produced by the introduction of jet airplanes to the airlines fleet. From the 50's till nowadays, governments and industries massively invested in technology development for aircraft noise reduction. Nowadays, we observe that the application of innovations combined with regulatory restrictions resulted to significant aircraft noise reduction along the time.

The aircraft noise problem is recurrent in several airports around the globe, therefore we chose the Brussels Airport as a case closer to our reality which can concisely exemplify the aircraft noise problem of other societies. Figure 1.1 presents how the flights distribution over the city of Brussels evolved along the time. From this example, we observe that besides successive workaround rerouting, the only sustainable and long-term solution is the development of

noise reduction technologies.

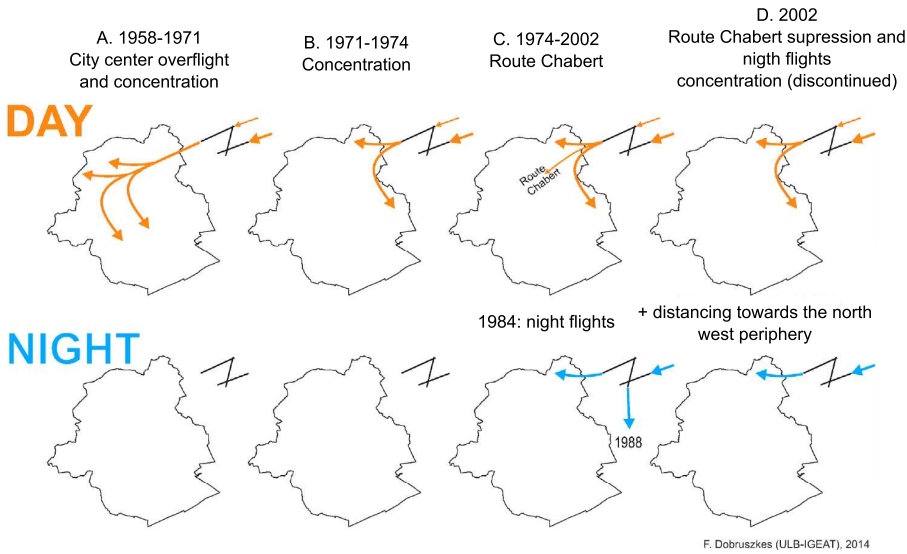

Figure 1.1: Historic view of the flights distribution over the city of Brussels. Figure adapted from Dobruszkes et al. [25]

From Fig. 1.1 it is observed that from 1958 until 1971 the preferred take-off flight route passed over the city of Brussels. With the concentration of flights, the first actions to mitigate the noise footprint were taken in 1971. Discussions at that time resulted in a proposal of an alternative flight route, passing over highly populated area of the city, in order to reduce the noise impact over other areas. By 1984, the introduction of night flights triggered new discussions about the environmental consequences of air traffic. In 2002, a new directive restricted severely the night flights, seemingly forcing the giant logistic operator DHL to move from Brussels airport to Leipzig, in Germany, directly impacting Brussels airport revenue, losses of jobs and business opportunities. From 2002 till nowadays further intensification of the discussions about the noise impact issues resulted in an ever-increasing number of proposed routes.

In 2014, a new aircraft noise crisis arrived, as a result of a new plan proposed by the authorities. This new crisis only ended recently, but it can be expected that it will be shortly followed by another one. Beyond the direct economic consequences of the iterative changes of route and of airport operation, the story depicted above is an obvious symptom of the stress that aircraft noise is causing to our society.

The expansion of the wind-farms is another example of the societal impact of the aerodynamically generated noise, where the research developed in this thesis has direct application. The wind-energy is a proven renewable power source, which suffers restrictions about possible areas of installation due to its noise impact. In most of the European countries, environmental certification rules constraints the wind-farm noise production, limiting their installation to locations close to roads, industrial areas or off-shore. With the raising demand for sustainable energy generation, the possible installation areas becoming scarce, thus, high density wind-turbine parks are turning into a common place. This trend has, as important side-effect, a considerable increase to the noise emission levels. Just as in the aircraft noise and perpetual re-routing problem, the NIMBY (Not In My Back Yard) attitude prevails for wind-turbine siting, promising conflictual future negotiations between local authorities, wind-turbine manufacturers, planners and opposition groups.

The two examples discussed above, which could be easily complemented by many others, clearly indicate that the only sustainable approach which allows increase the air-mobility and wind-energy usage, requires a reduction of the noise emissions at the source. This demands improved understanding, modeling and mitigation of the sound produced by turbulence as it interacts with airfoil profiles. In that perspective, the modeling strategy adopted in this work is based in low-CPU demanding methods, rather than high-fidelity numerical approaches. Being complementary to the latter, it was anticipated here that cheap (semi-)analytical methods would be more likely to integrate into optimization design tools, which can involve up to several hundreds of simulations.

1.2 Leading-edge airfoil noise generation mechanisms

When an airfoil is subjected to an incoming turbulence, lift fluctuations are induced, which radiate noise to the far-field as acoustic dipoles. The turbulent flow field can be either produced upstream the airfoil, by the presence of inflow distortions and other aerodynamic elements, or in case of a steady inflow, by the development of a turbulent boundary-layer over the airfoil surface. The first mechanism is usually linked with the noise produced close to the airfoil leading-edge, and is the subject studied in thesis, while the second is called a self-noise mechanism having already been discussed by other authors [7, 8, 13, 14, 15, 16, 45, 46, 55].

The two sound generation mechanisms can, simultaneously, be present.

However, when the incoming flow field turbulence intensity is large enough, the pressure fluctuations associated with boundary layer eddies will be small compared with the unsteady pressure due the incoming turbulence and the later mechanism becomes, then, the predominant noise generation phenomenon.

Paterson and Amiet [49], Migliore and Oerlemans [39] and Moreau et al. [47] show that leading-edge noise is predominantly a low-frequency source when the turbulent eddies, related with the acoustic generation, are large scale structures. The Amiet theory [3, 6, 7] demonstrates that the noise radiation pattern depends on the airfoil compactness with reference to the acoustic wavelength. For low-frequencies, where the acoustic wavelength is larger than the chord, the airfoil is considered a compact acoustic source and the noise radiates following a dipole directivity pattern. Oppositely, for higher frequencies, where the chord is larger than the acoustic wavelength, the airfoil behaves as a non-compact source and the acoustic directivity radiation pattern presents side-lobes, related with constructive and destructive interferences. The airfoil compactness is a key concept in Chapter 5, where the Amiet theory is extended to the compact airfoil case.

1.3 Semi-analytical approaches to airfoil noise prediction

Among the techniques to solve the linearized airfoil theory, state-of-art semi-analytical approaches are a good combination between computational efficiency and noise prediction accuracy. The research of improved semi-analytical methodologies has been challenging authors from the early years of the aeroacoustics studies till nowadays. The first basis of this investigation has been launched before Lighthill's [37, 38] aeroacoustics seminal papers by Sears [61, 63]. Sears' studies were initially directed towards the aeroelasticity field but it had been shown applicable to aeroacoustics. In this study, the flow is considered incompressible and inviscid and the phenomena linear, such that the flow could be modeled as a velocity potential solution of a Laplace equation. If a flat-plate airfoil geometry is considered, this problem can be solved analytically, with results valid for low excitation frequencies.

Several authors proposed corrections to the Sears function to include compressibility effects and, consequently, increase the valid frequency range. Important evolution to the theory was achieved with the flow being modeled by a Helmholtz equation [2, 5, 32, 48]. However, difficulties in analytically solving the boundary value problem limited the application of this methodology to approximate and/or asymptotic solutions.

An important theoretical contribution has been given by Amiet. Based on Graham [32] and Adamczyk [2] results, he proposed iterative applications of the Schwarzschild theorem [60] to solve the Helmholtz equation [6]. Besides the absence of a formal proof of convergence, results showed successful validation against experimental data for frequencies where the airfoil is considered a non-compact noise source [13, 49, 50]. The combination of an aerodynamic model to compute the airfoil response to a periodic gust, with a theory to compute the airfoil far-field acoustic radiation, resulted in what, today, we name the Amiet theory [3, 7, 8].

A following important contribution to the Amiet theory has been given by Roger and Moreau [55]. In this work, the Amiet theory is extended to consider the back-scattering phenomena effects to the airfoil response, extending the applicability of this approach to finite span airfoils, and to frequencies where the airfoil can be considered a compact noise source. The original Roger and Moreau's method is developed for the trailing-edge noise problem. Followed by Rozenberg and Christophe [19, 58] developments which applied this methodology to the leading-edge problem of rectangular geometry profiles. Further contribution to the semi-analytical leading-edge noise prediction is given by Roger [54]. In this work, expressions for a annular geometry airfoil are developed and the acoustic prediction is compared with experiments with very low background noise, showing the potentialities of the technique. Extensions and limitations are discussed by Roger and Moreau [56] and applications of the extended Amiet theory have been done to stochastic and deterministic inflow excitations by Roger, Moreau and Schram [46, 57].

Analytical approaches to solve the linearized airfoil theory, classically, approximate the profile to a flat-plate and do not consider geometric effects. Some methodologies have been considered to overcome this limitation. A first method, proposed by Atassi [9], revisits the Sears problem following a second order theory which is limited to the frequency regime where the airfoil is adopted as a compact source. Moreau [47] assumes that the airfoil response function is unaffected by the geometry, being modeled by the response proposed by Amiet [6], and considers the angle of attack and profile shape effects on the acoustic scattering. This study shows improved noise prediction accuracy, compared to experiments, demonstrating that the geometry affects the sound radiation, besides the shape is not considered in the airfoil response function. Chapter 6 of this thesis, proposes an alternative to this methodology where the airfoil response is numerically calculated and the geometry is considered for the acoustic radiation. Glegg and Devenport [26] use the generalized form of the Blasius theorem and a conformal mapping, which maps the airfoil surface onto a circle, to solve the flow represented by the Laplace equation. This method models the inflow modified by the Rapid Distortion Theory [11, 34],

thus considering airfoil shape effects to the inflow distortion and aerodynamic airfoil response including scattering effects. Given that this model solves the Laplace equation, no compressibility effect related with the non-compact (high-frequency) regime is, however, considered.

Glegg, Devenport and Grace [28, 30] further contributed to the theory with the development of numerical panel methods to solve the Laplace equation which accounts the noise generated by realistic airfoil geometries. This approach allows the airfoil response computation in geometries impossible to be described by conformal transformations. Additionally, this methodology permits the application of the Rapid-Distortion-Theory, leading to the computation of a complete acoustic spectra with CPU cost that is not many orders of magnitude higher than the pure semi-analytical approaches. This technique has been shown successful for the compact frequency regime, however, the proposed vortex-airfoil interaction formulation, does not allow to distinguish effects of turbulence distortion from the actual geometry influence to the airfoil aerodynamic response.

From the experimental point of view, recent contributions of Mish, Glegg, Devenport and co-authors [24, 27, 41, 42, 43, 44] studied the effect of realistic airfoil geometries considering the airfoil aerodynamic response and the radiated airfoil noise in NACA airfoils. Furthermore, Moreau and co-authors studied the Controlled Diffusion airfoil [21, 22, 46, 52, 65] developing an extensive experimental and numerical database to this profile.

1.4 Thesis objectives and contributions

This thesis has as main objective the development and validation of improved methodologies for leading-edge airfoil noise prediction. These techniques are valid for the compact and non-compact regimes and are directly applicable to industrial designs. The studied approaches are appropriate to perform the complete acoustic spectra prediction within less than 12 hours, using a table PC. The proposed methodologies are validated through a new experimental database developed. In those experiments, the canonical turbulence-airfoil case has been studied together with a more complex inflow given by the rod-airfoil configuration.

The approaches studied in this thesis propose improved methodologies for the airfoil noise source calculation:

- In the frequency regime where the airfoil is considered a compact noise source, this work revisits the Amiet theory and proposes the application of

two extra iterations of the Schwarzschild theorem. Numerical corrections are developed to extend the validity of the Amiet theory to the low-frequency regime. Comparing results obtained with this approach and experiments, it is verified that the original Amiet theory does not present a convergence in the compact airfoil frequency regime. The addition of two extra iterations improves the range of frequencies with good agreement between calculations and empirical results;

- In the high-frequency regime we propose a methodology which considers geometrical aspects to the airfoil response and acoustic radiation. The technique developed observes the similarity of the boundary value problem prescribed by the linearized airfoil theory and the acoustic propagation formulation. It is proposed to adopt a commercial acoustic Boundary Element Method solver. Comparison of noise predictions with experiments shows the importance of considering geometrical aspects on the airfoil response computation.

From the experimental point of view this work contributes:

- with the development of a solid empirical database to the turbulence-airfoil and rod-airfoil configurations. The flow is characterized in detail to the rod- and turbulence-airfoil cases, in the presence and absence of the airfoil using hot-wire and stereoscopic-PIV techniques. These results, which served to validate the semi-analytical methodologies proposed in this thesis, are described with enough detail such that could be adopted by other authors for validation;
- with a comprehensive study about the inflow models to be adopted in semi-analytical predictions. This work evaluates from the first models proposed by Amiet [3] to the current state-of-art models which consider the Rapid-Distortion-Theory. Furthermore, experimental evidence is provided of the physical phenomena that have to be considered in semi-analytical predictions.

The chapters organization is the following:

In Chap. 2 the leading-edge Amiet theory is reviewed and points of the theory related with further discussions developed in this work are highlighted.

In Chap. 3 the flow facility developed is presented and aeroacoustically characterized. Measurements conducted in this rig provide an experimental database for the validation modeling approaches developed in this thesis.

In Chap. 4 the evaluation of the leading-edge generated airfoil noise when subjected two different inflow mechanisms is performed. Firstly, the rod-

airfoil configuration is studied, and, secondly, the rod-airfoil flow is detailed. In this chapter a detailed aeroacoustic database of those two complementary phenomena is presented together with quantitative physical evidence of the Rapid-Distortion-Theory.

In Chap. 5 the Amiet theory is extended to cases where the airfoil is considered a compact noise source. This chapter proposes that, for the low-frequency regime, two extra applications of the Schwarzschild theorem are necessary to obtain convergence in the airfoil response to monochromatic perturbations. The predicted airfoil noise is compared with experiments results showing improved agreement of results in the compact airfoil regime.

In Chap. 6 the effects of realistic airfoil geometries are taken into account at the frequencies where the airfoil is a non-compact noise source. This chapter proposes the application of the Boundary Element Methodology (BEM) to solve the compressible linearized flow equations. It is demonstrated that a commercial acoustic solver can be used to solve the aerodynamic equations in a procedure similar to the one proposed by Amiet. The predicted airfoil noise is also compared with experimental results demonstrating the applicability of this technique to more accurate noise predictions.

Finally in Chap. 7 the conclusions and future perspectives are presented.

Chapter 2

Amiet theory for leading-edge airfoil noise prediction

This chapter revisits the leading-edge Amiet theory presenting essential concepts, notation, results and theoretical aspects discussed with further detail along the developments of this thesis. Similarly to other aeroacoustic studies, the Amiet theory decouples the noise sources computation from the acoustic radiation calculation. In this chapter, the first section introduces the methodology adopted to compute the airfoil noise radiation, and the second presents the technique adopted to calculate the airfoil unsteady surface pressure distribution. This second procedure is detailed in Appendix A.

2.1 Airfoil noise radiation

The Amiet theory considers the noise radiation of an infinitely thin airfoil with chord $2b$ and span $2d$. The right-handed axis system is placed at the center of the airfoil, which lays in the plane $z = 0$. This geometry is schematically represented in Fig. 2.1.

The airfoil is subjected to a flow with uniform mean velocity U which contain a velocity perturbation (u, v, w) with amplitude much smaller than U, i.e. $\sqrt{u^2 + v^2 + w^2} \ll U$. The Amiet theory assumes that the flow interacting with the airfoil surface predominantly generates noise sources which can be modeled by dipole type singularities. Curle [23, 29] proposes that the acoustic

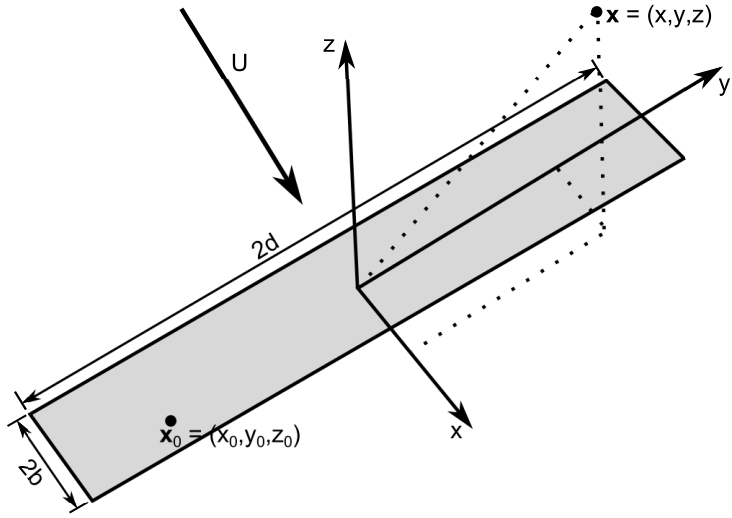

Figure 2.1: Schematic representation of the Amiet problem. An airfoil with chord $2b$ and span $2d$ subjected to a mean flow with velocity U. Source localized at $\mathbf{x}_0$ and observer placed in $\mathbf{x}$.

pressure radiated by a single dipole can be calculated by:

$$p\left(\mathbf{x},\omega,\mathbf{x}_0\right)=\frac{\mathrm{i}\,k\,\mathbf{x}_t\cdot\hat{\mathbf{F}}\left(\mathbf{x}_0,\omega\right)}{4\pi\,\sigma_s^2}\mathrm{e}^{-\mathrm{i}\,k\sigma_t}\left(1+\frac{1}{\mathrm{i}\,k\sigma_s}\right), \tag{2.1}$$

where $\hat{\mathbf{F}}$ is the surface force vector which generates the dipole, described in the frequency domain, $k=\omega/c_0$ and:

$\mathbf{x}=(x,y,z)$ is the observer position;

$\mathbf{x}_0=(x_0,y_0,z_0)$ is a position in the airfoil surface;

$\mathbf{x}_t=\left(((x-x_0)-M\sigma_s)/\beta^2,y-y_0,z\right)$ is the relative position between source and observer, considering compressibility effects;

$\sigma_s=\sqrt{(x-x_0)^2+\beta^2\left[(y-y_0)^2+(z-z_0)^2\right]}$ is the distance between source and observer, considering compressibility effects;

$\sigma_t=\left(\sigma_s-M\left(x-x_0\right)\right)/\beta^2$ is the propagation distance corrected for convection effects.

The $1/(\mathrm{i}k\sigma_s)$ is the near-field term which is considered negligible at distances larger than the order of magnitude of a wavelength and the over-hat term ($\hat{\cdot}$) corresponds to the Fourier transform defined as:

$$\hat{f}(\omega) = \frac{1}{2\pi} \int_{-\infty}^{\infty} f(t)\, e^{-\mathrm{i}\omega t}\, \mathrm{d}t\,. \tag{2.2}$$

By considering an infinitely thin airfoil, it is possible to infer that only the force component perpendicular to the airfoil surface will contribute to the noise generation. Consequently, the dipole radiated noise can be written as a function of the local lift component $\hat{l}$, in the frequency domain, as:

$$p\left(\mathbf{x}, \omega, \mathbf{x}_0\right) = \frac{\mathrm{i}\, k\, z\, \hat{l}(\mathbf{x}_0, \omega)}{4\pi\, \sigma_s^2} \mathrm{e}^{-\mathrm{i}k\,\sigma_t} \left(1 + \frac{1}{\mathrm{i}k\,\sigma_s}\right)\,, \tag{2.3}$$

The infinitely thin airfoil geometry assumption is an approximation valid, in principle, for airfoils subjected to reduced aerodynamic loading, i.e. reduced thickness and small camber. From a theoretical point of view, this approximation is required to keep the calculations written in terms of analytical expressions. Mish, Moreau, Glegg and collaborators. [24, 26, 44, 47] show that the airfoil geometry plays an important role on the noise radiation. In this thesis, the infinitely thin airfoil hypothesis is relaxed in Chapter 6, where geometrical aspects, i.e. thickness and camber, are considered to both the noise radiation and the aerodynamic response computation.

Now returning to the Amiet developments, by considering a continuous surface distribution of dipole type singularities over the infinitely thin airfoil surface, the total airfoil radiated noise can be calculated through the surface integral:

$$p\left(\mathbf{x}, \omega, \mathbf{x}_0\right) = \int_{-d}^{d} \int_{-b}^{b} \frac{\mathrm{i}\, k\, z\, \hat{l}(\mathbf{x}_0, \omega)}{4\pi\sigma_s^2} \mathrm{e}^{-\mathrm{i}\, k\sigma_t} \left(1 + \frac{1}{\mathrm{i}k\sigma_s}\right) \mathrm{d}x_0 \mathrm{d}y_0 \tag{2.4}$$

$$= \int_{S_y} \frac{\mathrm{i}\, k\, z\, \hat{l}(\mathbf{x}_0, \omega)}{4\pi\sigma_s^2} \mathrm{e}^{-\mathrm{i}k\sigma_t} \left(1 + \frac{1}{\mathrm{i}\, k\sigma_s}\right) \mathrm{d}S_y\,, \tag{2.5}$$

where S_y represents the airfoil surface. Since this theory is intended to compute the grid-airfoil interaction noise, which is essentially a random phenomenum, it is convenient to represent the acoustic radiation in terms of statistical quantities, instead of deterministic variables. The acoustic Power Spectral Density (PSD) is written as a function of the statistical expected value operator ($E[\cdots]$) as:

$$S_{pp}\left(\mathbf{x}, \omega\right) = \lim_{T \to +\infty} \left\{ \frac{\pi}{T}\, E\left[p\left(\mathbf{x}, \omega, \mathbf{x}_0\right)\, p^*\left(\mathbf{x}, \omega, \mathbf{x}_0'\right)\right] \right\}\,, \tag{2.6}$$

where $(\cdot)^*$ represents the complex conjugated operator.

Therefore the acoustic pressure produced due to dipole type sources distribution over the airfoil surface is expressed as:

$$S_{pp}\left(\mathbf{x},\omega\right) = \int_{S_y}\int_{S_y'} \left(\frac{kz}{4\pi}\right)^2 \frac{1}{\sigma_s^2\sigma_s'^2}\left(1+\frac{1}{\mathrm{i}\,k\sigma_s}\right)\left(1+\frac{1}{\mathrm{i}\,k\sigma'^s}\right)^* S_{ll}(\mathbf{x}_0,\mathbf{x}_0',\omega)\mathrm{e}^{-\mathrm{i}\,k\left(\sigma_t-\sigma_t'\right)}\mathrm{d}S_y\mathrm{d}S_y' \,, \tag{2.7}$$

where S_{ll} is the lift fluctuation function cross-power spectral density, which is, similarly, defined as a function of the expected value operator as:

$$S_{ll}(\mathbf{x}_0,\mathbf{x}_0',\omega) = \lim_{T\to+\infty}\left\{\frac{\pi}{T}\,E\left[\hat{l}(x,y,\omega)\,\hat{l}^*(x',y',\omega)\right]\right\} . \tag{2.8}$$

The S_{ll} term is directly related to the incoming pressure jump induced at the airfoil surface. Its computation considers a convected sinusoidal gust impacting the airfoil surface, written as:

$$w(\mathbf{x}_0,t) = \hat{\hat{w}}(k_x,k_y)\,\mathrm{e}^{\mathrm{i}(k_x(Ut-x_0)-k_y y_0)} \,, \tag{2.9}$$

where $\hat{\hat{w}}$ represents the double spatial Fourier transform of the incident perturbation w.

The pressure jump ($\Delta P(\mathbf{x}_0,t)$) is defined as the difference between the upper and lower side pressure at an airfoil's surface point. For a flat plate, the upper and lower side pressure have the same absolute value and opposite signal, therefore, $\Delta P(\mathbf{x}_0,t)$ is twice the pressure computed at one side. In Chapter 5 this approach is similarly adopted to the proposed extension of the Amiet theory. Nevertheless, in Chapter 6 the pressure is computed along the airfoil surface.

For an infinitely thin airfoil, the corresponding surface pressure jump is written as:

$$\begin{aligned}\tilde{l}(\mathbf{x}_0,t) &= \Delta P(\mathbf{x}_0,t) = p^{\text{upper}} - p^{\text{lower}} \\ &= 2\pi\,\rho\,U\,\hat{\hat{w}}(k_x,k_y)\,g(x_0,k_x,k_y)\,\mathrm{e}^{\mathrm{i}(k_x Ut-k_y y_0)} \,,\end{aligned} \tag{2.10}$$

where g is defined as a transfer function which links the gust amplitude to the airfoil surface pressure jump. Next section is dedicated to compute g. Considering the contribution of all incoming gusts, the local lift is written in the time domain as:

$$l(\mathbf{x}_0,t) = 2\pi\,\rho\,U\int_{-\infty}^{\infty}\int_{-\infty}^{\infty}\hat{\hat{w}}(k_x,k_y)\,g(x_0,k_x,k_y)\,\mathrm{e}^{\mathrm{i}(k_x Ut-k_y y_0)}\mathrm{d}k_x\mathrm{d}k_y \,, \tag{2.11}$$

the local lift response is described in the frequency domain by the Fourier-transform application, leading to:

$$\hat{l}(\mathbf{x}_0,\omega) = 2\pi\,\rho \int_{-\infty}^{\infty}\int_{-\infty}^{\infty} \hat{\hat{w}}(k_x,k_y)\, g(x_0,k_x,k_y)\, \mathrm{e}^{-\mathrm{i}k_y y_0} \left(\frac{U}{2\pi}\int_{-\infty}^{\infty} \mathrm{e}^{\mathrm{i}(k_x U-\omega)t}\mathrm{d}t\right)\mathrm{d}k_x\mathrm{d}k_y\,, \tag{2.12}$$

the parenthesis term is recognized as the Dirac delta Fourier transform. Using its properties to perform the integration, the local lift density is expressed as:

$$\hat{l}(\mathbf{x}_0,\omega) = 2\pi\,\rho \int_{-\infty}^{\infty} \hat{\hat{w}}(K_x,k_y)\, g(x_0,K_x,k_y)\, \mathrm{e}^{-\mathrm{i}k_y y_0}\mathrm{d}k_y\,, \tag{2.13}$$

where $K_x = \omega/U$ is a particular chordwise wave number. This operation brings an important result to the theory by indicating that the noise produced in a particular frequency (ω) is related with a unique component (K_x), of the chordwise incoming perturbation wavenumber.

Since the local lift density $\hat{l}(\mathbf{x}_0,\omega)$ is a deterministic quantity, its statistical representation is done by the lift cross-power spectral density, written as:

$$S_{ll}(\mathbf{x}_0,\mathbf{x}_0',\omega) = (2\pi\,\rho)^2 \int_{-\infty}^{\infty}\int_{-\infty}^{\infty} \hat{\hat{w}}(K_x,k_y)\, \hat{\hat{w}}^*(K_x,k_y')\, g(x_0,K_x,k_y)\, g^*(x_0,K_x,k_y')\mathrm{d}k_y\mathrm{d}k_y'\,, \tag{2.14}$$

with the assumption of isotropic turbulence, it is possible to infer the turbulence wavevectors statistical orthogonality property [3], which is expressed by:

$$\hat{\hat{w}}(K_x,k_y)\hat{\hat{w}}^*(K_x,k_y') = U\,\delta(k_y-k_y')\,\Phi_{ww}(K_x,k_y)\,, \tag{2.15}$$

where Φ_{ww} is the two-dimensional turbulence spectrum. In conclusion, the infinitely thin airfoil surface lift function cross-power spectral density is written as:

$$S_{ll}(\mathbf{x}_0,\mathbf{x}_0',\omega) = (2\pi\,\rho)^2 U \int_{-\infty}^{\infty} \Phi_{ww}(K_x,k_y)\, \mathrm{e}^{-\mathrm{i}k_y(y_0-y_0')}\, g(x_0,K_x,k_y) g^*(x_0',K_x,k_y)\mathrm{d}k_y\,. \tag{2.16}$$

By knowing the S_{ll} expression, it is possible to compute the airfoil radiated acoustic pressure PSD as:

$$S_{pp}(\mathbf{x},\omega) = \int_{S_y}\int_{S'_y} \left(\frac{\rho\, k\, z}{2}\right)^2 U \frac{1}{\sigma_s^2 \sigma_s'^2} \left(1+\frac{1}{\mathrm{i}\, k\, \sigma_s}\right)\left(1+\frac{1}{\mathrm{i}\, k\, \sigma'_s}\right)^* \mathrm{e}^{-\mathrm{i}k(\sigma_t-\sigma'_t)} \int_{-\infty}^{\infty} \Phi_{ww}(K_x,k_y)\mathrm{e}^{-\mathrm{i}k_y(y_0-y'_0)} g(x_0,K_x,k_y) g^*(x'_0,K_x,k_y)\mathrm{d}k_y \mathrm{d}S_y \mathrm{d}S'_y \,. \tag{2.17}$$

From Eq. 2.17 it is observed the presence of terms of three different nature:

1. variables related with the geometry and frequency, e.g. $(\rho k z)/2$, σ_s, σ_t and $(y_0 - y'_0)$, ...;
2. terms associated with the incoming flow mean velocity and turbulence: U and $\Phi_{ww}(K_x, k_y)$.
3. the airfoil lift response to a monochromatic gust: given by the transfer function $g(x_0, K_x, k_y)$;

In this thesis, special attention is given to the calculation of the second and third items.

In Chapter 4 it is presented a discussion about the $\Phi_{ww}(K_x, k_y)$ model. The theory originally developed by Amiet [3] describes Φ_{ww} following the von Kármán spectrum for isotropic turbulence. More recent advances [55, 44, 24] demonstrate that, as the turbulence approaches the thick airfoil leading-edge, the mean flow distorts the turbulent eddies, which become anisotropic. This chapter shows physical evidence of this phenomena and its important impact to the airfoil noise radiation. In addition, it is evaluated the effect of a non-uniform span-wise flow, i.e. U and $\Phi_{ww}(K_x, k_y)$ to the airfoil acoustic radiation.

In Chapter 6 realistic airfoil geometric effects will be considered to the computation of the transfer function g, for the non-compact noise case.

Returning to Eq. 2.17, it is important to understand that, at this stage, the theory makes no assumptions of acoustic or geometrical far-field. This equation involves the solution of five integrals which could be cumbersome for practical applications, unless advanced integration techniques are applied [19]. The acoustic and geometric far-field assumptions bring important simplifications to the theory.

Acoustic far-field formulation By assuming the receiver placed in a distance much larger than the acoustic wavelength ($|\mathbf{x}_t| \gg \lambda$), it is possible to neglect, in Eq. 2.17, the acoustic near-field term $(1/(\mathrm{i}k\sigma_s))$. Consequently, the noise PSD formula is be simplified to:

$$S_{pp}(\mathbf{x},\omega) = \int_{S_y}\int_{S'_y} \left(\frac{\rho k z}{2}\right)^2 U \frac{1}{\sigma_s^2 \sigma_s'^2} \mathrm{e}^{-\mathrm{i}k(\sigma_t - \sigma'_t)}$$

$$\int_{-\infty}^{\infty} \Phi_{ww}(K_x,k_y)\mathrm{e}^{-\mathrm{i}k_y(y_0-y'_0)} g(x_0,K_x,k_y) g^*(x'_0,K_x,k_y)\mathrm{d}k_y\mathrm{d}S_y\mathrm{d}S'_y\,. \quad (2.18)$$

This equation have terms regrouped as:

$$\begin{aligned} S_{pp}(\mathbf{x},\omega) = \left(\frac{\rho k z}{2}\right)^2 U \int_{-\infty}^{\infty} \Phi_{ww}(K_x,k_y) \\ \left[\int_{-d}^{d}\int_{-d}^{d} \frac{1}{\sigma_s^2\sigma_s'^2} \mathrm{e}^{-\mathrm{i}(k_y/\sigma_0 - k_y)(y'_0-y_0)}\mathrm{d}y_0\mathrm{d}y'_0\right] \\ \left\{\int_{-b}^{b} g(x_0,K_x,k_y)\mathrm{e}^{\mathrm{i}[k(x-M\sigma_0)x_0]/(\beta^2\sigma_0)}\mathrm{d}x_0\right\} \\ \left\{\int_{-b}^{b} g^*(x'_0,K_x,k_y)\mathrm{e}^{-\mathrm{i}[k(x-M\sigma_0)x'_0]/(\beta^2\sigma_0)}\mathrm{d}x'_0\right\}\mathrm{d}k_y\,, \end{aligned} \quad (2.19)$$

where $\sigma_0^2 = x^2 + \beta^2\left(y^2+z^2\right)$. The curly brackets terms evidences the aeroacoustic transfer function:

$$\mathcal{L}(\mathbf{x},K_x,k_y) = \int_{-1}^{1} g(x_0,K_x,k_y)\mathrm{e}^{-\mathrm{i}kb/\beta^2(M-x/\sigma_0)}\mathrm{d}x_0, \quad (2.20)$$

which will be calculated in the next section, from the airfoil response to a monochromatic aerodynamic gust. With the $\mathcal{L}(\mathbf{x},K_x,k_y)$ definition the airfoil radiated noise PSD is written as:

$$\begin{aligned} S_{pp}(\mathbf{x},\omega) = \left(\frac{\rho U k z b}{2}\right)^2 U \int_{-\infty}^{\infty} \Phi_{ww}(K_x,k_y)|\mathcal{L}(\mathbf{x},K_x,k_y)|^2 \\ \left[\int_{-d}^{d}\int_{-d}^{d} \frac{1}{\sigma_s^2\sigma_s'^2} \mathrm{e}^{-\mathrm{i}(k_y/\sigma_0 - k_y)(y'_0-y_0)}\mathrm{d}y_0\mathrm{d}y'_0\right]\mathrm{d}k_y\,. \end{aligned} \quad (2.21)$$

Geometric far-field formulation Further simplification is added to the formulation if the observer is placed at a distance large compared with the airfoil span. By assuming geometric far-field, the approximation $(y - y_0) \approx y$ become acceptable and the relation is valid:

$$\frac{1}{\sigma_s^2} \approx \frac{1}{\sigma_0^2} \,. \tag{2.22}$$

By keeping all the other terms identical, the square bracket term term of Eq. 2.21 is expressed by a sine cardinal function as:

$$\int_{-d}^{d}\int_{-d}^{d} \frac{1}{\sigma_0^4} \mathrm{e}^{-\mathrm{i}(k_y/\sigma_0 - k_y)(y_0' - y_0)} \mathrm{d}y_0 \mathrm{d}y_0' = \frac{4}{\sigma_0} \frac{\sin^2\left[(K_y - k_y)d\right]}{(K_y - k_y)^2} \,, \tag{2.23}$$

with $K_y = y/\sigma_0 k$, leading to the relation:

$$S_{pp}(\mathbf{x}, \omega) = \left(\frac{\rho k z b}{\sigma_0^2}\right)^2 \pi U d \int_{-\infty}^{\infty} \frac{\sin^2\left[(K_y - k_y)d\right]}{(K_y - k_y)^2} \Phi_{ww}(K_x, k_y) |\mathcal{L}(\mathbf{x}, K_x, k_y)|^2 \mathrm{d}k_y \,. \tag{2.24}$$

In case the airfoil semi-span (d) is large compared to the airfoil chord, the sine cardinal tends to a Dirac delta:

$$\lim_{d\to\infty} \left(\frac{\sin^2\left[(K_y - k_y)d\right]}{(K_y - k_y)^2}\right) = \delta(K_y - k_y) \,, \tag{2.25}$$

consequently, Eq. 2.24 replaces the argument k_y by K_y of $\mathcal{L}$ and Φ_{ww}. This consideration shows that the velocity at which the gust sweeps the airfoil leading-edge determines the radiated noise angle. Therefore the observer exclusively hears the noise produced by the gust which produces an acoustic wavefront normal to the line joining the airfoil and the observer [3].

If K_x is large enough compared with a specific k_y value it is verified that the gust wavefront moves supersonically relative to the fluid and the problem becomes similar to a two-dimensional compressible gust propagation. According to Graham [32], if $MK_x \ll k_y$, the airfoil response becomes independent from k_y. In this sense, if the parameter $\Lambda = MK_x d$ tends to infinity, the terms $\mathcal{L}$ and Φ_{ww} can be taken outside the integral resulting to:

$$S_{pp}(\mathbf{x}, \omega) = \left(\frac{\rho k z b}{\sigma_0^2}\right)^2 \pi U d \Phi_{ww}(K_x, K_y) |\mathcal{L}(\mathbf{x}, K_x, K_y)|^2 \,, \tag{2.26}$$

where K_y can be assumed equal to zero if the observer is localized at $y = 0$.

The experimental set-up studied in this thesis allows to evaluate the geometric and acoustic far-field hypotheses. This study is done in Chapter 4 where the predicted noise computed, with each far-field assumption is compared against experimental results.

2.2 Airfoil aerodynamic response computation

Problem formulation The previous section computed the airfoil acoustic radiation given a source distribution represented by the transfer function $g(x_0, k_x, k_y)$ and the aeroacoustic transfer function $\mathcal{L}(\mathbf{x}, K_x, K_y)$. Now, this section presents the methodology to compute these functions.

Revisiting the Amiet theory, it is important to remember that this approach considers a flat-plate airfoil with span $2d$ lying in the $z = 0$ plane localized between $0 \leq x/b \leq 2$ subjected to an mean flow with components $(U_\infty \cos(\theta), U_\infty \sin(\theta), 0)$ and an aerodynamic monochromatic skewed velocity perturbation gust. This model admits the intensity of the lift dipole much larger than the drag dipole, thus, only the incident[1] gust component perpendicular to the airfoil surface (w^I), is considered to contribute to the noise generation. This problem is schematically represented in Fig. 2.2.

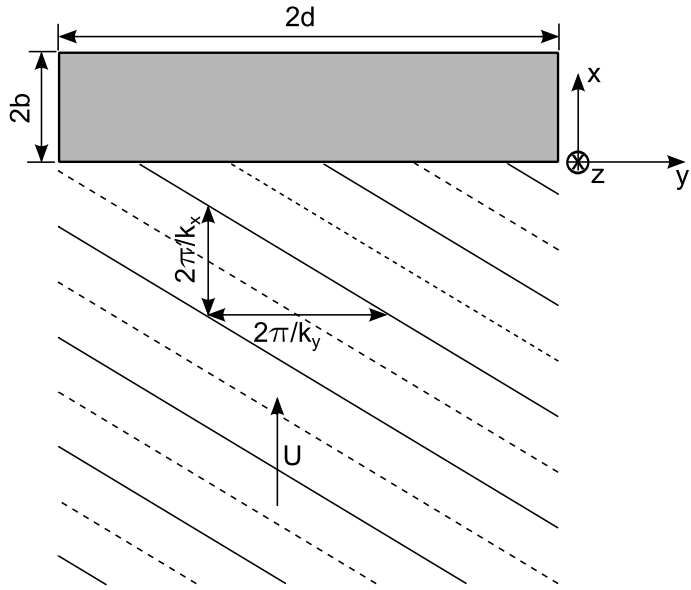

Figure 2.2: Airfoil interacting a periodic velocity gust perturbation schematic representation.

The Amiet problem is solved considering the linearized airfoil theory prescribing as boundary condition: zero velocity potential (Φ) upstream of the airfoil

[1]For the definition of incidence and scaterred field, please refer to Appendix A.

leading-edge; zero airfoil surface normal velocity and zero pressure jump at the airfoil trailing-edge (Kutta condition) and downstream [6]:

$$\Phi(x,0,t) = 0 \qquad x/b \leq 0\,, \tag{2.27}$$

$$\frac{\partial \Phi(x,0,t)}{\partial z} = -w^I \qquad 0 \leq x/b \leq 2\,, \tag{2.28}$$

$$\frac{\mathrm{D}\Phi(x,0,t)}{\mathrm{D}t} = 0 \qquad x/b \leq 2\,, \tag{2.29}$$

where the total derivative operator is defined as:

$$\frac{\mathrm{D}}{\mathrm{D}t} = \frac{\partial}{\partial t} + U\frac{\partial}{\partial x}\,, \tag{2.30}$$

Considering the mean velocity component normal to the xy plane equal to zero, the linearized flow can be represented in term of velocity potential as:

$$\left[\nabla^2 - \frac{1}{c_0^2}\frac{\mathrm{D}^2}{\mathrm{D}t^2}\right]\Phi\left(x,y,z,t\right) = 0\,. \tag{2.31}$$

Assuming the velocity potential as a harmonic function, we can write:

$$\Phi\left(x,y,z,t\right) = \phi(x,y,z)\mathrm{e}^{\mathrm{i}\omega t}\,. \tag{2.32}$$

By applying the spatial Fourier transform to the velocity potential ϕ along the span-wise direction (y) we obtain:

$$\phi\left(x,y,z\right) = \varphi\left(x,z\right)\mathrm{e}^{\mathrm{i}\gamma x}\mathrm{e}^{\mathrm{i}\alpha y}\,, \tag{2.33}$$

where $\gamma = \frac{kM}{\beta^2}$ and $\alpha = -k_y$. Replacing Eqs. 2.32 and 2.33 into Eq. 2.31 we obtain:

$$\beta^2\frac{\partial^2\varphi}{\partial x^2} + \left(\frac{k^2}{\beta^2} - \alpha^2\right)\varphi + \frac{\partial^2\varphi}{\partial z^2} = 0\,. \tag{2.34}$$

Considering the dimensionless parameters:

$$\bar{x} = \frac{x}{b}\,, \quad \bar{y} = \frac{\beta y}{b}\,, \quad \bar{z} = \frac{\beta z}{b}\,, \tag{2.35}$$

after rearranging terms and adopting the following wave-number definitions:

$$k_x = \frac{\omega}{U}\,, \quad k = \frac{\omega}{c_0}\,, \quad k = k_x M\,, \quad \text{and} \quad \bar{k}_i = k_i b\,, \tag{2.36}$$

we retrieve a canonical Helmholtz equation:

$$\frac{\partial^2\varphi}{\partial\bar{x}^2}+\frac{\partial^2\varphi}{\partial\bar{z}^2}+\kappa^2\varphi=0\,, \tag{2.37}$$

where

$$\kappa^2=\mu^2-\frac{\bar{k}_y}{\beta^2},\qquad \mu=\frac{\bar{k}_xM}{\beta^2}=\bar{k}_x^*M\quad\text{and}\quad \bar{k}_x^*=\frac{\bar{k}_x}{\beta^2}\,. \tag{2.38}$$

The boundary conditions, presented in Eqs. 2.27, 2.28 and 2.29, are time and space Fourier-transformed and non-dimentionalized, resulting to the relations:

$$\varphi(\bar{x},0)=0 \qquad \bar{x}\le 0\,, \tag{2.39}$$

$$\frac{\partial}{\partial\bar{z}}\varphi\left(\bar{x},0\right)=\frac{-w_0b}{\beta}\mathrm{e}^{-\mathrm{i}\bar{k}_x^*\bar{x}} \qquad 0<\bar{x}\le 2\,, \tag{2.40}$$

$$\left(\mathrm{i}\bar{k}_x^*+\frac{\partial}{\partial\bar{x}}\right)\varphi\left(\bar{x},0\right)=0 \qquad \bar{x}>2\,, \tag{2.41}$$

which together with Eq. 2.37 compose the boundary value problem proposed by Amiet [6]. The characteristics of this boundary value problem differ depending on κ^2:

- if $\kappa^2>0$, i.e. $\bar{k}_y<\frac{\bar{k}_xM}{\beta}$, the equation is hyperbolic and the gust is named supercritical;
- if $\kappa^2<0$, i.e. $\bar{k}_y>\frac{\bar{k}_xM}{\beta}$, the equation is elliptic and the problem is named subcritical;
- if $\kappa^2=0$, i.e. $\bar{k}_y=\frac{\bar{k}_xM}{\beta}$, the Helmholtz equation reduces to the Laplace equation and the gust is named critical.

Amiet proposes to apply the Schwarzschild theorem [60] in order to solve this boundary value problem. This theorem demonstrates that a canonical Helmholtz equation (i.e. Eq. 2.37) subjected to the boundary condition pair:

$$\varphi\left(\bar{x},0\right)=f\left(\bar{x}\right) \qquad \bar{x}\ge 0 \tag{2.42}$$

$$\frac{\partial\varphi}{\partial\bar{z}}\left(\bar{x},0\right)=0 \qquad \bar{x}<0 \tag{2.43}$$

has a solution given by:

$$\varphi\left(\bar{x},0\right)=\frac{1}{\pi}\int_0^\infty G\left(\bar{x},\xi,0\right)f\left(\xi\right)\mathrm{d}\xi\,, \tag{2.44}$$

where $G(\bar{x}, \xi, 0)$ is the Green's function, defined by the system response to an impulsive excitation, and $f(\xi)$ is a generic function dependent on ξ. For this problem, Amiet adopts a Green's function representative of a semi-infinite flat plate:

$$G(\bar{x}, \xi, 0) = \sqrt{\frac{-\bar{x}}{\xi} \frac{\mathrm{e}^{-\mathrm{i}\kappa(\xi-\bar{x})}}{\xi - \bar{x}}}\,. \tag{2.45}$$

The gust-airfoil problem consists of a Helmholtz equation and three boundary conditions. Amiet proposes an iterative procedure where, at each step, a pair of boundary equations are solved. This strategy proposes a solution in three stages. Initially, the aerodynamic gust is imposed to an infinite flat-plate and the Helmholtz equation is calculated, subjected to the non-penetration boundary condition. Secondly, the zero flow potential, upstream of the airfoil leading-edge, is imposed together with the non-penetration boundary condition and solved using the Schwarzschild theorem. Finally, the Kutta condition and the zero pressure jump, downstream of the airfoil trailing-edge, are imposed together with the no penetration boundary equation, in a consecutive application of the Schwarzschild theorem.

At this stage, this thesis proposes a different approach from Amiet to consider the realistic geometric effects. Amiet proposes the Green's function of a semi-infinite plane, i.e. Eq. 2.45. This approach is necessary mainly to keep the derivations written in term of analytical expressions. Furthermore, the derivation of tailored Green's functions for a specific airfoil geometry is a complex task, which requires long and deep mathematical analysis, with no guarantee of success for any arbitrary geometry. As a solution to this limitation, Chapter 6 proposes a numerical approach to compute the Green's function of a generic geometry using the Boundary Element method.

Supercritical gusts pressure trace As discussed, if $\kappa^2 > 0$, the Helmholtz equation is hyperbolic and and the gust amplitude slowly decays with the distance, compared with the subcritical case. The derivation of the supercritical and subcritical cases are essentially similar, therefore this paragraph discusses the supercritical case and the subcritical calculation is presented in detail in Appendix A.

The Amiet procedure firstly computes the velocity potential for an infinite flat-plate subjected to periodic velocity perturbation. In this calculation, Eq. 2.37 is solved for the upper part of an infinite domain subjected to Eq. 2.40 boundary condition, as schematized in Fig. 2.3. For a flat-plate geometry, the solution is given by:

$$\varphi^{(0)}(\bar{x}, \bar{z}) = -\frac{w_0 b}{\bar{k}} \mathrm{e}^{-\mathrm{i}\bar{k}_x^* \bar{x} - \bar{k}\bar{z}/\beta}\,. \tag{2.46}$$

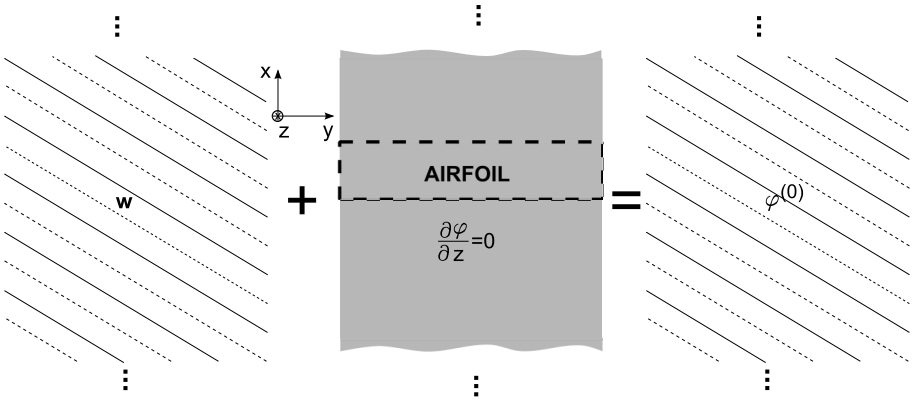

Figure 2.3: Schematic representation of the first iteration of the Amiet theory.

Noteworthy, the solution to the lower part is the same as presented in Eq. 2.46, however, with opposite signal. In the next step, the boundary condition which imposes zero velocity potential upstream of the airfoil leading-edge (Eq. 2.39) is solved simultaneously with the non-penetration boundary condition, imposed downstream the airfoil leading-edge (Eq. 2.40). This boundary value problem, represented below and schematized in Fig. 2.4, is solved by the application of the Schwarzschild theorem, where the scattered potential ψ_1 in obtained:

$$\frac{\partial^2 \psi_1}{\partial \bar{x}^2} + \frac{\partial^2 \psi_1}{\partial \bar{z}^2} + \kappa^2 \psi_1 = 0\,, \tag{2.47}$$

$$\psi_1\left(\bar{x}, 0\right) = -\varphi^{(0)}\left(\bar{x}, 0\right) \qquad \bar{x} \leq 0\,, \tag{2.48}$$

$$\frac{\partial \psi_1}{\partial \bar{z}}\left(\bar{x}, 0\right) = 0 \qquad \bar{x} > 0\,. \tag{2.49}$$

This second iteration of the Amiet theory considers the airfoil a semi-infinite flat-plate extending from the leading-edge to the downstream direction. By superimposing the potential calculated in the first iteration with the potential computed in the second, it is obtained the correction potential $\varphi^{(1)} = \varphi^{(0)} + \psi_1$ given by:

$$\varphi^{(1)}\left(\bar{x}, 0\right) = -\frac{w_0 b}{\bar{k}}\left(1 - \mathrm{i}\right) \mathrm{E}\left[\left(\bar{k}_x^* - \kappa\right)\bar{x}\right] \mathrm{e}^{-\mathrm{i}\bar{k}_x^* \bar{x}}\,. \tag{2.50}$$

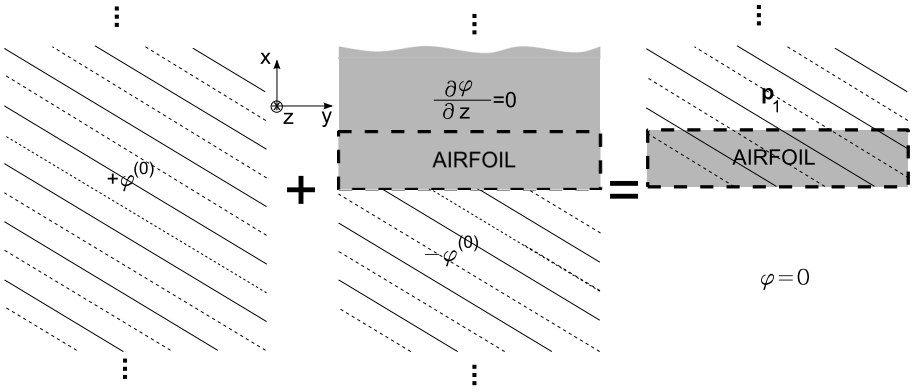

Figure 2.4: Schematic representation of the second iteration of the Amiet theory.

With the Fourier transformed corrected potential $\varphi^{(1)}$ it is possible to obtain the potential $\Phi^{(1)}$, which is written in terms of time and space variables:

$$\Phi^{(1)}(x,y,0,t) = \varphi^{(1)} \mathrm{e}^{\mathrm{i}\omega t} \mathrm{e}^{\mathrm{i}\gamma x} \mathrm{e}^{\mathrm{i}\alpha y} \tag{2.51}$$

$$= -\frac{w_0(1-\mathrm{i})}{\sqrt{(k_x^2+k_y^2)}} E\left[\left(\bar{k}_x^* - \kappa\right)\bar{x}\right] \mathrm{e}^{\mathrm{i}(\omega t - k_x x - k_y y)}. \tag{2.52}$$

The relation between the flow potential and the surface pressure trace is:

$$p_1(x,y,0,t) = -\rho \frac{\mathrm{D}\Phi^{(1)}}{\mathrm{D}t} = -\rho\left(\frac{\partial \Phi^{(1)}}{\partial t} + U\frac{\partial \Phi^{(1)}}{\partial x}\right), \tag{2.53}$$

which, by replacing Eq. 2.52, results on:

$$p_1(x,y,0,t) = \rho U w_0 \frac{\mathrm{e}^{-\mathrm{i}\pi/4}\left(\bar{k}_x^* - \kappa\right)}{\sqrt{\pi\left(\bar{k}_x^* - \kappa\right)\left(\bar{k}_x^2 + \bar{k}_y^2\right)\bar{x}}} \mathrm{e}^{\mathrm{i}\left(\omega t - \left[\left(\bar{k}_x^* - \kappa\right)/b - k_x\right]x - k_y y\right)}. \tag{2.54}$$

This is the final expression for the surface pressure trace computed by the second iteration of the Amiet theory.

At this stage the airfoil is considered a semi-infinite flat plate and this solution can already be considered a good high-frequency approximation. To extend this theory to lower frequencies, finite chord effects should be considered [55]. In this way the Kutta condition together with the zero pressure jump downstream

the airfoil leading-edge condition should be satisfied, in a third iteration of the Amiet procedure. The scattered pressure P_2 is computed by the boundary value problem - schematically represented in Fig. 2.5:

$$\frac{\partial^2 P_2}{\partial \bar{x}^2} + \frac{\partial^2 P_2}{\partial \bar{z}^2} + \kappa^2 P_2 = 0\,, \tag{2.55}$$

$$P_2\left(\bar{x}, 0\right) = -P_1\left(\bar{x}, 0\right) \qquad \bar{x} \geq 2\,, \tag{2.56}$$

$$\frac{\partial P_2}{\partial \bar{z}}\left(\bar{x}, 0\right) = 0 \qquad \bar{x} < 2\,. \tag{2.57}$$

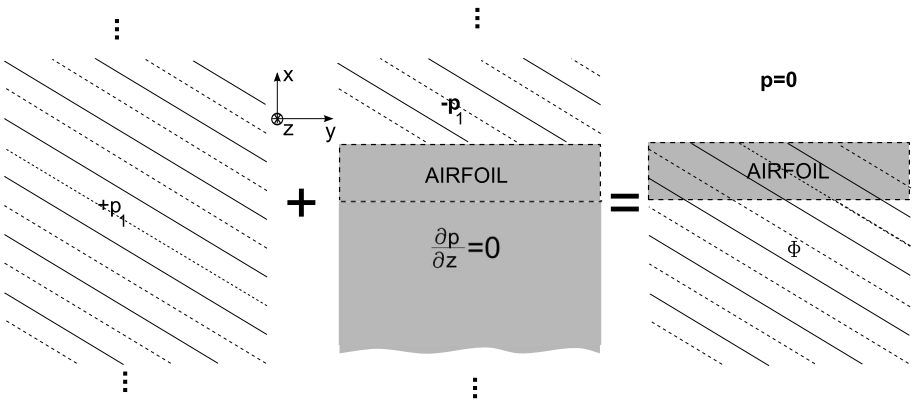

Figure 2.5: Schematic representation of the third iteration of the Amiet theory.

This boundary value problem has no exact analytical expression for $P_2\left(\bar{x}, 0\right)$. However, it is possible to obtain an approximate solution, valid for high frequencies given by:

$$P_2\left(\bar{x}, 0\right) \approx -\rho U w_0 \frac{\mathrm{e}^{-\mathrm{i}\pi/4}\mathrm{e}^{-\mathrm{i}\kappa\bar{x}}}{\sqrt{2\pi\left(\bar{k}_x^2 + \beta^2\kappa\right)}}\left[1 - (1+\mathrm{i})\,\mathrm{E}^*\left(2\kappa\left(2-\bar{x}\right)\right)\right]\,, \tag{2.58}$$

which results into a scattered pressure $p_2\left(x, y, 0, t\right)$ given by:

$$p_2\left(x, y, 0, t\right) \approx \frac{-\rho U w_0}{\sqrt{2\pi\left(\bar{k}_x^2 + \beta^2\kappa\right)}}\left[1 - (1+\mathrm{i})\,\mathrm{E}^*\left(2\kappa\left(2-\bar{x}\right)\right)\right]\mathrm{e}^{\mathrm{i}\left[\left(\bar{k}_x^* M^2\right)\bar{x} - \pi/4 + \omega t - k_y y\right]}\,. \tag{2.59}$$

As demonstrated in Appendix A the approximation used to compute the scattered pressure $p_2\left(x, y, 0, t\right)$ is essentially valid to the high-frequency regime,

i.e. non-compact airfoils. In Chapter 5 a correction to this function which extends the validity of this approximation to the compact airfoil regime is proposed. In addition, the effect of this correction to the noise prediction is compared with experimental results.

Aeroacoustics transfer functions After computing the hydrodynamic pressure trace at the airfoil surface, it is possible to calculate the noise radiation using the aeroacoustic transfer function $\mathcal{L}(x, y, z, k_x, k_y)$. Noteworthy that the pressure $p_1(x, y, 0, t)$ and $p_2(x, y, 0, t)$ are computed at the positive side of the infinite plane. Consequently, the total pressure difference $\Delta p(x, 0, t)$ is related with the transfer function $g(x, k_x, k_y)$, which relates the gust amplitude w_0, flow velocity U and density ρ with the pressure jump $\Delta p(x, 0, t)$ as:

$$\begin{aligned}\Delta p(x,0,t) &= p^{\text{upper}} - p^{\text{lower}} \\ &= 2\left(p_1(x,y,0,t) + p_2(x,y,0,t)\right) \\ &= 2\pi\,\rho\,U\,w_0\,g(x,k_x,k_y)\,\mathrm{e}^{\mathrm{i}\omega t}\,,\end{aligned} \tag{2.60}$$

where $g(x, k_x, k_y)$ is the defined as the transfer function between the incoming gust and the airfoil pressure jump response:

$$g(x,k_x,k_y) = \frac{p(x,y,0,t)\,\mathrm{e}^{\mathrm{i}k_y y}\mathrm{e}^{-\mathrm{i}\omega t}}{\pi\,\rho\,U\,w_0}\,, \tag{2.61}$$

by replacing Eqs. 2.54 and 2.59 into Eq. 2.61 the transfer functions g_1 and g_2 are obtained:

$$g_1(\bar{x},k_x,k_y) = \frac{\mathrm{e}^{-\pi/4}}{\pi\sqrt{2\pi\left(\bar{k}_x+\beta^2\kappa\right)(\bar{x}+1)}}\mathrm{e}^{-\mathrm{i}\left(\kappa-\bar{k}_x^* M^2\right)(\bar{x}+1)}\,, \tag{2.62}$$

$$g_2(\bar{x},k_x,k_y) \approx -\frac{\mathrm{e}^{-\pi/4}}{\pi\sqrt{2\pi\left(\bar{k}_x+\beta^2\kappa\right)}}\left[1-(1+\mathrm{i})\,\mathrm{E}^*\left(2\kappa\left(1-\bar{x}\right)\right)\right]\mathrm{e}^{-\mathrm{i}\left(\kappa-\bar{k}_x^* M^2\right)(\bar{x}+1)}\,. \tag{2.63}$$

The aeroacoustic transfer function $\mathcal{L}(x, y, z, k_x, k_y)$, which is necessary to propagate the noise radiated by the unsteady pressure jump, regarded as a distribution of dipoles, to the listener position is defined as [7]:

$$\mathcal{L}(x,y,z,k_x,k_y) = \int_{-1}^{1} g(\xi,k_x,k_y)\,\mathrm{e}^{-\mathrm{i}\mu(M-x/\sigma)\xi}\mathrm{d}\xi\,, \tag{2.64}$$

with $\sigma = \sqrt{x^2 + \beta^2 \left(y^2 + z^2\right)}$. With this definition it is possible to compute the aeroacoustics transfer function $\mathcal{L}_1$ and $\mathcal{L}_2$ as:

$$\mathcal{L}_1 \left(x, y, z, k_x, k_y\right) = \frac{1}{\pi} \sqrt{\frac{2}{\left(\bar{k}_x + \beta^2 \kappa\right) \theta_1}} \mathrm{E}^* \left(2\theta_1\right) \mathrm{e}^{\mathrm{i}\theta_2} \,, \tag{2.65}$$

$$\mathcal{L}_2 \left(x, y, z, k_x, k_y\right) \approx \frac{\mathrm{e}^{\mathrm{i}\theta_2}}{\theta_1 \pi \sqrt{2\pi \left(\bar{k}_x + \beta^2 \kappa\right)}} \left\{ \mathrm{i} \left(1 - \mathrm{e}^{-\mathrm{i}2\theta_1}\right) + (1 - \mathrm{i}) \left[\mathrm{E}^* \left(4\kappa\right) - \sqrt{\frac{2\kappa}{\theta_3}} \mathrm{e}^{-\mathrm{i}2\theta_1} \mathrm{E}^* \left(2\theta_3\right) \right] \right\} , \tag{2.66}$$

with $\theta_1 = \kappa - \mu x/\sigma$, $\theta_2 = \mu \left(M - x/\sigma\right) - \pi/4$ and $\theta_3 = \kappa + \mu x/\sigma$.

A similar procedure can be applied to compute the pressure response and aeroacoustic transfer function of subcritical gusts. This approach is detailed presented in Appendix A.

At this stage, after two iterative Schwarzschild theorem applications, the Amiet development is valid to non-compact airfoils. Chapter 5 continue the developments from this point. In addition, this chapter shows that this iterative procedure converges to high frequencies, i.e. non-compact airfoils. To extend this theory to the compact airfoil regime, it proposed two extra Schwarzschild theorem applications.

Acoustic compactness definition A key concept to be discussed in Chapter 5 is the acoustic compactness. In this chapter the Amiet analytical theory to compute the thin leading-edge airfoil response to an aerodynamic gust is extended to compact airfoils. According to Rienstra and Hirschberg [53] (page 14) a body can be considered compact if the Helmholtz number (He) is much smaller than one. In this work the Helmholtz number is given by the variable kc:

$$k\,c = \frac{2\pi\, f}{c_0}\, c = \frac{2\pi}{\lambda} c \,, \tag{2.67}$$

where c_0 is the sound speed, c is the airfoil chord and λ is the acoustic wavelength.

Chapter 3

Aeroacoustic facility characterization and experimental campaign

The previous chapter introduces the semi-analytical approach proposed by Amiet to perform leading-edge airfoil noise prediction. In these developments, the importance of the accurate inflow characterization to the noise prediction is highlighted. The semi-analytical technique discussed can be applied to either numerical or experimental databases and the second methodology is chosen to this thesis. Therefore, a solid rod- and grid-airfoil empirical database is developed and applied to validate the techniques proposed in the next chapters, where the most relevant experimental results are presented here.

This chapter details the facility, the testing matrix, experimental apparatus and relevant validation results applied to the two experimental cases studied in this thesis: the grid-airfoil and the rod-airfoil interaction cases.

3.1 Experimental campaign

Facility description A testing facility previously developed by Schram [59] and schematically represented in Fig. 3.1 has been adapted to comply with this project requirements. This rig is installed in the von Kármán Institute for Fluid Dynamicsand consists of a semi-anechoic room with $4 \times 3 \times 4$ m^3

and cut-off frequency of 200 Hz [36]. Regarding the former configuration, the major changes applied to the facility for this project are the replacement of the previous compressed air flow ejectors and coaxial jet by a centrifugal fan powered by a 18.5 kW electric engine and a circular-to-rectangular contraction designed specifically for this project, respectively. Details about the contraction design are present in Appendix B.

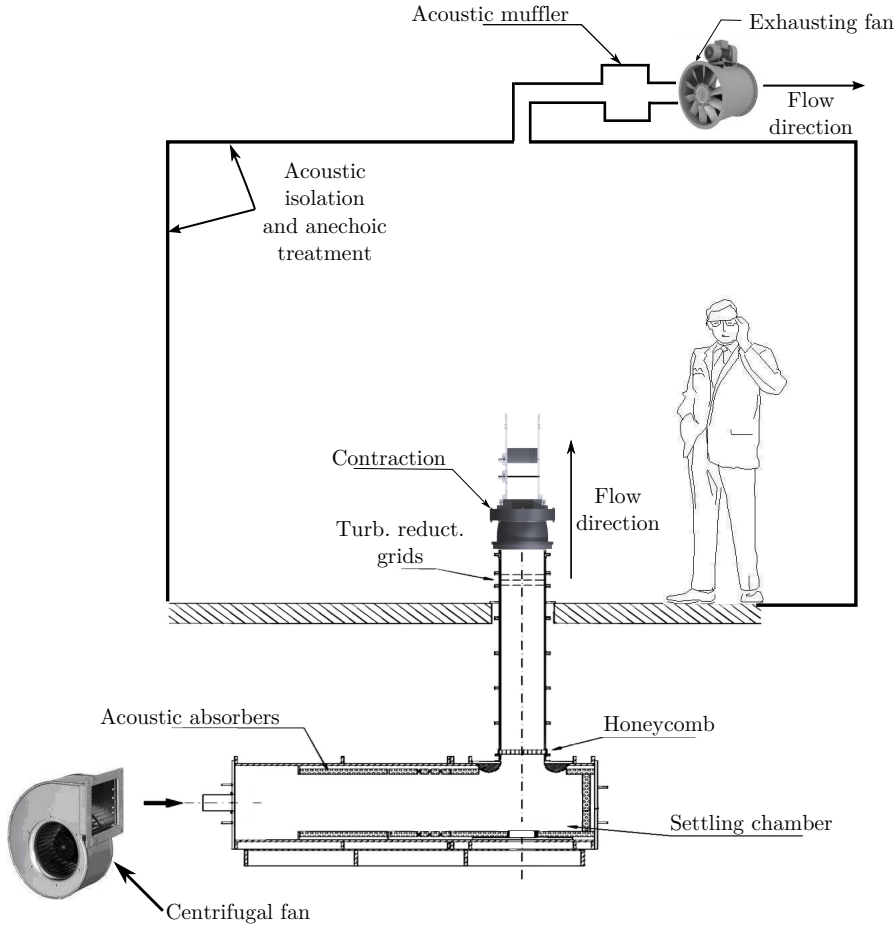

Figure 3.1: Experimental facility schematic representation.

This rig is inspired to be a 2/3 scaling of a facility used by Jacob [35] to perform the rod-airfoil benchmark noise case. Nevertheless this factor served as a design

guideline, the proportion was not applied to all facility dimensions, due to installation and available engine power limitations. As shown in Appendix B, the application of these constraints resulted into a jet contraction with exit dimensions of 0.2 m span by 0.15 m width and flow speed ranging from 5 to 35 m/s.

After defining the major design guidelines, a new contraction was developed to adapt the circular geometry imposed by the previous rig configuration to the rectangular geometry, aimed to this project. Constraints of maximum flow uniformity, minimum risk of separation and turbulence intensity guided the task (see Appendix B). The final contraction, mounted with the side plates and testing objects is schematized in Fig. 3.2. Figure 3.3 shows the facility instrumented for the stereoscopic-PIV measurements.

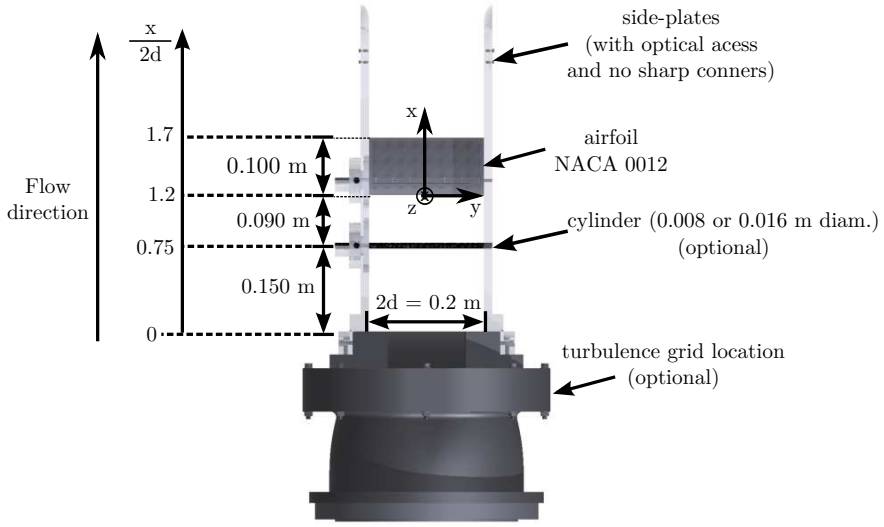

Figure 3.2: Schematic representation of the contraction and testing objects.

A NACA-0012 airfoil with 0.1 m chord and 0.2 m span is studied. The axis system, hereafter adopted, coincides with the reference system proposed by the Amiet theory. In this orientation frame, the origin is placed in the leading-edge at mid-span. As schematically represented in Fig. 3.2, the x axis is aligned

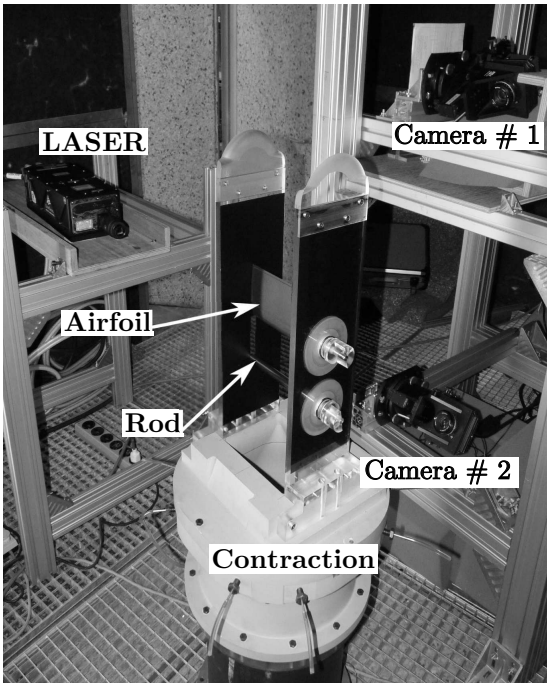

Figure 3.3: Experimental set-up configured for stereo-PIV measurements.

with the airfoil chord line, the y axis is oriented in the span-wise direction and the z axis forms a right-handed coordinate system with the two other axes.

Experiments description The experimental set-up presented in Fig. 3.2 allows to study the rod-airfoil and grid-airfoil noise interaction mechanisms. The rod-airfoil configuration involves periodic (the von Kármán vortex shedding) and broadband (the cylinder wake turbulence) phenomena. In contrast, the grid-airfoil case can be considered as a canonical experiment to study the broadband noise emitted by an airfoil subjected to isotropic and homogeneous turbulence. For the rod-airfoil configuration, two rod with 0.008 and 0.016 m diameter where chosen and the reference flow velocity, noted hereafter as U_{ref} was set to 10, 20 and 30 m/s. The testing case where a 0.016 m diameter rod is subjected to a 30 m/s flow has Reynolds and Mach numbers comparable to one of Jacob's [35] benchmark testing case. For all testing cases evaluated on this work, the Reynolds and Mach numbers are presented in Tab. 3.1:

Table 3.1: Rod-airfoil experimental parameters.

	rod 0.008 m			rod 0.016 m		
U_{ref} (m/s)	10	20	30	10	20	30
$Re_d \times 10^3$	5.1	10.2	15.3	10.2	15.3	30.6
$Re_c \times 10^4$	6.4	12.8	25.6	6.4	12.8	25.6
M	0.03	0.06	0.09	0.03	0.06	0.09
$f_{Sr=0.18}$	225	450	675	112.5	225	337.5

where Re_d and Re_c are the Reynolds number based, respectively, on the rod diameter and airfoil chord. In addition, $f_{Sr=0.18}$ is the frequency where the rod vortex shedding has been observed. In this work, it has been systematically observed that the vortex shedding occurred at $Sr = 0.18$. Noteworthy that considering a laminar incoming flow, for Re_d with order of magnitude of 10^3 to 10^4 the expected cylinder Strouhal number is 0.2. However, this discrepancy is attributed to the facility inflow turbulence intensity of approximately 4%, which is believed to be high enough to not satisfy the laminar incoming flow hypothesis.

The reference velocity U_{ref} is the jet center line velocity measured at the airfoil leading-edge height ($x = 0$). Details about the methodology applied to quantify the reference velocity are described in Appendix C. As shown in this appendix, the velocity is acquired with uncertainty of approximately 2.5% when the flow temperature varies up to 6℃. A common practice adopted during this experimental campaign consisted to run the flow facility until reach a stable temperature before performing the velocity calibration and further measurements (see Appendix D). Following this approach the reference velocity is measured with uncertainty of 1%.

For the grid-airfoil noise studies, two turbulence generation grids have been adopted. These grids are placed inside the contraction, as represented in Fig. 3.2. The grid is fairly coarse, with a grid made of two layers of parallel square rods superimposed at right angle. The downstream edges of the rows are manually chamfered to reduce grid-generated noise. When in used, the grid is inserted about 0.1 m upstream of the nozzle outlet, to allow a longer development of the turbulence before it interacts with the airfoil, and to partly shield the grid-generated noise from the microphone measurements.

The turbulence grids adopted are schematically represented in Fig. 3.4 and the geometric parameters are shown in Tab. 3.2.

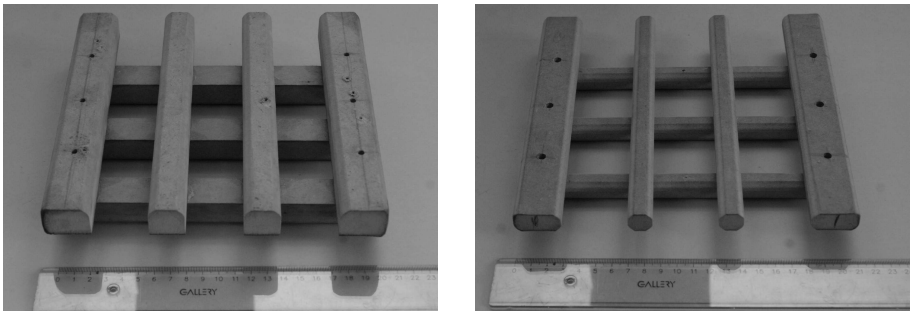

(a) Grid # 1 (b) Grid # 2

Figure 3.4: Turbulence generation grids.

Table 3.2: Turbulence grid parameters.

	Grid # 1	Grid # 2
Rod diameter (m)	0.022	0.015
Rod interlacing (m)	0.036	0.040
Open area ratio (%)	38	40

Table 3.3 indicates the flow velocity and corresponding longitudinal turbulence integral length scale (Λ_f) and velocity fluctuation u' characterized by hot-wire anemometry at the point (0,0,0) - corresponding to the jet center and airfoil leading-edge position.

Table 3.3: Grid-airfoil experimental parameters.

	Grid # 1			Grid # 2		
U_{ref} (m/s)	10	20	30	10	20	30
$Re_c \times 10^4$	6.4	12.8	25.6	6.4	12.8	25.6
M	0.03	0.06	0.09	0.03	0.06	0.09
u'	0.64	1.30	1.88	0.97	1.94	2.50
Λ_f (m)	0.010	0.012	0.012	0.013	0.013	0.013

From Tab. 3.3 it is important to remark that different turbulence grids leads to different velocity fluctuation RMS, while the turbulence integral length scale is

similar between grids.

3.2 Data acquisition and flow measurement hardware

Analog-to-digital data converter For the data acquisition a National Instruments cDAQ 9234 card is used. This acquisition card has a dynamic range of ± 5 V with 24 bit resolution. This system has an embedded analogic anti-alias filter with cut-off frequency automatically set from the selected sampling frequency. Consequently, only sampling frequencies

$$f_s = \frac{51200}{2^n} \tag{3.1}$$

can be set, where n is an integer number ranging from 0 to 5. This acquisition card is used for pressure and temperature transducers, hot-wire anemometry and microphone data acquisition.

Hot-wire anemometer For the hot-wire anemometry, a single wire, constant temperature, in-house system is used. The anemometer probe is placed in a carriage system moved by an EPOS controlled brushless DC electric motor which allows the probe to move within the plane yz, at a given height x, with precision of 0.1 mm.

The hot-wire anemometer dynamic calibration is performed through a square-wave test [17] (ref. page 52) which allows to conclude that the system can measure velocity fluctuation with frequency up to approximately 20 kHz. The hot-wire anemometer is statically calibrated in-situ using a Prandtl tube to measure the reference velocity, as presented in Fig. 3.5. As shown in Appendix C the King's Law with $n = 0.45$ is adopted for the static calibration. More details and issues related to the hot-wire calibration procedure are present in Appendix C.

For the hot-wire anemometer data acquisition, the sampling frequency is set to 51.2 kHz, which results to an anti-alias filter set to 25.6 kHz. Since the maximum hot-wire probe response is 20 kHz, results presented are limited to this frequency. For velocity and turbulence intensity measurements, the sampling time is defined to range 3 to 5 seconds, while for the cases where the power-spectral density is measured, the data is acquired during 60 seconds.

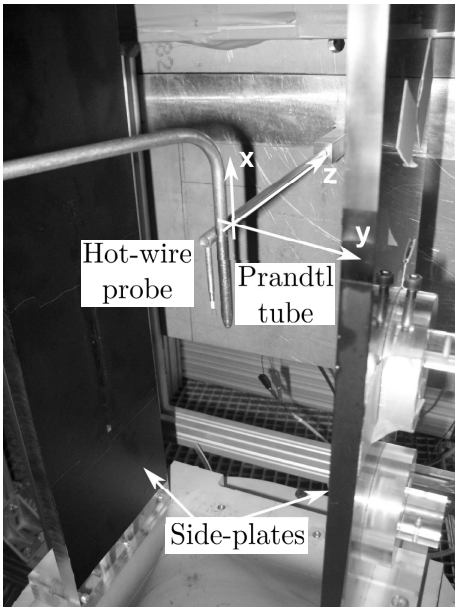

Figure 3.5: Hot-wire probe placed in the carriage system near the Prandtl tube. Representation of the hot-wire in-situ static calibration set-up. The horizontal distance between the hot-wire probe and the Prandtl tube is set to approximately 0.05 m.

Particle Image Velocimetry This work adopted the Stereoscopic Particle Image Velocimetry technique (stereo-PIV) to characterize the flow upstream of the airfoil leading-edge. This method allows to obtain the three flow velocity components in a plane (2D3C). The sub-plane chosen for PIV measurements is coincident with the xy plane, positioned upstream of the airfoil leading-edge and aligned with the airfoil. This rectangular sub-plane is limited by the points: (0,-0.375d,0), (0,0.375d,0), (-0.56d,-0.375d,0) and (-0.56d,0.375d,0), where d is the airfoil semi-span (2d = 0.2 m).

The stereo-PIV data is acquired with a LaVision FlowMaster PIV system, which is composed of two high-sensitivity, high-resolution digital cameras model Imager SX 4M. These cameras allow double frame image acquisition with 12 bit grayscale dynamic range and image area of 2360 x 1776 pixels. During the acquisition, the sampling frequency ranged from 0.625 Hz to 5 Hz, depending on the available computer RAM memory. Since the sampling frequency is much lower than the time scales of the phenomena studied in

this work, the acquisitions are statistically uncorrelated. Both cameras are equipped with 50 mm focal length Nikon Nikkor lenses. For the acquisitions, a focal ratio (f-number) of 5.6 is generally used, and in very specific cases, a focal ratio of 8 is adopted to increase the signal-to-noise-ratio of close to wall measurements. To obtain the Scheimpflug condition, these cameras are mounted with a support which allows the camera rotation with respect the objective lenses, therefore, the image is focused all over the studied plane. The distance between the objective lens and the camera sensor is carefully set to adapt the investigated plane field-of-view to the full height and length of the camera sensor. For this experiment, it was possible to measure an area of 75 mm width by 56 mm height, this dimensions corresponds, respectively 0.75d and 0.56d. For measurements close to the wall (in this case the airfoil leading-edge) measurements, the closest dimension achieved, respecting the minimum signal-to-noise requirements specified below, was of 0.19 mm. This distance corresponds to 12% of the airfoil leading-edge radius.

The PIV calibration plate is composed of precisely printed dots of 0.25 mm diameter spaced in a rectangular grid by 25 mm. Remembering that stereo-PIV requires 3-dimensional calibration, the plate is mounted on a traverse support, moved by a micrometer, which allows displacements along the z axis with precision of 20 μm. By turn, this calibration plate support is firmly fixed to a structure attached to the jet contraction, resulting to a system which is believed not to move during the calibration process. During the calibration procedure, three calibration planes are acquired: a first aligned with the laser light sheet; a second and a third, displaced by, respectively, 240 μm and 520 μm behind the first plane. The calibration images, acquired from both cameras, are automatically processed using the LaVision Davis 8 software resulting in a third order polynomial mapping function, which relates pixel to a geometrical position. Figure 3.3 shows the PIV experimental set-up.

A two cavities Quantel EverGreen double-pulse Nd:YAG laser was adopted which permits the maximum energy of 200mJ per pulse. A 25 mm semi-spherical lens is employed to obtain a focused light sheet. The laser emitter is placed on a table rigidly fixed to the ground, which allows two-degree of freedom movements on a plane controlled by two micrometers. This arrangement facilitates laser sheet geometrical alignment with the plane containing the airfoil leading-edge, minimizing undesirable wall reflections and improving the experimental repeatability. The laser intensity has been set, at each measurement, depending the seeding characteristics such as to improve the signal-to-noise ratio.

The seeding is produced by a PIVTEC PivPart45 aerosol generator. The chosen operating liquid is the DEHS (Di-Ethyl-Hexyl-Sebacat). The inlet/outlet pressure relation and aerosol generator valves position were set to produce

particles with size distribution following a PDF (Probability Density Function) with mean size distribution of 1 μm. The particle concentration was tested, in each experiment, trying to maximize the signal-to-noise-ratio of the acquired PIV images. The generated seeding particles are inserted in the centrifugal fan entrance, guarantying homogeneous mixing at the flow facility exit.

To achieve convergence on the flow quantities determination, the grid-airfoil case was sampled with 1,000 images per experiment while 1,500 images are acquired for the rod-airfoil experiments. This second case demanded the higher number of images given the higher turbulence intensity.

The image processing was performed by the LaVision Davis 8 software. In a pre-processing phase, the images are minimum-maximum normalized and then a mask is applied to remove the image zones outside the range of interest. The vector calculation is performed in a multi-pass approach, where, the two first passes adopts rectangular window with 32 by 32 pixel. For the further passages an adaptive algorithm is used, where the window size and weight is automatically set by the software up to the final size of 8 by 8 pixel, which should be achieved in a maximum of 5 passages. This leads to the computation of vectors with a spatial resolution of 0.1406 by 0.1406 mm. For the vectors calculation, after each passage, a post-processing step identifies vectors with peak-to-peak ratio smaller than 1.5 and discard these vectors. In a final post-processing phase, vectors with difference to average higher than 1.5 the standard deviation of the neighbor vectors are also discarded. Finally, only images with more than 97% of valid vectors are used for calculations.

Acoustic measurements The acoustic measurements are performed with a 1/2-inch Brüel & Kjaer microphone. The microphone type adopted is the 4133 and with pre-amplifier model 2669. This free-field microphone permits flat response at frequencies from 10 Hz to up to 20 kHz.

For the microphone signal conditioning – filtering and amplification – the low noise Brüel & Kjaer Nexus system type 2690 is adopted. The conditioner the high-pass filter frequency is set to 20 Hz and the low-pass frequency is set to 22.6 kHz.

The microphones are calibrated, in amplitude, using a Brüel & Kjaer type 4231 calibrator, with a 1 kHz tone at levels of 94 or 114 dB. For the analogic digital conversion, the system described before has been used. For the experiments performed, the sampling frequency is, in general, set to 51.2 kHz and the sampling time to 60 seconds.

3.3 Facility aeroacoustic characterization

This section presents the facility characterization by means of hot-wire and PIV techniques. These measurements are performed in the plane $x = 0$, which is the yz plane at the height occupied by the airfoil leading-edge. The distance between this plane and the airfoil leading-edge corresponds to 1.2d. Considering a general rule which says that the jet potential extends up to 6 or 7 times its diameter, depending the Reynolds number, it is possible to assume that the airfoil is within the jet core. This study determines the flow uniformity in the following configurations: free-jet; grid turbulence # 1 and # 2; rod with 0.008 and 0.016 m diameter. This quantification is important for the validation of the semi-analytical techniques proposed in this thesis. By comparing hot-wire and PIV data measured along the y axis at the $x = 0$ position, it is possible to cross-verify each technique and obtain insights about validity and limitations of each flow measurement approach. In addition, flow spatial correlation and turbulence energy spectra are studied indicating the turbulence (an)isotropy characteristics. The facility background noise is analyzed and presented together with the rod-airfoil and grid-airfoil acoustic baseline results, to be used for semi-analytical methodologies validation.

Free-jet configuration The nomenclature free-jet refers to flow in presence of side-plates with no turbulence grid nor rod installed. The free-jet velocity profile is characterized in the plane $x = 0$. For this measurement, a traverse system is employed to place the hot-wire probe at different positions along the xz plane. The points distribution, in this plane, is chosen following a rectangular grid with higher refinement at regions with larger velocity gradients. In this study, a total of 500 points distributed along the yz plane are acquired. For each measurement position the data is sampled at a rate of 51.2 kHz during 3 seconds. Results for the case with reference velocity U_{ref} of 30 m/s are shown in Fig. 3.6.

From this figure it is noticed that, for the free jet configuration, the flow mean velocity is practically uniform within the jet exit area. Regarding the turbulence intensity, it is verified that at the region of interest, the flow turbulence intensity equal to 4% and practically uniform over the line $z/d = 0$ where the airfoil leading-edge will be located. This turbulence intensity level is relatively large, mostly due to the low contraction ratio of this flow facility, the absence of turbulence reduction grids and the presence of a single honeycomb section localized in the duct, just after the settling chamber. By considering that the major objective of this thesis is to study the grid-airfoil interaction phenomena, this turbulence intensity level does not raise any further concern once the flow velocity is uniform along the region of interest to this study.

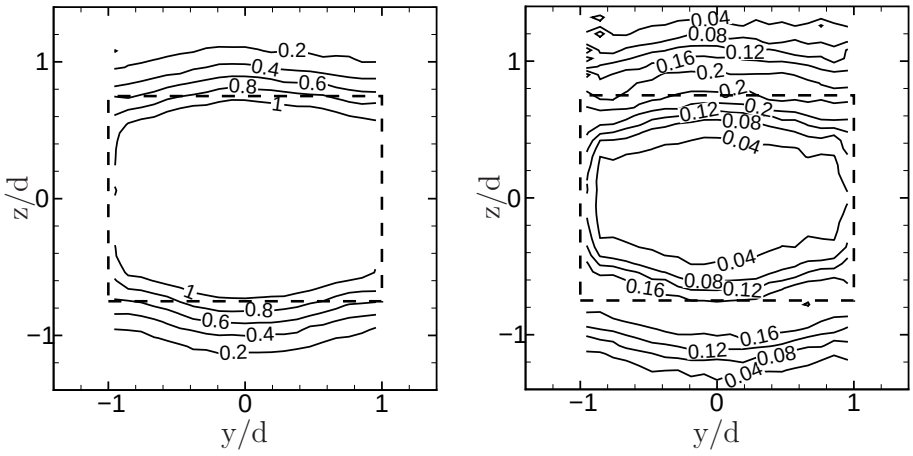

(a) U_0/U_{ref} - Free jet (b) u'/U_{ref} - Free jet

Figure 3.6: Average velocity and turbulence intensity contour lines for the free-jet at $x = 0$. Reference velocity (U_{ref}) of 30 m/s. The dashed line represents the projection of the nozzle outlet to the velocity measurement plane.

Figure 3.7 presents the free-jet background noise comparing the configurations with and without side-plates. The acoustic measurements presented in this section are performed using the microphone, data conditioner and acquisition card previously described. The microphone is placed 90° from the flow direction at 1 m distance from the airfoil leading-edge. The data is acquired during 60 seconds at a sampling frequency of 51.2 kHz. The power spectral density is computed using the Welch algorithm [64], where the data is divided in 50% overlap blocks of 4096 samples which are hanning windowed. This algorithm performs approximately 1500 averages and the noise spectra has frequency resolution of 12.5 Hz.

This figure shows that the background noise scales with the 6^{th} power of the flow velocity for the the cases with reference velocity equal to 20 and 30 m/s and frequency below 3,000 Hz. The 6^{th} power scaling, in principle, may indicate that the major noise source is related with solid boundaries interacting with flow. Noteworthy, the amplitude of the background noise does not decay uniformly with the frequency, but it presents a "bump" in the frequency range between 1,000 and 3,000 Hz. Observing the noise scaling at this frequency range it is observed that the shape of the "bump" does not present a Strouhal dependency, e.g. not related with the flow velocity. Investigations was conducted to understand the reason why this "bump" scales with the 6^{th} power

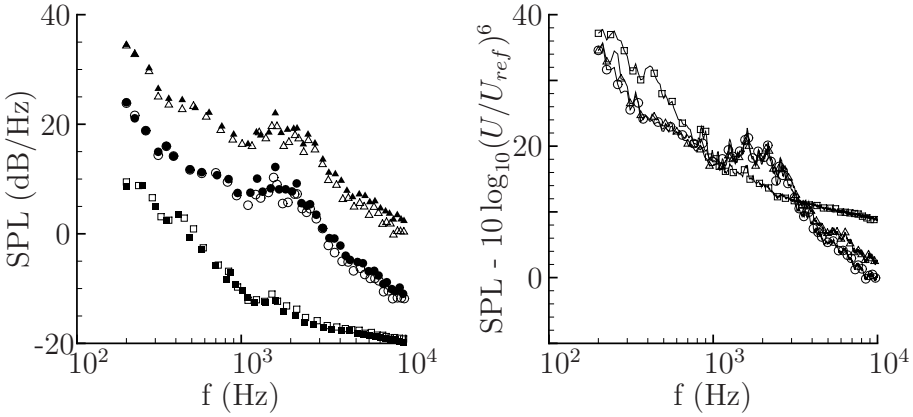

(a) Free-jet background noise with and without side-plate

(b) Free-jet background noise scaled with the reference flow velocity

Figure 3.7: Free-jet background noise comparison, for the jet with and without side-plates. The full symbols represents the jet noise measured with side-plate, while the empty symbols represents the measurements with no side plate. Square: $U_{ref} = 10$ m/s; Circle: $U_{ref} = 20$ m/s; Triangle: $U_{ref} = 30$ m/s.

of the flow velocity but does not have a Strouhal dependency with inconclusive results. No extra effort was made to comprehend this effect since its influence was not observed in the grid and rod background noise.

The non-scaling for the 10 m/s case indicates a different noise generation mechanism. Observations performed in-situ indicates that, at this flow velocity, the noise generated at the centrifugal fan dominates the observable noise, but the differentiation between the flow and the mechanically generated noise is hard to be experimentally verified since one implicates the other. Now comparing the side-plate effect, it is seen that this structure only contributes, with some relevance, to the total background noise produced at a flow velocity of 30 m/s, with more pronounced participation at higher frequencies. Figure 3.8 presents the noise amplitude scaling with the 8^{th} power of the reference flow velocity. From where it is observed that for frequencies higher than 3,000 Hz the noise amplitude scales with the 8^{th} power of the reference flow velocity. This result likely indicate that, for this frequency range, quadrupole type noise sources related with the flow stress tensors present in the jet is the predominant noise source.

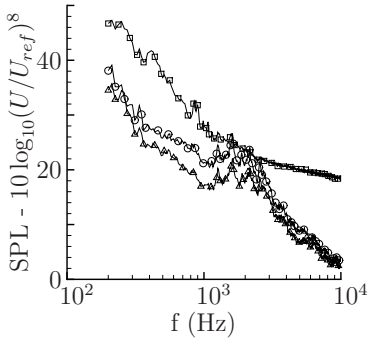

Figure 3.8: Free-jet background noise scaling with the 8^{th} power of the reference flow velocity. Square: U_{ref} = 10 m/s; Circle: U_{ref} = 20 m/s; Triangle: U_{ref} = 30 m/s.

Turbulence grid configuration Initially, the flow velocity is characterized at the plane $x = 0$. For this measurement, similarly to the free-jet configuration, hot-wire traverse measurements are performed to determine the flow mean velocity and turbulence intensity. These acquisitions are performed for the turbulence generation grids # 1 and # 2, with results shown in Fig. 3.9 and Fig. 3.10.

From Figs. 3.9 and 3.10 it is verified that the presence of the turbulence generation grid causes flow acceleration at the region close to the side plates. In addition, it is verified a larger mean flow velocity gradient along the y axis for the grid #2 compared with the grid #1. Regarding the turbulence intensity, u' is practically uniform along the area of interest. In addition, it is observed that both turbulence grids have turbulence intensity of approximately 8%.

After characterizing the facility at the plane where the airfoil leading-edge is placed, now we analyze the flow at the line where the airfoil leading-edge is localized. This study is important since is from this specific position that the experimental inputs to the semi-analytical techniques are generally taken. Figure 3.11 compares the longitudinal mean velocity measured with hot-wire and PIV techniques for each turbulence grid with data acquired for a reference velocity (U_{ref}) of 30 m/s.

From Fig. 3.11 it is, initially, observed an excellent agreement between both measurement techniques for the average flow velocity computation. In both cases, the flow closer to the side walls is accelerated when compared with the flow at the center of the jet. For the grid # 1, the flow presents higher uniformity at the center of the jet, while for the grid # 2 the flow accelerates,

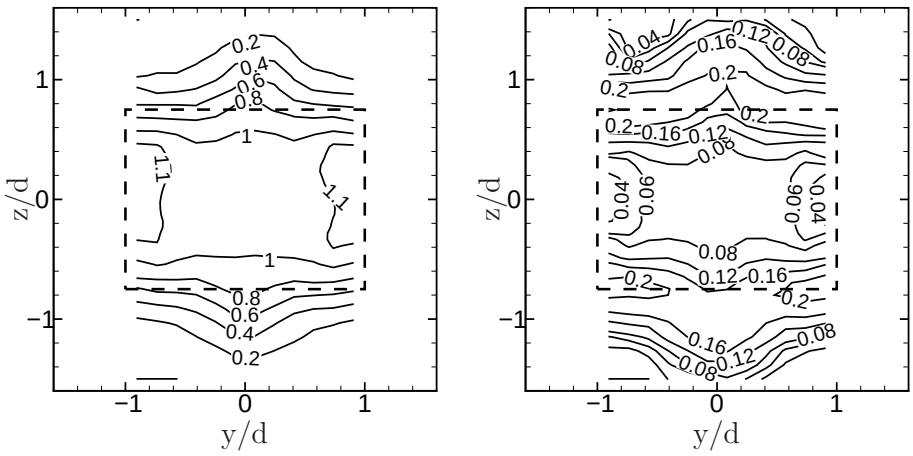

(a) U_0/U_{ref} - Grid # 1 (b) u'/U_{ref} - Grid # 1

Figure 3.9: Mean velocity and turbulence intensity contour lines measured at $x = 0$ for the grid # 1. Data acquired for a flow with reference velocity of 30 m/s. The dashed line represents the projection of the nozzle outlet to the velocity measurement plane.

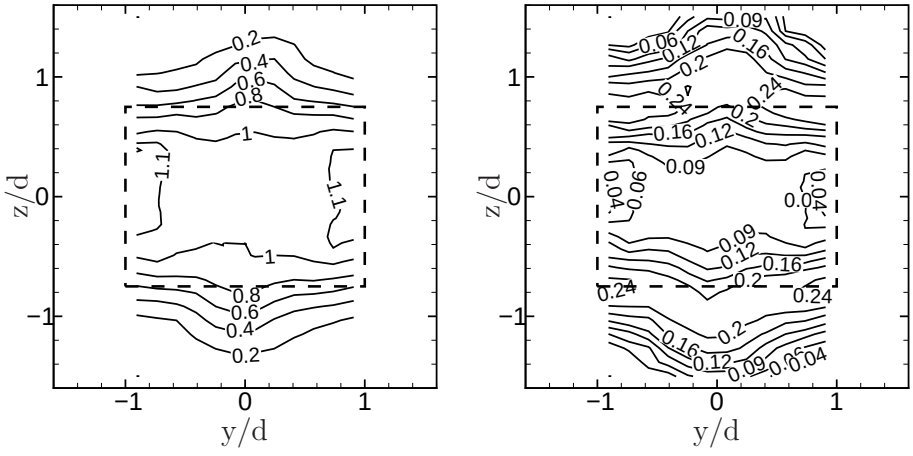

(a) U_0/U_{ref} - Grid # 2 (b) u'/U_{ref} - Grid # 2

Figure 3.10: Mean velocity and turbulence intensity contour lines measured at $x = 0$ for the grid # 2. Data acquired for a flow with reference velocity of 30 m/s. The dashed line represents the projection of the nozzle outlet to the velocity measurement plane.

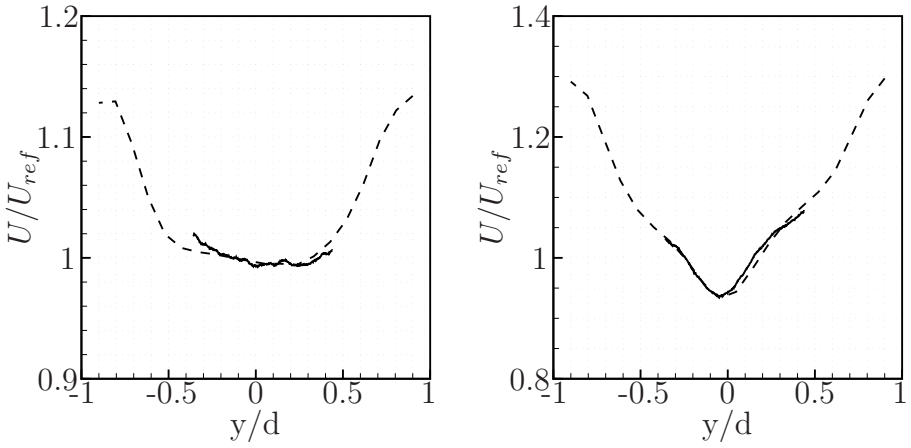

(a) Grid # 1 (b) Grid # 2

Figure 3.11: Comparison of the longitudinal average velocity measured with hot-wire and PIV techniques. Data measured for the grid # 1 and # 2 at the line which corresponds to the airfoil leading-edge position, for a flow with reference velocity of 30 m/s. Dashed line: hot-wire measurement; Continuous line: stereo-PIV measurement.

close to the borders, up to 30% compared with than the center line velocity.

After characterizing the average flow at the line where the airfoil leading-edge is placed, another important quantity to be characterized is the flow velocity fluctuation root-mean-square. This quantity is formally defined by Eq. E.2 and Fig. 3.12 compares results obtained with the hot-wire anemometry and PIV techniques.

Figure 3.12 shows, for both turbulence grid analyzed, that the PIV technique slightly underpredicts the velocity fluctuation root-mean-square. Furthermore, it is observed for both grids that the velocity fluctuation u' decreases as it gets closer to the side plates, and, for grid # 2 it is verified a small reduction at the center of the jet.

The uncertainty related with the mean velocity and turbulence intensity is determined considering random and systematic errors. For the hot-wire measurement, the systematic uncertainties are the related with the calibration and the drift in the ambient temperature, while the random error considers 95% of confidence on the determination of the mean velocity and turbulence intensity. For the PIV measurement, the systematic errors are related with the

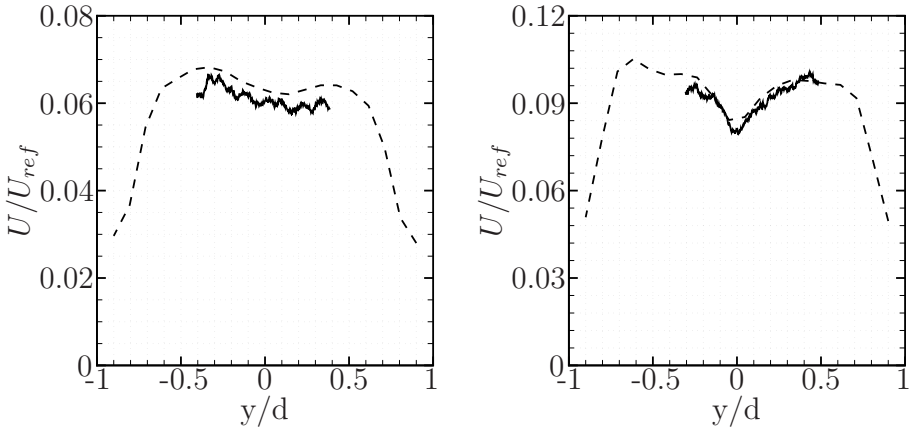

(a) Grid # 1 (b) Grid # 2

Figure 3.12: Comparison of the normalized longitudinal root-mean-square velocity fluctuation measured with hot-wire and PIV techniques. Data measured for the grid # 1 and # 2 at the line which corresponds to the airfoil leading-edge position, for a flow with reference velocity of 30 m/s. Dashed line: hot-wire measurement; Continuous line: stereo-PIV measurement.

image magnification factor, the displacement error and the separation time, while the random error is determined with 95% of confidence level in the determination of the mean velocity and turbulence intensity. Therefore the uncertainty breakdown is:

- Mean velocity

  Hot-wire anemometry:

  calibration error (1.2%);

  ambient temperature drift (0.8%);

  random error (0.4%);

  Total: 1.5%.

  PIV:

  Magnification factor (0.3%);

  Displacement (2%);

  Separation time (0.1%);

  random error (2.5%);

  Total: 3.2%.

- Turbulence intensity

  Hot-wire anemometry:

  calibration error (1.2%);

  ambient temperature drift (0.8%);

  random error (0.6%);

  Total: 1.5%.

  PIV:

  Random error – total error considered – (1.9%).

A next flow quantity to be characterized is the spatial correlation. The analysis of this flow quantity, combined with other quantities presented next, indicates if the flow turbulence can be described by an isotropic and homogeneous turbulence model. The flow correlations are defined by:

$$f(x) = \frac{\overline{u(\xi)u(\xi+x)}}{u'(\xi)u'(\xi+x)}\,, \tag{3.2}$$

$$g(x) = \frac{\overline{v(\xi)v(\xi+x)}}{v'(\xi)v'(\xi+x)}\,, \tag{3.3}$$

$$h(x) = \frac{\overline{w(\xi)w(\xi+x)}}{w'(\xi)w'(\xi+x)}\,, \tag{3.4}$$

where u', v' and w' are, respectively, the longitudinal, transverse and normal velocity fluctuation components. The time longitudinal and transverse correlations are given by:

$$R_E(t) = \frac{\overline{u(\tau)u(\tau+t)}}{u'(\tau)u'(\tau+t)}\,, \tag{3.5}$$

and the space correlations are defined by:

$$\Lambda_f = \int_0^\infty f(x)\mathrm{d}x\,, \tag{3.6}$$

$$\Lambda_g = \int_0^\infty g(x)\mathrm{d}x\,, \tag{3.7}$$

$$\Lambda_h = \int_0^\infty h(x)\mathrm{d}x\,. \tag{3.8}$$

Furthermore the Taylor hypothesis, which relates the time and space correlations is defined as:

$$\Lambda_f = \overline{U} T_E \,. \tag{3.9}$$

Figures 3.13 and 3.14 presents, respectively, the longitudinal and transverse correlations comparing the hot-wire and PIV techniques with theoretical results obtained from the von Kármán and Liepmann models for isotropic turbulence. In this calculation, the time correlation, obtained with hot-wire measurements, is transformed into longitudinal space correlation through the Taylor's hypothesis.

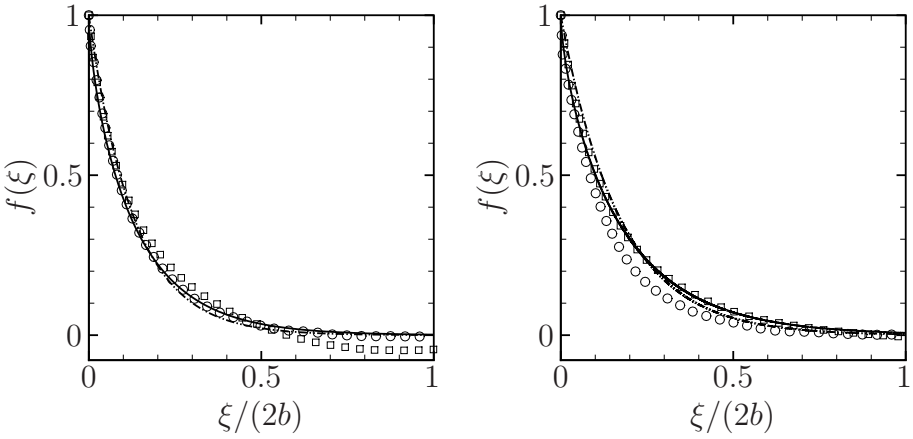

(a) Grid # 1 (b) Grid # 2

Figure 3.13: Comparison of the longitudinal correlation measured with hot-wire and PIV techniques against the von Kármán and Liepmann models for isotropic turbulence. Open circle symbol: Hot-wire measurement; Open square symbol: stereo-PIV measurement; Continous line: von Kármán model; Dash dot dot line: Liepmann model.

From Fig. 3.13 it is observed that for the grid # 1 the correlation results obtained from the PIV measurements agrees very well with the von Kármán and Liepmann theoretical models for isotropic turbulence. Discrepancy is observed for the correlation results obtained with the hot-wire technique. While, for the grid # 2, the hot-wire correlation better agrees with theoretical models for isotropic turbulence, and PIV measurements show some level of discrepancy.

Since the hot-wire anemometry experiments uses a single wire probe, only the velocity correlation related to the predominant flow velocity - in this case the

longitudinal velocity - is measured. Nevertheless, the PIV technique allows to distinguish each of the three flow velocity components, consequently it is possible to measure not only the longitudinal but also the transverse flow correlation. Figure 3.14 compares the experimentally obtained transverse correlation with theoretical results for isotropic turbulence given by the von Kármán and Liepmann theories.

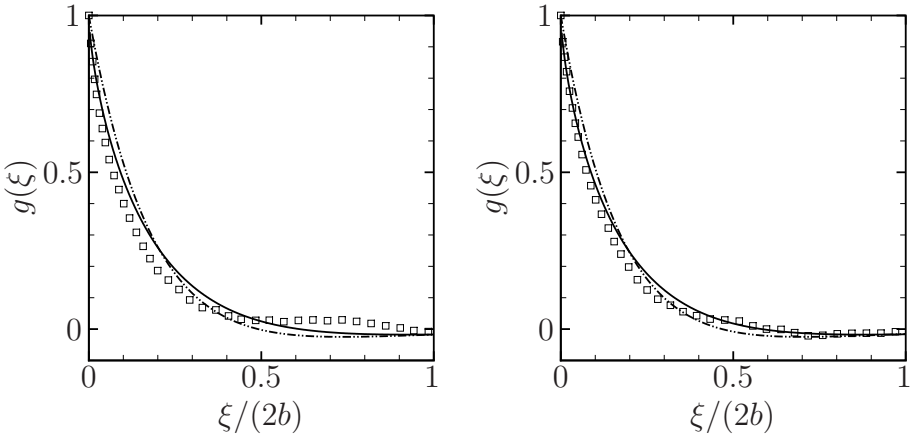

(a) Grid # 1 (b) Grid # 2

Figure 3.14: Comparison of the transverse correlation measured with hot-wire and PIV techniques against the von Kármán and Liepmann models for isotropic turbulence. Open square symbol: stereo-PIV measurement; Continous line: von Kármán model; Dash dot dot line: Liepmann model.

Observing Fig. 3.14 it is verified an overall good agreement between the measured results and theoretical models for isotropic turbulence.

This analysis shows that the longitudinal and transverse flow correlations are in reasonably good agreement with isotropic turbulence models.

From a practical sense, it is not possible to compute the previous integrals defined from zero to infinite. Among the proposed approaches to perform this integration from experimental data this work preferred the Hinze [33] methodology, which integrates from zero up to the first abscissa crossing of the functions f, g, R_E or R_L. More details about flow correlations for isotropic turbulence is presented in Appendix E. Figure 3.15 compares the integral correlation length measured with hot-wire anemometry - after the Taylor hypothesis application - and PIV techniques.

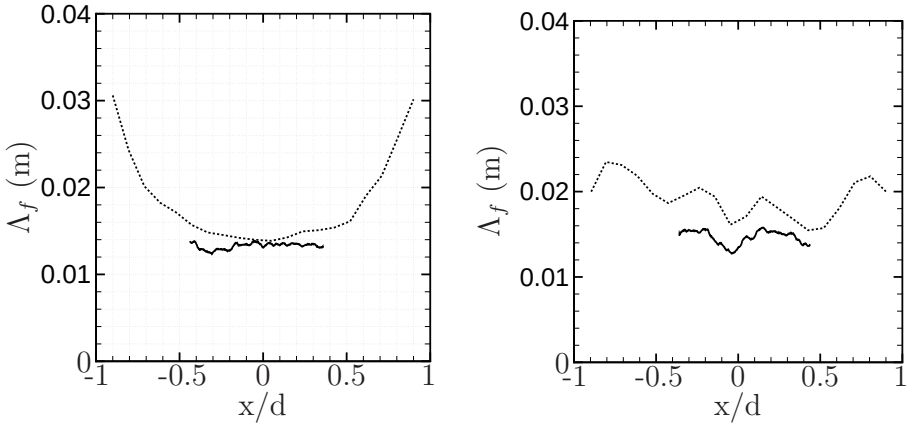

(a) Grid # 1 (b) Grid # 2

Figure 3.15: Comparison of the turbulence longitudinal integral correlation length measured with hot-wire and PIV techniques. Continous line: stereo-PIV measurements; Dotted line: Hot-wire measurements.

From Fig. 3.15 it overall good agreement is observed on the shape of the curves for both measurements techniques, with the PIV results slightly under predicting the integral correlation length scale when compared with hot-wire anemometry results. Furthermore for grid # 1, the integral turbulence length scale is larger closer to the side plates, while for the grid # 2 this flow quantity is practically constant along the axis y.

A final flow quantification study concerns the turbulence energy spectrum. The flow longitudinal energy spectrum is, firstly, solely characterized by the hot-wire anemometry technique. For this study the flow turbulence is measured at the center of the jet for flow velocities of 10, 20 and 30 m/s. As detailed in Appendix E, the turbulence power spectral density is computed accordingly:

$$\Phi_{uu}(f) = \frac{4u'}{\overline{U}} \int_0^\infty f(x)\cos(k_x x)\mathrm{d}x = 4u' \int_0^\infty R_E(t)\cos(\omega t)\mathrm{d}t \tag{3.10}$$

$$\Phi_{vv}(f) = \frac{4u'}{\overline{U}} \int_0^\infty g(x)\cos(k_x x)\mathrm{d}x = 4u' \int_0^\infty T_E(t)\cos(\omega t)\mathrm{d}t \tag{3.11}$$

with the relation between $\Phi_{uu}(f)$ and $\Phi_{uu}(k_x)$:

$$\Phi_{uu}(k_x) = \frac{\overline{U}}{2\pi}\Phi_{uu}(f) \qquad \Phi_{vv}(k_x) = \frac{\overline{U}}{2\pi}\Phi_{vv}(f) \tag{3.12}$$

In this measurement the hot-wire data is sampled for 60 seconds with a sampling rate of 51200 Hz. The power spectral density is estimated using the Welch algorithm with 4096 samples per block and 50% overlap between blocks. Each block is hanning windowed. With these parameters the power spectral density is estimated with approximately 1500 averages and frequency resolution of 12.5 Hz. The normalized turbulence energy results are present in Fig. 3.16 for both turbulence grids.

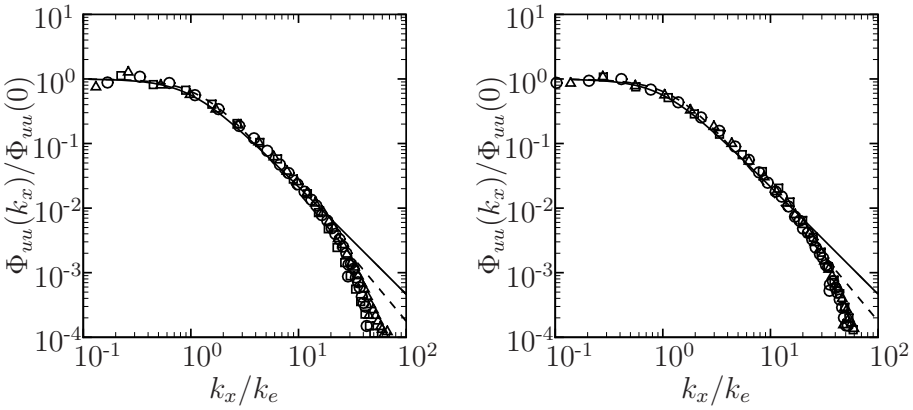

(a) Grid # 1 (b) Grid # 2

Figure 3.16: Longitudinal turbulence energy spectra measured with hot-wire anemometry compared with the von Kármán and Liepmann models for isotropic turbulence. Square symbols: v = 10 m/s; Triangle symbols: v = 20 m/s; Circle symbols: v = 30 m/s; Continuous line: von Kármán model; Dashed line: Liepmann model.

From Fig. 3.16 it is verified that, for both turbulence generation grids, the measured values agrees better with the von Kármán turbulence model for isotropic turbulence.

After comparing the turbulence energy spectrum measured with hot-wire anemometry, it is possible to compare results using both hot-wire and PIV techniques. The approach used in this work to compute the turbulence energy spectra, from PIV experiments, extracts the flow velocity component in study along the x line, at a height corresponding to $y = 0$ (same measurement location as the hot-wire probe). For the power spectral density estimation, the PIV velocity component is, firstly, hanning windowed, Fourier transformed, multiplied by the complex conjugated, divided by the spectral resolution, corrected to represent an one-sided spectrum and adjusted again to compensate

the energy loss imposed by the hanning window. This process is performed to each valid PIV image and, finally, the data is averaged. Figure 3.17 compares the turbulence energy spectra obtained from hot-wire anemometry with the energy spectra obtained from PIV for both turbulence grids at a reference flow velocity of 30 m/s.

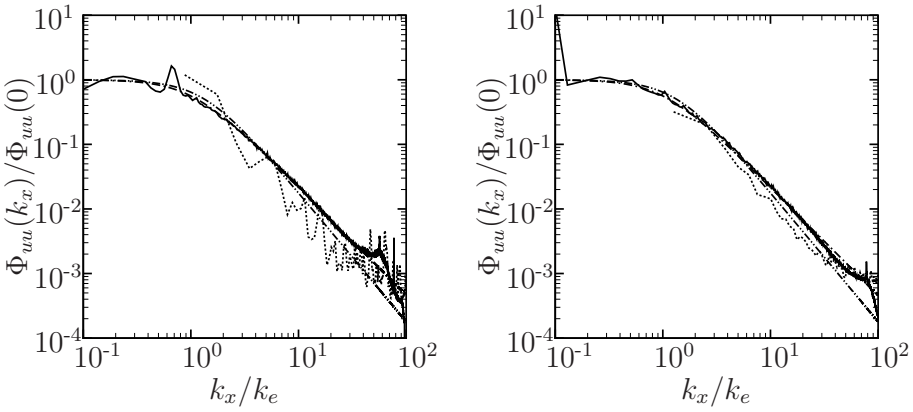

(a) Grid # 1 (b) Grid # 2

Figure 3.17: Comparison of the longitudinal turbulence energy spectra measured with hot-wire and PIV techniques compared against the von Kármán and Liepmann models for isotropic turbulence. Continous line: Hot-wire; Dotted line: stereo-PIV; Dash dot line: von Kármán model; Dash dot dot model: Liepmann model.

The overall good agreement between the energy spectra obtained with hot-wire and PIV techniques, presented in Fig. 3.17, indicates the validity of the approach proposed here aiming to use PIV data for turbulence energy spectra calculations. Due to the reduced quantity of images, it is observed that the PIV spectrum is, in general, noisier than the hot-wire. In addition, the limited block size, from where the PIV data is Fourier transformed, imposes the minimum spectral frequency.

The contribution of the turbulence generation grid # 1 and # 2 to the facility background noise together with the noise intensity scaling with the reference flow velocity are presented in Figs. 3.18 and 3.19. For these measurements the microphone position, sampling parameters and data processing are similar to the previously presented case.

From Figs. 3.18 and 3.19 it is observed that the turbulence generation grid #

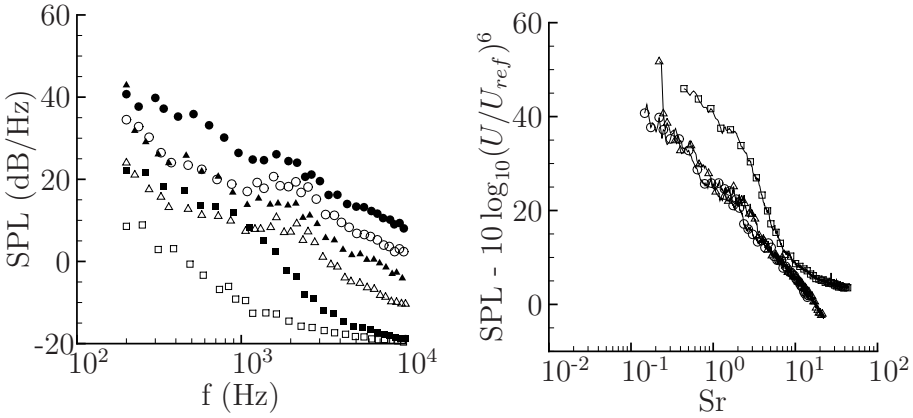

(a) Background noise comparison with and without the grid # 1

(b) Grid # 1 background noise scaled with the reference flow velocity

Figure 3.18: Comparison for the facility background noise with and without the turbulence generation grid # 1 and noise sound power level scaling against the reference flow velocity. The filled symbols refers to noise measurements with turbulence generation grid, while the empty marks refers to acoustics measurements without turbulence grid. Square: $U_{ref} = 10$ m/s; Triangle: $U_{ref} = 20$ m/s; Circle: $U_{ref} = 30$ m/s.

1 and # 2 contributes significantly to the facility background noise for all flow velocities. In addition, while the grid # 1 noise intensity scales very well with the 6^{th} power of the reference flow velocity, the grid # 2 scaling is reasonable. This indicates a change of the predominant noise generation mechanism at each configuration indicating that while the grid # 1 has predominantly sources related with the flow structure interaction, the grid # 2 presents a combination of flow structure interaction with flow turbulence generated noise.

Rod configuration The rod configuration refers to the flow facility equipped with the side-plate and the rod. Following the protocol of the turbulence grid configuration the rod case is studied. Initially, hot-wire traverses are measured at the plane $x = 0$, plane which contains the airfoil leading-edge. For these measurements, the area of interest is discretized in a rectangular grid with 720 points and higher nodes concentration regions higher velocity gradients. This measurement procedure has been performed for the rod with 0.008 and 0.016 m diameter, with results, respectively, presented in Figs. 3.20 and 3.21, where the mean and turbulence intensity results are shown.

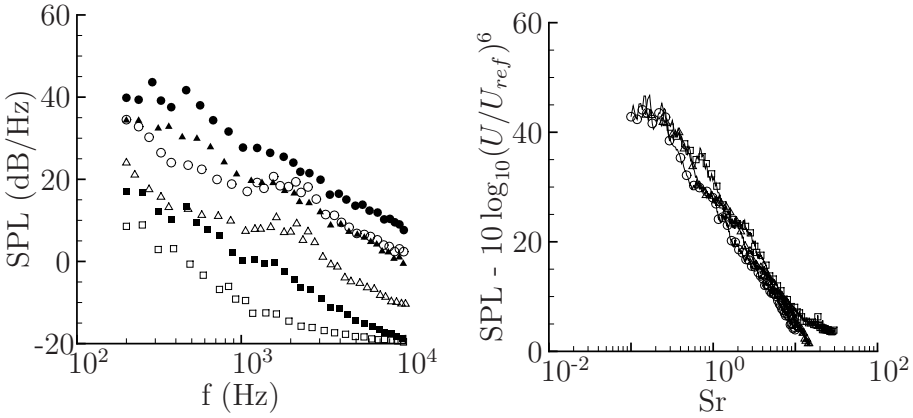

(a) Background noise comparison with and without the grid # 2

(b) Grid # 2 background noise scaled with the reference flow velocity

Figure 3.19: Comparison for the facility background noise with and without the turbulence generation grid # 2 and noise sound power level scaling against the reference flow velocity. The filled symbols refers to noise measurements with turbulence generation grid, while the empty marks refers to acoustics measurements without turbulence grid. Square: $U_{ref} = 10$ m/s; Triangle: $U_{ref} = 20$ m/s; Circle: $U_{ref} = 30$ m/s.

Observing the mean velocity profile presented for both rods in Fig. 3.20, it is firstly observed that along the airfoil leading-edge position the flow is decelerated to 90% of the reference velocity and that the average velocity varies less than 10% of the reference velocity. Figure 3.21 presents the turbulence intensity contour lines.

Observing the turbulence intensity results presented in Fig. 3.21 it is observed that, for the rod with 0.008 m diameter, this value reaches 12%, while for the rod with 0.016 m diameter the maximum is 20%. The velocity fluctuation is relatively uniform along the airfoil leading-edge position, being slightly reduced presumably due to the side plates.

The flow traverse acquisitions performed at the airfoil leading-edge position, presented in Fig. 3.22 and 3.22, respectively compares the mean velocity and turbulence intensity, measured by the hot-wire anemometry and PIV techniques, for the rod with 0.008 and 0.016 m diameter.

From Figs. 3.22 it is observed that the hot-wire and PIV techniques show some mismatch on the average velocity for the rod with 0.008 m diameter, while both techniques agree quite well for the rod with 0.016 m diameter. This

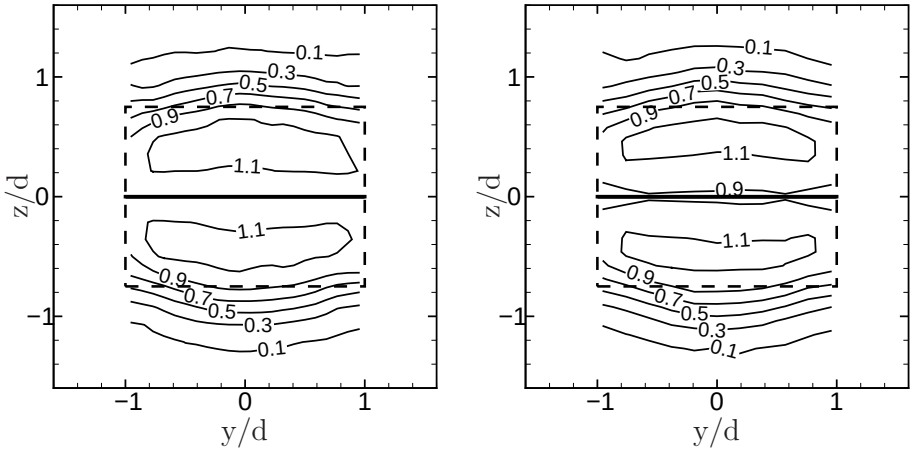

(a) Rod 0.008 m (b) Rod 0.016 m

Figure 3.20: Mean normalized velocity contour lines measured at $x = 0$ for the rod. The mean velocity is normalized by the reference velocity of 30 m/s. The dashed line represents the projection of the nozzle outlet to the velocity measurement plane. The Continous line represents the projection of the cylinder center line to the measurement plane.

disagreement is here explained by the fact that, since the rod configuration presents higher velocity gradients along the z axis, a small misalignment between the hot-wire traverse system and the PIV plane leads to important results differences between both techniques, when compared to the grid turbulence cases. In addition, it is seen that the average velocity remains practically constant, along the airfoil span, for the rod with 0.008 m diameter, while for the rod with 0.016 m diameter, the flow velocity decays approximately 10% of the reference velocity at regions closer to the side-plates. Figure 3.23 presents the comparison of the turbulence intensity measured with both techniques.

Comparing the turbulence intensity measured by hot-wire and PIV techniques, it is observed that, for both cylinder cases analyzed, the values and the general shape of the curves reasonably agrees. In addition, for both cylinders, the flow turbulence intensity decreases closer to the side-plates.

Figure. 3.24 presents a comparison between the flow turbulence power spectral density measured with hot-wire and PIV techniques for a flow with reference velocity (U_{ref}) of 30 m/s.

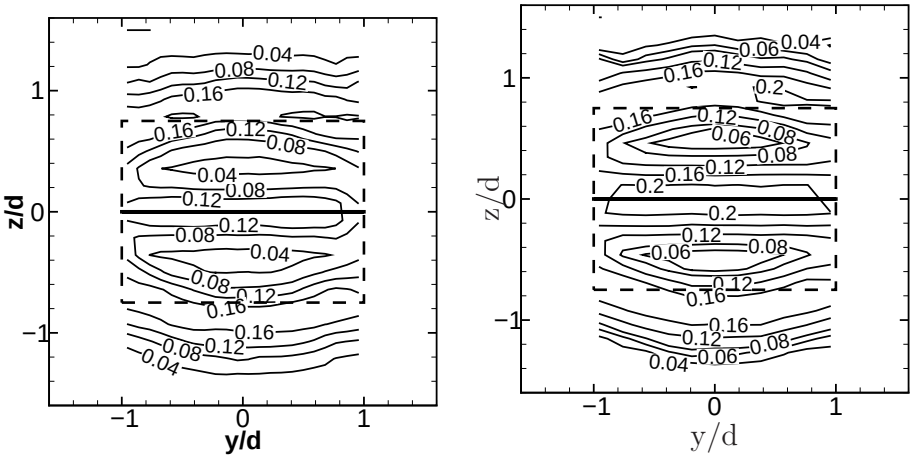

(a) Rod 0.008 m (b) Rod 0.016 m

Figure 3.21: Turbulence intensity contour lines measured at $x = 0$ for the rod. The turbulence intensity are normalized by the reference velocity of 30 m/s. The dashed line represents the projection of the nozzle outlet to the velocity measurement plane. The Continous line represents the projection of the cylinder center line to the measurement plane.

From Fig. 3.24 it is observed that the turbulence power spectral density measured by hot-wire and PIV techniques reasonably agrees. For both cylinder diameters the PIV technique is unable to capture the cylinder vortex shedding frequency - which corresponds to a tone at the turbulence spectra - due to the low spectral resolution linked to the domain size limitation.

Finally Figs. 3.25 and 3.26 presents the background noise for the rod with 0.008 m and 0.016 m diameter and its respectively scaling with the reference flow velocity. The microphone data are acquired and processed using the same parameters as the previous acoustic results presented.

From Figs. 3.25 and 3.26 it is observed the presence of a tone corresponding to the cylinder vortex shedding frequency. In both cases this tone is located at $Sr = 0.18$ which corresponds to the low Reynolds cylinder vortex shedding frequency. For the reference flow velocity of 10 m/s it is observed that the rod with 0.016 m diameter vortex shedding frequency is below the anechoic room cut-off frequency, consequently, the vortex shedding phenomena cannot be quantified at this flow velocity. Furthermore, the noise intensity of both cylinder scales with the sixth power of the reference flow velocity. This confirms the canonical dipole noise radiation characteristic of a cylinder.

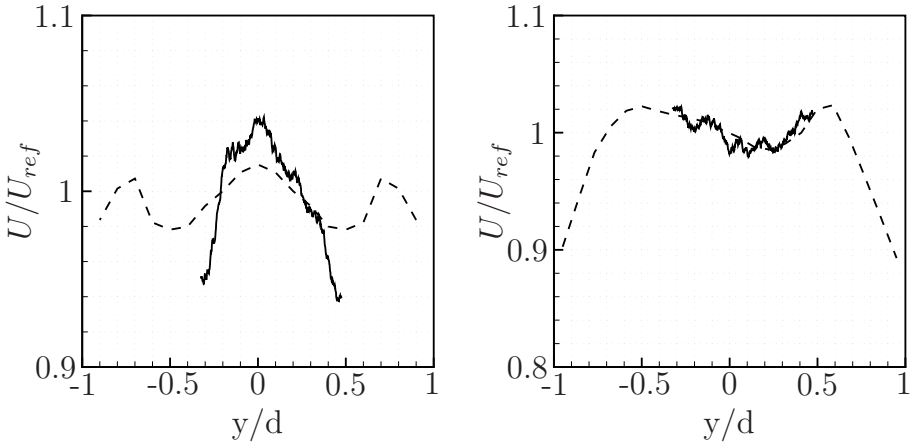

(a) Rod 0.008 m (b) Rod 0.016 m

Figure 3.22: Comparison of the longitudinal average velocity measured with hot-wire and PIV techniques. Data measured for the rod with 0.008 and 0.016 m diameter at the line corresponding to the airfoil leading-edge position, for a flow with reference velocity of 30 m/s. Continous line: stereo-PIV; Dashed line: Hot-wire.

3.4 Aeroacoustic results in presence of the airfoil

Grid-airfoil configuration Firstly, the grid-airfoil noise case is studied, where the rig background noise is compared with the noise produced in presence of the airfoil. These measurements and data processing are performed following the same experimental parameters previously presented, for the experimental facility noise characterization, results are presented in Fig. 3.27.

For low frequencies, the grid-airfoil interaction noise is higher than the background noise, but at higher frequencies the background noise becomes comparable to the sound generated by the airfoil.

In order to separate the facility background noise from the sound generated by the airfoil, the airfoil generated noise is considered to be statistically uncorrelated with the facility background noise. Thus the relation can be applied to express the noise pressure power spectral density (SPL):

$$SPL(f)\,[dB/Hz] = 10\log_{10}\frac{P_{xx}(f)^{airf+back} - P_{xx}(f)^{back}}{\left(2\times 10^{-5}\right)^2} \tag{3.13}$$

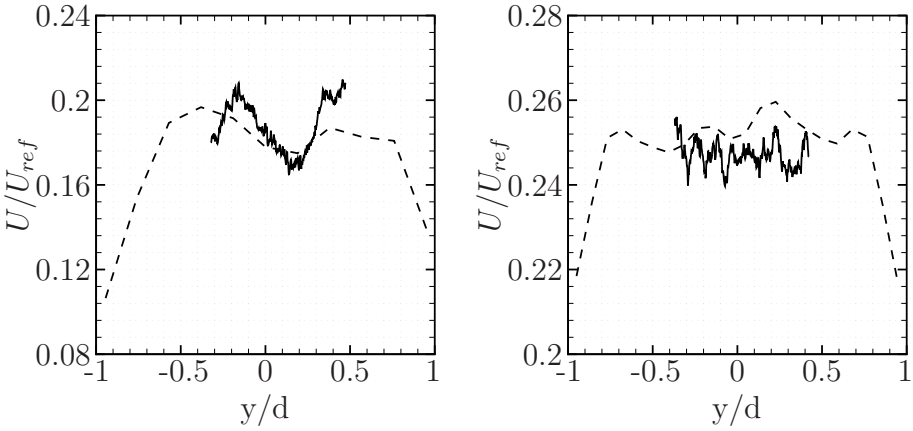

(a) Rod 0.008 m (b) Rod 0.016 m

Figure 3.23: Comparison of the turbulence intensity measured with hot-wire and PIV techniques. Data measured for the rod with 0.008 and 0.016 m diameter at the line which corresponds to the airfoil leading-edge position for a flow with reference velocity of 30 m/s. Continous line: stereo-PIV; Dashed line: Hot-wire.

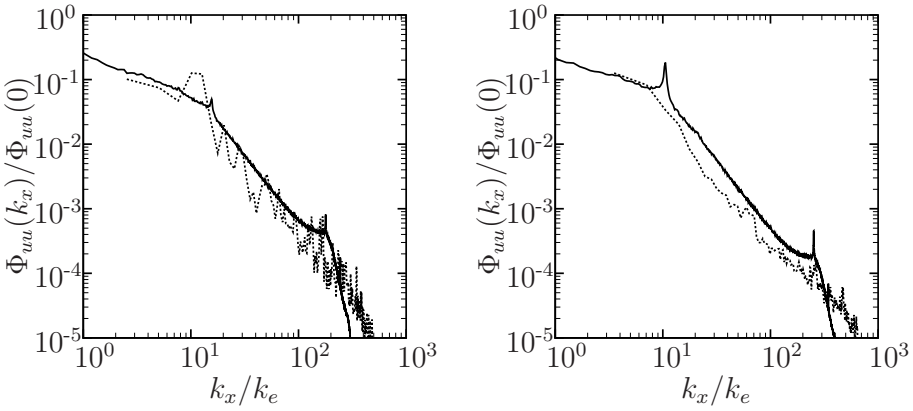

(a) Rod 0.008 m (b) Rod 0.016 m

Figure 3.24: Comparison between the longitudinal flow turbulence energy spectra measured with hot-wire anemometry and stereo-PIV techniques at a flow reference velocity of 30 m/s. Continous line: hot-wire; dotted line: stereo-PIV.

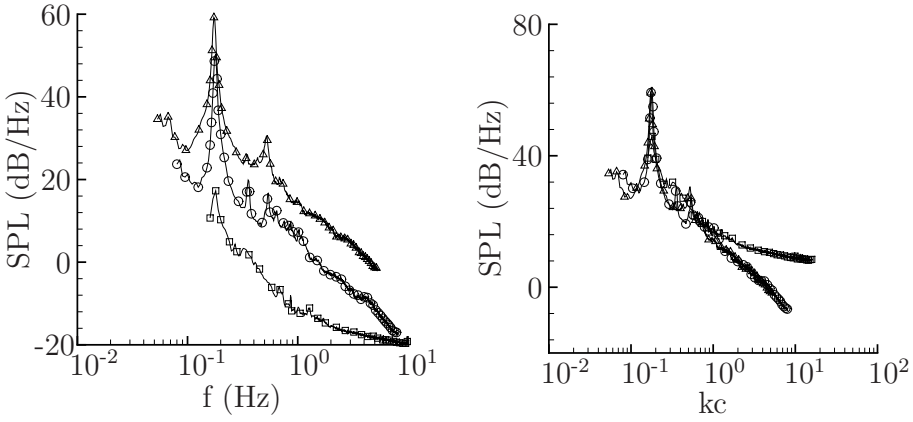

(a) Rod 0.008 m noise (b) Rod 0.008 m noise scaling

Figure 3.25: Rod 0.008 m noise and sound power level scaling against the reference flow velocity. Square: $U_{ref} = 10$ m/s; Circle: $U_{ref} = 20$ m/s; Triangle: $U_{ref} = 30$ m/s.

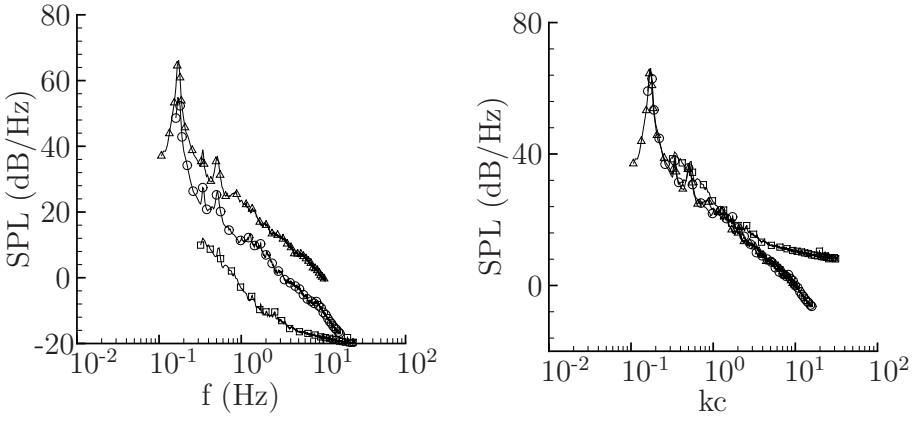

(a) Rod 0.016 m noise (b) Rod 0.016 m noise scaling

Figure 3.26: Rod 16 mm noise and sound power level scaling against the reference flow velocity. Square: $U_{ref} = 10$ m/s; Circle: $U_{ref} = 20$ m/s; Triangle: $U_{ref} = 30$ m/s.

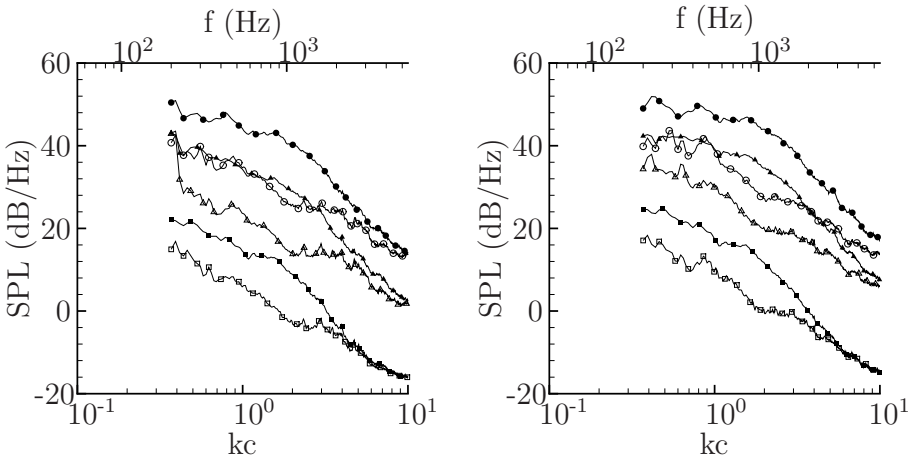

(a) Grid # 1 (b) Grid # 2

Figure 3.27: Grid-airfoil interaction noise compared with the background noise. The filled symbols refers to noise measurements in presence of the airfoil, while the empty marks refers to the background sound. Square: U_{ref} = 10 m/s; Triangle: U_{ref} = 20 m/s; Circle: U_{ref} = 30 m/s.

where $P_{xx}(f)^{back}$ is the background noise power spectral density, measured in the facility in absence of the airfoil - but equipped with side-plates, rod or turbulence grids, etc. $P_{xx}(f)^{airf+back}$ is the acoustic power spectral density measured with the presence of the airfoil. It was here decided to discard airfoil spectral data when its signal-to-noise ratio was smaller than 3 dB.

With these considerations, the subtracted grid-airfoil noise spectrum is presented in Fig. 3.28. This acoustic spectrum will be adopted for the validation of the proposed methodologies. Figure 3.29 shows the noise intensity scaling with the reference flow velocity.

A remark to be added is that the acoustic subtracted results presented to the grid # 1 and # 2 at 10 m/s does not respect the minimum signal to noise ratio for kc larger than 4. For 20 m/s and 30 m/s this minimum signal to noise ratio condition was relaxed to 1.7 dB for the grid # 1. This decision was taken in order to provide some experimental validation data, at this frequency range, such that the methodologies proposed in this work could be evaluated with the necessary care to the results interpretation.

From Fig. 3.29 it is observed that the noise spectrum scales very well with the 6^{th} power of the reference flow velocity for the cases with U_{ref} equal to 20 and

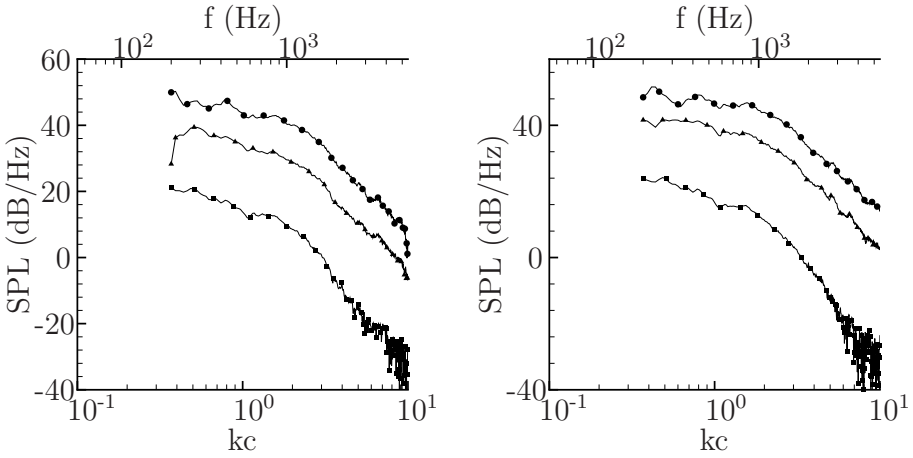

(a) Grid # 1 (b) Grid # 2

Figure 3.28: Grid-airfoil noise after background subtraction. Square: U_{ref} = 10 m/s; Triangle: U_{ref} = 20 m/s; Circle: U_{ref} = 30 m/s.

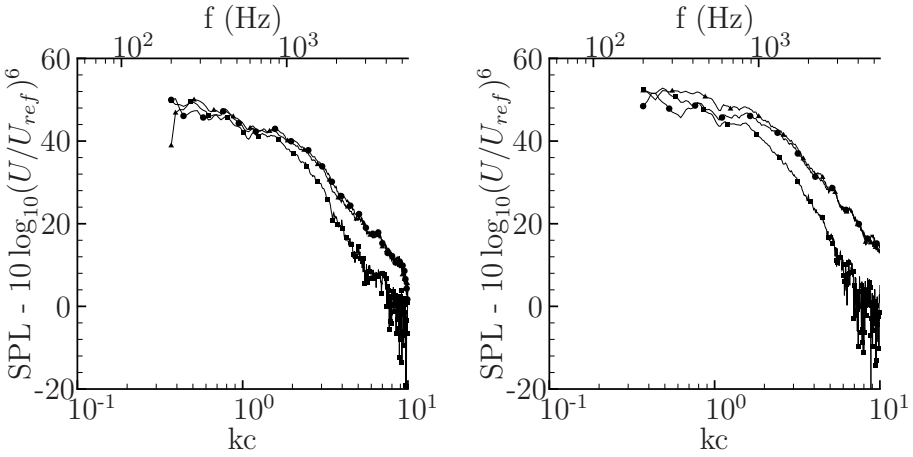

(a) Grid # 1 (b) Grid # 2

Figure 3.29: Grid-airfoil noise scaled with the reference flow velocity. Square: U_{ref} = 10 m/s; Triangle: U_{ref} = 20 m/s; Circle: U_{ref} = 30 m/s.

30 m/s. For the case with 10 m/s it is observed a poor scaling, which might be related with Reynolds number effects. Furthermore, during the development of this work, it is observed that, if the noise subtraction is not performed, the noise scaling with the 6^{th} power of the reference flow velocity is very poor.

Rod-airfoil configuration Similarly to the grid-airfoil case, the rod-airfoil noise is compared with the background sound generated by the facility when only the rod is installed. This comparsion is presented in Fig. 3.30 together with the noise intensity scaling with the reference flow velocity, shown in Fig. 3.32.

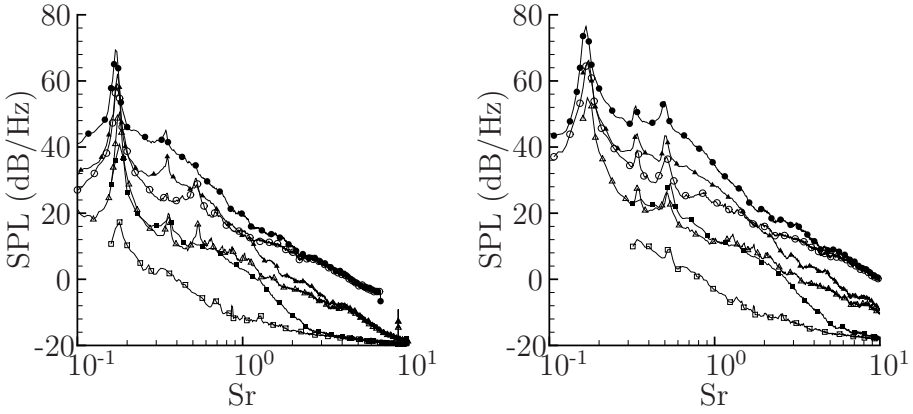

(a) Rod 8 mm (b) Rod 16 mm

Figure 3.30: Rod-airfoil interaction noise compared with the background noise. The filled symbols refers to noise measurements in presence of the airfoil, while the empty marks refers to the background sound. Square: $U_{ref} = 10m/s$; Triangle: $U_{ref} = 20m/s$; Circle: $U_{ref} = 30m/s$.

From Fig. 3.30 it is observed that the rod-airfoil configuration presents a better relation between the airfoil generated noise and background sound than the grid-airfoil case. Nevertheless, at higher frequencies the background noise becomes comparable. Figure 3.31 indicates as well a good scaling of the noise intensity with the 6^{th} power of the reference flow velocity. Now Fig. 3.32 presents the airfoil noise after background subtraction for the rod-airfoil configuration. Similarly to the previous case, these acoustic results are adopted to the validation of the methodologies proposed in this thesis.

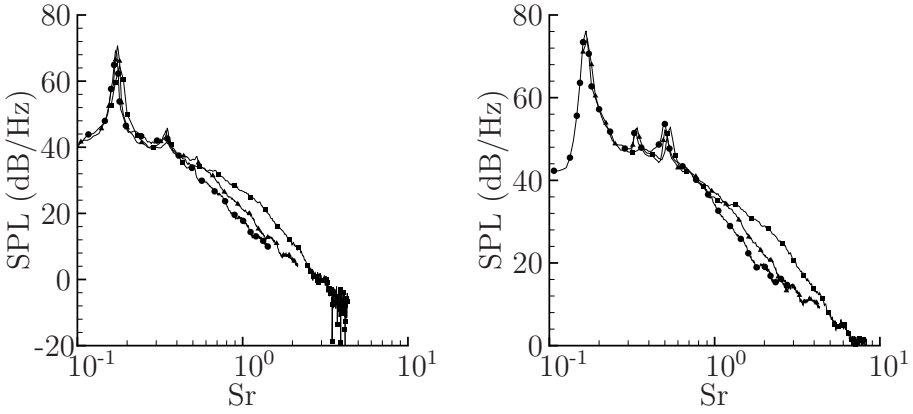

(a) Rod 8 mm (b) Rod 16 mm

Figure 3.31: Rod-airfoil noise scaled with the reference flow velocity. Square: U_{ref} = 10 m/s; Triangle: U_{ref} = 20 m/s; Circle: U_{ref} = 30 m/s.

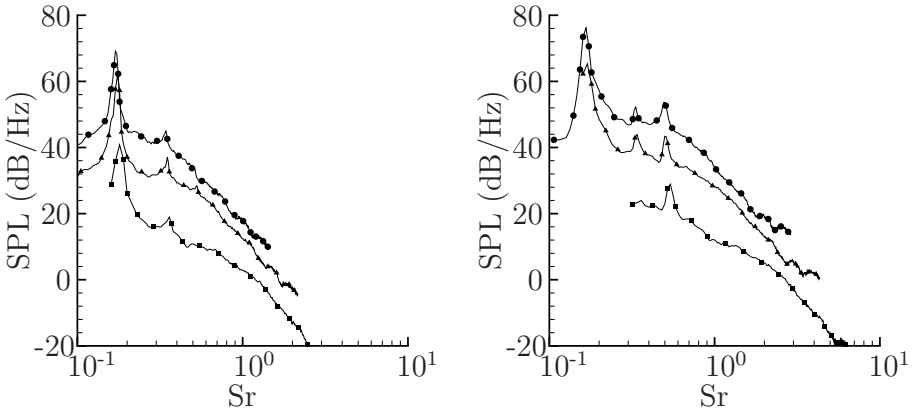

(a) Rod 8 mm (b) Rod 16 mm

Figure 3.32: Rod-airfoil noise after background subtraction. Square: U_{ref} = 10 m/s; Triangle: U_{ref} = 20 m/s; Circle: U_{ref} = 30 m/s.

3.5 Conclusions

In this chapter a new testing facility has been characterized aerodynamically and acoustically. The aerodynamic measurements are mainly performed with hot-wire and stereo-PIV techniques. Experimental results shows good agreement of results for the mean velocity and fluctuation RMS, spatial correlations and velocity spectra. This conclusion indicates that results from either measurement technique can be used as input to semi-analytical predictions. Hot-wire traverse measurements showed that in absence of the grid generation turbulence, the flow is uniform along the line where the airfoil leading-edge will be placed, while accelerations close to the side plate are observed for measurements in presence of the turbulence generation grid. Comparison between measured longitudinal and traverse correlations, in addition to turbulence velocity spectra shows that the flow can be represented by isotropic turbulence models. Background noise measurements was performed and compared with acoustic results in presence of the airfoil in the rod- and grid-airfoil configurations. These results shows a signal-to-noise-ratio of at least 3 dB for frequencies below the anechoic room cut-off frequency (200 Hz) up to $kc = 10$ (approximately 5,400 Hz). The results presented in this chapter are used as validation data for the rest of this work.

Chapter 4

Inflow models for semi-analytical airfoil noise prediction

In previous chapters, the leading-edge Amiet theory has been presented and the testing facility aeroacoustically characterized. Following these developments, the inflow model investigation is a next important step to validate the semi-analytical methodologies proposed in this work. In addition to the incoming flow modeling parameters, this chapter evaluates the finite/infinite span hypothesis, presented in the Amiet theory. Furthermore, are discussed the advantages of dividing the airfoil in small span sections and apply the strip theory technique to account the spanwise flow non-uniformity effects in semi-analytical noise predictions.

Firstly, the grid-airfoil case is studied. In this noise configuration, the inflow is modeled by the spectrum proposed by von Kármán and the turbulence spectrum modified by the Rapid-Distortion-Theory are discussed. Experimental evidence which support the choice to the second inflow turbulence model is presented. The finite/infinite span hypothesis, proposed in the noise radiation part of the Amiet theory, are evaluated together with the inverse strip theory. For each inflow model, comparison between the measured noise spectrum and the predicted sound are verified, in addition to the finite/infinite span hypotheses proposed for noise radiation computation by Amiet.

Later, a more complex inflow generated by the vortex shedding of a rod is evaluated. In this configuration, the deterministic phenomenon is not tackled,

but special attention is given to the broadband noise. In this case, a stochastic methodology to reconstruct the turbulence spectrum from PIV measurements is proposed and effects of the rapid turbulence distortion by the mean flow are discussed focusing its impact to the aeroacoustic prediction.

4.1 Grid-airfoil configuration

This section evaluates the isotropic turbulence von Kármán spectrum and the modification of this model by the Rapid-Distortion-Theory [11, 34]. In this assessment, the Amiet [3] hypotheses of (in)finite span airfoil are tested together with the noise prediction calculated by the inverse strip theory [20, 19].

von Kármán spectrum A critical step towards the grid-airfoil noise prediction is the definition of the incoming flow turbulence model. Amiet [3] proposes to apply the von Kármán isotropic turbulence model to the noise prediction. To assess the application of this model to the noise prediction results three different hypotheses are evaluated here:

1. the mean flow is considered to have span-wise uniform velocity and constant turbulence intensity, in addition, the airfoil is assumed to have infinite span. In this case the average is calculated by the span-wise integral, divided by the span. The noise prediction is compared with experimental results in Fig. 4.1;

2. the same mean flow hypotheses before considered are assumed, and the airfoil is now considered finite span. The acoustic prediction is verified against empirical measurements in Fig. 4.2;

3. the flow is considered span-wise non-uniform and the inverse strip theory is adopted to the noise calculations. In this case, the span-wise distribution of the mean flow velocity and turbulence intensity are obtained from hot-wire anemometry with results presented in Fig. 4.3.

To initiate this evaluation, on the airfoil noise radiation computation, the Amiet sine-cardinal formulation, for clarity repeated here in Eq. 4.1, states that if the quantity $\Lambda = MK_x d$ tends to infinity the sine-cardinal term tends to a Dirac delta and the airfoil can be considered of infinite span. Fig. 4.1 verifies this hypothesis together with the von Kármán isotropic turbulence

model consideration to $\Phi_{ww}(K_x, k_y)$.

$$S_{pp}(\mathbf{x},\omega) = \left(\frac{\rho\, k\, z\, b}{\sigma_0^2}\right)^2 \pi\, U\, d \int_{-\infty}^{\infty} \frac{\sin^2\left[(K_y - k_y)d\right]}{(K_y - k_y)^2} \Phi_{ww}(K_x, k_y) |\mathcal{L}(\mathbf{x}, K_x, k_y)|^2 \mathrm{d}k_y \tag{4.1}$$

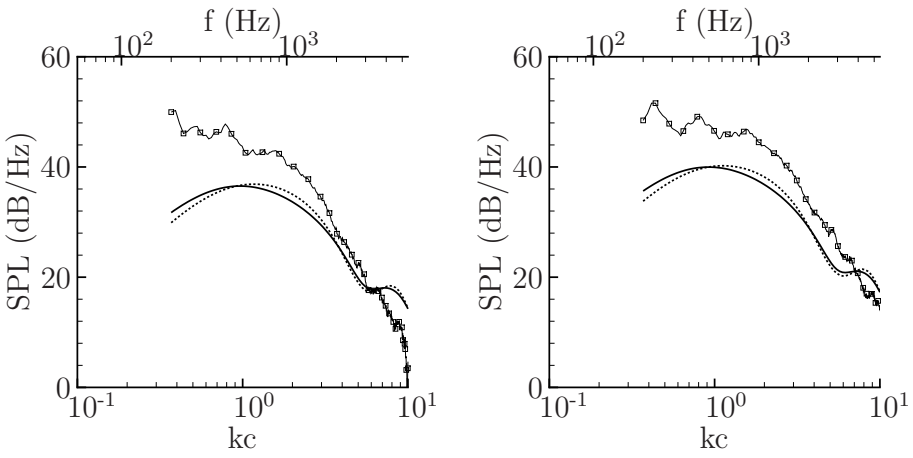

(a) Grid # 1 (b) Grid # 2

Figure 4.1: Noise prediction using von Kármán spectrum and considering the infinite-span airfoil formulation compared with experimental results. Results calculated using two iterations of the Amiet theory. Acoustic computation assumed the case with reference flow velocity of 30 m/s and observer placed 1 m distance from the airfoil at a 90° position. Continuous line with open square symbols: experiments; Continous line: Amiet theory prediction – 1^{st} iteration; Amiet theory prediction – 2^{nd} iteration.

From Fig. 4.1 it is observed that, for both turbulence generation grid cases, the shape of the predicted noise spectrum assimilates to the experimental. It is seen, in addition, that at low-frequencies, the noise spectra are under-predicted, meanwhile at higher frequencies, it occurs an over-prediction.

Now considering the experiment subject of this work, the non-dimensional parameter Λ ranges from 0.42 to 20.94, thus its approximation to infinity might be abusive. Consequently, it is expected that the noise cancellation phenomenum, which occur for gusts with $k_y \neq 0$, will not to be observed in this experimental case. Considering a finite span formulation, where the cardinal

sine is not approximated by a Dirac delta, Fig. 4.2 presents the predicted noise compared with experimental results.

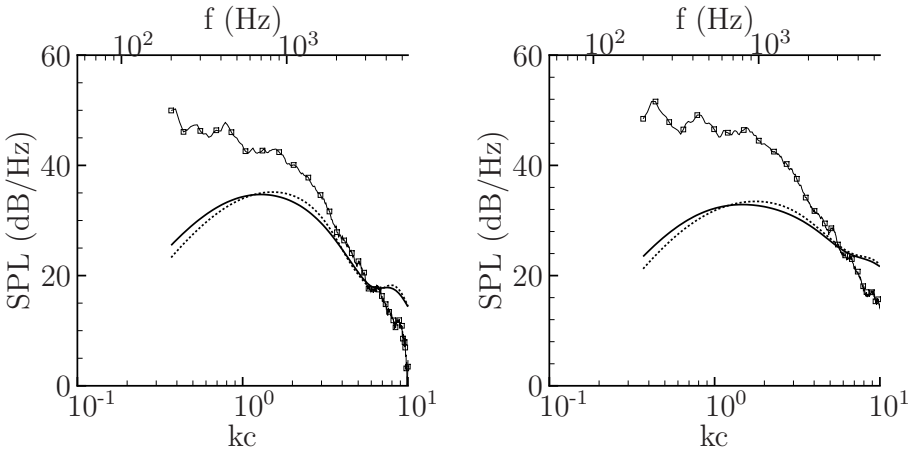

(a) Grid # 1 (b) Grid # 2

Figure 4.2: Noise prediction using von Kármán spectrum and considering the finite-span airfoil formulation. Noise computed considering the case with reference flow velocity of 30 m/s and observer placed 1 m distance from the airfoil at a 90° position. Continuous line with open square symbols: experiments; Continous line: Amiet theory prediction – 1^{st} iteration; Amiet theory prediction – 2^{nd} iteration.

The finite-span airfoil hypothesis yields a poor the agreement between noise prediction and experimental results. This result demonstrates that there are still important physical phenomena not considered in this problem.

The two previous noise prediction approaches considered that the flow mean velocity and turbulence intensity are uniform along the airfoil span. To consider the effect of the flow span-wise non-uniformity the inverse strip theory [20] is applied to the noise prediction. This approach divides the airfoil span in strips of small and the noise is computed at each strip considering the local flow velocity and turbulence intensity. These inputs are obtained, here, from hot-wire anemometry measurements performed for the undisturbed flow at the airfoil leading-edge height. Convergence analysis showed that a minimum of 128 strips is necessary to make the predicted noise independent from the number of strips. Comparison between experiments and noise prediction are shown in Fig. 4.3.

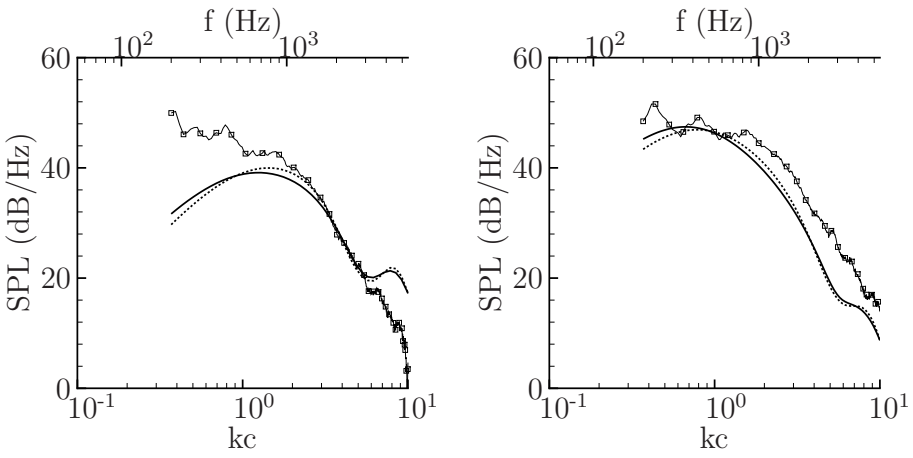

(a) Grid # 1 (b) Grid # 2

Figure 4.3: Noise prediction using von Kármán spectrum and considering the inverse strip theory to the noise prediction. Noise computed considering the case with reference flow velocity of 30 m/s and observer placed 1 m distance from the airfoil at a 90° position. Continuous line with open square symbols: experiments; Continous line: Amiet theory prediction – 1^{st} iteration; Amiet theory prediction – 2^{nd} iteration.

From Fig. 4.3 it is observed that for the frequency range where kc varies from, approximately, 2 to 6, this approach leads to acoustic calculations with relatively good agreement against experimental results. Nevertheless, it is observed, respectively, noise under prediction and over prediction, for frequencies where kc is less than 2 or kc is higher than 6. This improved agreement between measurements and calculations indicates the importance of considering the actual span-wise variation of the mean velocity and turbulence intensity. Discrepancies remain however for lower and higher frequencies.

Experimental evidence of the Rapid Distortion Theory More accurate noise predictions can be obtained through the implementation of the Rapid-Distortion-Theory [47, 44, 19]. This section intends to present physical evidence of this phenomena and demonstrate its impact on the noise prediction.

According to Batchelor [11], turbulence Rapid Distortion occurs when a variation in the mean velocity field occurs due to the change in the boundary conditions, e.g. flow approaching a body or an area restriction. An additional condition to the application of this theory requires that the turbulence

distortion should occur so rapidly that the contribution to the change in relative position of the fluid particles from the turbulence is negligible.

Let us consider the mean velocity variation as the flow approaches to the airfoil leading-edge. In this study stereoscopic-PIV measurement, performed in the plane $z = 0$, are adopted to compute the mean velocity along the x axis at $y = 0$ position. Figure 4.4 presents the comparison between experimental results and the inflow velocity calculated for a NACA-0012 airfoil and a cylinder with the same radius of curvature as the airfoil leading-edge. This evaluation is performed using the potential flow theory and the airfoil leading-edge radius r is calculated accordingly to NACA 4 digits airfoils tabulated formulas, resulting $r = 1.5867$ mm.

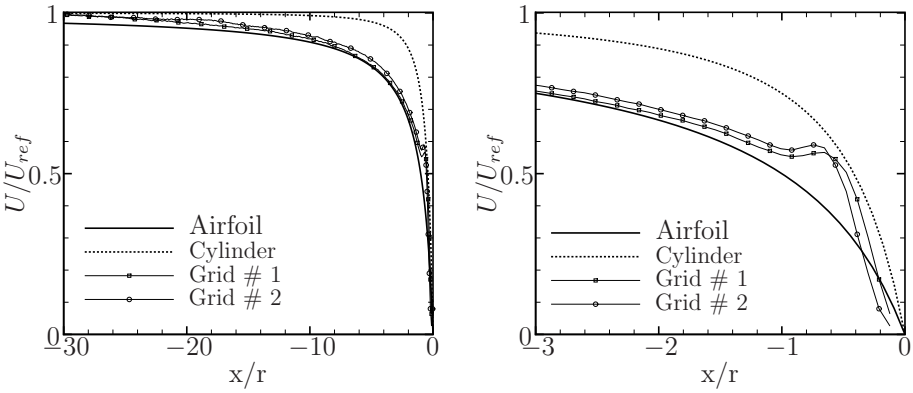

(a) General view (b) Detailed view

Figure 4.4: Mean velocity field calculated from PIV measurements along the x axis at $y = 0$. Stereoscopic-PIV measurement performed at the plane $z = 0$ considering a reference flow velocity of 30 m/s. The following notation is adopted: Airfoil: upstream velocity field computed though a steady panel method considering NACA-0012 airfoil; Cylinder: velocity field calculated with the potential flow theory along the stagnation streamline considering a cylinder with the same leading-edge radius as the NACA-0012 airfoil.

From Fig. 4.4 it is observed that, at distances larger than, approximately, 1 times the airfoil leading-edge radius the mean velocity approximates the prediction given by the flow potential solution calculated to a NACA-0012 airfoil, using a panel method. Furthermore, at a distance closer than 1 time the the airfoil leading-edge radius, it is observed a change of tendency and the mean upstream velocity approximates closely to the velocity profile of a cylinder with same leading-edge radius as the airfoil. This phenomena, verified

here experimentally, agrees with a hypothesis proposed by Mish [44], which states that the distortion tensor should be computed considering the mean velocity profile of a cylinder with the same leading-edge radius as the airfoil. This result experimentally confirms that the flow distortion depends more of the airfoil leading-edge radius and other downstream geometrical aspects are of secondary importance.

From those figures one can observe that as the flow approaches the airfoil leading-edge the signal-to-noise ratio is severely reduced, however this quantity still satisfies the minimum requirement prescribed to this analysis.

A second evaluation performed to infer the existence of flow distortion phenomenon observes the velocity fluctuation spatial correlation. In this analysis the spatial correlation is computed along the y axis, at different x/r positions, localized upstream the airfoil leading-edge. In this evaluation, the correlation f, by definition, is computed with the velocity component aligned with the y axis, while the correlation g is calculated adopting the velocity component aligned with the x axis, while the correlation h is processed assuming the velocity vector aligned with the z axis. Using these definitions, the correlation f, g and h are, respectively, presented in Figs. 4.5, 4.6 and 4.7.

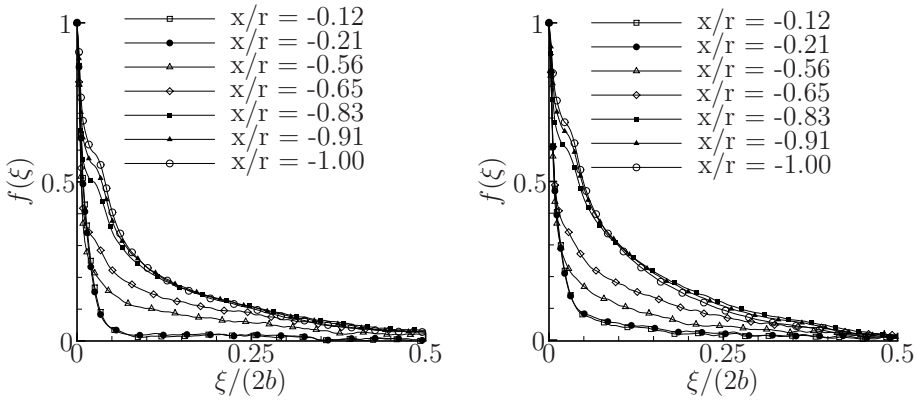

(a) Grid # 1 (b) Grid # 2

Figure 4.5: Spatial correlation of the flow velocity fluctuation component aligned with the y axis computed along the y axis at different positions x, upstream the airfoil leading edge. Data computed to the case with reference flow velocity of 30 m/s.

From Figs. 4.5, 4.6 and 4.7 it is observed that the correlations f, g and h present

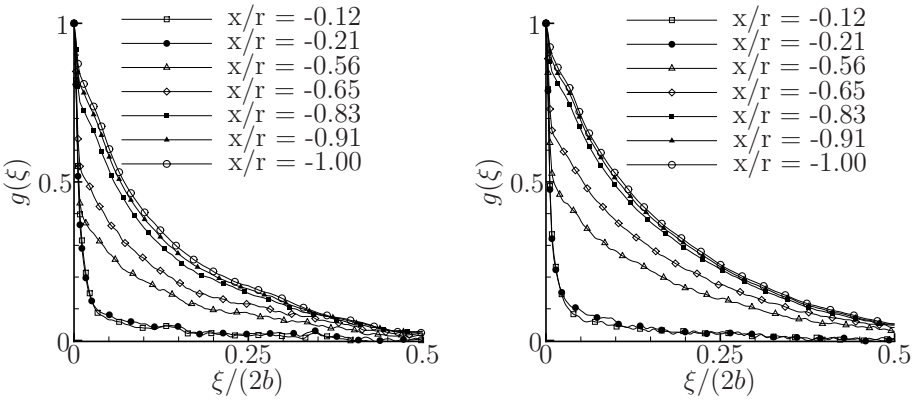

(a) Grid # 1 (b) Grid # 2

Figure 4.6: Spatial correlation of the flow velocity fluctuation component aligned with the x axis computed along the y axis at different positions x, upstream the airfoil leading edge. Data computed to the case with reference flow velocity of 30 m/s.

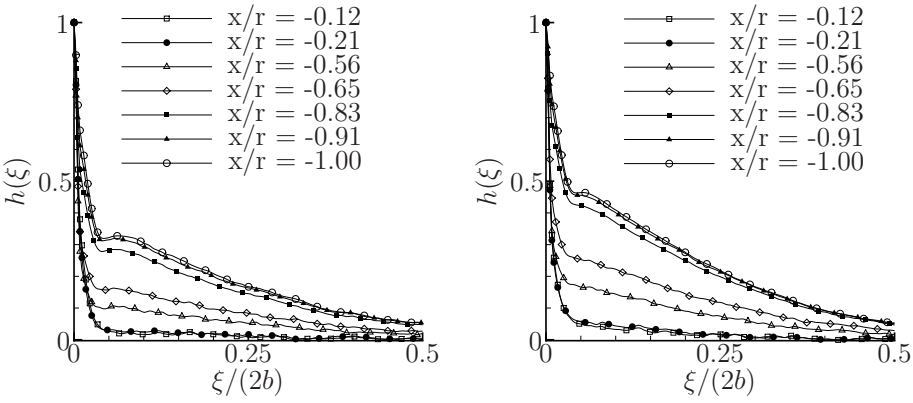

(a) Grid # 1 (b) Grid # 2

Figure 4.7: Spatial correlation of the flow velocity fluctuation component aligned with the z axis computed along the y axis at different positions x, upstream the airfoil leading edge. Data computed to the case with reference flow velocity of 30 m/s.

two kinds of behavior. At a positions x/r very close to the airfoil leading-edge the flow presents reduced correlation along the y axis and it noticed that, for distances smaller than $x/r = 0.21$, the correlation curves f, g and h becomes independent of the distance to the leading-edge. For x/r distances larger than 81% it is observed that the spatial correlation is, proportionally, larger and independent of the distance to the leading-edge. Finally for x/r between 21% and 81% it is observed, a transitional behavior between the two asymptotic limits described here.

A third analysis which support the presence Rapid Turbulence Distortion phenomena is the velocity fluctuation energy spectra. In this study the velocity component aligned with the z axis is considered. The energy spectra is computed at a given distance x/r from the airfoil leading-edge, and the velocity information is taken along the y-axis. Figures 4.8 and 4.9 presents the velocity fluctuation computed at distances x/r of -0.12, -0.21, -0.91 and -1.00.

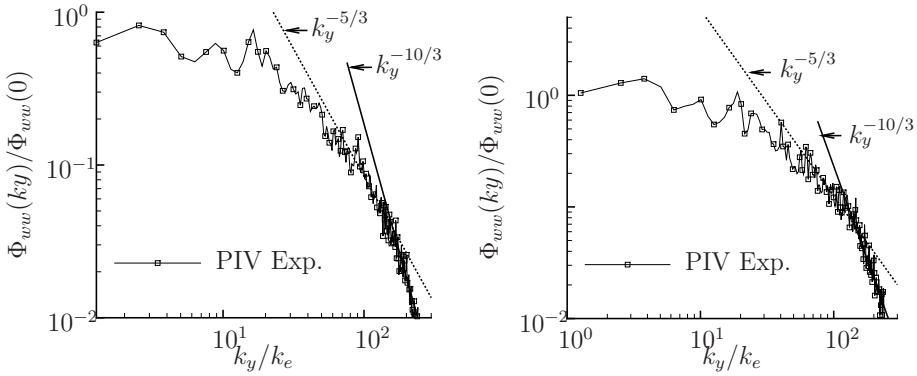

(a) x/r = -0.12 (b) x/r = -0.21

Figure 4.8: Turbulence energy spectra computed along the y axis to the velocity component aligned with the z axis at distances x relatively close to the airfoil leading-edge.

From Figs. 4.8 and 4.9 it is observed that, at closer distances from the airfoil leading-edge the turbulence energy spectra presents a an asymptotic decay following a $-5/3$ rule - for the intermediate wavenumbers - and a $-10/3$ decay for larger wavenumbers.

This behavior can be explained by the Rapid Distortion Theory proposed by Hunt [34] - which is a complement to the introductory work of Batchelor [11]. In this theory, Hunt proposes different asymptotic behavior to the flow energy spectra depending three major parameters: the relative transverse dimension

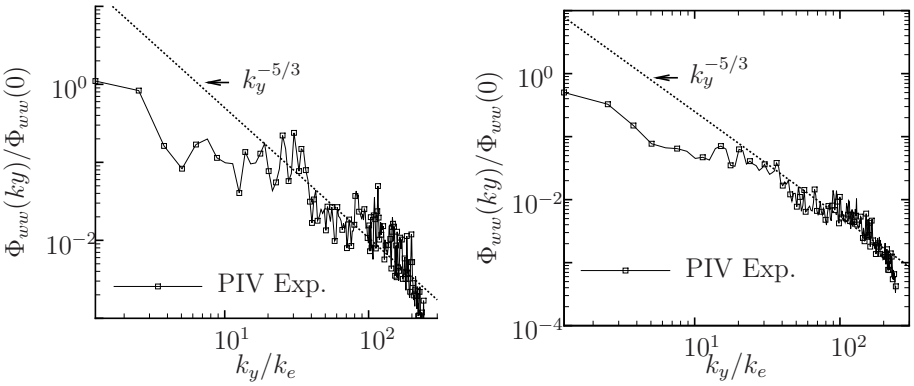

(a) x/r = -0.91 (b) x/r = -1.00

Figure 4.9: Turbulence energy spectra computed along the y axis to the velocity component aligned with the z axis at distances x comparable to the airfoil leading-edge radius.

of the body (a) compared with the longitudinal turbulence integral length scale Λ_f, and the non-dimensional distance between the analyzed point and the body ξ. Hunt proposes that, for small scale turbulence ($a/\Lambda_f \gg 1$), the flow energy spectra present two different asymptotic behaviors at high-frequencies $k_x/k_e \gg 1$: if $a/\Lambda_f\xi \to 0$ the flow energy spectra presents, at high frequencies, a slope proportional to the $-10/3$ power of the wavenumber; by turn, if $a/\Lambda_f\xi \gg 1$ the flow energy spectra presents, at high-frequencies, a slope proportional to the $-5/3$ power of the wavenumber.

In this application, the transverse dimension of the body is equal to the airfoil chord (0.1 m), while the longitudinal turbulence integral length scale is equal to 0.012 and 0.013 m, respectively to the grid # 1 and # 2, in a flow with reference velocity of 30 m/s. This leads to the parameter a/Λ_f equal to 8.3 and 7.7, to the grid # 1 and # 2, respectively. These values can be considered to satisfies the small scale turbulence hypothesis. Now the parameter ξ should be non-dimentionalized with a length scale relevant with the turbulence distortion phenomenum. From the previous analysis, it was observed that the turbulence distortion occurs at a distance proportional to the airfoil leading-edge radius, thus this dimension is used to the non-dimensionalization of ξ. When the distance from the wall is equal to the leading-edge radius ($\xi = 1$) the parameter $a/\Lambda_f\xi$ assumes values of 8.3 and 7.7, to the grid # 1 and # 2, respectively. This value satisfies the condition of $a/\Lambda_f\xi \gg 1$, what implicates in a flow with an energy spectra proportional to the $-5/3$ power of the wavelength. When the distance to the wall goes asymptotically to zero, the parameter $a/\Lambda_f\xi$, tends

to zero, leading to a flow energy spectra proportional, at high-frequencies, to the $-10/3$ of the wavelength.

Noise prediction with the Rapid Distortion Theory The presented physical evidence of the rapid turbulence distortion demonstrates the necessity of a modified turbulence energy spectra model. Considering that the Batchelor's Rapid Distortion Theory [11] does not consider any modification to the distorted turbulence energy spectra, this work adopts the modifications proposed by Hunt [34]. In this work, Hunt proposes that when the small scale turbulence approximates to the wall, the turbulence energy spectra is changed such that, at high-frequencies, it does not decay anymore following a $-5/3$ rule, but instead following a $-10/3$ asymptotic. Christophe [19] proposes a modification in the turbulence energy spectrum which considers that the exponent of the turbulence energy spectrum should be modified from 17/6, corresponding to the undistorted isotropic case to 22/6, referring to the anisotropic distorted case. Considering this hypothesis, the turbulence energy is written as:

$$E(k) = \frac{I\,k^4}{\left[1 + (k_x/k_e)^2\right]^{22/6}} \tag{4.2}$$

where $I = C\,u'^2/k_e^5$, where the coefficient C should is defined is order to satisfy the relationship:

$$\int_0^\infty E(k)\mathrm{d}k = \frac{3}{2}u'^2 \tag{4.3}$$

This relation leads to normal turbulence velocity fluctuation energy spectrum equal to:

$$\Phi_{ww} = \frac{91}{36\pi}\frac{u'^2}{k_e^2}\frac{(k_x/k_e)^2 + (k_y/k_e)^2}{\left[1 + (k_x/k_e)^2 + (k_y/k_e)^2\right]^{19/6}} \tag{4.4}$$

Figure 4.10 compares the noise calculated with the the turbulence energy spectra proposed by Christophe and the inverse strip theory, for each turbulence grid studied in this work.

From Fig. 4.10 it is observed the better agreement between the predicted noise and the results obtained empirically for the complete range of frequencies analysed in this work. These results should be evaluated with care. This apparent good match of results is not an expected tendency for this kind of noise prediction approach. The Amiet technique considers a flat-plate airfoil geometry, but accordingly to literature [24, 26, 39], the airfoil thickness should contribute reducing the airfoil response [41, 42, 43, 44], thus, decreasing the airfoil noise. Consequently, at this stage, it is expected that the Amiet theory should over-predict the airfoil noise.

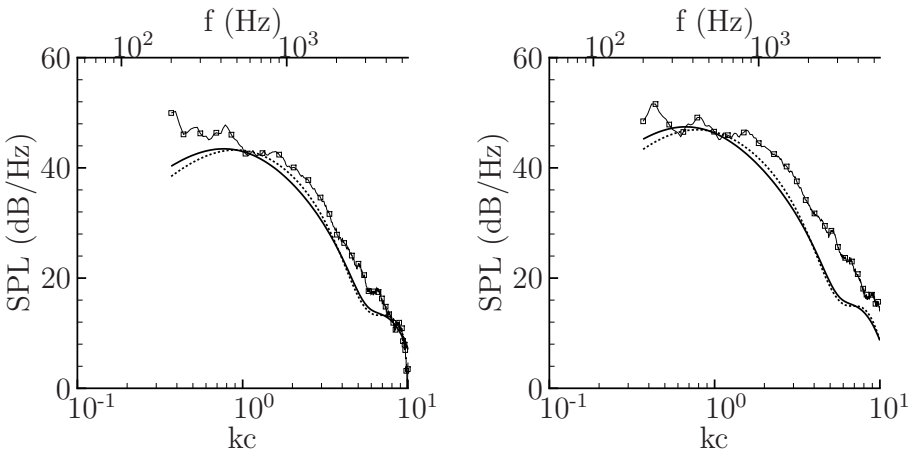

(a) Grid # 1 (b) Grid # 2

Figure 4.10: Noise prediction using the turbulence energy spectrum modified by the Rapid Distortion Theory, considering the inverse strip theory formulation, compared with experimental results. Noise computed considering the case with reference flow velocity of 30 m/s and observer placed 1 m distance from the airfoil at a 90° position. Continuous line with open square symbols: experiments; Continous line: Amiet theory prediction – 1^{st} iteration; Amiet theory prediction – 2^{nd} iteration.

This consideration demonstrates that there is still some relevant physical phenomena not considered in this problem. A possible phenomenon that we consider important to be considered in semi-analytical noise predictions is the change of the flow turbulence intensity as it approximates the airfoil leading-edge. Figure 4.11 analyzes the turbulence intensity variation, for each velocity component, along the x-axis at $y = 0$ position.

From Fig. 4.11 it is observed that, as the distance from the airfoil is comparable to the leading-edge radius (r), the turbulence intensity grows exponentially. This evidence demonstrates that the u'^2 value, adopted in Eq. 4.4 should be modified to take into account this effect. To consider this physical phenomena, this work considered that the ratio between the the turbulence intensity at the closest distance from the wall measurable by PIV and the undisturbed flow would remain constant along the airfoil span. With this hypothesis, Fig. 4.12 presents the predicted noise compared with experimental results.

From Fig. 4.12 it is observed that the modification of the flow turbulence intensity leads to a noise over prediction, which is a result in agreement with

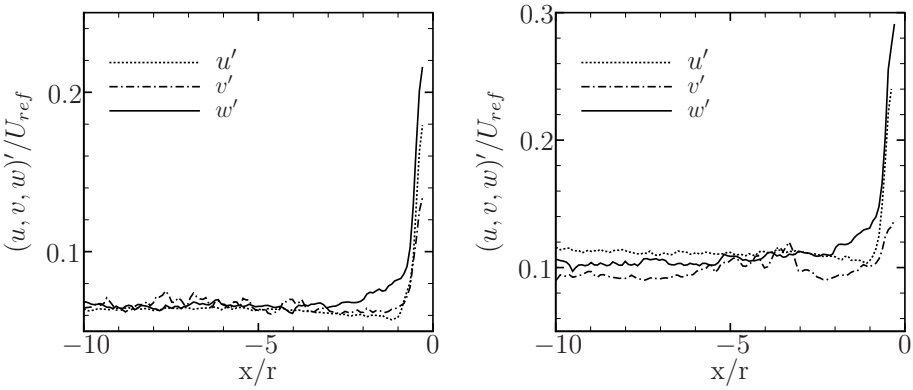

(a) Grid # 1 (b) Grid # 2

Figure 4.11: Turbulence intensity computed along the line $y = 0$. Results presented to the case measured at a reference velocity of 30 m/s.

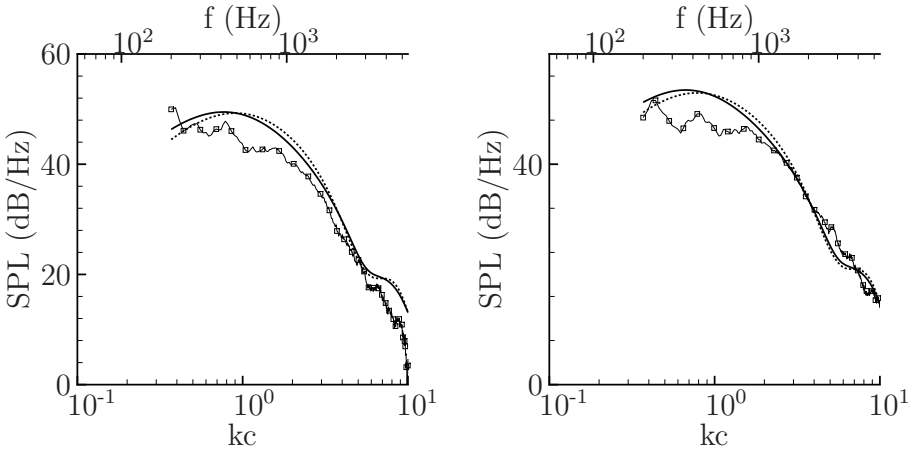

(a) Grid # 1 (b) Grid # 2

Figure 4.12: Comparison between experimental results and noise prediction using the turbulence energy spectrum modified by the Rapid Distortion Theory and the inverse strip theory. Noise computed considering the case with reference flow velocity of 30 m/s and observer placed 1 m distance from the airfoil at a 90° position. Continuous line with open square symbols: experiments; Continous line: Amiet theory prediction – 1^{st} iteration; Amiet theory prediction – 2^{nd} iteration.

literature expectations.

At this stage we consider that most of the relevant phenomena have been taken into account. Consequently, the inflow model, modified by the Rapid Distortion Theory and assuming the turbulence intensity change by the approximation to the leading-edge will be taken as inflow input to the validation of the semi-analytical techniques proposes in this thesis.

4.2 Rod-airfoil configuration

The rod-airfoil configuration provides extra challenges to the inflow modeling. The phenomena has a periodic component related with the rod vortex shedding and a random part linked with the flow turbulence. Casalino [18] already tackled the development of an analytical rod vortex shedding model, with inconclusive results. Since the noise prediction of periodic flows implies the application of semi-analytical theories in a distinct form from the cases developed along this thesis, e.g. refs [4, 51, 57], the periodic phenomena will not be addressed in this work. Consequently, the tone will be excluded from the prediction and only the broadband part of the acoustic spectra will be computed.

Flow characterization Initially, elements which may indicate the presence of the turbulence rapid distortion phenomenum will be analyzed. Similarly to the grid-airfoil case, the PIV measured mean velocity is compared with predictions to the upstream velocity field calculated using the potential flow theory assuming a NACA-0012 airfoil and a rod with the same leading-edge radius as the airfoil. Results are presented in Fig. 4.13.

Figure 4.13 shows that the rod-airfoil configuration presents a similar mean flow behavior as the grid-airfoil case. At large distances from the leading-edge the mean flow follows the profile predicted to a NACA-0012 airfoil, and, as the flow approaches the leading-edge, the tendency is changed and the velocity profile follows the prediction given by the potential flow theory for a rod with the same leading-edge as the airfoil.

The next analysis evaluates the flow turbulence intensity variation the flow approximates the airfoil leading-edge. Figure 4.14 shows the turbulence intensity measured for each flow velocity component along the x-axis at the position $y = 0$.

From Fig. 4.14 it is observed that, similarly to the grid-airfoil cases, when the distance to the leading-edge is comparable to the airfoil front radius, the

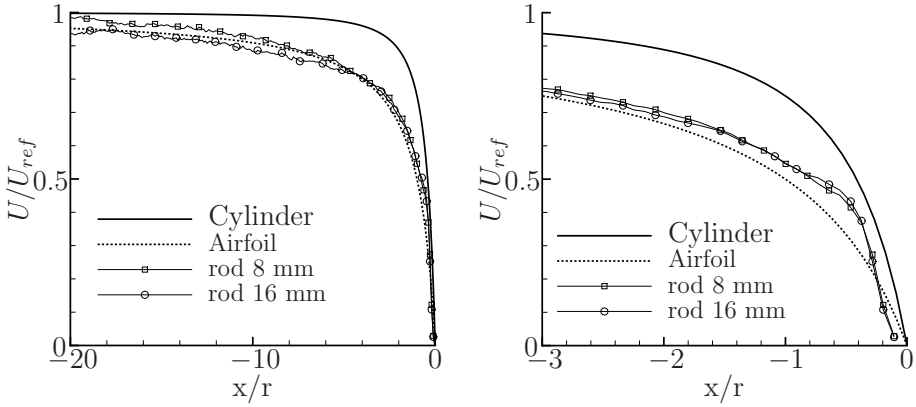

(a) General view (b) Detailed view

Figure 4.13: Mean velocity field calculated from PIV measurements along the x-axis at $y = 0$. Stereoscopic-PIV measurement performed at the plane $z = 0$ considering a reference flow velocity of 30 m/s. The following notation is adopted: Airfoil: upstream velocity field computed though a steady panel methodology considering NACA-0012 airfoil; Cylinder: velocity field calculated with the potential flow theory along the stagnation streamline asuming a cylinder with the same leading-edge radius as the NACA-0012 airfoil.

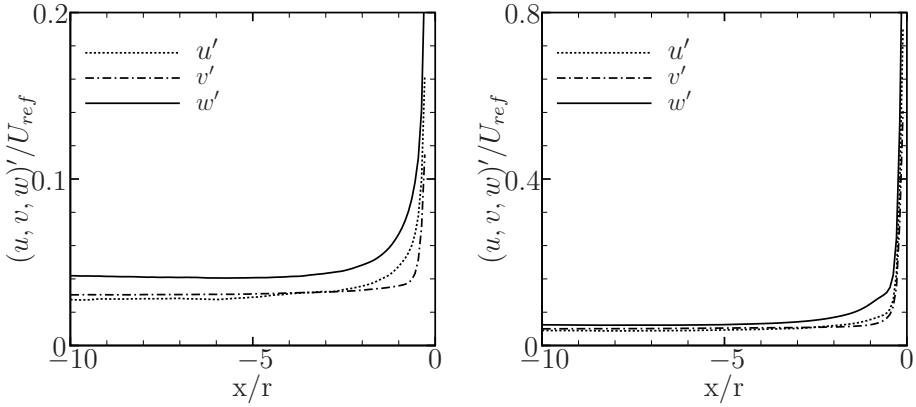

(a) Rod 0.008 m (b) Rod 0.016 m

Figure 4.14: Turbulence intensity computed along the line $y = 0$. Results measured to the case with reference velocity of 30 m/s.

turbulence intensity grows exponentially as it approximates the airfoil leading-edge.

Flow velocity power spectral density calculation from spatial correlation As described in Chapter 3, the the single wire hot-wire measurements done in this work does not allow to distinguish between the longitudinal and the normal flow velocity components. To overcome these limitations, this work proposes an approach which considers the PIV measured flow velocity spatial correlation to compute a broadband velocity power spectral density.

Initially, this methodology assumes that, accordingly to Hinze [33], the turbulence velocity spectra relates with the spatial correlation as:

$$\Phi_{uu}(k_x) = \frac{4u'}{2\pi}\int_0^\infty f(x)\cos(k_x x)\mathrm{d}x \tag{4.5}$$

$$\Phi_{vv}(k_x) = \frac{4u'}{2\pi}\int_0^\infty g(x)\cos(k_x x)\mathrm{d}x \tag{4.6}$$

$$\Phi_{ww}(k_x) = \frac{4u'}{2\pi}\int_0^\infty h(x)\cos(k_x x)\mathrm{d}x \tag{4.7}$$

This work adopt the correlations f, g and h computed from PIV measurements. These three correlations are presented in Figs. 4.15, 4.16 and 4.17.

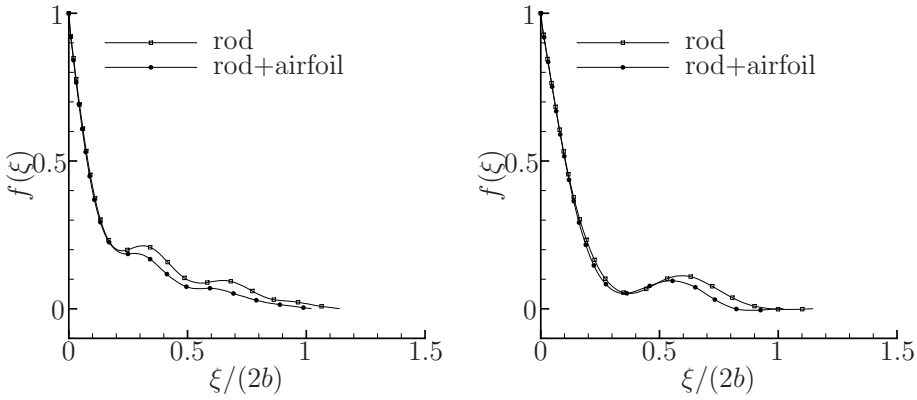

(a) Rod 0.008 m (b) Rod 0.016 m

Figure 4.15: Longitudinal velocity spatial correlation measured along the x-axis at $y = 0$ position using PIV information.

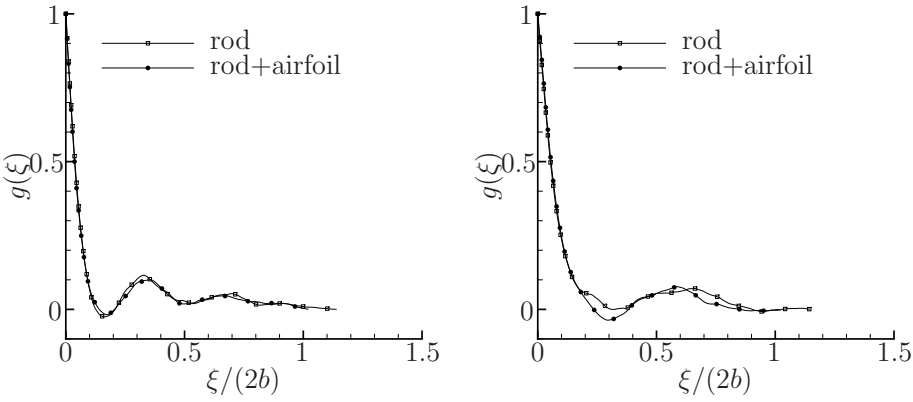

(a) Rod 0.008 m (b) Rod 0.016 m

Figure 4.16: Transverse velocity spatial correlation measured along the x-axis at $y = 0$ position using PIV information.

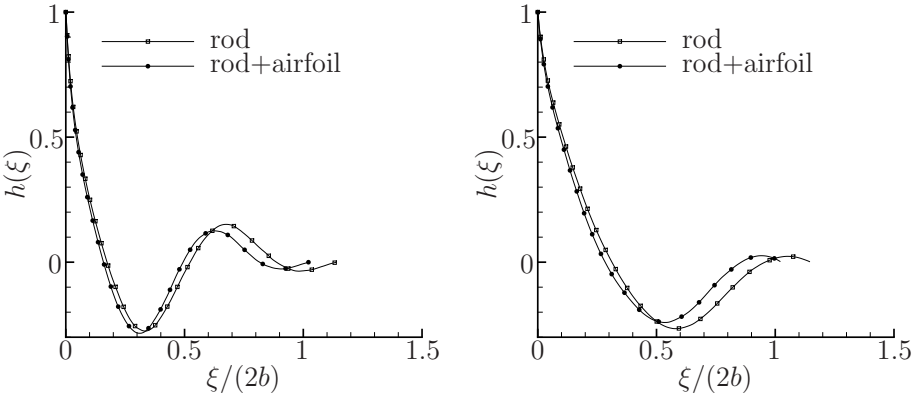

(a) Rod 0.008 m (b) Rod 0.016 m

Figure 4.17: Normal velocity spatial correlation measured along the x-axis at $y = 0$ position using PIV information.

From Figs. 4.15, 4.16 and 4.17 it is observed that the airfoil presence does not change significantly the spatial correlation. As discussed before, the airfoil presence impacts significantly in the mean flow and the most relevant turbulence related phenomena occur at very close distances from the airfoil leading-edge. The correlation f and g presents mild oscillations around zero, indicating that these velocity components presents relatively small periodic behavior. While the component h shows comparative significant amplitude oscillations around zero indicating that the velocity component normal to the measurement plane presents a more important periodicity than the other two direction velocities.

With these considerations, the flow velocity power spectral density is computed. Figures 4.18 and 4.19 present a comparison between the velocity power spectral density calculated with the proposed methodology and results from measurements computed from PIV data along the x-axis at $y = 0$, respectively, to the rod and the rod-airfoil cases.

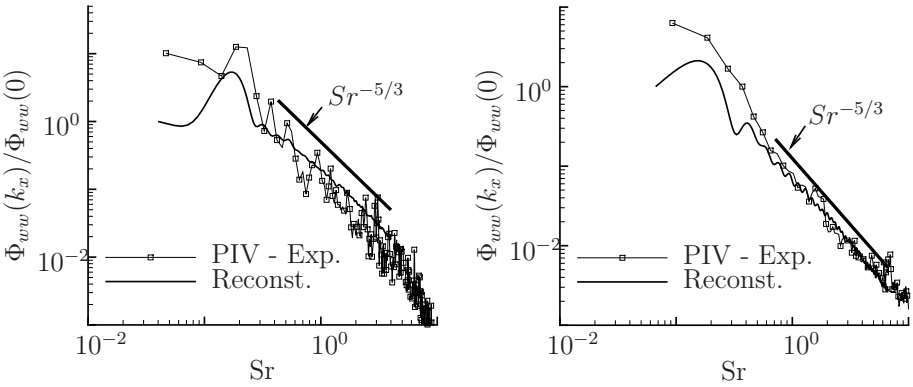

(a) Rod 0.008 m only

(b) Rod 0.016 m only

Figure 4.18: Normal velocity power spectral density comparison between PIV measurements and its reconstruction calculated with the proposed technique. Results presented to the rod only case, measured at a reference velocity of 30 m/s.

From Figs. 4.18 and 4.19 it is observed an overall good agreement between the flow velocity power spectral density PIV measured and the reconstructed values, computed with the methodology proposed here. For all cases a mild peak is captured, corresponding to the vortex shedding phenomenum. The maximum value of this peak is close to the expected Strouhal number ($Sr = 0.18$).

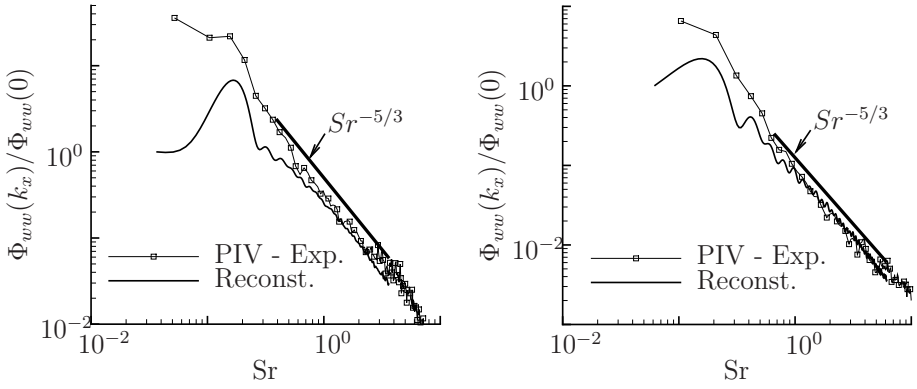

(a) Rod 0.008 m + airfoil (b) Rod 0.016 m + airfoil

Figure 4.19: Normal velocity power spectral density comparison between PIV measurements and its reconstruction calculated with the proposed technique. Results presented to the rod-airfoil case, measured at a reference velocity of 30 m/s.

After the normal velocity power spectral density spectra calculation, it possible to predict the airfoil noise. Figure 4.20 presents the acoustic spectra computed using the reconstruction technique proposed here, compared with experiments.

From Fig. 4.20 it is observed that the proposed technique significantly over-predicts the noise. In addition, the shape of the noise spectra does not resembles the measurements. These results indicates that there are important physics not considered at this stage. In example of the grid-airfoil case, it is expected that the turbulence rapid distortion, occurring close to the airfoil leading-edge, plays an important role to the noise prediction. Since this work does not have time resolved PIV information, it is not possible to obtain the distorted turbulence velocity spectrum, as a function of the longitudinal wavenumber (k_x), in a position close enough to the airfoil leading-edge. To deal with this limitation, it is proposed to consider the undisturbed PIV measured turbulence velocity spectrum and then fit an isotropic turbulence von Kármán spectrum. This fit aims to obtain the parameters u' and k_e and which will then be applied to the Rapid Distortion Theory modified turbulence energy spectra. Figure 4.21 presents the reconstructed normal velocity power spectral density fit against the isotropic turbulence von Kármán spectrum.

From Fig. 4.21 it is observed that the reconstructed turbulence velocity spectra fits very well the von Kármán spectrum for the rod 0.008 m diameter case,

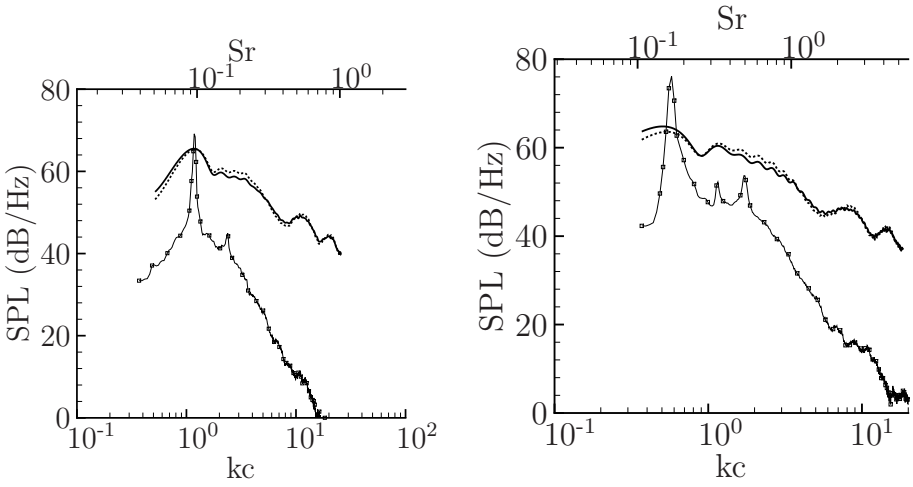

(a) Rod 0.008 m (b) Rod 0.016 m

Figure 4.20: Noise prediction using the reconstruction technique proposed in this work. Noise computed considering the case with reference flow velocity of 30 m/s and observer placed 1 m distance from the airfoil at a 90° position. Continuous line with open square symbols: experiments; Continous line: Amiet theory prediction – 1^{st} iteration; Amiet theory prediction – 2^{nd} iteration.

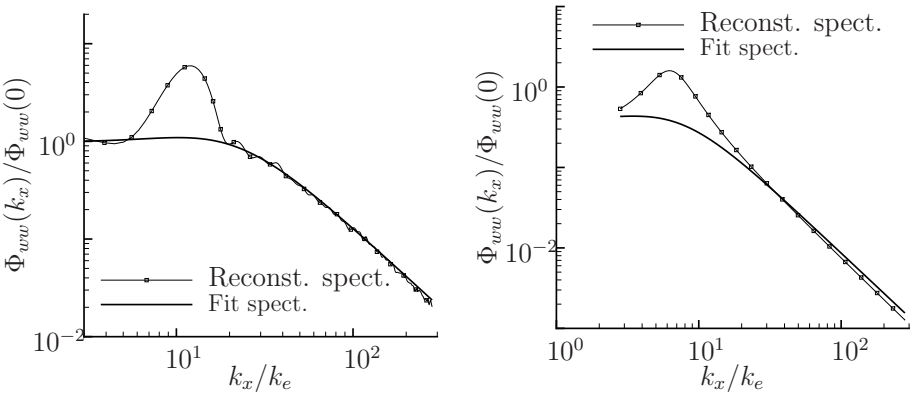

(a) Rod 0.008 m (b) Rod 0.016 m

Figure 4.21: Comparison between the normal velocity power spectral density computed with the technique here proposed and the best fit von Kármán spectrum for isotropic turbulence.

while this agreement has an amplitude bias to the rod 0.016 m diameter case. From the fitting it is obtained turbulence fluctuations u' values of 2.1 and 2.8 m/s, and longitudinal integral correlation lengths Λ_f of 0.006 and 0.015, respectively to the rod with 0.008 and 0.016 m diameter. With these parameter we have the relationship a/Λ_f equal to 16.7 and 6.7 m, respectively to the rod with 0.008 and 0.016 m diameter, thus the small scale turbulence hypothesis is verified. With this fitting the two input parameters necessary to characterize the distorted turbulence spectrum are obtained. As discussed in the grid-airfoil case, it is observed in the rod-airfoil case that the turbulence intensity grows as the flow approximates to the airfoil leading-edge. Consequently, to the noise calculation performed here, the same approach used before, where the free stream u' is proportionally corrected using the closest to the wall PIV measurable value. With these considerations, Fig. 4.22 compares the predicted acoustic spectra against experimental results.

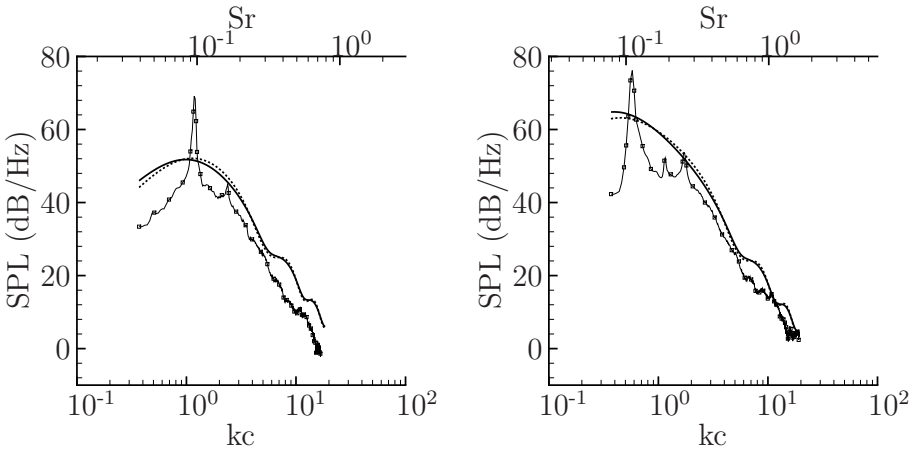

(a) Rod 0.008 m (b) Rod 0.016 m

Figure 4.22: Noise prediction using the Rapid Distortion Theory modified turbulence spectrum. The parameters to this spectrum are obtained from the best fit of the reconstructed normal velocity with the von Kármán spectrum for isotropic turbulence. Noise computed considering the case with reference flow velocity of 30 m/s and observer placed 1 m distance from the airfoil at a 90° position. Continuous line with open square symbols: experiments; Continous line: Amiet theory prediction – 1^{st} iteration; Amiet theory prediction – 2^{nd} iteration.

From Fig. 4.22 it is observed that the technique proposed here is able to predict

satisfactorily the broadband part of the acoustic spectra. In addition it is observed that following the methodology proposed here, it is observed the occurs noise over-prediction.

4.3 Conclusions

This chapter shows the importance of an accurate inflow characterization to the noise prediction in addition to physical evidence of the turbulence distortion approaching the airfoil leading-edge. It is evaluated the sensitivity inflow turbulence models which consider isotropic and anisotropic phenomena to the noise calculations and the impact of far-field hypotheses. Results shows that the application of the inverse strip theory combined with an anisotropic turbulence model, which considers the turbulence modification by the Rapid-Distortion-Theory, yields to accurate noise prediction for all the experimental cases studied here. Quantitative close to wall stereo-PIV analysis shows the presence of the turbulence distortion with results in agreement with the theory proposed by Hunt [34]. The grid-airfoil is studied as a canonical testing case and the rod-airfoil configuration as a more challenging incoming flow. In this configuration the periodic phenomena is not taken into account and only the random component of the flow is analyzed. The turbulence spectra is reconstructed from stereo-PIV spatial correlations measured in absence of the airfoil. The von Kármán isotropic turbulence spectra is then fit to the reconstructed turbulence spectra, which allows to obtain the turbulence velocity fluctuation u' and the integral correlation length Λ_e. These values serves as input to the turbulence spectra modified by the Rapid-Distortion Theory. When this model is applied to the noise prediction it is observed, now in a more complex inflow, predictions in good agreement with experimental results.

Chapter 5

Extension of the Amiet theory to the low-frequency regime

In the previous chapters the testing facility and the experiments which provide validation data to the technique proposed in this chapter have been presented. Additionally, physical considerations which guides the inflow model to be adopted in semi-analytical noise predictions have been discussed.

The classical Amiet theory is especially applicable to the high-frequency regime [6]. Adamczyk and Moreau [2, 47] compared noise predictions performed by this approach against experimental results finding that the compressibility parameter μ should satisfy the condition:

$$\mu = \bar{k}_x^* M = \frac{\bar{k}_x M}{\beta^2} > \pi/4\,, \tag{5.1}$$

to the calculated noise agrees with empirical data. Where:

$$\bar{k}_x = k_x b \quad , \quad k_x = \frac{\omega}{U} \quad \text{and} \quad \beta = \sqrt{1 - M^2}\,. \tag{5.2}$$

From this definition, the relationship between kc and μ as: $kc = 2\mu\beta^2$. Thus, as an illustration, for flows with Mach number 0.25, 0.5 and 0.75, the Amiet theory is valid for Helmholtz numbers (kc) higher than 1.47, 1.17 and 0.69, respectively. This chapter develops a methodology which allows to evaluate the Amiet theory at conditions where kc is closer and below the minimum value prescribed by Adamczyk and Moreau [2, 47].

In this thesis, the classical Amiet [6] approach is rewritten, for the leading-edge case, following the work of Rozenberg and Christophe [19, 58]. These derivations are an application of Roger and Moreau [55] developments, derived to the trailing-edge noise case. This chapter focus to overcome a current theory limitation, which results into noise over-prediction, at low-frequencies, where the airfoil is considered a compact noise source. The proposed methodology applies two more iterative applications of the Schwarzschild theorem, resulting in a better converged sound prediction.

5.1 Problem statement

The Amiet theory, introduced in Chapter 2 and detailed in Appendix A, iteratively solves the gust-airfoil interaction boundary value problem. As solution strategy, it proposes two successive applications of the Schwarzschild theorem, where leading- and trailing-edge corrections are imposed. The iterative procedure has no formal proof of convergence and supposes that the residual flow potential, at the region upstream of the airfoil leading-edge, is very small compared with the flow potential, present at the first iteration of the process. To evaluate this assumption Fig. 5.1 compares the initial potential $\phi_0(\bar{x}, 0)$ computed, at the first iteration of the Amiet theory (see Eq. 2.46) to the potential $\phi_3(\bar{x}, 0)$ computed, in a third iteration, proposed here. This velocity potential is calculated from the integration of the residual pressure $p_2(\bar{x}, 0)$ (Eq. 2.59), present upstream of the airfoil leading-edge, computed using Eq. 2.53.

Fig. 5.1 shows that, when the airfoil is considered a non-compact noise source, the residual flow potential $\phi_3(\bar{x}, 0)$ is small compared with the original flow potential $\phi_0(\bar{x}, 0)$. Conversely, as the airfoil can be considered as a compact noise source, the residual potential $\phi_3(\bar{x}, 0)$ has same order of magnitude as the original potential $\phi_0(\bar{x}, 0)$. This last result disagrees with the convergence after two iteration hypothesis, proposed by the Amiet theory.

5.2 Correction to the second iteration aeroacoustic transfer function

Before starting the core derivations of this chapter, it is important to treat a secondary problem associated with non-compactness effects, which influences the calculation of the aeroacoustic transfer function $\mathcal{L}_2(\mathbf{x}, k_x, k_y)$. As discussed in Chapter 2, the first iteration computes the pressure trace and aeroacoustic

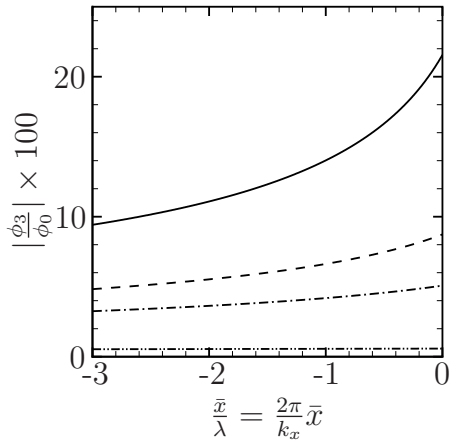

Figure 5.1: Compare potential $\phi_3(\bar{x},0)/\phi_0(\bar{x},0)$. Continuous line: $kc = 0.1$; Dashed line: $kc = 0.5$; Dash dot line: $kc = 1$; Dash dot dot line: $kc = 10$.

transfer function $\mathcal{L}_1(\mathbf{x}, k_x, k_y)$ at the airfoil surface without analytical approximations. However, the second iteration involves an approximation in the calculation of the trailing-edge scattered pressure $P_2(\bar{x},0)$, which is reproduced from Appendix A here, for clarity.

The trailing-edge back-scattered pressure $P_2(\bar{x},0)$ is computed from the application of the Schwarzschild theorem as:

$$P_2\left(\bar{x},0\right) = -\frac{1}{\pi}\int_0^\infty G(\bar{x}-2,\xi,0)P_1(2+\xi,0)\mathrm{d}\xi, \tag{5.3}$$

where G is the Green's function. The substitution of G and P_1 leads to:

$$P_2\left(\bar{x},0\right) = -\rho\, U\, w_0 \frac{\mathrm{e}^{-\mathrm{i}\pi/4}}{\pi\sqrt{\pi\left(\bar{k}_x+\beta^2\kappa\right)}}\,\mathrm{e}^{-4\mathrm{i}\kappa\bar{x}}\int_0^\infty \sqrt{\frac{2-\bar{x}}{\xi(\xi+2)}}\frac{\mathrm{e}^{-2\mathrm{i}\kappa\xi}}{\xi+2-\bar{x}}\mathrm{d}\xi\,. \tag{5.4}$$

The integral term has no primitive, and, an approximation is necessary for the sake of analytical tractability. The dominant contribution to the final integral value is obtained for small values of ξ, e.g. $1/\sqrt{\xi(2+\xi)}$ is large, then it is likely to approximate the term $\xi(2+\xi)$ under the square root to 2ξ, e.g. $1/\sqrt{\xi(2+\xi)} \approx 1/\sqrt{2\xi}$ for small ξ, leading to the approximation:

$$\int_0^\infty \sqrt{\frac{2-\bar{x}}{\xi(\xi+2)}}\frac{\mathrm{e}^{-2\mathrm{i}\kappa\xi}}{\xi+2-\bar{x}}\mathrm{d}\xi \approx \int_0^\infty \sqrt{\frac{2-\bar{x}}{2\xi}}\frac{\mathrm{e}^{-2\mathrm{i}\kappa\xi}}{\xi+2-\bar{x}}\mathrm{d}\xi\,. \tag{5.5}$$

With this approximation, $P_2(\bar{x}, 0)$ can be derived analytically and is presented in Eq. 2.58. This proposed approximation is accurate in the non-compact frequency regime. For the compact regime, this approach overpredicts the aeroacoustic transfer function $\mathcal{L}_2(\mathbf{x}, k_x, k_y)$. To evaluate the impact of the approximation on computing $P_2(\bar{x}, 0)$, Fig. 5.2 compares the analytical expression against the numerical integration of $P_2(\bar{x}, 0)$, calculated by Eq. 5.4 with numerical accuracy of 0.1%.

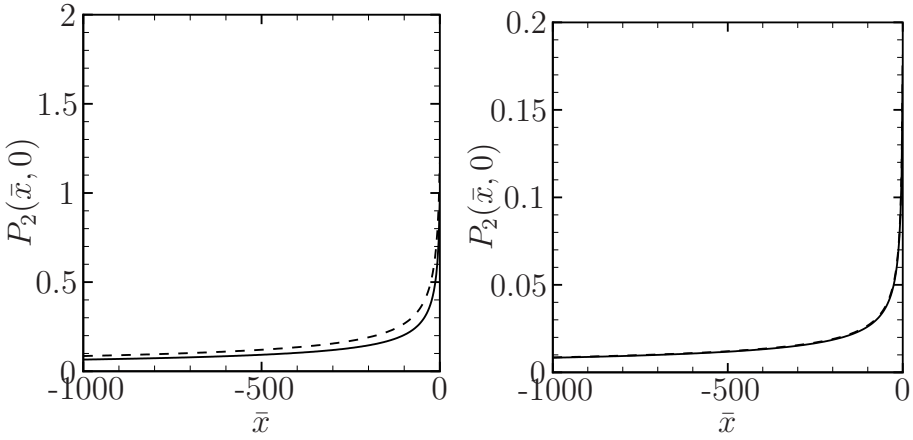

(a) kc = 0.1; $\kappa = 0.0667$ (b) kc = 1; $\kappa = 0.6667$

Figure 5.2: Compare the analytical approximation to compute the airfoil pressure trace $P_2(\bar{x}, 0)$ with the exact values computed numerically. Values calculated with $M = 0.5$. Continuous line: Numerically computed results; Dashed line: Analytically computed results.

Noteworthy remember at this point that:

$$\kappa^2 = \left[\left(\frac{\bar{k}_x M}{\beta^2} \right)^2 - \frac{\bar{k}_y^2}{\beta^2} \right]. \tag{5.6}$$

From Fig. 5.2 it is noticed that in the high-frequency regime (e.g. $kc = 1$) the analytical approximation matches perfectly the numerical value of $P_2(\bar{x}, 0)$. However, a small difference between the numeric $P_2(\bar{x}, 0)$ and the analytical approximation is observed in the low-frequency regime (e.g. $kc = 0.1$). These differences motivate the investigation of a correction function which can compensate the analytical inaccuracy in the calculation of $\mathcal{L}_2(\mathbf{x}, k_x, k_y)$. Therefore the correction function $\mathcal{C}$, which is defined by the ratio between the

numerical and the analytical aeroacoustic transfer functions $\mathcal{L}_2(\mathbf{x}, k_x, k_y)$ is presented in Fig. 5.3.

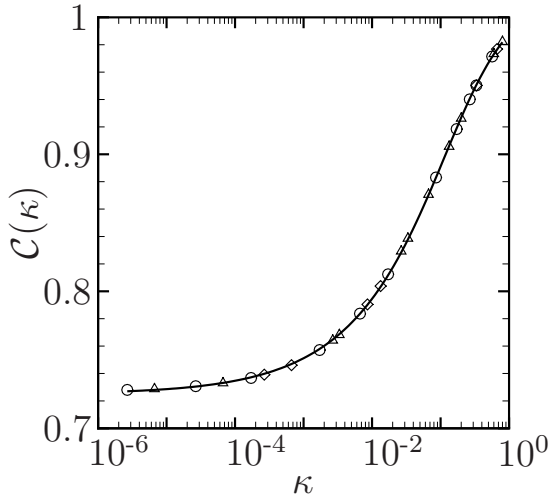

Figure 5.3: Correction factor numerically computed for $\mathcal{L}_2$. Triangle: $M = 0.25$; Circle: $M = 0.5$; Diamond: $M = 0.75$.

From this figure it is observed that the correction function $\mathcal{C}$ exclusively depends on κ, i.e. is not affected by the Mach number. The following regression function:

$$\mathcal{C}(\kappa) = \frac{\mathcal{L}_2^{\text{Numerical}}}{\mathcal{L}_2^{\text{Analytical}}} = 0.725 + 0.29\left(1 + \frac{0.27}{\kappa}\right)^{-0.43} \tag{5.7}$$

will be used in the further developments of this thesis. Therefore the relation between the corrected aeroacoustic transfer function $\mathcal{L}_2^*$ and the analytical approximate expression $\mathcal{L}_2$ is:

$$\mathcal{L}_2^*(\mathbf{x}, k_x, k_y) = \mathcal{C}(\kappa)\mathcal{L}_2(\mathbf{x}, k_x, k_y)\,. \tag{5.8}$$

To assess the effect of this correction, Fig. 5.4 compares against experimental results the noise prediction by the Amiet theory with and without the correction.

Remembering that the anechoic room of this experiment can be considered as such for frequencies higher than 200 Hz, it is observed from Fig. 5.4 that the correction only affects the noise prediction at frequencies below the range of validity of the current experiment. This correction would have a higher importance for smaller chord airfoils.

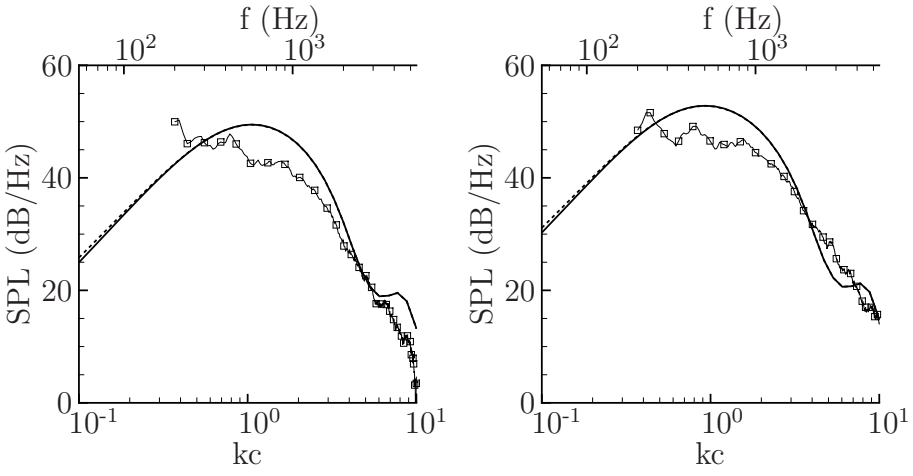

(a) Grid # 1 (b) Grid # 2

Figure 5.4: Evaluation of the correction function $\mathcal{C}(\kappa)$ effect to the noise prediction. Calculations performed using the inverse strip theory considering an observer localized at a distance of 1 m from the airfoil leading-edge at an angle of 90°. Continuous line with square symbol: experiment; Continuous line: No correction $\mathcal{C}(\kappa)$ applied; Dashed line: with correction $\mathcal{C}(\kappa)$ applied.

5.3 Third iteration of the Amiet methodology

The original Amiet theory prescribes two applications of the Schwarzschild theorem to satisfy the boundary conditions, which imposes zero potential upstream of the airfoil leading-edge and zero pressure jump at the trailing-edge and downstream of it. This section intends to compute a third iteration to correct the residue potential present, after the second iteration, upstream of the airfoil leading-edge.

The residual potential present upstream of the airfoil trailing-edge The calculation starts with the final step of the Amiet theory described by Christophe [19] and reviewed in Chapter 2. To calculate the residual potential, upstream of the airfoil leading-edge, it is necessary to develop the relation between pressure and flow potential. We introduce a notation where a variable and its time Fourier transform, are written in normal and bold face,

respectively:

$$\Phi(x,y,z,t) = \boldsymbol{\phi} \mathrm{e}^{\mathrm{i}\alpha y}\, \mathrm{e}^{\mathrm{i}\omega t}\,,$$

$$p_2(x,y,z,t) = \mathbf{P_2}(x,0) \mathrm{e}^{\mathrm{i}\alpha y}\, \mathrm{e}^{\mathrm{i}\omega t}\,.$$

This notation is as well valid to the variables with a subscript or superscript, referring for the iteration number.

According to Roger and Moreau [55] the pressure trace is related to the flow potential as:

$$\mathbf{P_2}(x,0)\, \mathrm{e}^{\mathrm{i}\omega t} = -\rho_0 \frac{\mathrm{D}\Phi}{\mathrm{D}t}. \tag{5.9}$$

Considering that the residual potential $\Phi^{(3)}$ can be written as:

$$\Phi^{(3)}(x,z,t) = \boldsymbol{\phi}(x,z)\, \mathrm{e}^{\mathrm{i}\omega t} = \varphi^{(3)}(x,z)\, \mathrm{e}^{\mathrm{i}\gamma x}\, \mathrm{e}^{\mathrm{i}\omega t}\,, \tag{5.10}$$

it is possible to replace the potential $\Phi^{(3)}$ (Eq. 5.10) into Eq. 5.9 to obtain:

$$\frac{-\mathbf{P_2}(x,0)\, b}{\rho_0\, U} = \frac{\partial}{\partial \bar{x}} \boldsymbol{\phi}(x,z) + \mathrm{i}\, \bar{k}_x\, \boldsymbol{\phi}(x,z) \tag{5.11}$$

where Eq. 5.11 represents a partial differential equation, which solution is given as:

$$\boldsymbol{\phi}^{(3)}(x,z) = \varphi^{(3)}(x,z)\, \mathrm{e}^{\mathrm{i}\gamma x} = \frac{-b}{\rho\, U} \int_{-\infty}^{\bar{x}} \mathbf{P_2}(\xi,0)\, \mathrm{e}^{-\mathrm{i}\bar{k}_x(\bar{x}-\xi)} \mathrm{d}\xi\,. \tag{5.12}$$

In Chapter 2 it is shown that the trailing-edge scattered pressure $\mathbf{P_2}(\bar{x},0)$ is given by:

$$\mathbf{P_2}(\bar{x},0) = P_2\, \mathrm{e}^{\mathrm{i}\gamma x} = -\rho_0\, w_0\, U \frac{\mathrm{e}^{-\mathrm{i}\pi/4}\, \mathrm{e}^{-\mathrm{i}(K-\bar{k}_x^* M^2)\bar{x}}}{\sqrt{2\pi(\bar{k}_x + \beta^2\kappa)}} \left[1 - (1+\mathrm{i})\mathrm{E}^*\left(2\kappa(2-\bar{x})\right)\right]\,, \tag{5.13}$$

where E^* is the complex conjugate of the Fresnel integral, defined as:

$$\mathrm{E}^* = \int_0^x \frac{\mathrm{e}^{-\mathrm{i}t}}{\sqrt{2\pi t}} \mathrm{d}t\,. \tag{5.14}$$

Replacing Eq. 5.13 into Eq. 5.12 we have the corresponding flow potential due to the trailing-edge scattered pressure $\mathbf{P_2}(\bar{x},0)$:

$$\boldsymbol{\phi}^{(3)}(x,z) = \frac{b w_0 \mathrm{e}^{-\mathrm{i}\pi/4} \mathrm{e}^{-\mathrm{i}\bar{k}_x\bar{x}}}{\sqrt{2\pi(\bar{k}_x + \beta^2\kappa)}} \int_{-\infty}^{\bar{x}} \left[1 - (1+\mathrm{i})\mathrm{E}^*\left(2\kappa(2-\bar{x})\right)\right] \mathrm{e}^{-\mathrm{i}(K-\bar{k}_x^* M^2 - \bar{k}_x)\xi} \mathrm{d}\xi\,, \tag{5.15}$$

which can be solved by integration by parts, as:

$$\int_a^b u\,\mathrm{d}v = uv(b) - uv(a) - \int_a^b v\mathrm{d}u\,, \tag{5.16}$$

with:

$$u = \left[1 - (1+\mathrm{i})\mathrm{E}^*\left(2\kappa(2-\xi)\right)\right]\,, \tag{5.17}$$

$$\mathrm{d}u = \frac{(1+\mathrm{i})\sqrt{2\kappa}\,\mathrm{e}^{-4\mathrm{i}\kappa}\,\mathrm{e}^{2\mathrm{i}\kappa\xi}}{\sqrt{2\pi(2-\xi)}}\mathrm{d}\xi\,, \tag{5.18}$$

$$v = \frac{\mathrm{i}\mathrm{e}^{-\mathrm{i}(\kappa-\bar{k}_x^*)\xi}}{\kappa-\bar{k}_x^*}\,, \tag{5.19}$$

$$\mathrm{d}v = \mathrm{e}^{-\mathrm{i}(\kappa-\bar{k}_x^*)\xi}\mathrm{d}\xi\,, \tag{5.20}$$

for the calculation of the second integral of Eq. 5.16, a change of variables is applied to retrieve the Fresnel integral definition:

$$t = 2-\xi \qquad \xi = 2-t \qquad \mathrm{d}t = -\mathrm{d}\xi\,, \tag{5.21}$$

which after some algebra yields:

$$\boldsymbol{\phi}^{(3)}(x,z) = \frac{\mathrm{i}\,b\,w_0\,\mathrm{e}^{-\mathrm{i}\pi/4}\,\mathrm{e}^{-\mathrm{i}\bar{k}_x\bar{x}}}{\sqrt{2\pi(\bar{k}_x+\beta^2\kappa)}(\kappa-\bar{k}_x^*)}\Big\{\left[1-(1+\mathrm{i})\mathrm{E}^*\left(2\kappa(2-\bar{x})\right)\right]\mathrm{e}^{-\mathrm{i}(\kappa-\bar{k}_x^*)\bar{x}}$$

$$-\frac{\sqrt{2\kappa}\mathrm{e}^{-2\mathrm{i}(\kappa-\bar{k}_x^*)}}{\sqrt{\kappa+\bar{k}_x^*}}\left[1-(1+\mathrm{i})\mathrm{E}^*((2-\bar{x})(\kappa+\bar{k}_x^*))\right]\Big\}\,. \tag{5.22}$$

Using the relation between the complementary error function and the Fresnel integral:

$$(1+\mathrm{i})\mathrm{E}^*(x) - 1 = -\mathrm{erfc}^*\left((1-\mathrm{i})\sqrt{\frac{x}{2}}\right) = -\mathrm{erfc}\left((1+\mathrm{i})\sqrt{\frac{x}{2}}\right)\,, \tag{5.23}$$

it is possible to define the flow potential in terms of the complementary error function as:

$$\boldsymbol{\phi}^{(3)}(x,z) = \frac{-\mathrm{i}\,b\,w_0\,\mathrm{e}^{-\mathrm{i}\pi/4}}{\sqrt{2\pi(\bar{k}_x+\beta^2\kappa)}(\kappa-\bar{k}_x^*)}\Big\{-\mathrm{erfc}\left[(1+\mathrm{i})\sqrt{\kappa(2-\bar{x})}\right]\mathrm{e}^{-\mathrm{i}(\kappa-\bar{k}_x^*M^2)\bar{x}}$$

$$+\frac{\sqrt{2\kappa}\mathrm{e}^{-2\mathrm{i}(\kappa-\bar{k}_x^*)}}{\sqrt{\kappa+\bar{k}_x^*}}\mathrm{erfc}\left[(1+\mathrm{i})\sqrt{\frac{(2-\bar{x})(\kappa+\bar{k}_x^*)}{2}}\right]\mathrm{e}^{-\mathrm{i}\bar{k}_x\bar{x}}\Big\}\,. \tag{5.24}$$

The next calculation step is the second leading-edge correction, imposing a zero flow potential upstream of the leading-edge and a non-penetration boundary condition downstream of the leading-edge. This problem is solved through the application of the Schwarzschild theorem which yields an integral with no analytical primitive. For analytical treatment, the complementary error function is expanded as a power series and the zeroth order term is considered (please refer to Abramowitz [1] page 297). This approach is verified to be asymptotically valid for larger arguments of the complex error function:

$$\operatorname{erfc}\left[(1+\mathrm{i})x\right] \approx \frac{(1-\mathrm{i})\mathrm{e}^{-2\mathrm{i}x^2}}{2\sqrt{\pi}x}\,, \tag{5.25}$$

where erfc is the complementary error function. With this approximation Eq. 5.24 becomes:

$$\begin{aligned}\boldsymbol{\phi}^{(3)}(x,z) \approx & \frac{-(1+\mathrm{i})\,b\,w_0\,\mathrm{e}^{-\mathrm{i}\pi/4}\,\mathrm{e}^{-4\mathrm{i}\kappa}}{\pi\sqrt{2(\bar{k}_x+\beta^2\kappa)}(\kappa-\bar{k}_x^*)} \\ & \left(-\frac{\mathrm{e}^{\mathrm{i}(\kappa+\bar{k}_x^*M^2)\bar{x}}}{2\sqrt{\kappa(2-\bar{x})}}+\frac{\sqrt{\kappa}\mathrm{e}^{2\mathrm{i}\bar{k}_x^*}\mathrm{e}^{\mathrm{i}(\kappa+\bar{k}_x^*M^2)\bar{x}}}{\sqrt{\kappa+\bar{k}_x^*}\sqrt{(2-\bar{x})(\kappa+\bar{k}_x^*)}}\right)\,. \end{aligned} \tag{5.26}$$

The approximation for $\boldsymbol{\phi}^{(3)}(x,z)$ is valid for large arguments $\bar{x}$. Figure. 5.5 compares the exact $\boldsymbol{\phi}^{(3)}(x,z)$ formulation with the approximate expression.

Figure 5.5 indicates that the approximation becomes less accurate as $\bar{x}/\bar{\lambda}$ approaches zero. The differences between the numerical and analytical solutions will be accounted for in a next step of the calculation. This requires to include as well the approximation adopted to compute $P_2(\bar{x},0)$.

Thus to obtain a more precise value of $\boldsymbol{\phi}^{(3)}(x,z)$, the pressure $P_2(\bar{x},0)$ is numerically computed with sufficient accuracy and then numerically integrated, following Eq. 5.12. The correction function is seen in Fig. 5.6 to depend only of κ and is fitted, by numerical regression, by the function:

$$\mathcal{F}(\kappa) = \left(1+\frac{7}{90\kappa}\right)^{-1/3}\,. \tag{5.27}$$

It is shown in Fig. 5.6 that the correction factor tends to unity, indicating that the analytical approximation is precise in the non-compact regime. Figure 5.7 shows a comparison between $\boldsymbol{\phi}^{(3)}(x,z)$ computed by Eq. 5.26 and corrected by Eq. 5.27, against the numerical calculations. This example is computed for

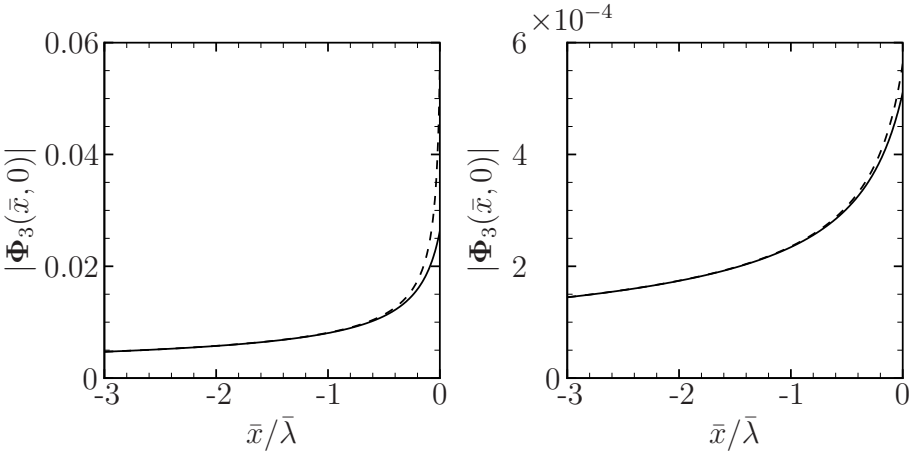

(a) $kc = 0.1$ (b) $kc = 1$

Figure 5.5: Compare the exact and the approximate formulation to compute $\boldsymbol{\phi}^{(3)}(x,z)$. Where $\bar{\lambda}$ is the perturbation wave length normalized by the airfoil chord (2b). Calculation performed considering flow Mach number $M = 0.5$. Continuous line: Exact $\boldsymbol{\phi}^{(3)}(x,z)$ computed by Eq. 5.24. Dashed line: approximate $\boldsymbol{\phi}^{(3)}(x,z)$ computed by Eq. 5.26.

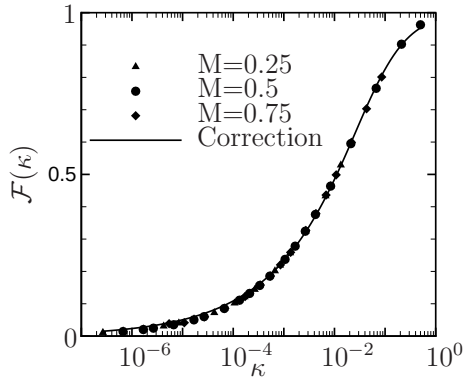

Figure 5.6: Correction factor for $\boldsymbol{\phi}^{(3)}(x,z)$.

$kc = 0.01$, a gust wavenumber where the airfoil can be surely considered a compact noise source.

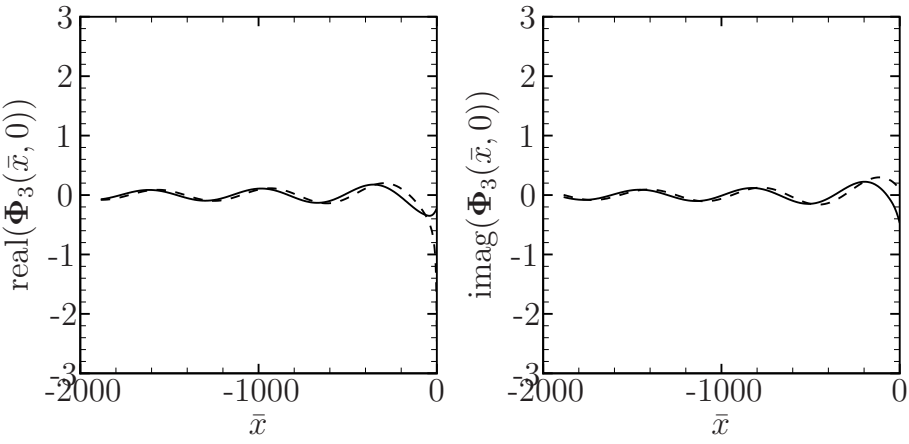

(a) real (b) imag

Figure 5.7: Compare the $\boldsymbol{\phi}^{(3)}(x,z)$ computed numerically with exact $P_2(\bar{x},0)$ values against the approximation given by Eq. 5.26 and corrected by Eq. 5.27. Values calculated for $kc = 0.01$ and $M = 0.5$. Continuous line: $\boldsymbol{\phi}^{(3)}(x,z)$ computed numerically with exact $P_2(\bar{x},0)$; Dashed line: $\boldsymbol{\phi}^{(3)}(x,z)$ computed by Eq. 5.26 and corrected by Eq. 5.27.

It is seen that $\boldsymbol{\phi}^{(3)}(x,z)$, calculated from the exact $P_2(\bar{x},0)$, has a small phase difference when compared to values calculated using the approximation for $P_2(\bar{x},0)$. It is important here to remember that the approximation of $\boldsymbol{\phi}^{(3)}(x,z)$, given by Eq. 5.26, is necessary for the next steps.

Now, as a preparation for the next iteration, the time- and space-Fourier transform for the potential as $\boldsymbol{\phi}^{(3)}(x,z)$ is:

$$\boldsymbol{\phi}^{(3)}(x,z)\exp(\mathrm{i}\omega t) = \varphi^{(3)}(x,z)\exp(\mathrm{i}\gamma x)\exp(\mathrm{i}\omega t)\,, \tag{5.28}$$

it is possible to write the Fourier transformed potential $\varphi^{(3)}(x,z)$ as:

$$\varphi^{(3)}(x,z) \approx \mathcal{F}(\kappa)\frac{-(1+\mathrm{i})\,b\,w_0\,\mathrm{e}^{-\mathrm{i}\pi/4}\,\mathrm{e}^{-4\mathrm{i}\kappa}}{\pi\sqrt{2(\bar{k}_x+\beta^2\kappa)}(2\sqrt{\kappa}(\kappa+\bar{k}_x^*))}\frac{\mathrm{e}^{\mathrm{i}\kappa\bar{x}}}{\sqrt{2-\bar{x}}}\,, \tag{5.29}$$

using the notation for the correction:

$$\varphi^{(3)*}(x,z) = \mathcal{F}(\kappa)\varphi^{(3)}(x,z)\,. \tag{5.30}$$

Third application of the Schwarzschild theorem For the third iteration the procedure proposed here corrects the residual potential upstream of the airfoil leading-edge, imposing the boundary condition of zero flow potential there. This boundary value problem is one more time solved by the application of the Schwarzschild theorem, resulting into the leading-edge scattered potential $\Psi_3(\bar{x},0)$:

$$\Psi_3(\bar{x},0) = -\frac{1}{\pi}\int_0^\infty \sqrt{\frac{\bar{x}}{\xi}}\frac{\mathrm{e}^{-\mathrm{i}\kappa(\xi+\bar{x})}}{\xi+\bar{x}}\varphi^{(3)*}(-\xi,0)\mathrm{d}\xi\,, \tag{5.31}$$

replacing the potential $\varphi^{(3)*}(x,z)$ into Eq. 5.31 results to the relation:

$$\Psi_3(\bar{x},0) = \mathcal{F}(\kappa)\frac{(1+\mathrm{i})\,b\,w_0\,\mathrm{e}^{-\mathrm{i}\pi/4}\,\mathrm{e}^{-4\mathrm{i}\kappa}\,\mathrm{e}^{-\mathrm{i}\kappa\bar{x}}}{\pi^2\sqrt{2(\bar{k}_x+\beta^2\kappa)}(2\sqrt{\kappa}(\kappa+\bar{k}_x^*))}\int_0^\infty \sqrt{\frac{\bar{x}}{\xi}}\frac{1}{\xi+\bar{x}}\frac{\mathrm{e}^{-2\mathrm{i}\kappa\xi}}{\sqrt{2+\xi}}\mathrm{d}\xi\,. \tag{5.32}$$

The integral term in Eq. 5.32 has no analytical solution. Analytical treatment can performed though the approximation:

$$\int_0^\infty \sqrt{\frac{\bar{x}}{\xi}}\frac{1}{\xi+\bar{x}}\frac{\mathrm{e}^{-2\mathrm{i}\kappa\xi}}{\sqrt{2+\xi}}\mathrm{d}\xi \approx \int_0^\infty \sqrt{\frac{\bar{x}}{2\xi}}\frac{\mathrm{e}^{-2\mathrm{i}\kappa\xi}}{\xi+\bar{x}}\mathrm{d}\xi\,, \tag{5.33}$$

giving:

$$\Psi_3(\bar{x},0) = \mathcal{F}(\kappa)\frac{(1+\mathrm{i})\,b\,w_0\,\mathrm{e}^{-\mathrm{i}\pi/4}\,\mathrm{e}^{-4\mathrm{i}\kappa}\,\mathrm{e}^{\mathrm{i}\kappa\bar{x}}}{2\pi\sqrt{(\bar{k}_x+\beta^2\kappa)}(2\sqrt{\kappa}(\kappa+\bar{k}_x^*))}\left[1-(1+\mathrm{i})\mathrm{E}^*(2\kappa\bar{x})\right]\,. \tag{5.34}$$

The integral in Eq. 5.33 gives an approximation for $\Psi_3(\bar{x},0)$, valid for the high-frequency regime, which, however, needs to be corrected for the low-frequency regime. This correction will compensate the small argument error observed in Fig. 5.5. To find a correction function to $\Psi_3(\bar{x},0)$, Eq. 5.32 is integrated numerically. The comparison between the numerical solution and the analytical expression of Eq. 5.34 shows, from numerical regression, the function which corrects the error present in the low-frequency regime:

$$\mathcal{I}(\kappa) = \left(1+\frac{1}{4\kappa^{13/9}}\right)^{-1/3}\,. \tag{5.35}$$

Figure 5.8 shows a comparison between $\mathcal{I}$ computed for flow Mach number $M = 0.25$, $M = 0.5$ and $M = 0.75$ and the correction function obtained by numerical regression:

From Fig. 5.8 it is verified that, similarly with the previous cases, the correction function only depends on κ and it tends to zero for a small κ value, while it

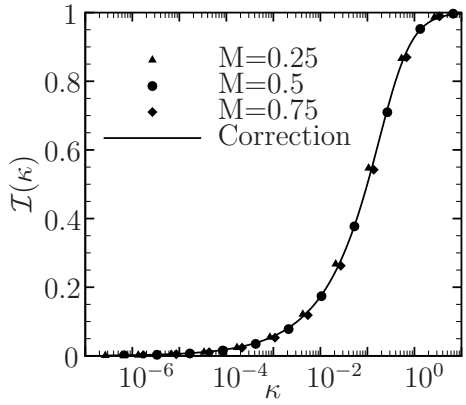

Figure 5.8: Correction factor for $\Psi_3(\bar{x}, 0)$.

tends to the unit when κ is larger than 1. Using this correction function, it is possible to note the corrected potential Ψ_3 as Ψ_3^*, according to the definition:

$$\Psi_3^*(\bar{x}, 0) = \Psi_3(\bar{x}, 0)\mathcal{I}(\kappa)\,. \tag{5.36}$$

After the computation of the leading-edge scattered potential $\Psi_3^*(\bar{x}, 0)$, it is possible to write the total potential $\boldsymbol{\phi}^{(4)}$ by the superposition of the residual potential $\boldsymbol{\phi}^{(3)*}$ and the leading-edge scattered potential Ψ_3^* as:

$$\boldsymbol{\phi}^{(4)}(\bar{x}, 0) = \boldsymbol{\phi}^{(3)*}(\bar{x}, 0) + \Psi_3^*(\bar{x}, 0)\mathrm{e}^{\mathrm{i}\gamma x}\,. \tag{5.37}$$

Noteworthy that the potential $\boldsymbol{\phi}^{(3)}$ should be computed according Eq. 5.24, noticing that the large arguments approximation is useful to allow the analytically compute the Eq. 5.31 integral.

Pressure jump calculation Once the leading-edge corrected potential $\boldsymbol{\phi}^{(4)}(\bar{x}, 0)$ is computed, it is possible to derive the resulting pressure jump trace $\mathbf{P_3}(x, z)$, according to:

$$\mathbf{P_3}(x, z) = P_3(x, z)\mathrm{e}^{\mathrm{i}\gamma x} = -\frac{\rho U}{b}\left(\frac{\partial}{\partial \bar{x}}\boldsymbol{\phi}^{(4)}(x, z) + \mathrm{i}\bar{k}_x\boldsymbol{\phi}^{(4)}(x, z)\right)\,, \tag{5.38}$$

where the derivative of the potential $\boldsymbol{\phi}^{(4)}(\bar{x}, 0)$ can be written as:

$$\frac{\partial \boldsymbol{\phi}^{(4)}}{\partial \bar{x}} = \frac{\partial \boldsymbol{\phi}^{(3)*}}{\partial \bar{x}} + \left(i\bar{k}_x^* M^2 \psi_3^* + \frac{\partial \psi_3^*}{\partial \bar{x}}\right)\mathrm{e}^{\mathrm{i}\bar{k}_x^* M^2 \bar{x}}\,, \tag{5.39}$$

now, calculating the parenthesis term, it is possible to show that:

$$\left(\mathrm{i}\bar{k}_x^* M^2 \psi_3^* + \frac{\partial \psi_3^*}{\partial \bar{x}}\right) \mathrm{e}^{\mathrm{i}\bar{k}_x^* M^2 \bar{x}} = \mathcal{F}(\kappa)\mathcal{I}(\kappa) f_1 \left\{ \mathrm{i}(\kappa + \bar{k}_x^* M^2)\left[1 - (1+\mathrm{i})\mathrm{E}^*(2\kappa\bar{x})\right] + \right.$$

$$\left. -(1+\mathrm{i})\sqrt{\frac{\kappa}{\pi}}\frac{\mathrm{e}^{-2\mathrm{i}\kappa\bar{x}}}{\sqrt{\bar{x}}} \right\} \mathrm{e}^{\mathrm{i}(\kappa + \bar{k}_x^* M^2)\bar{x}}\,, \tag{5.40}$$

with:

$$f_1 = \frac{(1+\mathrm{i})\, b\, w_0\, \mathrm{e}^{(-\mathrm{i}\pi/4)}\, \mathrm{e}^{-4\mathrm{i}\kappa}}{4\pi\sqrt{\bar{k}_x + \beta^2\kappa}\sqrt{\kappa}(\kappa + \bar{k}_x^*)}\,, \tag{5.41}$$

$$\frac{\partial \boldsymbol{\phi}^{(3)*}}{\partial \bar{x}} = \mathcal{F}(\kappa) f_2(\alpha_1 + f_3\alpha_2)\,, \tag{5.42}$$

with the terms:

$$\alpha_1 = \left(-\mathrm{i}(\kappa - \bar{k}_x^* M^2)\left(1 - (1+\mathrm{i})\mathrm{E}^*\left[2\kappa(2-\bar{x})\right]\right) + (1+\mathrm{i})\sqrt{\frac{\kappa}{\pi}}\frac{\mathrm{e}^{-4\mathrm{i}\kappa}\mathrm{e}^{2\mathrm{i}\kappa\bar{x}}}{\sqrt{2-\bar{x}}}\right)$$

$$\mathrm{e}^{-\mathrm{i}(\kappa - \bar{k}_x^* {}^* M^2)\bar{x}}\,, \tag{5.43}$$

$$\alpha_2 = \left(\frac{\sqrt{\kappa + \bar{k}_x^*}}{\sqrt{2\pi}}(1+\mathrm{i})\mathrm{e}^{-2\mathrm{i}(\kappa + \bar{k}_x^*)}\frac{\mathrm{e}^{\mathrm{i}(\kappa + \bar{k}_x^*)\bar{x}}}{\sqrt{2-\bar{x}}} - \mathrm{i}\bar{k}_x\left(1 - (1+\mathrm{i})\mathrm{E}^*\left[(2-\bar{x})(\kappa + \bar{k}_x^*)\right]\right)\right)$$

$$\mathrm{e}^{-\mathrm{i}\bar{k}_x\bar{x}}\,, \tag{5.44}$$

and constants:

$$f_2 = \frac{\mathrm{i}\, b\, w_0\, \mathrm{e}^{-\mathrm{i}\pi/4}}{\sqrt{2\pi(\bar{k}_x + \beta^2\kappa)}(\kappa - \bar{k}_x^*)}\,, \tag{5.45}$$

$$f_3 = -\frac{\sqrt{2\kappa}\mathrm{e}^{-2\mathrm{i}(\kappa - \bar{k}_x^*)}}{\sqrt{\kappa + \bar{k}_x^*}}\,. \tag{5.46}$$

From this point the analytical expressions start to be too cumbersome to be treated as a single equation. To facilitate the analytical calculations, the leading-edge scattered pressure $\mathbf{P_3}(x,z)$ can be written as a sum of 5 terms as:

$$\mathbf{P_3}(x,z) = \frac{-\rho\, U}{b}\left(\beta_1 + \beta_2 + \beta_3 + \beta_4 + \beta_5\right)\,, \tag{5.47}$$

with

$$\beta_1 = -\mathcal{F}(\kappa)\mathcal{I}(\kappa)k_1(1+\mathrm{i})\sqrt{\frac{\kappa}{\pi}}\frac{\mathrm{e}^{-\mathrm{i}(\kappa-\bar{k}_x^* M^2)\bar{x}}}{\sqrt{\bar{x}}}\,, \tag{5.48}$$

$$\beta_2 = \mathcal{F}(\kappa)\mathcal{I}(\kappa)\mathrm{i}k_1\left(\kappa+\bar{k}_x^* M^2+\bar{k}_x\right)\left(1-(1+\mathrm{i})\mathrm{E}^*(2\kappa\bar{x})\right)\mathrm{e}^{\mathrm{i}(\kappa+\bar{k}_x^* M^2)\bar{x}}\,, \tag{5.49}$$

$$\beta_3 = -\mathcal{F}(\kappa)\mathrm{i}k_3\left(\kappa-\bar{k}_x^* M^2-\bar{k}_x\right)\left(1-(1+\mathrm{i})\mathrm{E}^*\left[2\kappa(2-\bar{x})\right]\right)\mathrm{e}^{-\mathrm{i}(\kappa-\bar{k}_x^* M^2)\bar{x}}\,, \tag{5.50}$$

$$\beta_4 = \mathcal{F}(\kappa)k_3(1+\mathrm{i})\left(\sqrt{\frac{\kappa}{\pi}}\mathrm{e}^{-4\mathrm{i}\kappa}+k_4\frac{\sqrt{\kappa+\bar{k}_x^*}}{\sqrt{2\pi}}\mathrm{e}^{-2\mathrm{i}(\kappa+\bar{k}_x^*)}\right)\frac{\mathrm{e}^{\mathrm{i}(\kappa+\bar{k}_x^* M^2)\bar{x}}}{\sqrt{2-\bar{x}}}\,, \tag{5.51}$$

$$\beta_5 = \mathcal{F}(\kappa)\left(-i\bar{k}_x k_3 k_4 - k_2\sqrt{2\kappa}\frac{\mathrm{e}^{-2\mathrm{i}(\kappa-\bar{k}_x^*)}}{\sqrt{\kappa+\bar{k}_x^*}}\right)\left(1-(1+\mathrm{i})\mathrm{E}^*((2-\bar{x})(\kappa+\bar{k}_x^*))\right)\mathrm{e}^{-\mathrm{i}\bar{k}_x\bar{x}}\,, \tag{5.52}$$

and constants

$$k_1 = \frac{(1+\mathrm{i})bw_0\mathrm{e}^{-\mathrm{i}\pi/4}\mathrm{e}^{-4\mathrm{i}\kappa}}{4\pi\sqrt{\bar{k}_x+\beta^2\kappa}(\sqrt{\kappa}(\kappa+\bar{k}_x^*))}\,, \tag{5.53}$$

$$k_2 = -\frac{\bar{k}_x bw_0\mathrm{e}^{-\mathrm{i}\pi/4}}{\sqrt{2\pi(\bar{k}_x+\beta^2\kappa)}(\kappa-\bar{k}_x^*)}\,, \tag{5.54}$$

$$k_3 = \frac{\mathrm{i}bw_0 e^{(-\mathrm{i}\pi/4)}}{\sqrt{2\pi(\bar{k}_x+\beta^2\kappa)}(\kappa-\bar{k}_x^*)}\,, \tag{5.55}$$

$$k_4 = -\frac{\sqrt{2\kappa}\mathrm{e}^{-2\mathrm{i}(\kappa-\bar{k}_x^*)}}{\sqrt{\kappa+\bar{k}_x^*)}}\,. \tag{5.56}$$

It is verified that:

$$\beta_4 = 0 \quad \text{and} \quad \beta_5 = 0\,, \tag{5.57}$$

consequently, only the constants k_1 and k_3 are used.

Aeroacoustic transfer function calculation After the leading-edge scattered pressure $\mathbf{P_3}(x,z)$ calculation we can compute the aeroacoustic transfer function.

To keep the tractability of the problem, the aeroacoustic transfer function will be split into three components, where:

$$\mathcal{L}_3(\mathbf{x}, k_x, k_y) = \mathcal{L}_3^{(1)}(\mathbf{x}, k_x, k_y) + \mathcal{L}_3^{(2)}(\mathbf{x}, k_x, k_y) + \mathcal{L}_3^{(3)}(\mathbf{x}, k_x, k_y)\,, \tag{5.58}$$

and the vector $\mathbf{x} = (x, y, z)$ represents the observer position at the fixed reference frame of coordinates.

Aeroacoustic transfer function $\mathcal{L}_3^{(1)}(\mathbf{x}, k_x, k_y)$ In this paragraph the detailed calculation of the aeroacoustic transfer function $\mathcal{L}_3^{(1)}(\mathbf{x}, k_x, k_y)$ will be presented and for the next paragraphs, only the main passages will be presented since the procedure is similar.

Starting from the leading-edge scattered pressure $\mathbf{P_3}^{(1)}(x, z) = \frac{-\rho U}{b}\beta_1$, which is given by:

$$\mathbf{P_3}^{(1)}(x, z) = \mathrm{i}\mathcal{F}(\kappa)\mathcal{I}(\kappa)\rho U w_0 \sqrt{\frac{\kappa}{\pi}} \frac{\mathrm{e}^{-\mathrm{i}\pi/4}\mathrm{e}^{-4\mathrm{i}\kappa}}{2\pi\sqrt{\bar{k}_x + \beta^2\kappa}\sqrt{\kappa}((\kappa + \bar{k}_x^*))} \frac{\mathrm{e}^{-\mathrm{i}(\kappa - \bar{k}_x^* M^2)\bar{x}}}{\sqrt{\bar{x}}}\,, \tag{5.59}$$

using the pressure non-dimensionalization, which is similar to the Eq. 2.60 definition presented in Chapter 2:

$$g_3^{(1)}(x, z) = \frac{\mathbf{P_3}^{(1)}(x, z)}{\pi\rho U w_0}\,, \tag{5.60}$$

and adopting the change of coordinates $\bar{x}_{new} = \bar{x}_{old} - 1$, we have the dimensionless pressure relation:

$$g_3^{(1)}(x, z) = \mathrm{i}\mathcal{F}(\kappa)\mathcal{I}(\kappa) \sqrt{\frac{\kappa}{\pi}} \frac{\mathrm{e}^{-\mathrm{i}\pi/4}\mathrm{e}^{-4\mathrm{i}\kappa}}{2\pi^2\sqrt{\bar{k}_x + \beta^2\kappa}\sqrt{\kappa}(\kappa + \bar{k}_x^*)} \frac{\mathrm{e}^{-\mathrm{i}(\kappa - \bar{k}_x^* M^2)(\bar{x}+1)}}{\sqrt{\bar{x}+1}}\,. \tag{5.61}$$

With the aeroacoustic transfer function definition:

$$\mathcal{L}_3^{(1)}(\mathbf{x}, k_x, k_y) = \int_{-1}^{1} g_3^{(1)}(x, z)\mathrm{e}^{-\mathrm{i}\mu(M - x/\sigma)\xi}\mathrm{d}\xi\,, \tag{5.62}$$

by replacing the $g_3^{(1)}(x, z)$ we have:

$$\mathcal{L}_3^{(1)}(\mathbf{x}, k_x, k_y) = \mathrm{i}\mathcal{F}(\kappa)\mathcal{I}(\kappa) \sqrt{\frac{\kappa}{\pi}} \frac{\mathrm{e}^{-\mathrm{i}\pi/4}\mathrm{e}^{-4\mathrm{i}\kappa}}{2\pi^2\sqrt{\bar{k}_x + \beta^2\kappa}\sqrt{\kappa}(\kappa + \bar{k}_x^*)} \int_{-1}^{1} \frac{\mathrm{e}^{-\mathrm{i}(\kappa - \bar{k}_x^* M^2)(\xi+1)}}{\sqrt{\xi+1}} \mathrm{e}^{-\mathrm{i}\mu(M - x/\sigma)\xi}\mathrm{d}\xi\,, \tag{5.63}$$

which after integration, using change of variables, results in:

$$\mathcal{L}_3^{(1)}(\mathbf{x}, k_x, k_y) = \mathrm{i}\mathcal{F}(\kappa)\mathcal{I}(\kappa)\sqrt{\frac{\kappa}{2}}\frac{\mathrm{e}^{-\mathrm{i}\pi/4}\mathrm{e}^{-4\mathrm{i}\kappa}}{\pi^2\sqrt{\bar{k}_x+\beta^2\kappa}\sqrt{\kappa}(\kappa+\bar{k}_x^*)}\frac{\mathrm{E}^*\left(2(\kappa-\mu x/\sigma)\right)\mathrm{e}^{\mathrm{i}\mu(M-x/\sigma)}}{\sqrt{(\kappa-\mu x/\sigma)}}\,. \tag{5.64}$$

Aeroacoustic transfer function $\mathcal{L}_3^{(2)}(\mathbf{x}, k_x, k_y)$ Similarly to the previous calculation, the dimensionless pressure $g_3^{(2)}(x,z)$ is written as:

$$g_3^{(2)}(x,z) = \mathcal{F}(\kappa)\mathcal{I}(\kappa)\frac{(1-\mathrm{i})\mathrm{e}^{-\mathrm{i}\pi/4}\mathrm{e}^{-4\mathrm{i}\kappa}}{4\pi^2\sqrt{\bar{k}_x+\beta^2\kappa}\sqrt{\kappa}(\kappa+\bar{k}_x^*)}\left(\kappa+\bar{k}_x^*M^2+\bar{k}_x\right)$$
$$\left(1-(1+\mathrm{i})\mathrm{E}^*(2\kappa(\bar{x}+1))\right)\mathrm{e}^{\mathrm{i}(\kappa+\bar{k}_x^*M^2)(\bar{x}+1)} \tag{5.65}$$

and the aeroacoustics transfer function $\mathcal{L}_3^{(2)}(\mathbf{x}, k_x, k_y)$ as:

$$\mathcal{L}_3^{(2)}(\mathbf{x}, k_x, k_y) = \mathcal{F}(\kappa)\mathcal{I}(\kappa)\frac{(1-\mathrm{i})\mathrm{e}^{-\mathrm{i}\pi/4}\mathrm{e}^{-4\mathrm{i}\kappa}}{4\pi^2\sqrt{\bar{k}_x+\beta^2\kappa}\sqrt{\kappa}(\kappa+\bar{k}_x^*)}\left(\kappa+\bar{k}_x^*M^2+\bar{k}_x\right)$$
$$\int_{-1}^{1}\left(1-(1+\mathrm{i})\mathrm{E}^*(2\kappa(\bar{x}+1))\right)\mathrm{e}^{\mathrm{i}(\kappa+\bar{k}_x^*M^2)(\xi+1)}\mathrm{e}^{-\mathrm{i}\mu(M-x/\sigma)\xi}\mathrm{d}\xi\,. \tag{5.66}$$

After integration, change of variables and simplifications, we have:

$$\mathcal{L}_3^{(2)}(\mathbf{x}, k_x, k_y) = \mathcal{F}(\kappa)\mathcal{I}(\kappa)\frac{(1-\mathrm{i})\mathrm{e}^{-\mathrm{i}\pi/4}\mathrm{e}^{-4\mathrm{i}\kappa}}{4\pi^2\sqrt{\bar{k}_x+\beta^2\kappa}\sqrt{\kappa}(\kappa+\bar{k}_x^*)}\frac{\left(\kappa+\bar{k}_x^*M^2+\bar{k}_x\right)}{\kappa+\mu x/\sigma}\mathrm{e}^{\mathrm{i}\mu(M-x/\sigma)}$$
$$\left\{-\mathrm{i}\left(1-(1+\mathrm{i})\mathrm{E}^*(4\kappa)\right)\mathrm{e}^{2\mathrm{i}(\kappa+\mu x/\sigma)}+\mathrm{i}+\frac{\sqrt{2\kappa}(1-\mathrm{i})}{\sqrt{(\kappa-\mu x/\sigma)}}\mathrm{E}^*\left[2(\kappa-\mu x/\sigma)\right]\right\}\,. \tag{5.67}$$

Aeroacoustic transfer function $\mathcal{L}_3^{(3)}(\mathbf{x}, k_x, k_y)$ The dimensionless pressure $g_3(x,z)_3$ is written as:

$$g_3(x,z)_3 = -\mathcal{F}(\kappa)\frac{\mathrm{e}^{-\mathrm{i}\pi/4}(\kappa-\bar{k}_x^*M^2-\bar{k}_x)}{\sqrt{2\pi(\bar{k}_x+\beta^2\kappa)}\pi(\kappa-\bar{k}_x^*)}$$
$$\int_{-1}^{1}\left(1-(1+\mathrm{i})\mathrm{E}^*(2\kappa(1-\xi))\right)\mathrm{e}^{-\mathrm{i}(\kappa-\bar{k}_x^*M^2)(\xi+1)}\mathrm{e}^{-\mathrm{i}\mu(M-x/\sigma)\xi}\mathrm{d}\xi\,, \tag{5.68}$$

and the aeroacoustics transfer function $\mathcal{L}_3(x, y, z, k_x, k_y)_3$, after integration using change of variables, as:

$$\mathcal{L}_3^{(3)}(\mathbf{x}, k_x, k_y) = -\mathcal{F}(\kappa)\frac{\mathrm{e}^{-\mathrm{i}\pi/4}(\kappa - \bar{k}_x^* M^2 - \bar{k}_x)}{\sqrt{2\pi(\bar{k}_x + \beta^2\kappa)}\pi(\kappa - \bar{k}_x^*)}\frac{\mathrm{e}^{\mathrm{i}\mu(M - x/\sigma)}}{(\kappa - \mu x/\sigma)}$$

$$\left\{\mathrm{i}\mathrm{e}^{-2\mathrm{i}(\kappa-\mu x/\sigma)} - \mathrm{i}\left(1 - (1+\mathrm{i})\mathrm{E}^*\left[4\kappa\right]\right) - \mathrm{i}\sqrt{2\kappa}(1+\mathrm{i})\frac{\mathrm{e}^{-2\mathrm{i}(\kappa-\mu x/\sigma)}}{\sqrt{\kappa + \mu x/\sigma}}\mathrm{E}^*\left(2(\kappa + \mu x/\sigma)\right)\right\}. \tag{5.69}$$

5.4 Fourth iteration

The airfoil surface pressure and corresponding aeroacoustic transfer function have been computed in the previous iteration. Now the Kutta condition and the zero pressure jump downstream of the airfoil trailing-edge boundary conditions must be satisfied. To fulfill this condition a fourth iteration is required.

The residual potential present downstream of the airfoil trailing-edge In the previous step the residual potential $\boldsymbol{\phi}(\bar{x}, 0)^{(3)}$ has been computed for $\bar{x} \leq 2$. Following the same approach, the potential $\boldsymbol{\phi}(\bar{x}, 0)^{(3)}$ is computed for $\bar{x} \geq 2$ as:

$$\boldsymbol{\phi}(\bar{x}, 0)^{(3)} = -\frac{b}{\rho U}\int_2^{\bar{x}} 0\mathrm{e}^{-\mathrm{i}\bar{k}_x(2-\xi)}\mathrm{d}\xi - \frac{b}{\rho U}\int_{-\infty}^{2} \mathbf{P}_2(\xi, 0)\mathrm{e}^{-\mathrm{i}\bar{k}_x(\bar{x}-\xi)}\mathrm{d}\xi \qquad \bar{x} \geq 2\,. \tag{5.70}$$

Noticing that the residual pressure at $\bar{x} \geq 2$ has been set to zero, at the second iteration of the Amiet theory, it is possible to conclude that:

$$\boldsymbol{\phi}(\bar{x}, 0)^{(3)} = \boldsymbol{\phi}(2, 0)^{(3)} \qquad \bar{x} \geq 2\,, \tag{5.71}$$

considering this, the total potential $\boldsymbol{\phi}^{(4)}(\bar{x}, 0)$ is given as the superimposition of the scattered potential $\Psi_3(\bar{x}, 0)$ and $\boldsymbol{\phi}(2, 0)^{(3)}$ as:

$$\boldsymbol{\phi}^{(4)}(\bar{x}, 0) = \boldsymbol{\phi}(2, 0)^{(3)} + \Psi_3(\bar{x}, 0)\mathrm{e}^{\mathrm{i}\bar{k}_x^* M^2 \bar{x}}\,, \tag{5.72}$$

which has Fourier components:

$$\phi^{(4)}(\bar{x}, 0) = \phi(2, 0)^{(3)} + \Psi_3(\bar{x}, 0)\,. \tag{5.73}$$

The total potential $\phi^{(4)}(\bar{x},0)$ implies the existence of a residual pressure $P_3(\bar{x},0)$, defined for $\bar{x}\geq 2$, which is computed as:

$$\mathbf{P}_3(\bar{x},0) = -\frac{\rho U w_0 \mathcal{F}(\kappa)\mathcal{I}(\kappa)(1+\mathrm{i})\mathrm{e}^{-\mathrm{i}\pi/4}\mathrm{e}^{-4\mathrm{i}\kappa}}{4\pi\sqrt{\bar{k}_x+\beta^2\kappa}\sqrt{\kappa}(\kappa+\bar{k}_x^*)}$$

$$\left(\mathrm{i}(\kappa+\bar{k}_x^* M^2+\bar{k}_x)(1-(1+\mathrm{i})\mathrm{E}^*(2\kappa\bar{x}))-\sqrt{\frac{\kappa}{\pi}}(1+\mathrm{i})\frac{\mathrm{e}^{-2\mathrm{i}\kappa\bar{x}}}{\sqrt{\bar{x}}}\right)\mathrm{e}^{\mathrm{i}(\kappa+\bar{k}_x^* M^2)\bar{x}}+$$

$$-\mathrm{i}\frac{\rho U}{b}\bar{k}_x\boldsymbol{\phi}(\mathbf{2},\mathbf{0})^{(\mathbf{3})}\,. \tag{5.74}$$

This residual pressure $P_3(\bar{x},0)$, defined for $\bar{x}\geq 2$, does not satisfy the boundary condition of zero pressure jump downstream of the airfoil trailing-edge. If this boundary condition is imposed, together with the non-penetration upstream of the airfoil leading-edge condition, it is now obtained a new boundary value problem, which can be solved with a fourth Schwarzschild theorem application.

Fourth application of the Schwarzschild theorem The Schwarzschild theorem application has simplified analytical treatment if the pressure variable $P_3(\bar{x},0)$ is considered before the time Fourier transformation, e.g. $P_3(\bar{x},0) = \mathbf{P}_3(\bar{x},0)\mathrm{e}^{\mathrm{i}\omega t}$. Therefore, the Schwarzschild theorem allows to compute the trailing-edge scattered pressure $P_4(\bar{x},0)$ as:

$$P_4(\bar{x},0) = -\frac{1}{\pi}\int_0^\infty G(\bar{x}-2,\xi,0)P_3(2+\xi,0)\mathrm{d}\xi\,,$$

$$= -\frac{1}{\pi}\int_0^\infty \sqrt{\frac{2-\bar{x}}{\xi}}\frac{\mathrm{e}^{-\mathrm{i}\kappa(\xi+2-\bar{x})}}{\xi+2-\bar{x}}P_3(\xi+2,0)\mathrm{d}\xi\,. \tag{5.75}$$

The equations to compute $P_3(x,z)$ are split into three components, to simplify the analytical calculations. The integral in Eq. 5.75 is divided in components with constants defined as:

$$k_1 = -\frac{\rho U w_0 \mathcal{F}(\kappa)\mathcal{I}(\kappa)(1+\mathrm{i})\mathrm{e}^{-\mathrm{i}\pi/4}\mathrm{e}^{-4\mathrm{i}\kappa}}{4\pi\sqrt{\bar{k}_x+\beta^2\kappa}\sqrt{\kappa}(\kappa+\bar{k}_x^*)}\,, \tag{5.76}$$

$$k_2 = \mathrm{i}(\kappa+\bar{k}_x^* M^2+\bar{k}_x)\,, \tag{5.77}$$

$$k_3 = -\sqrt{\frac{\kappa}{\pi}}(1+\mathrm{i})\,. \tag{5.78}$$

Each of the three components will be computed separately, where in a first step the trailing-edge scattered pressure $P_4^{(1,2,3)}(\bar{x},0)$ is determined, followed by the calculation of the dimensionless pressure $g_{1,2,3}(\bar{x},k_x,k_y)$ and, finally, the aeroacoustic transfer function $\mathcal{L}^{(1,2,3)}(\mathbf{x},k_x,k_y)$.

First term calculation The first term of the trailing-edge back scattered pressure $P_4^{(1)}(\bar{x},0)$ is computed as:

$$P_4^{(1)}(\bar{x},0) = -\frac{1}{\pi}k_1k_2\int_0^\infty \sqrt{\frac{2-\bar{x}}{\xi}}\frac{\mathrm{e}^{-\mathrm{i}\kappa(\xi+2-\bar{x})}}{\xi+2-\bar{x}}(1-(1+\mathrm{i})\mathrm{E}^*(2\kappa(\xi+2)))\mathrm{e}^{\mathrm{i}\kappa(\xi+2)}\mathrm{d}\xi\,, \tag{5.79}$$

the integrand has no primitive, consequently, to keep the analytical tractability of this problem, the large argument approximation to the Fresnel integral term is adopted:

$$(1-(1+\mathrm{i})\mathrm{E}^*(2\kappa(2+\xi))) = \mathrm{erfc}\left((1+\mathrm{i})\sqrt{\kappa(2+\xi)}\right) \approx \frac{(1-\mathrm{i})\mathrm{e}^{-2\mathrm{i}\kappa(2+\xi)}}{2\sqrt{\pi}\sqrt{\kappa(2+\xi)}}\,, \tag{5.80}$$

using this approximation, the term $P_4^{(1)}(\bar{x},0)$ can be computed as:

$$P_4^{(1)}(\bar{x},0) \approx -\frac{1}{\pi}k_1k_2\frac{\mathrm{e}^{-4\mathrm{i}\kappa}\mathrm{e}^{\mathrm{i}\kappa\bar{x}}(1-\mathrm{i})}{2\sqrt{\pi\kappa}}\int_0^\infty \sqrt{\frac{2-\bar{x}}{\xi(2+\xi)}}\frac{\mathrm{e}^{-2\mathrm{i}\kappa\xi}}{\xi+2-\bar{x}}\mathrm{d}\xi\,, \tag{5.81}$$

the integrand has still no analytical primitive requiring further high-frequency approximation given by:

$$\int_0^\infty \sqrt{\frac{2-\bar{x}}{\xi(2+\xi)}}\frac{\mathrm{e}^{-2\mathrm{i}\kappa\xi}}{\xi+2-\bar{x}}\mathrm{d}\xi \approx \int_0^\infty \sqrt{\frac{2-\bar{x}}{2\xi}}\frac{\mathrm{e}^{-2\mathrm{i}\kappa\xi}}{\xi+2-\bar{x}}\mathrm{d}\xi\,, \tag{5.82}$$

this approximated integrand has analytical solution given by:

$$\int_0^\infty \sqrt{\frac{2-\bar{x}}{2\xi}}\frac{\mathrm{e}^{-2\mathrm{i}\kappa\xi}}{\xi+2-\bar{x}}\mathrm{d}\xi = \frac{\pi}{\sqrt{2}}\mathrm{e}^{2\mathrm{i}\kappa(2-\bar{x})}\left[1-(1+\mathrm{i})\mathrm{E}^*(2\kappa(2-\bar{x}))\right]\,. \tag{5.83}$$

Replacing the integrand into Eq. 5.79 we obtain:

$$P_4^{(1)}(\bar{x},0) \approx \rho U w_0\frac{\mathcal{F}(\kappa)\mathcal{I}(\kappa)(1+\mathrm{i})\mathrm{e}^{-4\mathrm{i}\kappa}}{8\pi\kappa\sqrt{\pi(\bar{k}_x+\beta^2\kappa)}}\mathrm{e}^{-\mathrm{i}\kappa\bar{x}}\left(1-(1+\mathrm{i})\mathrm{E}^*(2\kappa(2-\bar{x}))\right)\,. \tag{5.84}$$

After the calculation of the trailing-edge back-scattered component $P_4^{(1)}(\bar{x},0)$, the non-dimentionalized pressure $g_4^{(1)}(\bar{x},k_x,k_y)$ is given by:

$$g_4^{(1)}(\bar{x},k_x,k_y)=\frac{\mathcal{F}(\kappa)\mathcal{I}(\kappa)(1+\mathrm{i})\mathrm{e}^{-4\mathrm{i}\kappa}}{8\pi^2\kappa\sqrt{\pi(\bar{k}_x+\beta^2\kappa)}}\mathrm{e}^{-\mathrm{i}(\kappa-\bar{k}_x^*M^2)(\bar{x}+1)}\left(1-(1+\mathrm{i})\mathrm{E}^*(2\kappa(1-\bar{x}))\right), \tag{5.85}$$

and the aeroacoustics transfer function $\mathcal{L}_4^{(1)}(\mathbf{x},k_x,k_y)$ is computed using the relation:

$$\int_{-1}^{1}\mathrm{e}^{-\mathrm{i}(\kappa-\bar{k}_x^*M^2)(\xi+1)}\left[1-(1+\mathrm{i})\mathrm{E}^*(2\kappa(1-\xi))\right]\mathrm{e}^{-\mathrm{i}\mu(M-x/\sigma)\xi}\mathrm{d}\xi=\mathrm{i}\frac{\mathrm{e}^{\mathrm{i}\mu(M-x/\sigma)}}{(\kappa-\mu x/\sigma)}$$

$$\left\{\mathrm{e}^{-2\mathrm{i}(\kappa-\mu x/\sigma)}\left[1-\sqrt{\frac{2\kappa}{\kappa+\mu x/\sigma}}(1+\mathrm{i})\mathrm{E}^*\left(2(\kappa+\mu x/\sigma)\right)\right]-\left[1-(1+\mathrm{i})\mathrm{E}^*(4\kappa)\right]\right\}, \tag{5.86}$$

resulting to:

$$\mathcal{L}_4^{(1)}(\mathbf{x},k_x,k_y)=-\frac{\mathcal{F}(\kappa)\mathcal{I}(\kappa)(1-\mathrm{i})\mathrm{e}^{-4\mathrm{i}\kappa}}{8\pi^2\kappa\sqrt{\pi(\bar{k}_x+\beta^2\kappa)}}\frac{\mathrm{e}^{\mathrm{i}\mu(M-x/\sigma)}}{(\kappa-\mu x/\sigma)}$$

$$\left\{\mathrm{e}^{-2\mathrm{i}(\kappa-\mu x/\sigma)}\left[1-\sqrt{\frac{2\kappa}{\kappa+\mu x/\sigma}}(1+\mathrm{i})\mathrm{E}^*\left(2(\kappa+\mu x/\sigma)\right)\right]-\left[1-(1+\mathrm{i})\mathrm{E}^*(4\kappa)\right]\right\}. \tag{5.87}$$

Second term calculation Similarly to the derivations previously done, the second term of the trailing-edge scattered pressure $P_4^{(2)}(\bar{x},0)$ is given by:

$$P_4^{(2)}(\bar{x},0)=-\frac{1}{\pi}k_1k_3\int_0^\infty\sqrt{\frac{2-\bar{x}}{\xi}}\frac{\mathrm{e}^{-\mathrm{i}\kappa(\xi+2-\bar{x})}}{\xi+2-\bar{x}}\frac{\mathrm{e}^{-\mathrm{i}\kappa(\xi+2)}}{\sqrt{\xi+2}}\mathrm{d}\xi \tag{5.88}$$

which can be solved by using the approximation of Eq. 5.82, which has solution given by Eq. 5.83, resulting to:

$$P_4^{(2)}(\bar{x},0)\approx-k_1\,k_3\frac{\mathrm{e}^{-\mathrm{i}\kappa\bar{x}}}{\sqrt{2}}\left[1-(1+\mathrm{i})\mathrm{E}^*(2\kappa(2-\bar{x}))\right], \tag{5.89}$$

which, after simplifications, can be written as:

$$P_4^{(2)}(\bar{x},0)\approx-\rho U w_0\frac{\mathcal{F}(\kappa)\mathcal{I}(\kappa)(1+\mathrm{i})\mathrm{e}^{-4\mathrm{i}\kappa}\mathrm{e}^{-\mathrm{i}\kappa\bar{x}}}{4\pi\sqrt{\pi(\bar{k}_x+\beta^2\kappa)}(\kappa+\bar{k}_x^*)}\left[1-(1+\mathrm{i})\mathrm{E}^*(2\kappa(2-\bar{x}))\right]. \tag{5.90}$$

The non-dimentionalized pressure $g_4^{(2)}(\bar{x}, k_x, k_y)$ is given by:

$$g_4^{(2)}(\bar{x}, k_x, k_y) = -\frac{\mathcal{F}(\kappa)\mathcal{I}(\kappa)(1+\mathrm{i})\mathrm{e}^{-4\mathrm{i}\kappa}\mathrm{e}^{-\mathrm{i}(\kappa-\bar{k}_x^* M^2)(\bar{x}+1)}}{4\pi^2\sqrt{\pi(\bar{k}_x+\beta^2\kappa)}(\kappa+\bar{k}_x^*)}\left[1-(1+\mathrm{i})\mathrm{E}^*(2\kappa(1-\bar{x}))\right], \tag{5.91}$$

and the aeroacoustics transfer function $\mathcal{L}(\mathbf{x}, k_x, k_y)_2$ is computed using the relation of Eq. 5.86:

$$\mathcal{L}_4^{(2)}(\mathbf{x}, k_x, k_y) = \frac{\mathcal{F}(\kappa)\mathcal{I}(\kappa)(1-\mathrm{i})\mathrm{e}^{-4\mathrm{i}\kappa}}{4\pi^2\sqrt{\pi(\bar{k}_x+\beta^2\kappa)}(\kappa+\bar{k}_x^*)}\frac{\mathrm{e}^{\mathrm{i}\mu(M-x/\sigma)}}{(\kappa-\mu x/\sigma)}$$

$$\left\{\mathrm{e}^{-2\mathrm{i}(\kappa-\mu x/\sigma)}\left[1-\sqrt{\frac{2\kappa}{\kappa+\mu x/\sigma}}(1+\mathrm{i})\mathrm{E}^*\left(2(\kappa+\mu x/\sigma)\right)\right]-\left[1-(1+\mathrm{i})\mathrm{E}^*(4\kappa)\right]\right\}. \tag{5.92}$$

Third term calculation Finally, the third term is computed as:

$$P_4^{(3)}(\bar{x}, 0) = \mathrm{i}\frac{1}{\pi}\frac{\rho U}{b}\bar{k}_x\phi(2,0)^{(3)}\int_0^\infty\sqrt{\frac{2-\bar{x}}{\xi}}\frac{\mathrm{e}^{-\mathrm{i}\kappa(\xi+2-\bar{x})}}{\xi+2-\bar{x}}\mathrm{d}\xi, \tag{5.93}$$

which the integral term is solved using the relation:

$$\int_0^\infty\sqrt{\frac{X}{\xi}}\frac{\mathrm{e}^{-\mathrm{i}A\xi}}{\xi+X}\mathrm{d}\xi = \pi\mathrm{e}^{\mathrm{i}AX}\left[1-(1+\mathrm{i})\mathrm{E}^*(AX)\right], \tag{5.94}$$

resulting to:

$$P_4^{(3)}(\bar{x}, 0) = \mathrm{i}\frac{\rho U}{b}\bar{k}_x\phi(2,0)^{(3)}\left[1-(1+\mathrm{i})\mathrm{E}^*\left(\kappa(2-\bar{x})\right)\right], \tag{5.95}$$

which is simplified to:

$$P_4^{(3)}(\bar{x}, 0) = -\frac{\rho\, U\, w_0\mathcal{F}(\kappa)\bar{k}_x\mathrm{e}^{-\mathrm{i}\pi/4}\mathrm{e}^{-2\mathrm{i}\kappa}}{\sqrt{2\pi(\bar{k}_x+\beta^2\kappa)}(K-\bar{k}_x^*)}\left(1-\sqrt{\frac{2\kappa}{\kappa+\bar{k}_x^*}}\right)\left(1-(1+\mathrm{i})\mathrm{E}^*(\kappa(2-\bar{x}))\right). \tag{5.96}$$

Noteworthy that the term $P_4^{(3)}(\bar{x}, 0)$ is computed with no approximations. The dimensionless pressure $g_4^{(3)}(\bar{x}, k_x, k_y)$ is given by:

$$g_4^{(3)}(\bar{x}, k_x, k_y) = -\frac{\mathcal{F}(\kappa)\bar{k}_x\mathrm{e}^{-\mathrm{i}\pi/4}\mathrm{e}^{-2\mathrm{i}\kappa}}{\pi\sqrt{2\pi(\bar{k}_x+\beta^2\kappa)}(\kappa-\bar{k}_x^*)}\left(1-\sqrt{\frac{2\kappa}{\kappa+\bar{k}_x^*}}\right)$$

$$\left(1-(1+\mathrm{i})\mathrm{E}^*(\kappa(1-\bar{x}))\right)\mathrm{e}^{\mathrm{i}\bar{k}_x^* M^2(\bar{x}+1)}, \tag{5.97}$$

and the aeroacoustics transfer function $\mathcal{L}_4^{(3)}(\mathbf{x}, k_x, k_y)$ is calculated as:

$$\mathcal{L}_4^{(3)}(\mathbf{x}, k_x, k_y) = \frac{\mathcal{F}(\kappa)\bar{k}_x \mathrm{e}^{-\mathrm{i}\pi/4}\mathrm{e}^{-2\mathrm{i}\kappa}}{\pi\sqrt{2\pi(\bar{k}_x + \beta^2\kappa)}(\kappa - \bar{k}_x^*)}\left(1 - \sqrt{\frac{2\kappa}{\kappa + \bar{k}_x^*}}\right)\frac{\mathrm{e}^{\mathrm{i}\bar{k}_x^* M^2}\mathrm{e}^{\mathrm{i}\mu x/\sigma}}{\mu x/\sigma}$$

$$\left\{\mathrm{i}\left[1 - (1 - (1+\mathrm{i})\mathrm{E}^*(2\kappa))\mathrm{e}^{-2\mathrm{i}\mu x/\sigma}\right] + (1-\mathrm{i})\sqrt{\frac{\kappa}{\kappa + \mu x/\sigma}}\mathrm{E}^*\left(2(\kappa + \mu x/\sigma)\right)\right\}. \tag{5.98}$$

Since the aeroacoustic transfer function $\mathcal{L}_4^{(1)}(\mathbf{x}, k_x, k_y)$ and $\mathcal{L}_4^{(2)}(\mathbf{x}, k_x, k_y)$ are approximated, numerical evaluations of these functions are conducted to define correction functions. These corrections are defined adopting a similar approach used in the previous sections, where the analytical approximation is compared to numerical results, computed with high enough accuracy to provide reliable corrections to the function. The obtained correction functions are:

$$\mathcal{P}(\kappa) = \left[1 + \frac{7}{40\kappa^{5/4}}\right]^{-1/3}, \tag{5.99}$$

$$\mathcal{Q}(\kappa) = 0.724 + \frac{3}{11}\left(1 + \frac{1}{5\kappa^{7/5}}\right)^{-3/11}, \tag{5.100}$$

and a comparison between the correction function and numerical results are shown in Fig. 5.9:

From where it is verified that the aeroacoustics transfer function $\mathcal{L}_4^{(1)}(\mathbf{x}, k_x, k_y)$ tends to zero for very small values of κ, while the aeroacoustics transfer function $\mathcal{L}_4^{(2)}(\mathbf{x}, k_x, k_y)$ becomes a constant. Noteworthy that no approximation has been done on the calculation of $\mathcal{L}_4^{(3)}(\mathbf{x}, k_x, k_y)$, consequently, no correction is prescribed.

Finally, the total aeroacoustic transfer function $\mathcal{L}_4(\mathbf{x}, k_x, k_y)$ is defined as:

$$\mathcal{L}_4(\mathbf{x}, k_x, k_y) = \mathcal{P}(\kappa)\mathcal{L}_4^{(1)}(\mathbf{x}, k_x, k_y) + \mathcal{Q}(\kappa)\mathcal{L}_4^{(2)}(\mathbf{x}, k_x, k_y) + \mathcal{L}_4^{(3)}(\mathbf{x}, k_x, k_y). \tag{5.101}$$

5.5 Results

Aeroacoustics transfer function comparison To evaluate the methodology developed in this chapter, the aeroacoustics transfer function $\mathcal{L}(\mathbf{x}, k_x, k_y)$ is

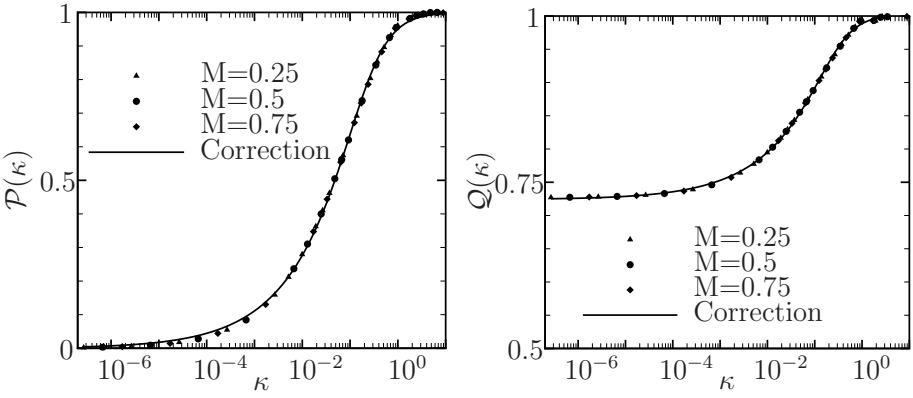

(a) $\mathcal{P}(\kappa)$ (b) $\mathcal{Q}(\kappa)$

Figure 5.9: Correction function to the aeroacoustic transfer function $\mathcal{L}_4^{(1)}(\mathbf{x}, k_x, k_y)$ and $\mathcal{L}_4^{(2)}(\mathbf{x}, k_x, k_y)$.

compared for different frequencies. In this analysis, the aeroacoustic transfer function is computed using the geometrical and flow parameters representative of the experiment subject of this thesis. The airfoil chord is considered 2b=0.1 m, the flow velocity is set to 30 m/s, the observer is localized at 1 m, measured from the airfoil leading-edge, and the frequency range selected for this study is representative of those of interest to this problem. Figs. 5.10, 5.11 and 5.12 show the comparison.

Figure 5.10 shows that, for low-frequencies ($kc = 0.1$ and $kc = 0.5$), more iterations leads to an amplitude reduction of the aeroacoustic transfer function. For $kc = 0.5$ it is verified that 4 iterations lead to converged noise polar, while, for $kc = 0.1$ it is seen that it is still necessary more iterations to obtain converged results.

In turn, for intermediate-frequencies ($kc = 1$ and $kc = 5$) more iterations yields larger noise radiation. In this frequency regime, the airfoil passes from a compact to a non-compact noise source, constructive and destructive acoustic interferences causes sidelobes in the noise radiation polar. From these plots, it is verified that, more iterations results into a larger noise radiation prediction in the downstream direction.

For the high-frequency regime ($kc = 10$ and $kc = 20$), the increasing of the number of iterations yields to, overall, small variations in the predicted aeroacoustic transfer functions. The major influence are noticed at observer angles of maximum destructive interference, where more iterations conducts to

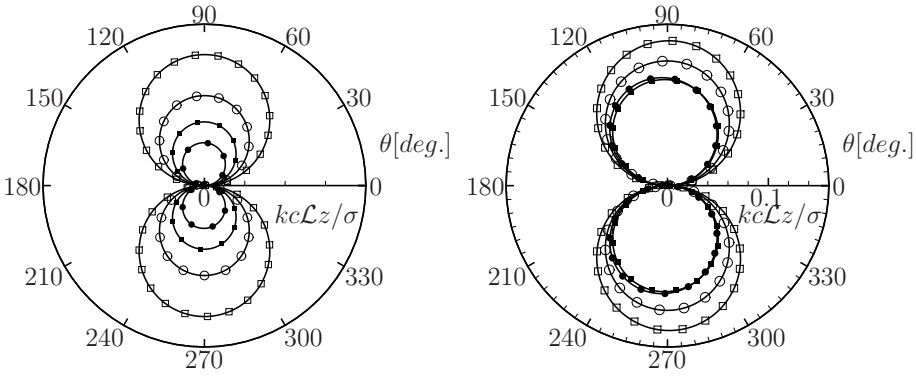

(a) kc = 0.1; f = 54.11 Hz; $\kappa = 0.05$ (b) kc = 0.5; f = 270.56 Hz; $\kappa = 0.25$

Figure 5.10: Aeroacoustic transfer function computed for kc equal to 0.1 and 0.5. Open square: 1^{st} iteration; Open circle: 2^{nd} iteration; Closed square: 3^{rd} iteration; Closed circle: 4^{th} iteration.

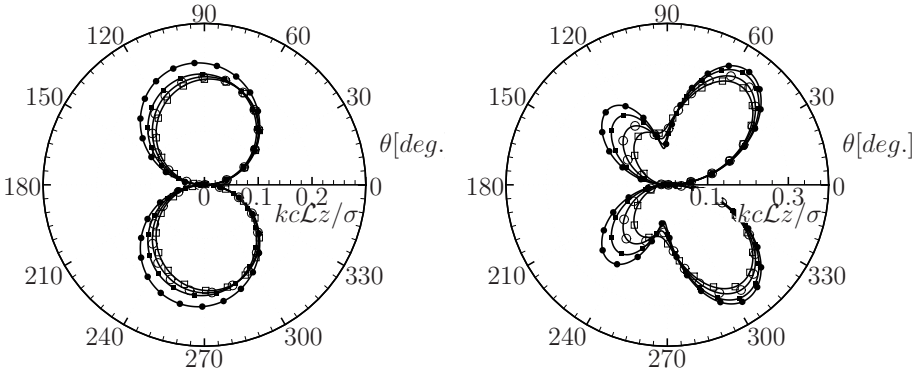

(a) kc = 1; f = 541.13 Hz; $\kappa = 0.50$ (b) kc = 5; f = 2.70 kHz; $\kappa = 2.52$

Figure 5.11: Aeroacoustic transfer function computed for kc equal to 1 and 5. Open square: 1^{st} iteration; Open circle: 2^{nd} iteration; Closed square: 3^{rd} iteration; Closed circle: 4^{th} iteration.

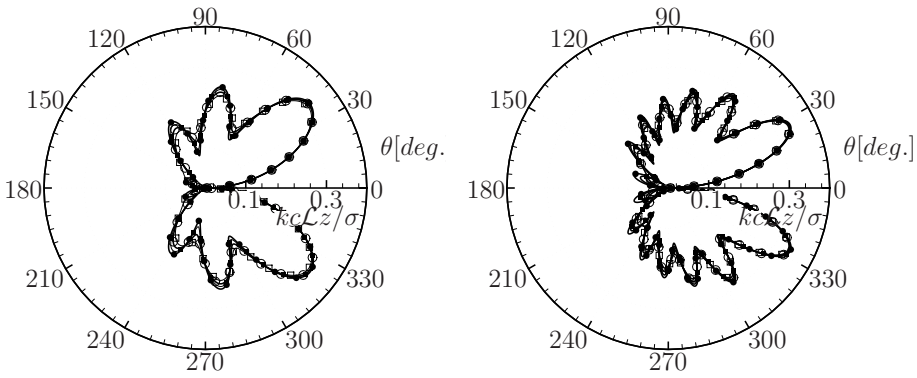

(a) kc = 10; f = 5.40 kHz; $\kappa = 5.04$ (b) kc = 20; f = 10.82 kHz; $\kappa = 10.08$

Figure 5.12: Aeroacoustic transfer function computed for kc equal to 10 and 20. Open square: 1^{st} iteration; Open circle: 2^{nd} iteration; Closed square: 3^{rd} iteration; Closed circle: 4^{th} iteration.

a reduction of the total predicted aeroacoustics transfer function.

Comparison with experiments The methodology developed in this chapter is validate against the experimental database produced in this thesis. The approach is applied to the rod- and grid-airfoil configurations in the cases with reference flow velocity equal to 30 m/s. The calculation is performed using the inverse strip theory and results are presented in Figs. 5.13 and 5.14, respectively, to the grid- and rod-airfoil configurations. In these figures, the first and second iterations reproduces results given by the Amiet theory, while the third and fourth iterations are proposed in this work.

From Figs. 5.13 and 5.14 it is observed that the addition of further iterations contributes to the predictions convergence. The spectrum lobes, present due leading- and trailing-edge scattered waves interference, shows more pronounced amplitude after each iteration. For kc approximately larger than 2, it is noticed that the acoustic calculations slightly depend on the number of iterations. This value, is close to the range of validity proposed by Adamczyk [2] to the Amiet theory - that the calculations can be done for $\mu > \pi/4$, which, in this application, is verified for $kc > 1.43$. In addition, for kc close to 1, the amplitude of the predicted spectrum increases with successive iterations, while an opposite behavior is observed for smaller frequencies.

Now comparing the predictions with the experiments it is observed that for intermediate frequencies, e.g. kc close to 1, the comparison between

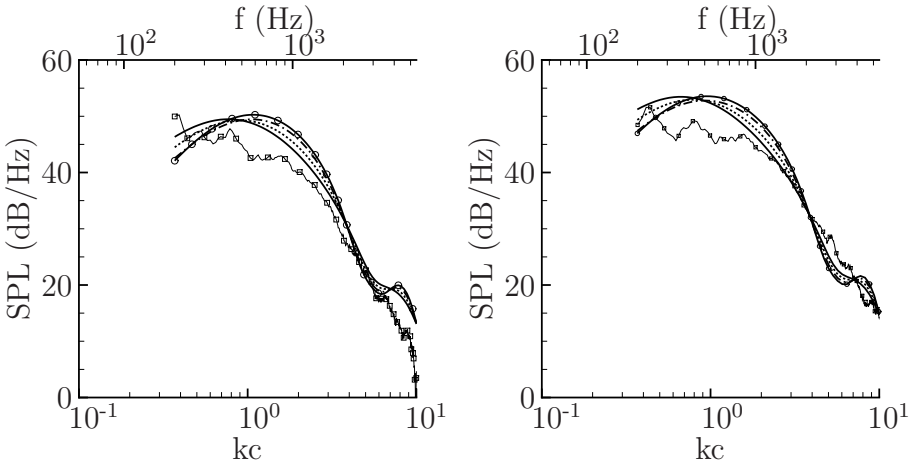

(a) Grid # 1 (b) Grid # 2

Figure 5.13: Comparison of the acoustic spectra computed with the iterative technique proposed in this chapter and the experimental noise spectra measured from the grid-airfoil configuration. Measurements performed with the observer localized 1 m distance from the airfoil leading-edge in an angle of 90°. Solid line: 1^{st} iteration; Dotted line: 2^{nd} iteration; Dash-dot line: 3^{rd} iteration; Continus line with square symbols: 4^{th} iteration.

predictions and empirical results are worst after successive iterations, while for lower frequencies the predictions shows a better tendency of agreement with measurements. An special case, which demonstrates that this approach improves the quality of the noise predictions is the case of the rod with 0.008 m diameter. In this measurement, for kc below the cylinder vortex shedding frequency, it is observed that the acoustic spectra decays similarly to the behavior expected by the predictions. In this frequency range it is clearly observable that the successive number of iterations contributes to a better similarity between the predicted and the experimental spectra.

Noteworthy that the reduced signal-to-noise ratio observed for the grid # 1 for $8 < kc < 10$ suggests that the noise spectrum amplitude in this frequency range is slightly smaller. These considerations do not jeopardize the conclusions since the objective of this chapter is the compact airfoil regime.

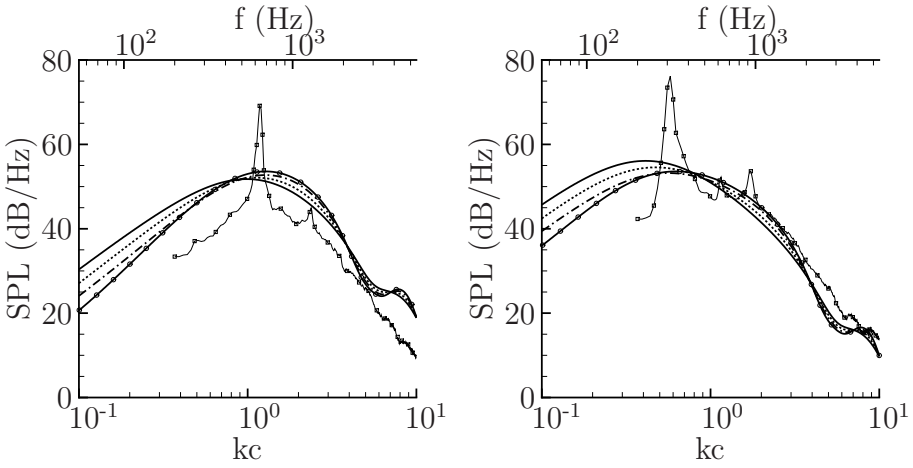

(a) Rod 0.008 m (b) Rod 0.016 m

Figure 5.14: Comparison of the acoustic spectra computed with the iterative technique proposed in this chapter and the experimental noise spectra measured from the rod-airfoil configuration. Measurements performed with the observer localized 1 m distance from the airfoil leading-edge in an angle of 90°. Solid line: 1^{st} iteration; Dotted line: 2^{nd} iteration; Dash-dot line: 3^{rd} iteration; Continuous line with square symbols: 4^{th} iteration.

5.6 Conclusions

This chapter presents an extension to the leading-edge Amiet theory to the compact airfoil regime. Analysis that motivate this work shows that the Amiet theory presents poor convergence in the low-frequency regime. Therefore we propose a continuation to the Amiet developments by applying two extra iterative applications of the Schwarzschild theorem. This approach yields to improved convergence for kc larger than 0.5 and suggests that even more iterations are necessary to converge the theory at lower frequencies. Acoustic predictions shows that successive iterations reduces the noise over-prediction amplitude, generally present in the compact airfoil regime noise calculations. It is observed that a third and a fourth interactions contributes significantly to the acoustic prediction amplitude for kc smaller than 2. Furthermore a more converged spectra has more pronounced spectra lobes present due constructive and destructive interferences.

Chapter 6

High-frequency regime realistic airfoil noise prediction

In the previous chapter, the Amiet theory has been extended to the compact airfoil regime. The airfoil has been assumed a finite span flat plate and no geometrical effect, e.g. thickness and camber, have been considered. To overcome this limitation, this chapter proposes an innovative numerical technique to compute the aeroacoustic response function of an airfoil subjected to incoming turbulence in the high-frequency regime, i.e. non-compact airfoil. The methodology adopts a commercial acoustic Boundary Element Method (BEM) solver to compute the linearized airfoil problem. This approach is valid for infinite-span airfoils subject to high-frequency subsonic wind-gusts where the trailing-edge back-scattering effects can be accounted. The flow is modeled by a linearized velocity potential field with terms regrouped to retrieve a Helmholtz equation, which is formally similar to the equation treated in acoustic wave propagation problem. An analogy between acoustic and flow variables is proposed which allows the application of a commercial acoustic solver to tackle this problem. This method shows advantages over the Amiet's formulation by not requiring an analytical Green's function, permitting to account for more realistic airfoil geometries. The proposed technique is compared with the infinitely thin airfoil solution proposed by the Amiet theory showing good agreement for both direct propagation and back-scattering correction. More realistic airfoil geometric features, e.g. thickness and camber are verified. Finally, the grid- and rod-airfoil noise case are evaluated showing

that the acoustic over-prediction, present in the non-compact regime, can be reduced by considering more realistic airfoil geometric features.

6.1 The BEM approach for solving linearized compressible flow equations

Solving the linearized flow equations using an acoustic solver Since the methodology presented in this chapter is designed to be computed by an acoustic commercial solver, it is necessary to translate acoustic into flow variables. A numerical acoustic solver calculates the Helmholtz equation for the acoustic pressure variable:

$$\nabla^2 p\,(x,y,z) + k^2 p\,(x,y,z) = 0 \tag{6.1}$$

subjected to the possible boundary conditions set:

- imposed pressure: $\bar{p} = p$;
- imposed normal velocity: $\bar{v}_n = \frac{\mathrm{i}}{\rho\,\omega}\frac{\partial p}{\partial n}$;
- imposed normal impedance: $p = \frac{\mathrm{i}\,\bar{Z}}{\rho\,\omega}\frac{\partial p}{\partial n}$.

Where the over-bar $(\bar{\cdot})$ represents the imposed variable. Comparing the Helmholtz equation solved by the linearized airfoil problem (reproduced here from Eq. 2.37 for completeness):

$$\frac{\partial^2 \varphi}{\partial \bar{x}^2} + \frac{\partial^2 \varphi}{\partial \bar{z}^2} + \kappa^2 \varphi = 0 \tag{6.2}$$

with Eq. 6.1 it is possible to find that both equations are formally the same if the following set of equalities are considered:

- $\varphi = p$;
- $\kappa^2 = k^2$;

This methodology proposes a three steps procedure to compute the generic geometry airfoil response to a periodic gust. From the first step, remembering Chapter 2 developments, Eq. 2.37 shows that the first step of the Amiet theory solves the Helmholtz equation:

$$\frac{\partial^2 \varphi^{(0)}}{\partial x^2} + \frac{\partial^2 \varphi^{(0)}}{\partial z^2} + \kappa^2 \varphi^{(0)} = 0, \tag{6.3}$$

subject to an incoming gust with profile:

$$w(x,\omega) = w_0(\omega)\, e^{-\mathrm{i}k_x x}\,. \tag{6.4}$$

This equation and boundary condition is equivalent to an acoustic BEM problem, if the following variable substitutions are made:

$$\varphi^{(0)} = p\,, \tag{6.5}$$

$$\kappa^2 = k^2\,, \tag{6.6}$$

$$w(x,\omega) = \frac{\mathrm{i}}{\rho\,\omega}\frac{\partial p}{\partial n}\,, \tag{6.7}$$

where the left hand side of Eqs. 6.5, 6.6 and 6.7 refer to the variables associated with to the aerodynamic problem, while the right hand side are the BEM solver variables.

In the second step, the correction potential $\varphi^{(1)}$ is found by imposing the zero velocity potential for $\bar{x} < 0$. Therefore, the potential ψ_1, which satisfies the relation $\varphi^{(1)} = \varphi^{(0)} + \psi_1$, should be computed. This step leads to a second Helmholtz equation to be solved:

$$\frac{\partial^2\psi_1}{\partial\bar{x}^2} + \frac{\partial^2\psi_1}{\partial\bar{z}^2} + \kappa^2\psi_1 = 0, \tag{6.8}$$

subjected to the boundary conditions:

$$\psi_1(\bar{x},0) = -\varphi^{(0)}(\bar{x},0) \qquad \bar{x} \le 0, \tag{6.9}$$

$$\frac{\partial\psi_1}{\partial\bar{z}} = 0 \qquad x > 0. \tag{6.10}$$

This problem is equivalent to an acoustic BEM problem if the variable substitutions is made:

$$\kappa^2 = k^2, \tag{6.11}$$

$$\psi_1 = p, \tag{6.12}$$

$$\varphi^{(0)} = \bar{p}, \tag{6.13}$$

where the left hand side of Eqs. 6.11, 6.12 and 6.13 refers to the variables associated with the aerodynamic problem, while the right hand side refers to the BEM solver variables.

In the third step the trailing-edge correction is performed. Therefore the boundary value problem is solved:

$$\frac{\partial^2 P_2}{\partial \bar{x}^2} + \frac{\partial^2 P_2}{\partial \bar{z}^2} + \kappa^2 P_2 = 0, \tag{6.14}$$

with the following boundary conditions:

$$P_2(\bar{x}, 0) = -P_1(\bar{x}, 0) \qquad \bar{x} \geq 2, \tag{6.15}$$

$$\frac{\partial P_2}{\partial \bar{z}}(\bar{x}, 0) = 0 \qquad \bar{x} < 2. \tag{6.16}$$

It is equivalent to an acoustic BEM problem if the following set of variable substitutions is made:

$$\kappa^2 = k^2 \tag{6.17}$$

$$P_2 = p \tag{6.18}$$

$$P_1 = \bar{p} \tag{6.19}$$

where the left hand side of Eqs. 6.17, 6.18 and 6.19 refers to the variables associated with the aerodynamic problem, while, the right hand-side refers to the BEM solver variables.

6.2 Methodology verification and mesh convergence analysis

The numerical methodology presented in this chapter is verified against analytical results computed by the Amiet theory for an infinitely thin airfoil. The commercial software LMS Virtual.Lab version 11-SL1 and, later, the release 13 is used for the indirect BEM computations. Since this chapter proposes a numerical approach, it is not obvious that this technique will lead to calculations with reduced turn-around time. To answer this question, this section shows the physical computational time dependency function of the mesh dimensions and evaluates this impact to the noise prediction error.

BEM model schematic representation The boundary value problem, described in the previous section, is numerically solved using a computational model sketched in Fig. 6.1

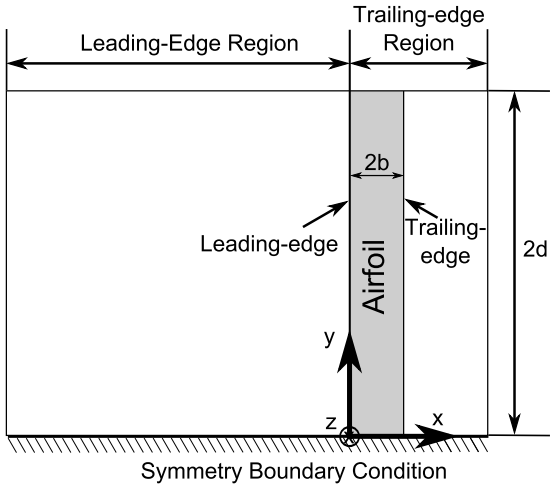

Figure 6.1: Computational model schematic representation.

The computational model sketched in Fig. 6.1 has been adopted in this approach. The mesh domain is divided into leading-edge (LE) and trailing-edge (TE) regions. The airfoil is placed in the trailing-edge region between $0 \leq x/b \leq 2$. For the first iteration, the incoming velocity is imposed on the complete domain and the resulting flow potential is obtained. For the second iteration, the flow potential is imposed on the LE region of the domain.

Using a three-dimensional solver, a symmetry boundary condition is adopted to reduce the computational cost. This condition is imposed perpendicularly to the plane, on the line indicated in Fig. 6.1, with a drawback of allowing only to assess problems with non-skewed gusts ($k_y = 0$).

Other mesh geometric parameters to be analyzed by convergence studies are the minimum required length for the LE and TE mesh regions domain and the minimum span.

CPU requirements During this work development, it has been verified that, depending on the required accuracy, the computational mesh could range from few to up to 80,000 quadrilateral elements. Consequently, the required computational time could range from minutes to hours per frequency. Therefore, matrix level parallelization is employed to minimize the calculation time.

To assess the optimal parallelization parameters and optimize the computational cost, a study about the necessary physical time to solve each of the three steps of the iterative procedure is developed. For this evaluation a computer equipped with a 32 cores 2 GHz Intel XEON E5 64 bit processor and 128 Gb of RAM memory was used. The Virtual Lab software allows matrix level parallelization which is achieved by dividing the computation in processes and, for each process, a given number of threads – a sequence of programmed instructions that can be managed independently – is defined. The computation physical time is dependent of these two parameters. Figures 6.2 and 6.3 show the physical time required to compute meshes with 10,000, 20,000, 40,000 and 60,000 quadrilateral elements.

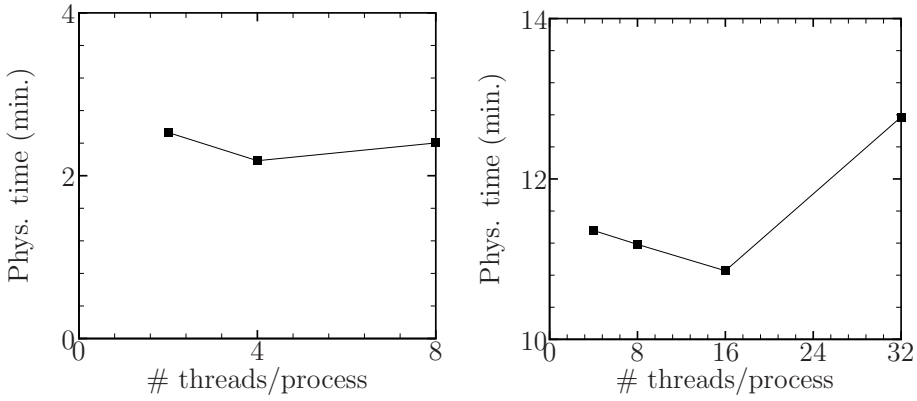

(a) n=10,000 quadrilaterals (b) n=20,000 quadrilaterals

Figure 6.2: Computation physical time for 10,000 and 20,000 quadrilateral mesh elements. Computation done with 2 processes.

Figure 6.2 shows that computational problems with approximately 10,000 elements can be solved in less than two minutes per frequency. However, when this mesh grows to 20,000 elements, the computational cost raises to approximately 10 minutes per frequency.

The required time to compute a mesh with a larger number of elements can reach more than one hour per frequency (Fig. 6.3). This demonstrates the importance of controlling the mesh size. Noteworthy the computational cost is reduced if the number of processes is a power of two.

Based on this analysis, we can relate the computational time to the number of mesh elements. These results are presented in Fig. 6.4 showing that, with

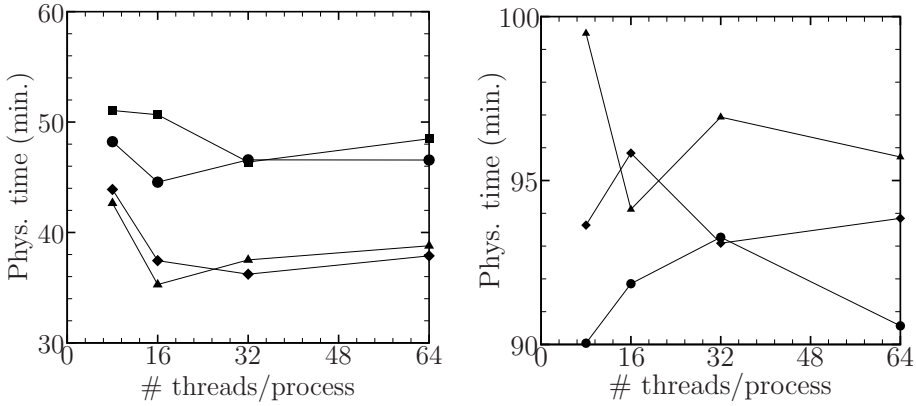

(a) n=40,000 quadrilaterals (b) n=60,000 quadrilaterals

Figure 6.3: Computation physical time for 40,000 and 60,000 quadrilateral mesh elements. In this case the physical time is dependent of the number of processes. Square: 2 processes; triangle: 4 processes; circle: 6 process; diamond: 8 processes

optimal parallelization, the computational time is a quadratic function of the number of elements.

Mesh convergence analysis Studies about the mesh convergence have been performed for Helmholtz numbers $kc = 1$, $kc = 5$, $kc = 10$ and $kc = 20$, this section presents only results for $kc = 10$. In this analysis, for each evaluation, a baseline mesh is chosen and a single parameter is modified.

For $kc = 10$, the baseline case has a mesh span $7.5b$, leading-edge (LE) region $7.5b$, trailing-edge (TE) region $3b$. The maximum quadrilateral element aspect ratio, defined as the ratio between the element span and length is equal to 5 and the minimum element length equal to $0.01b$.

Due to the integrable singularity of the solution, present at the airfoil leading- and trailing-edge, respectively, the second and third iterations requires mesh refinement in that region. During these mesh convergence analysis, it was verified that enough mesh refinement was essential for obtaining meaningful results.

Figure 6.5 shows the noise polar and the difference between the noise predicted using the numerical and analytical methodologies. In this analysis, the grid-airfoil noise prediction is performed on an infinitely thin airfoil with reference

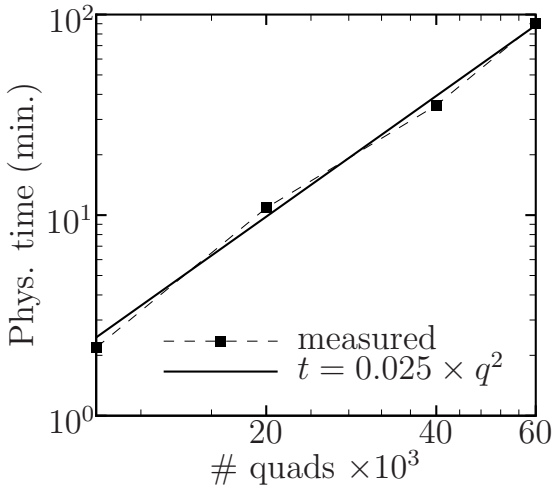

Figure 6.4: Relation between number of mesh elements and required physical time computed with optimal parallelization parameters. Where t is the required computational time, in minutes, and q is the number of quadrilateral elements dived by one thousand.

results calculated by the Amiet theory. The airfoil dimension and flow velocity are representative of this thesis experimental set-up, where the airfoil span is 0.2 m and chord 0.1 m, the observer is localized at 1 m distance from the airfoil leading-edge at different observer angles θ. The turbulence root-mean-square fluctuation (u') is equal to 2 m/s, turbulence integral correlation length scale is 0.2 m, the von Kármán isotropic turbulence spectra is used and the incoming mean velocity is 30 m/s.

Figure 6.5 verifies that a finer mesh, at the transition between LE and TE regions, yields a better agreement between numerical and analytical noise predictions. For the case with poorest resolution ($min(dx) = 0.04b$), the difference reaches approximately 0.8 dB at some observer angles. In this analysis, the mesh with the maximum resolution ($min(dx) = 0.005b$) has 73,800 quadrilateral elements while the least resolved has 8,200. Using the developed formula, we have 136 and 1.6 minutes per frequency, respectively.

A second mesh parameter with an important impact to the noise prediction is the mesh element with maximum aspect ratio (AR). The aspect ratio is the ratio between the length and span of a mesh quadrilateral element. To accurately describe the singularity present at the mesh LE to TE transition, it is convenient to refine the mesh as much as possible, in this region. However,

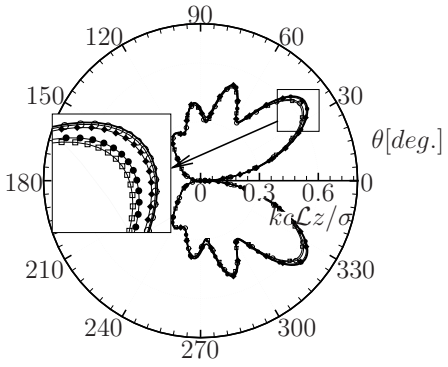

(a) Noise polar

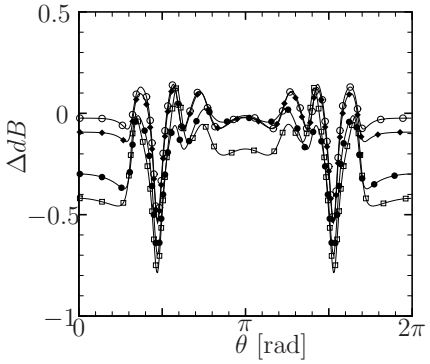

(b) Difference from the baseline

Figure 6.5: Minimum mesh resolution effect at the transition between TE and LE region. Continuous line: flat plate Amiet reference solution; Open circle: $min(dx) = 0.005b$; filled diamond: $min(dx) = 0.01b$; filled circle: $min(dx) = 0.025b$; Open square: $min(dx) = 0.04b$.

excessive refinement leads to quadrilateral elements with high aspect ratio and consequently numerical problems arise. Figure 6.6 shows the effect of the maximum element aspect ratio on the noise prediction:

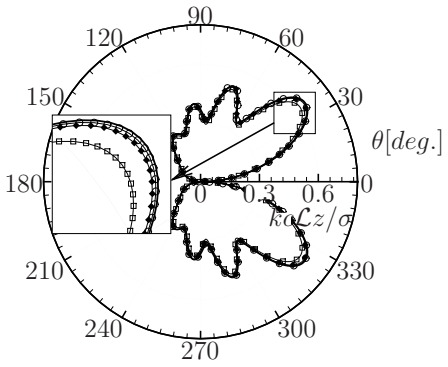

(a) Noise polar

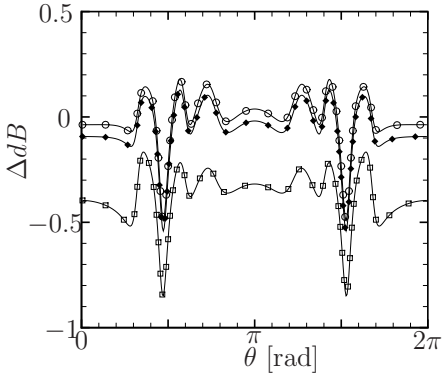

(b) Difference from the baseline

Figure 6.6: Effect of the mesh element with maximum aspect ratio on the noise prediction. Continuous line: flat plate Amiet reference solution; Open circle: $max(AR) = 2.5$; filled diamond: $max(AR) = 5$; Open square: $max(AR) = 10$.

This figure shows that, for a mesh with elements with maximum aspect ratio up to 10, the highest error is approximately 0.9 dB. The computational mesh with aspect ratio equal to 2.5 has 74,800 quadrilateral elements while the mesh with aspect ratio 10 has 18,400 elements, with respective computation physical time equal to 140 and 8.5 minutes.

A next mesh convergence analysis studies the effect of the mesh span (2d) to the predicted noise with results present in Fig. 6.7.

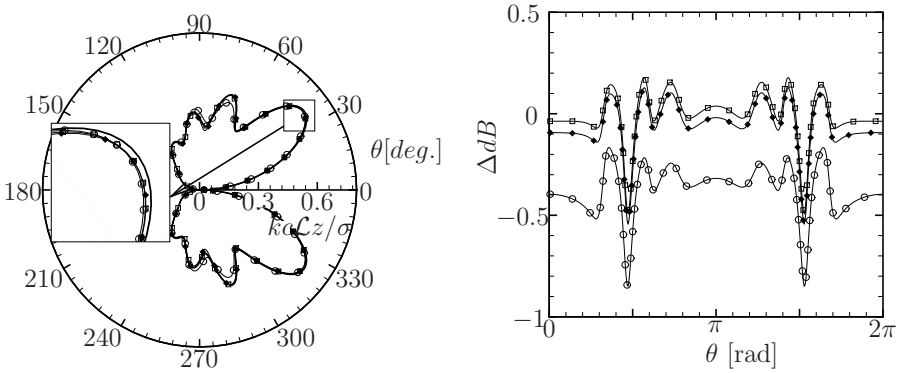

(a) Noise polar

(b) Difference from the baseline

Figure 6.7: Mesh span effect on predicted noise. Continuous line: flat plate Amiet reference solution; Open circle: $2d = 4b$; filled diamond: $2d = 7.5b$; Open square: $2d = 11b$.

Figure 6.7 shows that a mesh span equal to $4b$ leads to noise prediction errors up to 0.8 dB, while, if the span grows to $7.5b$, the error decays and, for larger spans, becomes practically independent of the mesh dimensions. Noteworthy that for a span $2d = 4b$, the error is quite significant for an observer angle of approximately 70° and 290°.

Figure 6.8 illustrates the effect mesh leading-edge (LE) region length to the noise prediction, showing that the mesh leading-edge length plays a secondary role in the numerical noise prediction. If this parameter becomes too small (e.g. $1.5b$) it is verified a maximum error of, approximately, 0.8 dB.

Finally, Fig. 6.9 shows the effect of the trailing-edge (TE) mesh region length to the noise prediction, indicating that the TE mesh region length has a secondary effect on the noise prediction results. Consequently, this mesh parameter, could be minimized, up to a certain point, to reduce computational cost.

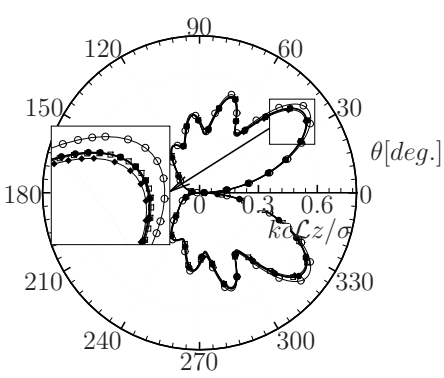

(a) Noise polar

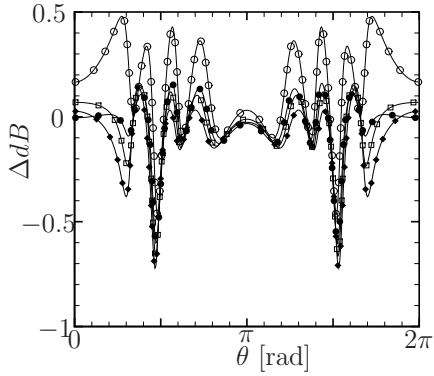

(b) Difference from the baseline

Figure 6.8: Effect of the leading-edge (LE) mesh region dimension to the predicted noise. Continuous line: flat plate Amiet reference solution; Open circle: $LE = 1.5b$; filled diamond: $LE = 3b$; Open square: $LE = 5b$; Filled circle: $LE = 10b$.

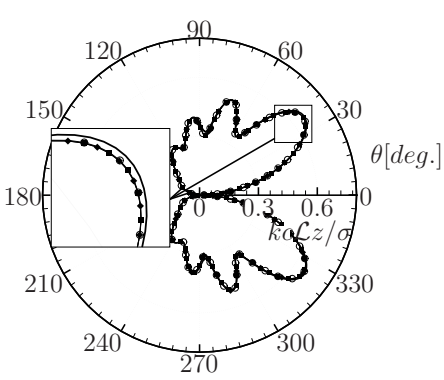

(a) Noise polar

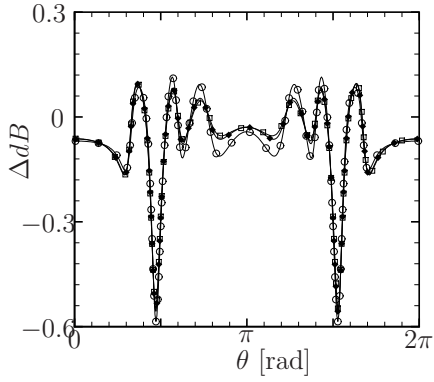

(b) Difference from the baseline

Figure 6.9: Effect of the trailing-edge (TE) dimension to the predicted noise. Continuous line: flat plate Amiet reference solution; Open circle: $TE = 3b$; filled diamond: $TE = 6b$; open square: $TE = 7.5b$.

6.3 Methodology application

This methodology allows to analyze the impact of airfoil geometrical features on the lift response to a monochromatic wind-gust and the consecutive noise radiation. To quantify this effect, this section, firstly, evaluates isolated airfoil geometrical features, such as camber and thickness, to next combine geometries with different camber lines and thicknesses. Noteworthy that, since the objective of this section is to observe first order geometrical effects, only the calculations of the leading-edge correction are performed. This decision it taken since it is known that, for the non-compact airfoil regime, the aeroacoustic transfer function corresponding to the leading-edge correction is much larger than the trailing-edge correction.

Camber effects The first airfoil geometrical feature evaluated is the camber line. In this evaluation, an infinitely thin airfoil is assumed, with profile given by a circle section, defined by:

$$\frac{z}{2b} = \sqrt{R_0^2 - \left(\frac{x}{2b}\right)^2} - \sqrt{R_0^2 - 1}\,, \qquad R_0 = \frac{1}{\sin(\xi/2)} \tag{6.20}$$

where ξ is the camber angle which defines the curvature radius R_0. For this study three different camber lines, with angles ξ of 10°, 20° and 30°, represented in Fig. 6.10, are evaluated.

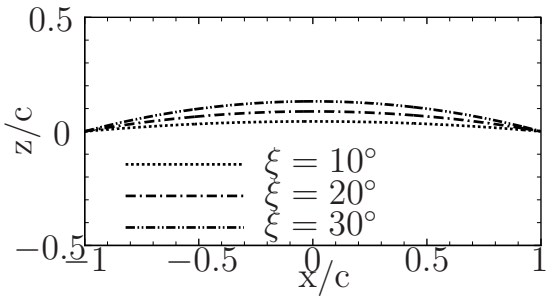

Figure 6.10: The three infinitely thin cambered airfoil evaluated in this section.

Figures 6.11 and 6.12 evaluate the aeroacoustic transfer function for different camber lines, considering Helmholtz numbers $kc = 1$, $kc = 5$, $kc = 10$, $kc = 20$. Showing that for $kc = 1$ the camber line has practically no effect in the aeroacoustic transfer function and that moderate alteration to the noise pattern radiation is observed when $kc = 5$.

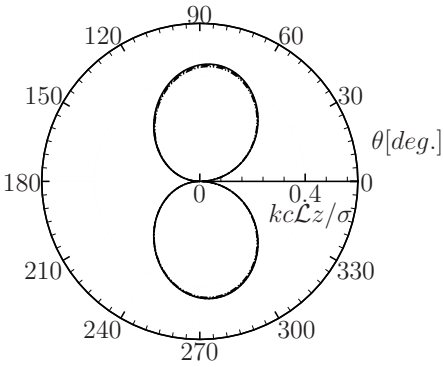

(a) kc=1

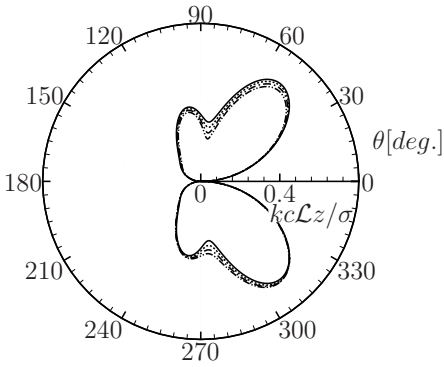

(b) kc=5

Figure 6.11: Aeroacoustic transfer function on an infinitely thin cambered airfoil. Results presented for Helmholtz number $kc = 1$ and $kc = 5$. Continuous line: Amiet solution for a flat plate; Dotted line: $\xi = 10°$; Dashed-dot line: $\xi = 20°$; Dashed-dot-dot line: $\xi = 30°$.

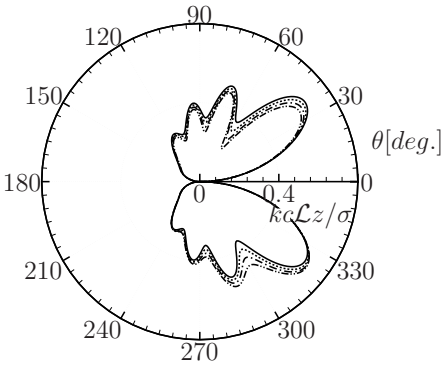

(a) kc=10

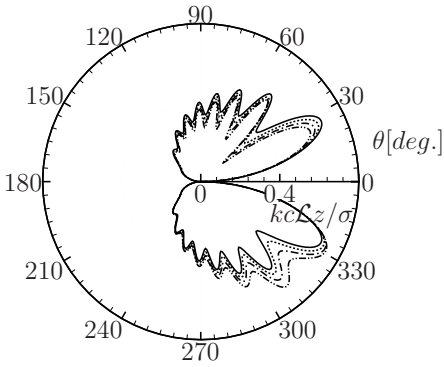

(b) kc=20

Figure 6.12: Aeroacoustic transfer function on an infinitely thin cambered airfoil. Results presented for Helmholtz number $kc = 10$ and $kc = 20$. Continuous line: Amiet solution for a flat plate; Dotted line: $\xi = 10°$; Dashed-dot line: $\xi = 20°$; Dashed-dot-dot line: $\xi = 30°$.

Considering the aeroacoustic transfer function presented in Fig. 6.12, it is possible to verify that for, higher frequencies, the noise polar of the cambered airfoils present more remarkable differences when compared to the baseline flat plate solution. The camber line imposes a reduction of the noise propagated along the suction side of the airfoil and noise amplification is present at the pressure side. In addition, it is verified that the noise extinction (due to destructive interference) is more remarkable at the cambered airfoils suction, while, for pressure side, this phenomena is less pronounced.

Aiming to evaluate the camber line effect, the noise power spectral density is computed. Similarly to the previous case, the airfoil is considered 0.1 m chord and 0.2 m span, the flow is considered uniform with mean velocity of 30 m/s dominated by uniform isotropic turbulence with u' equal to 0.2 m/s and integral correlation length scale (Λ_f) equal to 0.02 m, the observer is localized at a position of 90° distant 1 m from the airfoil leading-edge. Comparison of different camber lines to the noise power spectral density is presented in Fig. 6.13. This figure shows that the noise produced by an infinitely thin curved

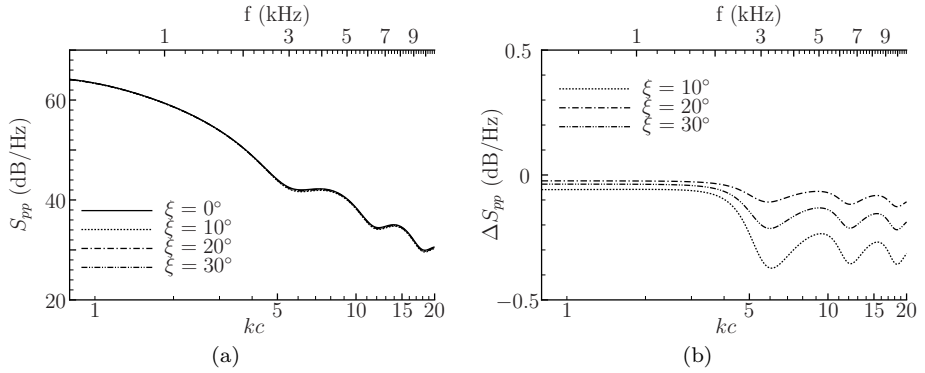

Figure 6.13: (a) Noise power spectral comparison for different camber lines. (b) Difference between the noise computed for a flat plate airfoil and airfoils with different camber lines.

airfoil is similar – within 1 dB – to the flat-plate airfoil. This methodology allows to verify that the camber line does not make remarkable effects to the airfoil aeroacoustic transfer function.

Thickness effects After evaluating the effect of an infinitely thin curved airfoil, the next step considers a thick airfoil. We consider an airfoil thickness distribution following the NACA 4 digits equation. For this analysis airfoils

with maximum thickness 6%, 12% and 24% of the chord are evaluated. These profiles are presented in Fig. 6.14. In this section only the high-

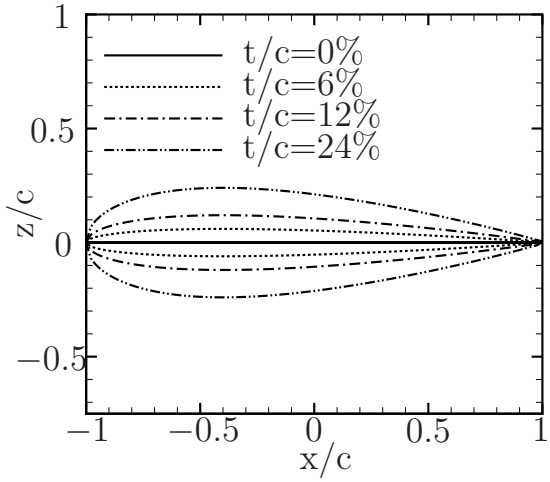

Figure 6.14: Three thick airfoil profiles evaluated in this section compared with the flat-plate airfoil.

frequency regime is considered for the evaluation of the thickness effect on the airfoil's aeroacoustic transfer function. Therefore, considering only the leading-edge correction yields to good solutions in the non-compact airfoil regime. Figures 6.15 and 6.16 presents the noise polar for the evaluated airfoils at different frequencies.

This figure shows that, even for the low-frequencies (kc=1), the airfoil thickness reduces the intensity of the airfoil radiated noise. It is possible to verify that the thicker is the airfoil the higher is the noise reduction.

Evaluating the Fig. 6.16 results we verify that, for the thick airfoil, the higher is the frequency the more pronounced is the noise reduction, independently of the observer angle.

The airfoil thickness, is evaluated, now, by a fixed observer. Same flow and geometry configuration previously analyzed is considered here. The evaluated noise power spectral density and the difference between the noise emitted by a flat plate and a thick airfoil are shown in Fig. 6.17.

Differently to the infinitely thin curved airfoil, Fig. 6.17 shows that the thick airfoil produces important noise reduction when compared with the flat

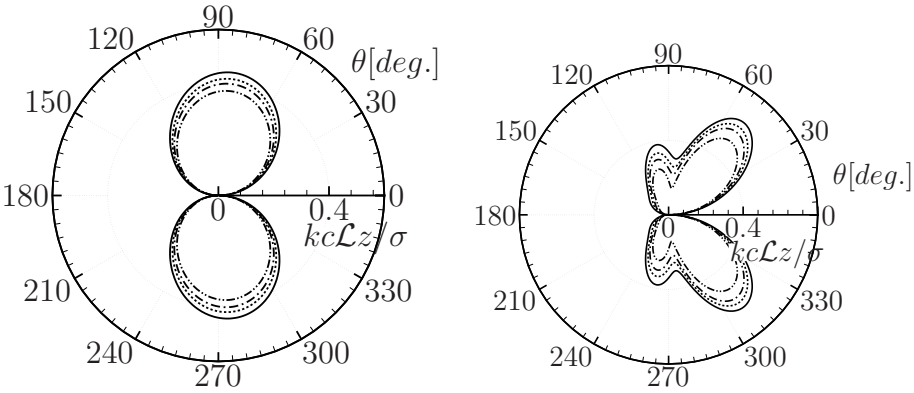

(a) kc=1 (b) kc=5

Figure 6.15: Thickness effects on the radiated noise polar. Results computed for $kc = 1$ and $kc = 5$. Continuous line: Amiet solution for a flat plate; Dotted line: $t/(2b) = 6\%$; Dashed-dot line: $t/(2b) = 12\%$; Dashed-dot-dot line: $t/(2b) = 24\%$.

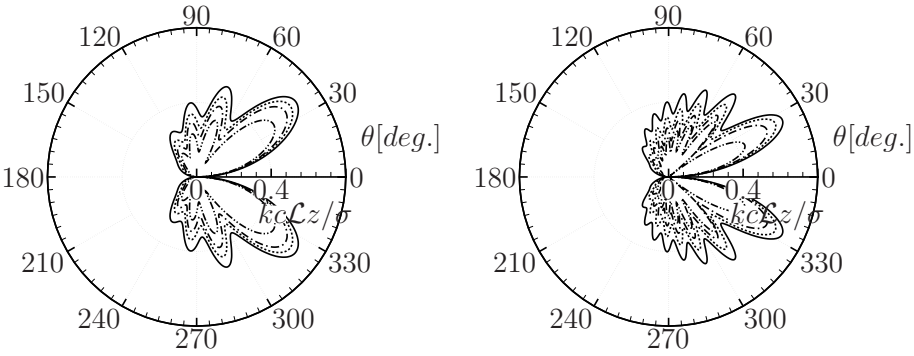

(a) kc=10 (b) kc=20

Figure 6.16: Thickness effects on the radiated noise polar. Results computed for $kc = 10$ and $kc = 20$. Continuous line: Amiet solution for a flat plate; Dotted line: $t/(2b) = 6\%$; Dashed-dot line: $t/(2b) = 12\%$; Dashed-dot-dot line: $t/(2b) = 24\%$.

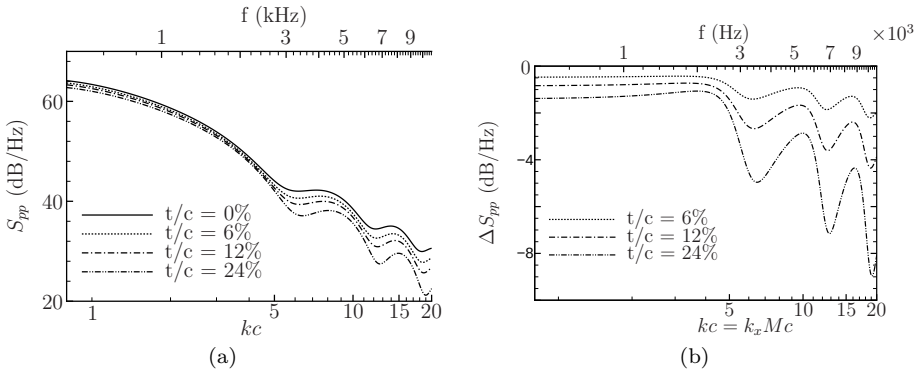

Figure 6.17: (a) Comparison of the noise power spectral density for airfoils of different thicknesses. (b) Difference between the noise emitted by a flat plate airfoil and the noise emitted by a thick airfoil.

plate. For smaller frequencies ($kc \leq 2.5$) the airfoil thickness imposes an approximately constant noise reduction and, for higher frequencies, the airfoil thickness imposes frequency dependent noise reduction. From this analysis, observing the oscillations present in the acoustic spectra due the destructive noise interference patterns, it is also possible to verify that the thickness slightly change these frequencies, showing the effect of this feature on the radiated noise scattering.

Thickness and camber effects As a final step, a cambered thick airfoil is evaluated. This analysis applies the methodology to more realistic cases and are intended to be similar to industrial design cases. For this application airfoils was chosen with 4%, 8% and 18% thickness and camber liner with $\xi = 30°$. These airfoil profiles are sketched in Fig. 6.18.

The radiated noise polar for the thick and cambered airfoil is compared with the infinitely thin airfoil in Figs. 6.19 and 6.20.

From this figure we observe that the thick and cambered airfoil presents a similar behavior to the thick airfoil uncambered. The radiated noise is reduced but, for this frequency range, no remarkable difference between the noise radiated to the suction and pressure side is noticed.

Figure 6.20 shows that the thickness and cambered airfoil have similar behavior of noise reduction with the increasing of the thickness. The noise directivity patterns show that, for higher frequencies, the noise radiated to the suction side is different from the noise radiated to the pressure side of the airfoil.

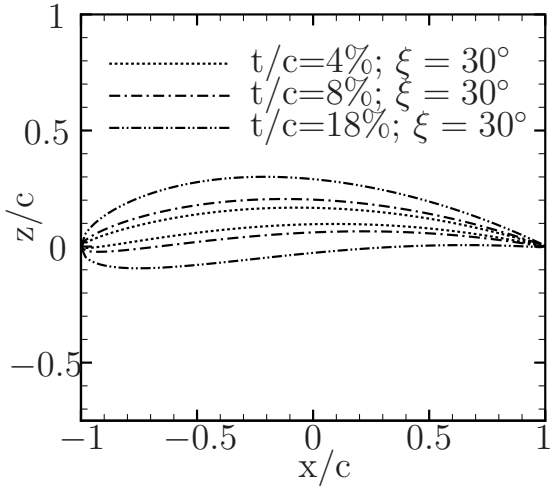

Figure 6.18: Thick and cambered airfoil profiles evaluated in this section.

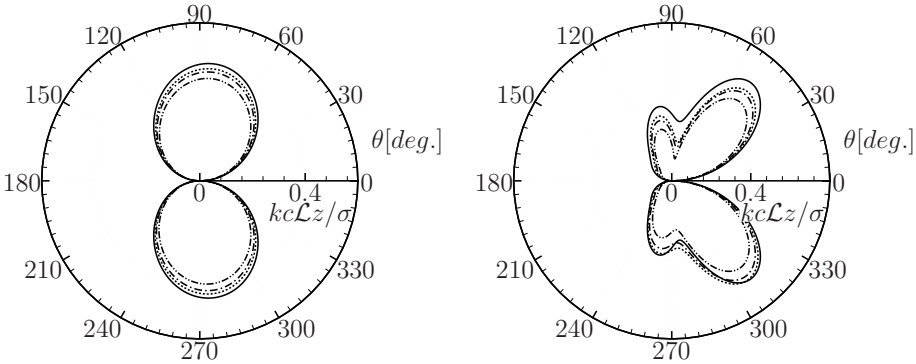

(a) kc=1 (b) kc=5

Figure 6.19: Thickness and camber effects on the radiated noise polar. Results computed for $kc = 1$ and $kc = 5$. Continuous line: Amiet solution for a flat plate; Dotted line: $t/(2b) = 4\%$ and $\xi = 30°$; Dashed-dot line: $t/(2b) = 8\%$ and $\xi = 30°$; Dashed-dot-dot line: $t/(2b) = 18\%$ and $\xi = 30°$.

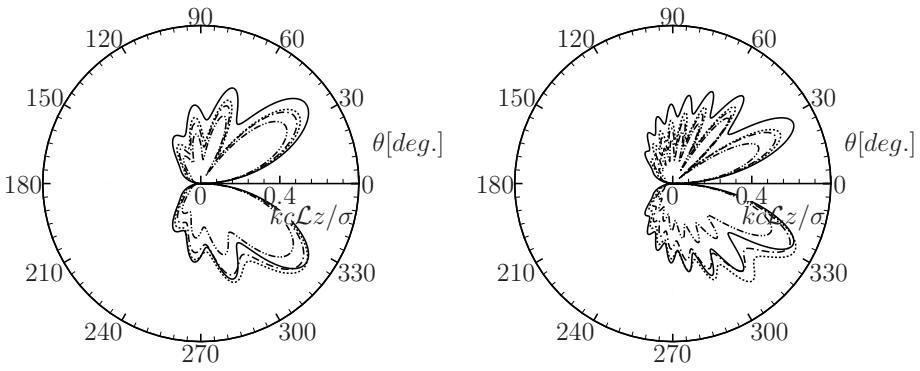

(a) kc=10 (b) kc=20

Figure 6.20: Thickness and camber effects on the radiated noise polar. Results computed for $kc = 10$ and $kc = 20$. Continuous line: Amiet solution for a flat plate; Dotted line: $t/(2b) = 4\%$ and $\xi = 30°$; Dashed-dot line: $t/(2b) = 8\%$ and $\xi = 30°$; Dashed-dot-dot line: $t/(2b) = 18\%$ and $\xi = 30°$.

A second testing case is performed evaluating the effect of different camber line and same thicknesses airfoils. In this analysis an airfoil with maximum thickness corresponding to 12% of the chord line is evaluated. Those airfoil profiles are presented in Fig. 6.21.

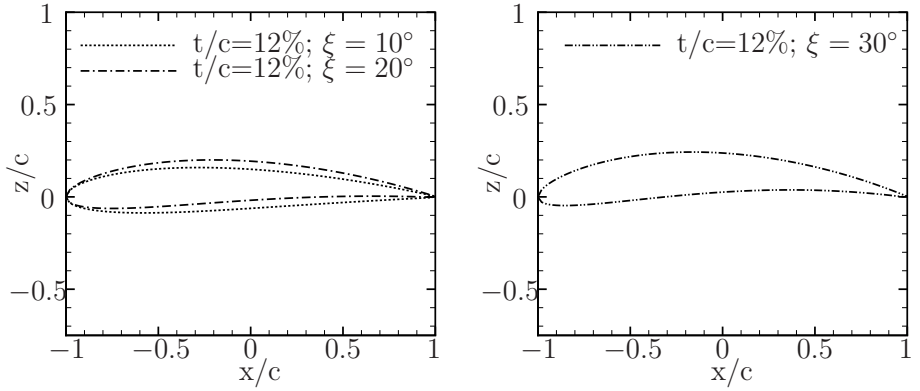

(a) (b)

Figure 6.21: Thick and cambered airfoil profiles with 12% of thickness and different camber lines.

The noise power spectral density is computed using flow and geometric parameters similar to those adopted in the previous sections. The computed noise power spectral density is presented in Fig. 6.22. From where it is seen

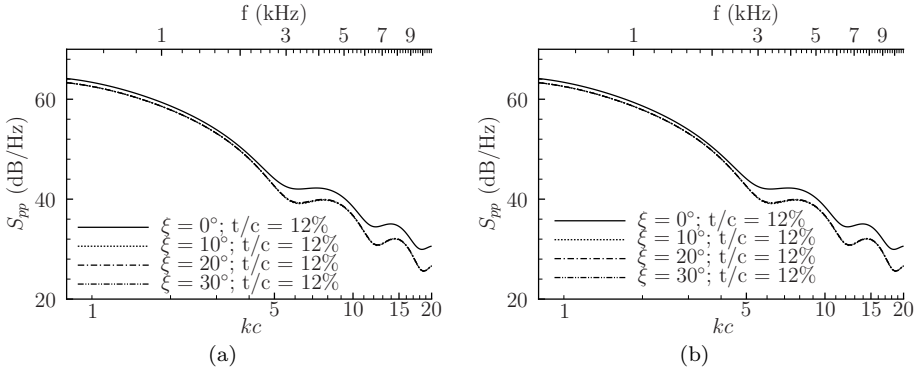

Figure 6.22: (a) Noise power spectral density computed for a 12% thickness cambered airfoil. (b) Difference between the computed noise power spectral density and the noise produced by an infinitely thin cambered airfoil.

that the airfoil the thick airfoil presents noise reduction when compared with the infinitely thin airfoil. But no important radiated noise difference is noticed for airfoils with different camber liners.

6.4 Experimental validation

In this section the proposed technique is validated against the experimental database. The thick airfoil aeroacoustic transfer function is computed for frequencies ranging from 200 to 5,500 Hz, following a logarithmic scale distribution of 101 points. This frequency range corresponds to kc varying approximately from 0.3 to 10. The BEM computation is automatized and the mesh dimension is set such that the computational time per frequency is not higher than 24 minutes. Noteworthy that the aeroacoustic transfer function depends only on the airfoil geometry and therefore it is independent of the upstream flow condition. In this approach, only the leading-edge case is computed, thus the solution is, in principle, valid for the non-compact frequency regime. The noise prediction results are compared in Figs. 6.23 and 6.24.

The airfoil thickness consideration to the noise prediction shows that the thicker is the profile reduces the lower is acoustic prediction – in the complete spectra

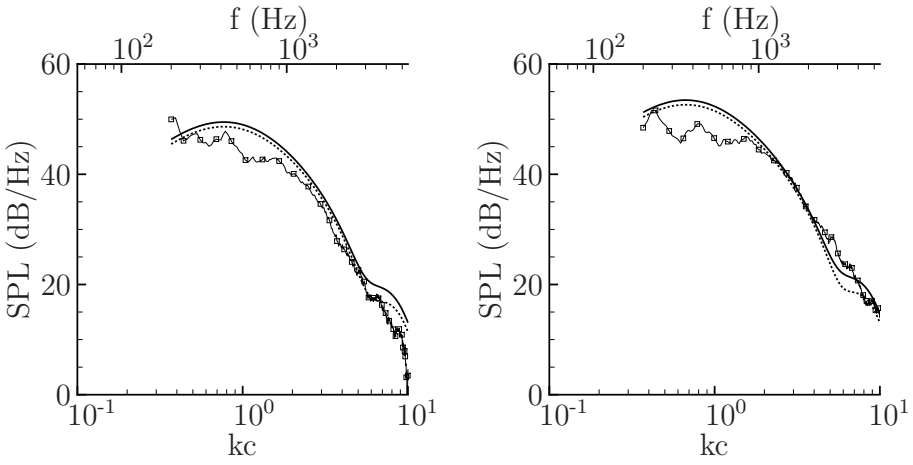

(a) Grid # 1 (b) Grid # 2

Figure 6.23: Comparison of the noise predicted using the classical Amiet theory and adopting the thickness correction. Open Square: experimental results; Continuous line: noise prediction for a flat-plate using Amiet theory; Dashed line: noise prediction considering the airfoil actual geometry.

range – with more pronounced results at high-frequencies. Considering higher frequencies, e.g. $kc > 6$, for the grid #1 the thick airfoil noise prediction has a better agreement with experimental results, while for grid #2 noise under prediction is verified. Noteworthy that the reduced signal-to-noise ratio observed for the grid # 1 for $8 < kc < 10$ suggests that the noise spectrum amplitude in this frequency range is slightly smaller. The rod-airfoil results show that the profile thickness reduces the predicted noise amplitude leading to a relative better agreement between predictions and experiments. This improved agreement is highlighted for the 0.016 m diameter rod, case with better signal-to-noise ratio when compared with the rod with 0.008 m diameter.

6.5 Conclusion

An innovative technique is proposed to compute the high-frequency leading-edge hydrodynamic response of realistic airfoil geometries. This chapter shows that the boundary value problem defined by the linearized airfoil theory is, after change of variables, similar to the acoustic wave propagation problem. The proposed technique employs a commercial acoustic solver to calculate the

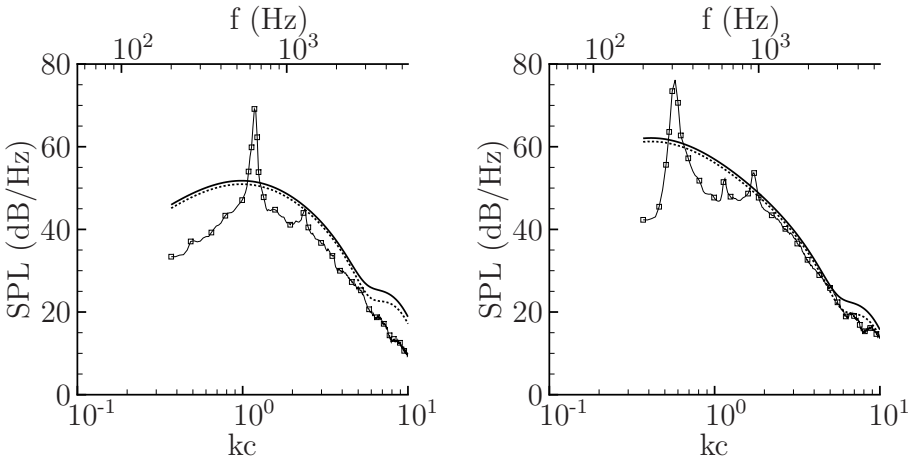

(a) Rod 0.008 m (b) Rod 0.016 m

Figure 6.24: Comparison of the noise predicted using the classical Amiet theory and adopting the thickness correction. Open Square: experimental results; Continuous line: noise prediction for a flat-plate using Amiet theory; Dashed line: noise prediction considering the airfoil actual geometry.

linearized airfoil theory problem following an iterative procedure, similar to the one proposed by Amiet. Mesh convergence analyses demonstrates that the noise prediction is performed with agreement of 0.8 dB with a computational cost not higher than 2.5 minutes per frequency. In case of high accuracy requirements, this approach computes one frequency in approximately 90 minutes. This methodology is applied to evaluate the impact of a particular airfoil feature to the predicted noise. Firstly, an infinitely thin cambered airfoil is analyzed showing it slightly contributes to the total airfoil radiated noise. Furthermore, it is observed that the higher the airfoil thickness is, the larger the noise reduction is. Additionally, these effects are pronounced in the high frequency regime. Finally, the technique is validated against experimental results showing overall improved noise prediction results when compared with calculations where geometric aspects are not considered.

Chapter 7

Conclusions and perspectives

7.1 Overview and discussion

Existing semi-empirical methodologies aimed at predicting incoming turbulence interaction noise, based on the Amiet framework, have been evaluated in detail in this thesis. Methodologies have been proposed to overcome limitations of some formulations described in literature. In addition, an experimental database to support these improvements has been developed for turbulence-airfoil and rod-airfoil interaction cases.

A new testing facility has thus been characterized, aerodynamically and acoustically, in Chapter 3. The aerodynamic measurements were mainly performed with hot-wire anemometry and stereoscopic-PIV techniques. Experimental results show good agreement between techniques for the mean and fluctuation RMS velocities, longitudinal and transverse velocity correlations and turbulence energy spectrum, indicating that data from either measurement method can be used as input to the noise prediction. Hot-wire measurements showed that in the absence of the turbulence generation grid, the flow velocity and turbulence intensity are practically uniform along the nozzle outlet. When the turbulence grid is placed, the flow becomes non-uniform with an acceleration close to the side-plates. However, a comparison between velocity spectra, longitudinal and transverse correlations, with isotropic turbulence models shows good agreement. This leads us to conclude that grids as coarse as used in our study lead to reasonably isotropic turbulence at the downstream distance adopted in this work. It is further shown in Chapter 4 that once this flow is characterized, no major difficulties are found to perform semi-

analytical noise predictions. Background noise measurements were performed and compared with acoustic results in presence of the airfoil, in the rod- and turbulence-airfoil configurations. These data showed signal-to-noise-ratio of at least 3 dB for frequencies above the anechoic room cut-off (200 Hz) and below $kc = 10$ (approximately 5,400 Hz). An exception was observed for the grid # 1, where for $8 < kc < 10$ a signal-to-noise-ratio of 1.7 dB was measured. The inflow and acoustics results developed in Chapter 3 are used as validation data for the rest of this work.

An analysis of the sensitivity of the noise prediction with respect to inflow characteristics, e.g. isotropic vs. anisotropic turbulence models, and far-field hypotheses is presented in Chapter 4. It is for example shown that applying a strip approach accounting for spanwise non-uniform incoming flow yields a sound prediction with reasonable accuracy. A thorough quantitative analysis of the turbulence distortion as it approaches the airfoil leading-edge was performed on the basis of stereo-PIV data described in Chapter 3. This investigation shows that the mean flow velocity follows the profile predicted by the potential theory, where the potential flow is obtained by a panel method using the complete airfoil geometry, for distances larger than the airfoil leading-edge radius. At shorter distance, the mean velocity profile deviates from the full-airfoil potential flow and follows close to the leading edge the potential flow calculated analytically for a cylinder with same airfoil leading-edge radius. Noteworthy, the transition region for the mean flow velocity is also a transition for the correlation and velocity spectrum decay, thereby indicating the region where turbulence distortion occurs. In agreement with previous studies, the flow velocity power spectral density is shown to follow a $-5/3$ decay exponent away from the leading-edge, turning into a $-10/3$ decay close to the leading-edge. Based on those experimental observations, a modification of the isotropic turbulence spectral model by the Rapid Distortion Theory (RDT) was tested. Noise predictions obtained using the von Kármán spectrum for isotropic turbulence and the RDT modified spectrum indicate that the latter yields better agreement with acoustic measurements.

In Chapter 4, the rod-airfoil case is studied as an application which produces a more complex inflow. The periodic component of the flow, linked with the vortex shedding, is not considered and only the random part is calculated. In an initial computation the PIV measured normal velocity component turbulence spectrum is adopted for calculations, showing poor agreement with acoustic measurements. As a solution approach, it was proposed to fit a von Kármán isotropic turbulence spectra to the reconstructed spectra measured at the rod-wake in the airfoil absence. The free parameters are the velocity fluctuation RMS u' and integral length scale Λ_e. The fitted turbulence spectra were then modified by RDT to be compared with the measured acoustic spectra, showing

again the importance of considering the turbulence distortion effect.

Chapter 5 presents an extension to the Amiet theory to the compact airfoil regime. The analysis that motivates this approach shows that the two iterative applications of the Schwarzschild theorem, proposed by Amiet, lead to poorly converged noise predictions in the low-frequency regime. To overcome this limitation, two extra iterations of the Schwarzschild theorem are proposed. The analytical expressions are derived, leading to expressions with no analytical solution unless approximations are introduced in the integrands. As those approximations introduce errors with the same order of magnitude as the corrections brought by the additional iterations, they are compensated for through a mixed numerical-analytical procedure. Those lengthy calculations eventually proved to reduce the noise over-prediction, typically observed in the compact frequency regime when applying the classical two-iterations approach. This conclusion is in agreement with experimental results, being more clearly observed in the rod-airfoil case with a 0.016 m diameter rod. Furthermore, it was shown that the two extra iterations lead to more pronounced spectral lobes, due to constructive and destructive interferences between the reciprocal leading-edge / trailing-edge back-scattering.

Chapter 6 is focused on the non-compact regime. This chapter proposes to solve the problem described by the linearized airfoil theory using a numerical approach. This generalizes the Amiet treatment, based on the half-infinite plane Green's function, to arbitrary airfoil geometries. The problem was solved using a Helmholtz acoustic solver, via a suitable change of variables. The methodology is compared with analytical results given by the Amiet theory for the infinitely thin airfoil. Results show that, even for meshes with reduced number of elements, it is possible to obtain reasonable predictions, which shows the applicability of this technique to industrial designs. Then the methodology is applied to thick airfoil geometries showing that the airfoil thickness has a major impact on the acoustic radiation while the camber has a minor effect. Noise predictions show that the airfoil thickness reduces the predicted noise for the complete acoustic spectra, with more pronounced results at higher frequencies.

7.2 Summary of main contribution

In Chapter 2 and Appendix A a comprehensive description of the Amiet theory is presented. These derivations include most of the calculation steps.

In Chapter 3 the experimental facility is aerodynamically and acoustically characterized by means of the hot-wire and stereoscopic-PIV techniques. The

results are presented with enough details to constitute a valuable validation database.

In Chapter 4 some important simplifications, such as assuming a uniform incoming flow, geometrical and acoustical far-field hypotheses, are evaluated. The use of an isotropic vs. anisotropic incoming flow spectra are assessed, showing that the turbulent flow is distorted as it approximates the airfoil leading-edge. Close to wall stereoscopic-PIV measurements shows quantitative evidence of the turbulence distortion by the influence of the airfoil leading-edge. These measurements show that a Rapid Turbulence Distortion occurs at distances comparable with the leading-edge radius, and provide data about the undistorted and distorted correlation signals and velocity spectra, both for the grid turbulence an rod turbulence cases. We believe these constitute original contributions to the field, as the RDT is mainly based on theoretical developments but was not substantiated (to the authors knowledge) by comprehensive experimental data.

In Chapter 5 the Amiet theory is extended to the compact airfoil regime. Starting from the Amiet derivations, this work contributes developing two extra iterative applications of the Schwarzschild theorem. This extension complements the paper proposed by Roger and Moreau [55], and represents an innovative contribution to the field.

Finally, Chapter 6 introduces a novel numerical procedure permitting to address realistic airfoil geometry effects in the non-compact regime. The proposed numerical approach solve the linearized airfoil theory considering arbitrary geometries not relying on the derivation of tailored analytical Green's function. It is shown that this problem can be solved by a commercial acoustic solver with small computational cost, being applicable to industrial designs. This original technique doesn't seem to have been reported in literature.

7.3 Open questions and future work

After the installation of the turbulence generation grid, the flow presented a non-uniform velocity and turbulence distribution along the position where the airfoil leading-edge is placed. Due to limitations of the flow supply system, an open area ratio larger than 90% had to be preserved to reach large enough velocities. This span-wise varying flow is interesting, from one side, since realistic applications include usually non-uniform flows, but, from the other side, more canonical flows would be desirable from a validation or benchmarking perspective.

For the grid-airfoil configuration, the facility background noise should be reduced, in order to achieve better signal-to-noise-ratio for kc values higher than 10. While for the grid # 2, a signal-to-noise-ratio of 3 dB was obtained for kc equal to 10, for grid # 1 this condition was obtained for kc equal to 8. In this case, the minimum signal-to-noise-ratio condition has been relaxed for $8 < kc < 10$, were a minimum value of 1.7 dB has been adopted.

The airfoil span could be larger to minimize the contribution of aerodynamic end effects and contamination due to side plate acoustic reflections. To the validation of the extension of the Amiet theory presented in Chapter 5 a smaller chord airfoil could be useful to validate the technique in the very-compact airfoil regime. Nevertheless, this could impact the signal to noise ration in higher frequencies, since the noise radiation amplitude is proportional to the airfoil chord.

In Chapter 6 only the leading-edge correction is considered in the numerical procedure. This approximation is valid for high-frequencies, and detailed investigations would be necessary to verify the effect of the trailing-edge correction in the compact regime. Preliminary tests showed that the second iteration has small contribution, i.e. less than 2 dB, but still further simulation could be done to substantiate this conclusion. During this approach developments it was verified that meshes with reduced number of elements resulted to numerical errors which may jeopardize the accuracy of further calculations. This methodology could be extended to the compact airfoil regime with more efficient acoustic Boundary Element solvers or even be applied to predict the trailing-edge noise case airfoil response.

Appendix A

Review of the leading-edge airfoil aerodynamic response function computed by the Amiet theory

In this appendix the airfoil aerodynamic response function derivation is reviewed with notation consistent with the rest of the thesis. Following Adamczyk [2] and Amiet [6] formulation, the theory presentation is divided in two cases, depending on the κ^2 value. If $\kappa^2 < 0$ the convective Helmholtz equation is classified as elliptic partial differential equation and the incoming gust is considered as subcritical and evanescent. Oppositely, if $\kappa^2 > 0$ the convective Helmholtz equation is assumed hyperbolic and the gust is characterized as supercritical and non-evanescent.

A.1 The linearized compressible flow potential

The inviscid mass and momentum conservation equations are written as

$$\frac{\partial \rho}{\partial t} + \frac{\partial(\rho u)}{\partial x} + \frac{\partial(\rho v)}{\partial y} + \frac{\partial(\rho w)}{\partial z} = 0\,, \tag{A.1}$$

$$\rho u \frac{\partial u}{\partial x} + \rho v \frac{\partial u}{\partial y} + \rho w \frac{\partial u}{\partial z} + \frac{\partial p}{\partial x} + \frac{\partial(\rho u)}{\partial t} = 0\,, \tag{A.2}$$

$$\rho u \frac{\partial v}{\partial x} + \rho v \frac{\partial v}{\partial y} + \rho w \frac{\partial v}{\partial z} + \frac{\partial p}{\partial y} + \frac{\partial(\rho v)}{\partial t} = 0\,, \tag{A.3}$$

$$\rho u \frac{\partial w}{\partial x} + \rho v \frac{\partial w}{\partial y} + \rho w \frac{\partial w}{\partial z} + \frac{\partial p}{\partial z} + \frac{\partial(\rho w)}{\partial t} = 0\,, \tag{A.4}$$

and the constitutive equation

$$\frac{\partial p}{\partial \rho} = c_0^2\,. \tag{A.5}$$

The previous equation set can be linearized by considering that the flow can be represented in terms of a mean – noted by an overbar $(\bar{\cdot})$ – and a perturbation – represented by a prime $(\cdot')$ – component. The linearization assumes that the perturbations are small compared to the mean values as well as their products and derivatives. Therefore, Eqs. A.1 are represented as

$$\begin{aligned} &\cancelto{0}{\frac{\partial \rho_0}{\partial t}} + \frac{\partial(\rho_0 u_0)}{\partial x} + \frac{\partial(\rho_0 v_0)}{\partial y} + \cancelto{0}{\frac{\partial(\rho_0 w_0)}{\partial z}} + \\ &\frac{\partial \rho'}{\partial t} + \rho_0 \left(\frac{\partial u'}{\partial x} + \frac{\partial v'}{\partial y} + \frac{\partial w'}{\partial z} \right) + \\ &u_0 \frac{\partial \rho'}{\partial x} + v_0 \frac{\partial \rho'}{\partial y} + w_0 \frac{\partial \rho'}{\partial z} = 0\,. \end{aligned} \tag{A.6}$$

The first line of Eq. A.1 is equal to zero since the mean flow satisfies the mass conservation. The x direction momentum conservation equation Eq. A.2 is

linearized to

$$\cancelto{0}{\rho_0 u_0 \frac{\partial u_0}{\partial x} + \rho_0 v_0 \frac{\partial u_0}{\partial y} + \rho_0 w_0 \frac{\partial u_0}{\partial z}} + \frac{\partial p_0}{\partial x} + \cancelto{0}{\frac{\partial(\rho_0 u_0)}{\partial t}} + \rho_0 \left(u_0 \frac{\partial u'}{\partial x} + v_0 \frac{\partial u'}{\partial y} + w_0 \frac{\partial u'}{\partial z} + \frac{\partial u'}{\partial t} \right) + \frac{\partial p'}{\partial x} = 0 \,, \tag{A.7}$$

similarly, the mean flow satisfies the momentum conservation equation, consequently, the first line of Eq. A.7 is zero. Therefore Eqs. A.3 and A.4 reads

$$\cancelto{0}{\rho_0 v_0 \frac{\partial v_0}{\partial x} + \rho_0 v_0 \frac{\partial v_0}{\partial y} + \rho_0 w_0 \frac{\partial v_0}{\partial z}} + \frac{\partial p_0}{\partial y} + \cancelto{0}{\frac{\partial(\rho_0 v_0)}{\partial t}} + \rho_0 \left(u_0 \frac{\partial v'}{\partial x} + v_0 \frac{\partial v'}{\partial y} + w_0 \frac{\partial v'}{\partial z} + \frac{\partial v'}{\partial t} \right) + \frac{\partial p'}{\partial y} = 0 \,, \tag{A.8}$$

$$\cancelto{0}{\rho_0 w_0 \frac{\partial w_0}{\partial x} + \rho_0 w_0 \frac{\partial w_0}{\partial y} + \rho_0 w_0 \frac{\partial w_0}{\partial z}} + \frac{\partial p_0}{\partial z} + \cancelto{0}{\frac{\partial(\rho_0 w_0)}{\partial t}} + \rho_0 \left(u_0 \frac{\partial w'}{\partial x} + v_0 \frac{\partial w'}{\partial y} + w_0 \frac{\partial w'}{\partial z} + \frac{\partial w'}{\partial t} \right) + \frac{\partial p'}{\partial z} = 0 \,, \tag{A.9}$$

For small perturbations the constitutive equation reads

$$p' = c_0^2 \rho' \,. \tag{A.10}$$

Supposing that the perturbation quantities can be written in terms of an incident – noted by the superscript I $(\cdot^I)$ – and scattered by the airfoil – represented by the superscript S $(\cdot^S)$ – component, at a region close to the airfoil, it is possible to write

$$\{p', \rho', u', v', w'\} = \left\{p^I + p^S, \rho^I + \rho^S, u^I + u^S, v^I + v^S, w^I + w^S\right\} \,, \tag{A.11}$$

while, in the far-field, one expects the scattered field vanishing

$$\{p', \rho', u', v', w'\} \xrightarrow{\text{far-field}} \left\{p^I, \rho^I, u^I, v^I, w^I\right\} \,. \tag{A.12}$$

In the far-field, the incident quantities $(\cdot^I)$ should satisfies the linearized flow equations. Additionally, in the region close to the airfoil, the scattered quantities $(\cdot^S)$, similarly, satisfy the linearized flow equation.

Given the problem linearity, the incident and the scattered field should, individually, satisfy the linearized flow equations at the region close to the airfoil.

The flow is considered inviscid, therefore, no change in vorticity is expected to happen as the flow passes the airfoil. Since the velocity field is irrotational, it can be represented by a flow potential, defined as

$$\left(u^S, v^S, w^S\right) = \left(\frac{\partial \Phi}{\partial x}, \frac{\partial \Phi}{\partial y}, \frac{\partial \Phi}{\partial z}\right) \tag{A.13}$$

now replacing Eq. A.13, into Eqs A.7, A.8, and A.9 and considering that, at the far-field, the scattered field is zero, it is possible to obtain the relation between the scattered pressure and the potential

$$p^S = -\rho_0 \left(\frac{\partial \Phi}{\partial t} + u_0 \frac{\partial \Phi}{\partial x} + v_0 \frac{\partial \Phi}{\partial y} + w_0 \frac{\partial \Phi}{\partial z}\right) \tag{A.14}$$

similar procedure is applied to the other two momentum conservation equations. Now substituting Eqs. A.14 and (Eq. A.10) into the linearized continuity equation (Eq. A.6) and summing equations, it is obtained the differential formulation which describes the potential flow scattered by the airfoil

$$\begin{aligned} c_0^2 \left(\nabla^2 \Phi - M_x^2 \frac{\partial^2 \Phi}{\partial x^2} - M_y^2 \frac{\partial^2 \Phi}{\partial y^2} - M_z^2 \frac{\partial^2 \Phi}{\partial z^2}\right) \\ -2c_0^2 \left(\frac{M_x}{c_0} \frac{\partial^2 \Phi}{\partial x \partial t} + \frac{M_y}{c_0} \frac{\partial^2 \Phi}{\partial y \partial t} + \frac{M_z}{c_0} \frac{\partial^2 \Phi}{\partial z \partial t}\right. \\ \left. M_x M_y \frac{\partial^2 \Phi}{\partial x \partial y} + M_x M_z \frac{\partial^2 \Phi}{\partial x \partial z} + M_y M_z \frac{\partial^2 \Phi}{\partial y \partial z}\right) - \frac{\partial^2 \Phi}{\partial t^2} = 0\,. \end{aligned} \tag{A.15}$$

A.2 Amiet's problem formulation

The Amiet theory considers a flat-plate airfoil localized between $0 \leq x/b \leq 2$ lying in the plane $z = 0$. This wing profile is subjected to an mean flow with components $(u_0 = U_\infty \cos(\theta), v_0 = U_\infty \sin(\theta), 0)$ and a monochromatic skewed velocity perturbation gust. In this problem, schematically represented in Fig. A.1, only the gust component w^I, perpendicular to the airfoil surface, is considered.

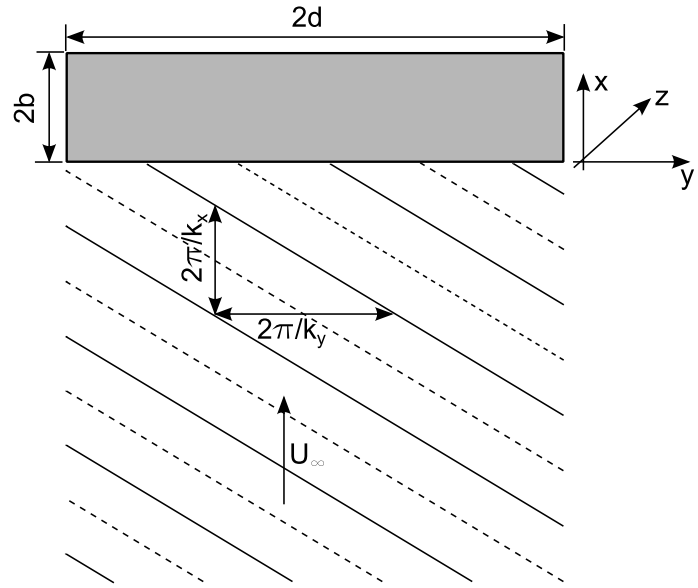

Figure A.1: Schematic representation of a flat plate airfoil airfoil subjected to a skewed aerodynamic gust perturbation.

The boundary conditions of this problem impose, respectively, zero potential upstream the airfoil leading edge, rigid airfoil surface (zero normal velocity) and zero pressure jump at the airfoil trailing-edge (Kutta condition) and downstream[6]:

$$\Phi(x,0,t) = 0 \qquad x/b \leq 0\,, \tag{A.16}$$

$$\frac{\partial \Phi(x,0,t)}{\partial z} = -w^I \qquad 0 \leq x/b \leq 2\,, \tag{A.17}$$

$$\frac{\mathrm{D}\Phi(x,0,t)}{\mathrm{D}t} = 0 \qquad x/b \leq 2\,, \tag{A.18}$$

where the total derivative operator is defined as:

$$\frac{\mathrm{D}}{\mathrm{D}t} = \frac{\partial}{\partial t} + U\frac{\partial}{\partial x} \tag{A.19}$$

Considering zero the mean flow component normal to the airfoil surface, Eq. A.15 can be rewritten as

$$\left[\nabla^2 - \frac{1}{c_0^2}\frac{D^2}{Dt^2}\right]\Phi\left(x,y,z,t\right) = 0\,, \tag{A.20}$$

in three dimensions Eq. A.20 is written as

$$\frac{\partial^2\Phi}{\partial x^2}+\frac{\partial^2\Phi}{\partial y^2}+\frac{\partial^2\Phi}{\partial z^2}-\frac{1}{c_0^2}\left[\frac{\partial^2\Phi}{\partial t^2}+2U\frac{\partial^2\Phi}{\partial t\partial x}+U^2\frac{\partial^2\Phi}{\partial x^2}\right]=0\,. \tag{A.21}$$

Now considering that the flow potential is time harmonic, it is possible to write

$$\Phi\left(x,y,z,t\right)=\phi(x,y,z)\mathrm{e}^{\mathrm{i}\omega t}\,. \tag{A.22}$$

The double spatial Fourier transform to the flow potential ϕ, leads to

$$\phi\left(x,y,z\right)=\varphi\left(x,z\right)\mathrm{e}^{\mathrm{i}\gamma x}\mathrm{e}^{\mathrm{i}\alpha y}\,, \tag{A.23}$$

where $\varphi(x,z)$ is the two-dimensional Fourier component of the potential ϕ,

$$\gamma=\frac{kM}{\beta^2}\,,\quad\text{and}\quad\alpha=-k_y\,. \tag{A.24}$$

According to Christophe [19] (Eq. C8, pag. 172), the spatial Fourier transformed potential (Eqs. A.22 and A.23) replaced into Eq. A.21 leads to

$$\beta^2\frac{\partial^2\varphi}{\partial x^2}+\left(\frac{k^2}{\beta^2}-\alpha^2\right)\varphi+\frac{\partial^2\varphi}{\partial z^2}=0\,. \tag{A.25}$$

With the non-dimensionalization parameters

$$\bar{x}=\frac{x}{b}\quad,\quad\bar{y}=\frac{\beta y}{b}\quad,\quad\bar{z}=\frac{\beta z}{b} \tag{A.26}$$

it is possible to rewrite Eq. A.25, in a non-dimentional form as

$$\frac{\beta^2}{b^2}\frac{\partial^2\varphi}{\partial\bar{x}^2}+\left(\frac{k^2}{\beta^2}-\alpha^2\right)\varphi+\frac{\beta^2}{b^2}\frac{\partial^2\varphi}{\partial\bar{z}^2}=0\,, \tag{A.27}$$

rearranging the terms, we have

$$\frac{\partial^2\varphi}{\partial\bar{x}^2}+\frac{\partial^2\varphi}{\partial\bar{z}^2}+\frac{b^2}{\beta^2}\left(\frac{k^2}{\beta^2}-\alpha^2\right)\varphi=0\,. \tag{A.28}$$

With the definitions of

$$k_x=\frac{\omega}{U}\quad,\quad k=\frac{\omega}{c_0}\quad,\quad k=k_xM\quad\text{and}\quad\bar{k}_i=k_ib \tag{A.29}$$

Eq. A.28 is simplified to

$$\frac{\partial^2\varphi}{\partial\bar{x}^2}+\frac{\partial^2\varphi}{\partial\bar{z}^2}+\left(\frac{\bar{k}_x^2M^2}{\beta^4}-\frac{\bar{k}_y^2}{\beta^2}\right)\varphi=0\,, \tag{A.30}$$

which is directly recognized as a convective Helmholtz equation

$$\frac{\partial^2\varphi}{\partial\bar{x}^2}+\frac{\partial^2\varphi}{\partial\bar{z}^2}+\kappa^2\varphi=0\,, \tag{A.31}$$

where

$$\kappa^2=\mu^2-\frac{\bar{k}_y}{\beta^2}\quad,\quad \mu=\frac{\bar{k}_xM}{\beta^2}=\bar{k}_x^*M\quad\text{and}\quad \bar{k}_x^*=\frac{\bar{k}_x}{\beta^2}\,. \tag{A.32}$$

The boundary conditions, described by Eqs. A.16, A.17 and A.18, are Fourier transformed regarding the time, x and y variables, and non-dimentionalized, leading to the relations:

$$\varphi(\bar{x},0)=0 \qquad \bar{x}\leq 0\,, \tag{A.33}$$

$$\frac{\partial}{\partial\bar{z}}\varphi\left(\bar{x},0\right)=\frac{-w_0b}{\beta}\mathrm{e}^{-\mathrm{i}\bar{k}_x^*\bar{x}} \qquad 0<\bar{x}\leq 2\,, \tag{A.34}$$

$$\left(\mathrm{i}\bar{k}_x^*+\frac{\partial}{\partial\bar{x}}\right)\varphi\left(\bar{x},0\right)=0 \qquad \bar{x}>2\,. \tag{A.35}$$

Summarizing, the convective Helmholtz equation to be solved and boundary conditions are

$$\frac{\partial^2\varphi}{\partial\bar{x}^2}+\frac{\partial^2\varphi}{\partial\bar{z}^2}+\kappa^2\varphi=0 \tag{A.36}$$

$$\phi\left(x,y,0,t\right)=0 \qquad \bar{x}\leq 0 \tag{A.37}$$

$$\frac{\partial}{\partial\bar{z}}\varphi\left(\bar{x},0\right)=\frac{-w_0b}{\beta}\mathrm{e}^{-\mathrm{i}\bar{k}_x^*\bar{x}} \qquad 0<\bar{x}\leq 2 \tag{A.38}$$

$$\left(\mathrm{i}\bar{k}_x^*+\frac{\partial}{\partial\bar{x}}\right)\varphi\left(\bar{x},0\right)=0 \qquad \bar{x}>2 \tag{A.39}$$

The problem nature differs depending κ^2 signal:

- if $\bar{k}_y<\frac{\bar{k}_xM}{\beta}$ the equation is hyperbolic and the gust is named supercritical;

- if $\bar{k}_y > \frac{\bar{k}_x M}{\beta}$ the equation is elliptic and the problem is named subcritical;
- if $\bar{k}_y = \frac{\bar{k}_x M}{\beta}$ the Helmholtz equation reduces to the Laplace equation and the gust is named critical.

To solve Eq. A.36 subjected to the three simultaneous boundary conditions (Eqs: A.37, A.38 and A.39) analytically Amiet adopted the Schwarzschild theorem [60] with the following strategy

1. Equation A.36 is solved subjected to the boundary condition of Eq. A.38, for a infinite plane. This problem can be analytically solved without the application of any special theorem. As a solution, the potential $\varphi^{(0)}$ is computed;
2. To satisfy the zero potential upstream the airfoil leading-edge (Eq. A.37), the potential is set to $-\varphi^{(0)}$ for $\bar{x} < 0$. The wavequation (Eq. A.36) is solved along with the non-penetration boundary condition, imposed for $\bar{x} \geq 0$. This leads to a first application of the Schwarzschild theorem. At this step, the potential ψ_1 is computed and summed with the potential $\varphi^{(0)}$ for $x \geq 0$, resulting on a potential $\varphi^{(1)}$;
3. After computing $\varphi^{(1)}$, it is possible to compute the pressure P_1. Now, to satisfy the boundary condition of zero pressure jump downstream the trailing-edge (Eq. A.39), the waveequation is written for the pressure variable. The pressure $-P_1$ is imposed as boundary condition for $\bar{x} \geq 2$ and the non-penetration boundary condition for $\bar{x} < 2$. This demands a second application of the Schwarzschild theorem. After this step, the correction pressure P_2 is computed.

Due to the iterative procedure designed by Amiet to solve the Helmholtz equation, after the second Schwarzschild theorem application the boundary condition of zero potential at region $\bar{x} < 0$ is not satisfied anymore. Amiet arguments that this residual potential is negligible for high frequencies when compared to the original incoming potential and, consequently, two iterations of the Schwarzschild procedure are enough to obtain a converged solution.

A.3 Supercritical gusts

Depending on the κ^2 signal the nature of the convective Helmholtz equation changes. If $\kappa^2 > 0$ the equation is hyperbolic and the gust is considered supercritical. Here the Amiet theory solution is presented for the supercritical case.

A.3.1 The infinite flat plate subjected to a gust flow potential

Following the Amiet procedure, the first step to solve Eq. A.31 is to verify the non-penetration boundary condition for an infinite plane. Considering that the potential $\varphi^{(0)}$ can be written as

$$\varphi^{(0)}\left(\bar{x},\bar{z}\right) = r\mathrm{e}^{s\bar{x}-\mathrm{i}\sqrt{\kappa^2+s^2}\bar{z}}\,, \tag{A.40}$$

we verify that this potential satisfies the Helmholtz equation (Eq. A.31) where the parameters:

$$s = -\mathrm{i}\bar{k}_x^* \quad , \quad r = \frac{w_0 b}{\bar{k}} \quad \text{and} \quad \bar{k} = \sqrt{\bar{k}_x^2 + \bar{k}_y^2}\,, \tag{A.41}$$

therefore the solution for the velocity potential is

$$\varphi^{(0)}\left(\bar{x},\bar{z}\right) = -\frac{w_0 b}{\bar{k}}\mathrm{e}^{-\mathrm{i}\bar{k}_x^*\bar{x}-\bar{k}\bar{z}/\beta}\,. \tag{A.42}$$

A.3.2 Leading-edge correction

The first iteration considers the airfoil as a semi-infinite airfoil extending downstream. The potential ψ_1 is determined to correct the potential $\varphi^{(1)} = \varphi^{(0)} + \psi_1$ and satisfy the boundary condition prescribed by Eq. A.33. In summary the problem to be solved, at this step, by means of the Schwarzschild theorem is:

$$\frac{\partial^2\psi_1}{\partial\bar{x}^2} + \frac{\partial^2\psi_1}{\partial\bar{z}^2} + \kappa^2\psi_1 = 0\,, \tag{A.43}$$

$$\psi_1\left(\bar{x},0\right) = -\varphi^{(0)}\left(\bar{x},0\right) \qquad \bar{x} \le 0\,, \tag{A.44}$$

$$\frac{\partial\psi_1}{\partial\bar{z}}\left(\bar{x},0\right) = 0 \qquad \bar{x} > 0\,. \tag{A.45}$$

The solution for the potential ψ_1 is given by Christophe[19]

$$\psi_1\left(\bar{x},0\right) = \frac{w_0 b}{\bar{k}}\mathrm{e}^{-\mathrm{i}\bar{k}_x^*\bar{x}}\left(1-(1-i)\,E\left[\left(\bar{k}_x^*-\kappa\right)\bar{x}\right]\right)\,, \tag{A.46}$$

and the potential $\varphi^{(1)}$ is

$$\varphi^{(1)}\left(\bar{x},0\right) = \varphi^{(0)} + \psi_1\,, \tag{A.47}$$

$$\varphi^{(1)}\left(\bar{x},0\right) = -\frac{w_0 b}{\bar{k}}\,(1-i)\,E\left[\left(\bar{k}_x^*-\kappa\right)\bar{x}\right]\mathrm{e}^{-\mathrm{i}\bar{k}_x^*\bar{x}}\,. \tag{A.48}$$

The complete expression for the potential $\Phi^{(1)}$ is

$$\Phi^{(1)}(x,y,0,t) = \varphi^{(1)} \mathrm{e}^{\mathrm{i}\omega t} \mathrm{e}^{\mathrm{i}\gamma x} \mathrm{e}^{\mathrm{i}\alpha y}\,, \tag{A.49}$$

$$\Phi^{(1)}(x,y,0,t) = -\frac{w_0\,(1-i)}{\sqrt{(k_x^2+k_y^2)}} E\left[\left(\bar{k}_x^* - \kappa\right)\bar{x}\right] \mathrm{e}^{\mathrm{i}(\omega t - k_x x - k_y y)}\,, \tag{A.50}$$

and the time Fourier transformed potential $\Phi^{(1)}$

$$\phi^{(1)}(x,y,0,\omega) = \varphi^{(1)} \mathrm{e}^{\mathrm{i}\gamma x} \mathrm{e}^{\mathrm{i}\alpha y}\,, \tag{A.51}$$

$$\phi^{(1)}(x,y,0,\omega) = -\frac{w_0\,(1-i)}{\sqrt{(k_x^2+k_y^2)}} E\left[\left(\bar{k}_x^* - \kappa\right)\bar{x}\right] \mathrm{e}^{\mathrm{i}(-k_x x - k_y y)}\,. \tag{A.52}$$

The pressure is computed as

$$p_1(x,y,0,t) = -\rho\frac{D\Phi_1}{Dt} \qquad = -\rho\left(\frac{\partial\Phi_1}{\partial t} + U\frac{\partial\Phi_1}{\partial x}\right)\,, \tag{A.53}$$

$$\tilde{p}_1(x,y,0,\omega) = \qquad -\rho\left(i\omega\phi_1 + U\frac{\partial\phi_1}{\partial x}\right)\,, \tag{A.54}$$

which leads to

$$p_1(x,y,0,t) = \rho U w_0 \frac{\mathrm{e}^{-\mathrm{i}\pi/4}\left(\bar{k}_x^* - \kappa\right)}{\sqrt{\pi\left(\bar{k}_x^* - \kappa\right)\left(\bar{k}_x^2 + \bar{k}_y^2\right)\bar{x}}} \mathrm{e}^{\mathrm{i}\left(\omega t - \left[\left(\bar{k}_x^* - \kappa\right)/b - k_x\right]x - k_y y\right)}\,. \tag{A.55}$$

Performing the time and space Fourier transforms, the pressure P_1 can be written as

$$p_1(x,y,0,t) = P_1(x,0)\,\mathrm{e}^{\mathrm{i}\omega t} \mathrm{e}^{\mathrm{i}\gamma x} \mathrm{e}^{\mathrm{i}\alpha y}\,, \tag{A.56}$$

$$\tilde{p}_1(x,y,0,\omega) = P_1(x,0)\,\mathrm{e}^{\mathrm{i}\gamma x} \mathrm{e}^{\mathrm{i}\alpha y}\,, \tag{A.57}$$

summarizing, for the second iteration, the equation to be solved is

$$\frac{\partial^2 P_1}{\partial\bar{x}^2} + \frac{\partial^2 P_1}{\partial\bar{z}^2} + \kappa^2 P_1 = 0\,, \tag{A.58}$$

with the boundary conditions

$$P_1(\bar{x},0) = 0 \qquad \bar{x} \geq 2\,, \tag{A.59}$$

$$\frac{\partial P_1}{\partial\bar{z}}(\bar{x},0) = 0 \qquad \bar{x} < 2\,, \tag{A.60}$$

A.3.3 Trailing-edge correction

A correction pressure P_2 is calculated to satisfy the boundary condition of zero pressure jump at the trailing-edge (Kutta condition) and downstream (Eq. A.59). Consequently, the following problem is solved by the Schwarzschild theorem

$$\frac{\partial^2 P_2}{\partial \bar{x}^2} + \frac{\partial^2 P_2}{\partial \bar{z}^2} + \kappa^2 P_2 = 0\,, \tag{A.61}$$

$$P_2\left(\bar{x},0\right) = -P_1\left(\bar{x},0\right) \qquad \bar{x} \geq 2\,, \tag{A.62}$$

$$\frac{\partial P_2}{\partial \bar{z}}\left(\bar{x},0\right) = 0 \qquad \bar{x} < 2\,, \tag{A.63}$$

According to Christophe [19], the solution for $P_2\left(\bar{x},0\right)$ is given by application of the Schwarzschild theorem

$$\begin{aligned} P_2\left(\bar{x},0\right) &= -\frac{1}{\pi}\int_0^\infty G(\bar{x}-2,\xi,0)P_1(2+\xi,0)\mathrm{d}\xi\,, \\ &= -\rho U w_0 \frac{\mathrm{e}^{-\mathrm{i}\pi/4}}{\pi\sqrt{\pi\left(\bar{k}_x+\beta^2\kappa\right)}}\mathrm{e}^{-4\mathrm{i}\kappa\bar{x}}\int_0^\infty \sqrt{\frac{2-\bar{x}}{\xi(\xi+2)}}\frac{\mathrm{e}^{-2\mathrm{i}\kappa\xi}}{\xi+2-\bar{x}}\mathrm{d}\xi\,. \end{aligned} \tag{A.64}$$

The integral cannot be analytically performed, however, the larger contribution of the integral is obtained for small values of $2-\bar{x}$ (near the trailing-edge), thus the term $2+\xi$ under the square root can be simplified to $2+\xi \approx 2$ leading to

$$\int_0^\infty \sqrt{\frac{2-\bar{x}}{\xi(\xi+2)}}\frac{\mathrm{e}^{-2\mathrm{i}\kappa\xi}}{\xi+2-\bar{x}}\mathrm{d}\xi \approx \int_0^\infty \sqrt{\frac{2-\bar{x}}{2\xi}}\frac{\mathrm{e}^{-2\mathrm{i}\kappa\xi}}{\xi+2-\bar{x}}\mathrm{d}\xi\,, \tag{A.65}$$

expression which can analytically compute $P_2\left(\bar{x},0\right)$ as

$$P_2\left(\bar{x},0\right) \approx -\rho U w_0 \frac{\mathrm{e}^{-\mathrm{i}\pi/4}\mathrm{e}^{-\mathrm{i}\kappa\bar{x}}}{\sqrt{2\pi\left(\bar{k}_x^2+\beta^2\kappa\right)}}\left[1-(1+i)\,E^*\left(2\kappa\left(2-\bar{x}\right)\right)\right]\,, \tag{A.66}$$

therefore the pressure $p_2\left(x,y,0,t\right)$ is computed as

$$\begin{aligned} p_2\left(x,y,0,t\right) \approx & \frac{-\rho U w_0}{\sqrt{2\pi\left(\bar{k}_x^2+\beta^2\kappa\right)}} \\ & \left[1-(1+\mathrm{i})\,E^*\left(2\kappa\left(2-\bar{x}\right)\right)\right]\mathrm{e}^{\mathrm{i}\left[\left(\bar{k}_x^* M^2\right)\bar{x}-\pi/4+\omega t-k_y y\right]}\,. \end{aligned} \tag{A.67}$$

Figure A.2 compares the airfoil pressure jump $P_1(\bar{x},0)$ and $P_2(\bar{x},0)$ for kc varying from 1 to 10 in steps of 1. This figure shows that for higher frequencies the scattered pressure concentrates at the leading-edge for P_1 and at the trailing-edge for P_2.

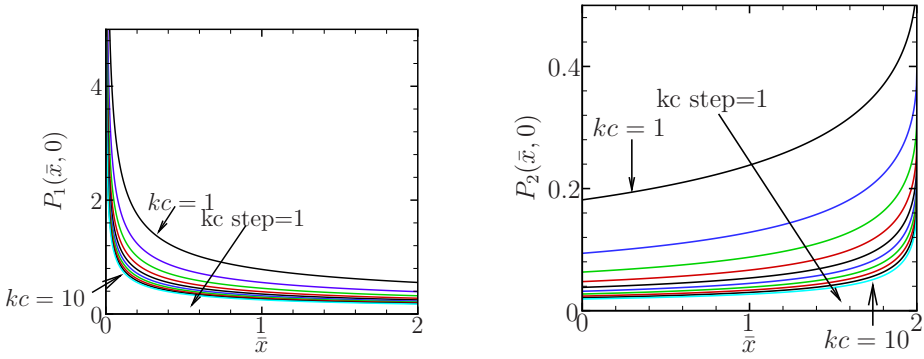

(a) P_1 superc. (b) P_2 superc.

Figure A.2: Pressure jump for different kc values varying from 1 to 10 at steps of 1.

A.3.4 Aeroacoustics transfer functions

The total pressure distribution on the airfoil surface is given by

$$p\left(x,y,0,t\right)=p_1\left(x,y,0,t\right)+p_2\left(x,y,0,t\right)\,, \tag{A.68}$$

and, since the airfoil here considered is a flat plate, the reduced lift function as

$$\Delta p\left(x,0,t\right)=2\pi\rho U w_0 g\left(x,k_x,k_y\right)\mathrm{e}^{\mathrm{i}\omega t}\,, \tag{A.69}$$

$$\Delta\tilde{p}\left(x,0,\omega\right)=2\pi\rho U w_0 g\left(x,k_x,k_y\right)\,, \tag{A.70}$$

where g is the transfer function between the incoming gust and the airfoil pressure jump, defined as

$$g\left(x,k_x,k_y\right)=\frac{p\left(x,y,0,t\right)\mathrm{e}^{\mathrm{i}k_y y}\mathrm{e}^{-\mathrm{i}\omega t}}{\pi\rho U w_0}\,, \tag{A.71}$$

$$g\left(x,k_x,k_y\right)=\frac{\tilde{p}\left(x,y,0,\omega\right)\mathrm{e}^{\mathrm{i}k_y y}}{\pi\rho U w_0}\,. \tag{A.72}$$

Replacing Eqs. A.55 and A.67 into Eq. A.71 we obtain

$$g_1\left(\bar{x}, k_x, k_y\right) = \frac{\mathrm{e}^{-\pi/4}}{\pi\sqrt{2\pi\left(\bar{k}_x + \beta^2\kappa\right)\left(\bar{x}+1\right)}}\mathrm{e}^{-\mathrm{i}\left(\kappa - \bar{k}_x^* M^2\right)(\bar{x}+1)}\,, \tag{A.73}$$

$$g_2\left(\bar{x}, k_x, k_y\right) = -\frac{\mathrm{e}^{-\pi/4}}{\pi\sqrt{2\pi\left(\bar{k}_x + \beta^2\kappa\right)}}\left[1 - (1+i)\,E^*\left(2\kappa\left(1-\bar{x}\right)\right)\right]\mathrm{e}^{-\mathrm{i}\left(\kappa - \bar{k}_x^* M^2\right)(\bar{x}+1)}\,. \tag{A.74}$$

The aeroacoustics transfer function is defined as

$$\mathcal{L}\left(x, y, z, k_x, k_y\right) = \int_{-1}^{1} g\left(\xi, k_x, k_y\right)\mathrm{e}^{-\mathrm{i}\mu(M - x/\sigma)\xi}\mathrm{d}\xi\,, \tag{A.75}$$

with $\sigma = \sqrt{x^2 + \beta^2\left(y^2+z^2\right)}$. Finally, according to Christophe [19] the aeroacoustic transfer function $\mathcal{L}_1\left(x, y, z, k_x, k_y\right)$ is given by

$$\mathcal{L}_1\left(x, y, z, k_x, k_y\right) = \frac{1}{\pi}\sqrt{\frac{2}{\left(\bar{k}_x + \beta^2\kappa\right)\theta_1}}E^*\left(2\theta_1\right)\mathrm{e}^{\mathrm{i}\theta_2} \tag{A.76}$$

with $\theta_1 = \kappa - \mu x/\sigma$ and $\theta_2 = \mu\left(M - x/\sigma\right) - \pi/4$. Additionally, the aeroacoustic transfer function $\mathcal{L}_2\left(x, y, z, k_x, k_y\right)$ is written as

$$\mathcal{L}_2\left(x, y, z, k_x, k_y\right) = \frac{\mathrm{e}^{\mathrm{i}\theta_2}}{\theta_1\pi\sqrt{2\pi\left(\bar{k}_x + \beta^2\kappa\right)}}$$

$$\left\{i\left(1 - \mathrm{e}^{-\mathrm{i}2\theta_1}\right) + (1-i)\left[E^*\left(4\kappa\right) - \sqrt{\frac{2\kappa}{\theta_3}}\mathrm{e}^{-\mathrm{i}2\theta_1}E^*\left(2\theta_3\right)\right]\right\} \tag{A.77}$$

with $\theta_3 = \kappa + \mu x/\sigma$.

A.4 Subcritical gusts

When $\kappa^2 < 0$ the wave equation is elliptic and the gust is subcritical. This section intends to deduce, in detail, this case, motivated by an incorrectness present on results of Rozenberg [58]. For the subcritical case, the set of equation and boundary conditions to be solved is

$$\frac{\partial^2\varphi'}{\partial\bar{x}^2}+\frac{\partial^2\varphi'}{\partial\bar{z}^2}-\kappa'^2\varphi'=0\,, \tag{A.78}$$

$$\varphi'(\bar{x},0)=0 \qquad \bar{x}\leq 0\,, \tag{A.79}$$

$$\frac{\partial}{\partial\bar{z}}\varphi'\left(\bar{x},0\right)=-\frac{w_0 b}{\beta}\mathrm{e}^{-\mathrm{i}\bar{k}_x^*\bar{x}} \qquad 0<\bar{x}\leq 2\,, \tag{A.80}$$

$$\left(\mathrm{i}\bar{k}_x^*+\frac{\partial}{\partial\bar{x}}\right)\varphi'\left(\bar{x},0\right)=0 \qquad \bar{x}>2\,. \tag{A.81}$$

A.4.1 The infinite flat plate subjected to a gust flow potential

Similarly to the supercritical case, this section finds the potential $\varphi'^{(0)}$ which satisfies the non-penetration boundary condition for a infinite flat plate. The solution to Eq. A.78, subjected to the non-penetration boundary condition, is supposed to have the form

$$\varphi'^{(0)}\left(\bar{x},\bar{z}\right)=r\mathrm{e}^{s\bar{x}+\mathrm{i}\bar{z}\sqrt{s^2-\kappa'^2}}\,, \tag{A.82}$$

which, after replacing, Eq. A.82 into Eq. A.78 we verify that

$$s^2\varphi'^{(0)}+\left(\kappa'^2-s^2\right)\varphi'^{(0)}-\kappa'^2\varphi'^{(0)}=0\,. \tag{A.83}$$

The constants r and s are determined by the non-penetraion bounary condition (Eq. A.80) as

$$\frac{\partial}{\partial\bar{z}}\varphi'\left(\bar{x},0\right)=ir\sqrt{s^2-\kappa'^2}\mathrm{e}^{s\bar{x}+\mathrm{i}\bar{z}\sqrt{s^2-\kappa'^2}}=-\frac{w_0 b}{\beta}\mathrm{e}^{-\mathrm{i}\bar{k}_x^*\bar{x}}\,, \tag{A.84}$$

from where we define s

$$\mathrm{e}^{s\bar{x}}=\mathrm{e}^{-\mathrm{i}\bar{k}_x^*\bar{x}} \qquad s=-\mathrm{i}\bar{k}_x^*\,. \tag{A.85}$$

To determine r

$$\mathrm{i}r\sqrt{s^2-\kappa'^2} = -\frac{w_0 b}{\beta}\,,$$

$$\mathrm{i}r\sqrt{\frac{-\bar{k}_x^2}{(1-M^2)^2} - \left[\frac{\bar{k}_y^2}{1-M^2} - \left(\frac{\bar{k}_x M}{1-M^2}\right)^2\right]} = -\frac{w_0 b}{\beta}\,,$$

$$\mathrm{i}r\sqrt{-\frac{\bar{k}_x^2}{1-M^2} - \frac{\bar{k}_y^2}{1-M^2}} = -\frac{w_0 b}{\beta}\,,$$

$$-\frac{r}{\beta}\sqrt{\bar{k}_x^2+\bar{k}_y^2} = -\frac{w_0 b}{\beta}\,,$$

$$r = \frac{w_0 b}{\bar{k}} \text{ with } \bar{k} = \sqrt{\bar{k}_x^2+\bar{k}_y^2}\,.$$

Finally, the potential $\varphi'^{(0)}(\bar{x},\bar{z})$ is defined as

$$\boxed{\varphi'^{(0)}(\bar{x},\bar{z}) = \frac{w_0 b}{\bar{k}} \mathrm{e}^{-\mathrm{i}\bar{k}_x^* \bar{x} - \bar{k}\bar{z}/\beta}}$$

A.4.2 Leading edge correction

After computing the flow potential for an infinite flat plate, the first iteration of the Amiet procedure is executed. At this iteration the zero flow potential boundary condition, at the region upstream the leading-edge (Eq. A.79) is imposed. For this correction, the boundary value problem to be solved, by means of the Schwarzschild theorem, is summarized:

$$\frac{\partial^2 \varphi'^{(1)}}{\partial \bar{x}^2} + \frac{\partial^2 \varphi'^{(1)}}{\partial \bar{z}^2} - \kappa'^2 \varphi'^{(1)} = 0\,, \tag{A.86}$$

$$\varphi'^{(1)}(\bar{x},0) = 0 \qquad \bar{x} \le 0\,, \tag{A.87}$$

$$\frac{\partial}{\partial \bar{z}^2}\varphi'^{(1)}(\bar{x},0) = -\frac{w_0 b}{\bar{k}} \mathrm{e}^{-\mathrm{i}\bar{k}_x^* \bar{x}} \qquad \bar{x} > 0\,. \tag{A.88}$$

To satisfy the boundary condition represented by Eq. A.87 it is necessary to define a potential ψ_1' such that the potential upstream to the leading-edge is

null. In this way the following problem should be solved using the Schwarzschild theorem

$$\frac{\partial^2 \psi_1{}'}{\partial \bar{x}^2} + \frac{\partial^2 \psi_1{}'}{\partial \bar{z}^2} - \kappa'^2 \psi_1{}' = 0\,, \tag{A.89}$$

$$\psi_1{}'(\bar{x},0) = -\varphi'^{(0)}(\bar{x},0) \qquad \bar{x} \leq 0\,, \tag{A.90a}$$

$$\frac{\partial}{\partial \bar{z}^2}\psi_1{}'(\bar{x},0) = 0 \qquad \bar{x} > 0\,. \tag{A.90b}$$

At this point of the derivation, there are still two solutions allowed for κ'. For the subcritical case, it is convenient to define the term κ'^2 as

$$\kappa'^2 = -\kappa^2 = \frac{\bar{k}_y^2}{\beta^2} - \mu^2\,, \tag{A.91}$$

$$\kappa' = \pm i\kappa\,, \tag{A.92}$$

by definition, κ' is a double valued constant, consequently, a correct choice of signal for this coefficient is necessary to guarantee the evanescence of the scattered flow potential by the incoming wave. For this problem it is necessary adopt $\kappa' < 0$. On Rozenberg thesis, a positive value was used for κ' which, consequently, lead the scattered field to grow to infinity instead of asymptotically decays to zero.

Using the Schwarzschild theorem the solution to Eq. A.89 is

$$\psi_1{}'(\bar{x},0) = -\frac{1}{\pi}\int_0^\infty \sqrt{\frac{\bar{x}}{\xi}}\frac{\mathrm{e}^{-\kappa'(\xi+\bar{x})}}{\xi+\bar{x}}\left(\varphi'^{(0)}(-\xi,0)\right)\mathrm{d}\xi\,, \tag{A.93}$$

$$\psi_1{}'(\bar{x},0) = -\frac{1}{\pi}\int_0^\infty \sqrt{\frac{\bar{x}}{\xi}}\frac{\mathrm{e}^{-\kappa'(\xi+\bar{x})}}{\xi+\bar{x}}\left(\frac{w_0 b}{\bar{k}}\mathrm{e}^{\mathrm{i}\bar{k}_x^*\xi}\right)\mathrm{d}\xi \tag{A.94}$$

$$\psi_1{}'(\bar{x},0) = -\frac{1}{\pi}\frac{w_0 b}{\bar{k}}\mathrm{e}^{-\kappa'\bar{x}}\int_0^\infty \sqrt{\frac{\bar{x}}{\xi}}\frac{\mathrm{e}^{\left(-\kappa'+\mathrm{i}\bar{k}_x^*\right)\xi}}{\xi+\bar{x}}\mathrm{d}\xi \tag{A.95}$$

From Gradshteyn and Ryzhik, [31] (ref. pag. 348, item 10 and sec. A.6):

$$\int_0^\infty \sqrt{\frac{\bar{x}}{\xi}}\frac{\mathrm{e}^{-\mathrm{i}A\xi}}{\xi+\bar{x}}\mathrm{d}\xi = \pi\mathrm{e}^{\mathrm{i}A\bar{x}}\left[1 - \frac{\mathrm{e}^{\mathrm{i}\pi/4}}{\sqrt{\pi}}\int_0^{A\bar{x}}\frac{\mathrm{e}^{-\mathrm{i}t}}{\sqrt{t}}\mathrm{d}t\right]\,, \tag{A.96}$$

with

$$A = -\left(i\kappa' + \bar{k}_x^*\right) . \tag{A.97}$$

According to Rozenberg [58] (ref. pag 34)

$$\frac{\mathrm{e}^{\mathrm{i}\pi/4}}{\sqrt{\pi}} \int_0^{-iZ^2} \frac{\mathrm{e}^{-\mathrm{i}t}}{\sqrt{t}} \mathrm{d}t = \mathrm{erf}(Z) \tag{A.98}$$

with the relation

$$-\mathrm{i}Z^2 = A\bar{x} \,, \tag{A.99}$$

$$Z^2 = \mathrm{i}A\bar{x} = \left(-\mathrm{i}\bar{k}_x^* + \kappa'\right)\bar{x} \,, \tag{A.100}$$

$$Z = \sqrt{\left(\kappa' - \mathrm{i}\bar{k}_x^*\right)\bar{x}} \qquad , \tag{A.101}$$

replacing we have

$$\frac{\mathrm{e}^{\mathrm{i}\pi/4}}{\sqrt{\pi}} \int_0^{A\bar{x}} \frac{\mathrm{e}^{-\mathrm{i}t}}{\sqrt{t}} \mathrm{d}t = \mathrm{erf}\left(\sqrt{\left(\kappa' - \mathrm{i}\bar{k}_x^*\right)\bar{x}}\right) \tag{A.102}$$

which replaced to the flow potential integral leads to

$$\psi_1{}'\left(\bar{x},0\right) = -\frac{1}{\pi}\frac{w_0 b}{\bar{k}}\mathrm{e}^{-\kappa'\bar{x}}\left(\pi \mathrm{e}^{-\mathrm{i}\left(i\kappa' + \bar{k}_x^*\right)\bar{x}}\left[1 - \mathrm{erf}\left(\sqrt{\left(\kappa' - \mathrm{i}\bar{k}_x^*\right)\bar{x}}\right)\right]\right) \tag{A.103}$$

$$\psi_1{}'\left(\bar{x},0\right) = -\frac{w_0 b}{\bar{k}}\mathrm{e}^{-\mathrm{i}\bar{k}_x^*\bar{x}}\left[1 - \mathrm{erf}\left(\sqrt{\left(\kappa' - \mathrm{i}\bar{k}_x^*\right)\bar{x}}\right)\right] . \tag{A.104}$$

For the region downstream the airfoil leading-edge, the total potential is given by the incident potential superimposed to the scattered potential as

$$\varphi'^{(1)}\left(\bar{x},0\right) = \varphi'^{(0)}\left(\bar{x},0\right) + \psi_1{}'\left(\bar{x},0\right) , \tag{A.105}$$

which leads to

$$\varphi'^{(1)}\left(\bar{x},0\right) = \frac{w_0 b}{\bar{k}}\mathrm{e}^{-\mathrm{i}\bar{k}_x^*\bar{x}} - \frac{w_0 b}{\bar{k}}\mathrm{e}^{-\mathrm{i}\bar{k}_x^*\bar{x}}\left[1 - \mathrm{erf}\left(\sqrt{\left(\kappa' - \mathrm{i}\bar{k}_x^*\right)\bar{x}}\right)\right] , \tag{A.106}$$

$$\varphi'^{(1)}\left(\bar{x},0\right) = \frac{w_0 b}{\bar{k}}\mathrm{e}^{-\mathrm{i}\bar{k}_x^*\bar{x}}\mathrm{erf}\left(\sqrt{\left(\kappa' - \mathrm{i}\bar{k}_x^*\right)\bar{x}}\right) , \tag{A.107}$$

the flow potential as a function of the Fourier components is

$$\phi'^{(1)}\left(\bar{x},\bar{y},t,0\right) = \varphi'^{(1)}\mathrm{e}^{\mathrm{i}\omega t}\mathrm{e}^{\mathrm{i}\gamma x}\mathrm{e}^{\mathrm{i}\alpha y} , \tag{A.108}$$

where the relation is verified

$$-\mathrm{i}\bar{k}_x^*\bar{x}+\frac{\mathrm{i}k_xM^2}{1-M^2}=\frac{-\mathrm{i}k_xb}{1-M^2}\frac{x}{b}+\frac{\mathrm{i}k_xM^2}{1-M^2}=-\mathrm{i}k_x\,, \tag{A.109}$$

the final leading-edge correction flow potential is given

$$\phi'^{(1)}\left(\bar{x},0\right)=\frac{w_0b}{\bar{k}}\mathrm{e}^{\mathrm{i}\omega t}\mathrm{e}^{-\mathrm{i}k_yy}\mathrm{e}^{-\mathrm{i}k_xx}\mathrm{erf}\left(\sqrt{\left(\kappa'-\mathrm{i}\bar{k}_x^*\right)\bar{x}}\right)\,, \tag{A.110}$$

remembering that the pressure is computed as

$$p\left(\bar{x},0\right)=-\rho\left(\frac{\partial\phi'^{(1)}}{\partial t}+U\frac{\partial\phi'^{(1)}}{\partial x}\right)\,, \tag{A.111}$$

we have

$$\frac{\partial\phi'^{(1)}}{\partial t}=\mathrm{i}\omega\phi'^{(1)}=\mathrm{i}k_xU\phi'^{(1)}\,, \tag{A.112}$$

$$U\frac{\partial\phi'^{(1)}}{\partial x}=-\mathrm{i}k_xU\phi'^{(1)}+U\frac{w_0b}{\bar{k}}\mathrm{e}^{\mathrm{i}\omega t}\mathrm{e}^{-\mathrm{i}k_yy}\mathrm{e}^{-\mathrm{i}k_xx}\frac{\partial\left[\mathrm{erf}\left(\sqrt{\left(\kappa'-\mathrm{i}\bar{k}_x^*\right)\bar{x}}\right)\right]}{\partial x}\,, \tag{A.113}$$

$$\frac{\partial\left[\mathrm{erf}\left(\sqrt{\left(\kappa'-\mathrm{i}\bar{k}_x^*\right)\bar{x}}\right)\right]}{\partial x}=\frac{\exp\left(-\left(\kappa'-\mathrm{i}\bar{k}_x^*\right)\bar{x}\right)\left(\kappa'-\mathrm{i}\bar{k}_x^*\right)}{b\sqrt{\pi\left(\kappa'-\mathrm{i}\bar{k}_x^*\right)\bar{x}}}\,. \tag{A.114}$$

The two previous terms cancel each other so

$$p\left(x,y,0,t\right)=-\rho U\frac{w_0b}{\bar{k}}\mathrm{e}^{\mathrm{i}\omega t}\mathrm{e}^{-\mathrm{i}k_yy}\mathrm{e}^{-\mathrm{i}k_xx}\frac{\exp\left(-\left(\kappa'-\mathrm{i}\bar{k}_x^*\right)\bar{x}\right)\left(\kappa'-\mathrm{i}\bar{k}_x^*\right)}{b\sqrt{\pi\left(\kappa'-\mathrm{i}\bar{k}_x^*\right)\bar{x}}}\,, \tag{A.115}$$

which simplifies to

$$p\left(x,y,0,t\right)=-\rho Uw_0\mathrm{e}^{\mathrm{i}\omega t}\mathrm{e}^{-\mathrm{i}k_yy}\mathrm{e}^{-\mathrm{i}k_xx}\frac{\exp\left(-\left(\kappa'-i\bar{k}_x^*\right)\bar{x}\right)\left(\kappa'-i\bar{k}_x^*\right)}{\sqrt{\pi\left(\bar{k}_x^2+\bar{k}_y^2\right)\left(\kappa'-i\bar{k}_x^*\right)\bar{x}}} \tag{A.116}$$

considering the simplification of the relation

$$\begin{aligned}
\frac{\kappa' - i\bar{k}_x^*}{\sqrt{\left(\bar{k}_x^2 + \bar{k}_y^2\right)\left(\kappa' - i\bar{k}_x^*\right)}} &= \frac{\kappa' - i\bar{k}_x^*}{\sqrt{\left(\bar{k}_x^2 + \bar{k}_y^2\right)\left(\kappa' - i\bar{k}_x^*\right)}} \frac{\sqrt{\left(\kappa' - i\bar{k}_x^*\right)\left(\kappa' + i\bar{k}_x^*\right)}}{\sqrt{\left(\kappa' - i\bar{k}_x^*\right)\left(\kappa' + i\bar{k}_x^*\right)}} \\
&= \frac{\sqrt{\kappa'^2 + \bar{k}_x^{*2}}}{\sqrt{\left(\bar{k}_x^2 + \bar{k}_y^2\right)\left(\kappa' + i\bar{k}_x^*\right)}} \\
&= \frac{\sqrt{\bar{k}_y^2/\beta^2 - \bar{k}_x^{*2}M^2 + \bar{k}_x^{*2}}}{\sqrt{\left(\bar{k}_x^2 + \bar{k}_y^2\right)\left(\kappa' + i\bar{k}_x^*\right)}} \\
&= \frac{\sqrt{\bar{k}_y^2/\beta^2 + \bar{k}_x^2/\beta^4\left(1 - M^2\right)}}{\sqrt{\left(\bar{k}_x^2 + \bar{k}_y^2\right)\left(\kappa' + \mathrm{i}\bar{k}_x^*\right)}} \\
&= \frac{1/\beta\sqrt{\bar{k}_y^2 + \bar{k}_x^2}}{\sqrt{\left(\bar{k}_x^2 + \bar{k}_y^2\right)\left(\kappa' + \mathrm{i}\bar{k}_x^*\right)}} \\
&= \frac{1/\beta}{1/\beta\sqrt{\left(\kappa'\beta^2 + \mathrm{i}\bar{k}_x\right)}} \\
&= \frac{1}{\sqrt{\left(\kappa'\beta^2 + \mathrm{i}\bar{k}_x\right)}}
\end{aligned}$$

it is possible to write

$$p\left(x, y, 0, t\right) = -\rho U w_0 \mathrm{e}^{\mathrm{i}\omega t}\mathrm{e}^{-\mathrm{i}k_y y}\mathrm{e}^{-\mathrm{i}k_x x}\frac{\mathrm{e}^{-\left(\kappa' - \mathrm{i}\bar{k}_x^*\right)\bar{x}}}{\sqrt{\pi\left(\kappa'\beta^2 + \mathrm{i}\bar{k}_x\right)\bar{x}}}\,. \tag{A.117}$$

Remembering

$$p\left(x, y, 0, t\right) = P_1 \mathrm{e}^{\mathrm{i}\omega t}\mathrm{e}^{-\mathrm{i}\alpha y}\mathrm{e}^{\mathrm{i}\gamma x}\,, \tag{A.118}$$

we have

$$P_1\left(\bar{x},0\right)=-\rho U\frac{w_0 b}{\bar{k}}\frac{\exp\left(-\left(\kappa'-\mathrm{i}\bar{k}_x^*\right)\bar{x}\right)\left(\kappa'-\mathrm{i}\bar{k}_x^*\right)}{b\sqrt{\pi\left(\kappa'-\mathrm{i}\bar{k}_x^*\right)\bar{x}}}\exp\left(-\mathrm{i}\bar{k}_x^*\bar{x}\right)\,, \tag{A.119}$$

$$P_1\left(\bar{x},0\right)=-\rho U w_0\frac{\mathrm{e}^{-\kappa'\bar{x}}}{\sqrt{\pi\left(\kappa'\beta^2+\mathrm{i}\bar{k}_x\right)\bar{x}}}\,. \tag{A.120}$$

A.4.3 Trailing-edge correction

Following the Amiet procedure a third step is necessary to impose the Kutta condition and the condition of zero pressure jump at the region downstream the airfoil trailing-edge.

At this iteration the following system of equations has to be solved:

$$\frac{\partial^2 P_2}{\partial\bar{x}^2}+\frac{\partial^2 P_2}{\bar{z}^2}-\kappa'^2 P_2=0\,, \tag{A.121}$$

$$P_2\left(\bar{x},0\right)=-P_1\left(\bar{x},0\right)\qquad \bar{x}<2\,, \tag{A.122a}$$

$$\frac{\partial P_2}{\partial\bar{z}}\left(\bar{x},0\right)=0\qquad \bar{x}\geq 2\,. \tag{A.122b}$$

In order to apply the Schwarzschild theorem the following change of variables is necessary $X=\bar{x}-2$

$$P_2\left(\bar{x},0\right)=-\frac{1}{\pi}\int_0^\infty\sqrt{\frac{2-\bar{x}}{\xi}}\frac{\mathrm{e}^{-\kappa'(\xi+2-\bar{x})}}{\xi+2-\bar{x}}P_1\left(2+\xi\right)\mathrm{d}\xi\,, \tag{A.123}$$

$$P_2\left(\bar{x},0\right)=-\frac{1}{\pi}\int_0^\infty\sqrt{\frac{2-\bar{x}}{\xi}}\frac{\mathrm{e}^{-\kappa'(\xi+2-\bar{x})}}{\xi+2-\bar{x}}\frac{-\rho U w_0\mathrm{e}^{-\kappa'(2+\xi)}}{\sqrt{\pi\left(\kappa'\beta^2+\mathrm{i}\bar{k}_x\right)(2+\xi)}}\mathrm{d}\xi\,, \tag{A.124}$$

$$P_2\left(\bar{x},0\right)=\frac{\rho U w_0\mathrm{e}^{\kappa'\bar{x}}\mathrm{e}^{-4\kappa'}}{\pi\sqrt{\pi\left(\kappa'\beta^2+\mathrm{i}\bar{k}_x\right)}}\int_0^\infty\sqrt{\frac{2-\bar{x}}{\xi\left(2+\xi\right)}}\frac{\mathrm{e}^{-2\kappa'\xi}}{\xi+2-\bar{x}}\mathrm{d}\xi\,. \tag{A.125}$$

This integral has no analytical solution, so the approximation is made

$$P_2\left(\bar{x},0\right) \approx \frac{\rho U w_0 \mathrm{e}^{\kappa'(\bar{x}-4)}}{\pi\sqrt{\pi\left(\kappa'\beta^2+\mathrm{i}\bar{k}_x\right)}}\int_0^\infty \sqrt{\frac{2-\bar{x}}{2\xi}}\frac{\mathrm{e}^{-2\kappa'\xi}}{\xi+2-\bar{x}}\mathrm{d}\xi\,. \tag{A.126}$$

Now the integral

$$\int_0^\infty \sqrt{\frac{2-\bar{x}}{2\xi}}\frac{\mathrm{e}^{-2\kappa'\xi}}{\xi+2-\bar{x}}\mathrm{d}\xi = \int_0^\infty \sqrt{\frac{X}{\xi}}\frac{\mathrm{e}^{-\mathrm{i}A\xi}}{\xi+X}\mathrm{d}\xi\,, \tag{A.127}$$

if the following coefficients are adopted

$$X = 2-\bar{x} \qquad -\mathrm{i}A\xi = -2\kappa'\xi \qquad A = -2\mathrm{i}\kappa' \tag{A.128}$$

using the results from Gradshteyn we have the relation

$$\int_0^\infty \sqrt{\frac{2-\bar{x}}{2\xi}}\frac{\mathrm{e}^{-2\kappa'\xi}}{\xi+2-\bar{x}}\mathrm{d}\xi = \frac{\pi}{\sqrt{2}}\mathrm{e}^{\mathrm{i}A\bar{x}}\left[1-\frac{\mathrm{e}^{\mathrm{i}\pi/4}}{\sqrt{\pi}}\int_0^{A\bar{x}}\frac{\mathrm{e}^{-\mathrm{i}t}}{\sqrt{t}}\mathrm{d}t\right], \tag{A.129}$$

remembering the complex error function definition

$$\mathrm{erf}\left(Z\right) = \frac{\pi}{\sqrt{\pi}}\int_0^{-\mathrm{i}Z^2}\frac{\mathrm{e}^{-\mathrm{i}t}}{\sqrt{t}}\mathrm{d}t \tag{A.130}$$

it is possible to do the replacement of variables

$$-\mathrm{i}Z^2 = A\bar{x} = -2\mathrm{i}\kappa'\left(2-\bar{x}\right), \tag{A.131}$$

$$Z^2 = 2\kappa'\left(2-\bar{x}\right), Z = \sqrt{2\kappa'\left(2-\bar{x}\right)}\,. \tag{A.132}$$

Finally

$$P_2\left(\bar{x},0\right) = \frac{\rho U w_0 \mathrm{e}^{\kappa'(\bar{x}-4)}}{\pi\sqrt{\pi\left(\kappa'\beta^2+\mathrm{i}\bar{k}_x\right)}}\frac{\pi}{\sqrt{2}}\mathrm{e}^{2\kappa'(2-\bar{x})}\left[1-\mathrm{erf}\left(\sqrt{2\kappa'\left(2-\bar{x}\right)}\right)\right], \tag{A.133}$$

$$P_2\left(\bar{x},0\right) = \frac{\rho U w_0}{\sqrt{2\pi\left(\kappa'\beta^2+\mathrm{i}\bar{k}_x\right)}}\mathrm{e}^{-\kappa'\bar{x}}\left[1-\mathrm{erf}\left(\sqrt{2\kappa'\left(2-\bar{x}\right)}\right)\right]. \tag{A.134}$$

Figure A.3 compares the airfoil pressure jump $P_1(\bar{x},0)$ and $P_2(\bar{x},0)$ for kc varying from 1 to 10 in steps of 1. This Figure shows that, also for the subcritical case, for higher frequencies the scattered pressure concentrates at the leading-edge for P_1 and at the trailing-edge for P_2.

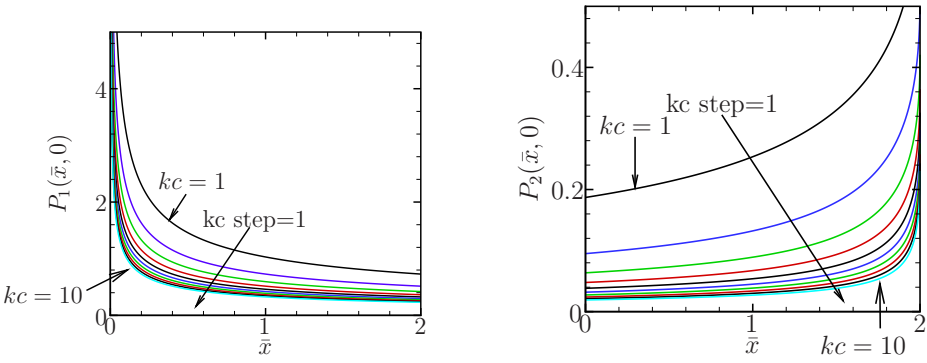

(a) P_1 supercritical (b) P_2 supercritical

Figure A.3: Pressure jump for different kc values varying from 1 to 10 at steps of 1.

A.4.4 Aeroacoustics transfer functions

Remembering that the definition of the transfer function between the incoming gust and the flow potential is written as

$$g\left(\bar{x},k_x,k_y\right)=\frac{p\mathrm{e}^{\mathrm{i}k_y y}\mathrm{e}^{-\mathrm{i}\omega t}}{\pi\rho U w_0}\,, \tag{A.135}$$

we have

$$g_1\left(\bar{x},k_x,k_y\right)=\frac{\exp\left(-\left(\kappa'-\frac{\mathrm{i}\bar{k}_x M^2}{1-M^2}\right)\left(\bar{x}+1\right)\right)}{\pi\sqrt{\pi\left(\kappa'\beta^2+\mathrm{i}\bar{k}_x\right)\left(\bar{x}+1\right)}} \tag{A.136}$$

given the aeroacoustics transfer function

$$\mathcal{L}_1\left(x,y,z,k_x,k_y\right)=\int_{-1}^{1} g\left(\xi,k_x,k_y\right)\mathrm{e}^{-\mathrm{i}\mu\xi(M-x/\sigma)}\mathrm{d}\xi\,, \tag{A.137}$$

we have

$$\mathcal{L}_1\left(x,y,z,k_x,k_y\right)=\frac{1}{\pi\sqrt{\pi\left(\kappa'\beta^2+\mathrm{i}\bar{k}_x\right)}}\int_{-1}^{1}\frac{\mathrm{e}^{-\left(\kappa'-\mathrm{i}\bar{k}_x^* M^2\right)(\xi+1)}}{\sqrt{\xi+1}}\mathrm{e}^{-\mathrm{i}\mu\xi(M-x/\sigma)}\mathrm{d}\xi\,, \tag{A.138}$$

since

$$1=\mathrm{e}^{-\mathrm{i}\mu(M-x/\sigma)}\mathrm{e}^{\mathrm{i}\mu(M-x/\sigma)}\,, \tag{A.139}$$

we can do:

$$\int_{-1}^{1} \frac{\mathrm{e}^{-\left(\kappa'-\mathrm{i}\bar{k}_x^* M^2\right)(\xi+1)}}{\sqrt{\xi+1}} \mathrm{e}^{-\mathrm{i}\mu\xi(M-x/\sigma)} \mathrm{d}\xi = \int_{-1}^{1} \frac{\mathrm{e}^{-\left(\kappa'-\mathrm{i}\bar{k}_x^* M^2\right)(\xi+1)}}{\sqrt{\xi+1}} \tag{A.140}$$

$$\mathrm{e}^{-\mathrm{i}\mu\xi(M-x/\sigma)} \mathrm{e}^{-\mathrm{i}\mu(M-x/\sigma)} \mathrm{e}^{\mathrm{i}\mu(M-x/\sigma)} \mathrm{d}\xi \tag{A.141}$$

$$INT = \mathrm{e}^{\mathrm{i}\mu(M-x/\sigma)} \int_{-1}^{1} \frac{\mathrm{e}^{-\left(\kappa'-\mathrm{i}\bar{k}_x^* M^2\right)(\xi+1)}}{\sqrt{\xi+1}} \mathrm{e}^{-\mathrm{i}\mu(M-x/\sigma)(\xi+1)} \mathrm{d}\xi\,, \tag{A.142}$$

$$INT = \mathrm{e}^{\mathrm{i}\mu(M-x/\sigma)} \int_{-1}^{1} \frac{\mathrm{e}^{-\left(\kappa'-\mathrm{i}\mu x/\sigma\right)(\xi+1)}}{\sqrt{\xi+1}} \mathrm{d}\xi\,, \tag{A.143}$$

$$INT = \mathrm{e}^{\mathrm{i}\mu(M-x/\sigma)} \int_{-1}^{1} \frac{\mathrm{e}^{-\mathrm{i}\left(-\mu x/\sigma-\mathrm{i}\kappa'\right)(\xi+1)}}{\sqrt{\xi+1}} \mathrm{d}\xi\,. \tag{A.144}$$

(A.145)

Defining

$$\theta = -\left(\frac{\mu x}{\sigma} + \mathrm{i}\kappa'\right) \tag{A.146}$$

we have the following relations to be used at the integration by parts

$$\nu = \theta\,(\xi+1) \qquad \xi+1 = \frac{\nu}{\theta} \qquad \mathrm{d}\nu = \theta \mathrm{d}\xi \qquad \mathrm{d}\xi = \frac{d\nu}{\theta}\,, \tag{A.147}$$

$$\xi = -1 \qquad\qquad \nu = 0\,, \tag{A.148}$$

$$\xi = 1 \qquad\qquad \nu = 2\theta\,, \tag{A.149}$$

using these relations the integral INT can be written as:

$$INT = \mathrm{e}^{\mathrm{i}\mu(M-x/\sigma)} \frac{\sqrt{\theta}}{\theta} \int_0^{2\theta} \frac{\mathrm{e}^{-\mathrm{i}\nu}}{\sqrt{\nu}} d\nu\,, \tag{A.150}$$

remembering the complex error function definition

$$\int_0^{-\mathrm{i}Z^2} \frac{\mathrm{e}^{-\mathrm{i}t}}{\sqrt{\mathrm{i}t}} \mathrm{d}t = \frac{\sqrt{\pi}}{\mathrm{e}^{\mathrm{i}\pi/4}} \mathrm{erf}\,(Z)\ , \tag{A.151}$$

with

$$2\theta = -\mathrm{i}Z^2 \qquad Z^2 = 2\mathrm{i}\theta \qquad Z = \sqrt{2\mathrm{i}\theta}\,, \tag{A.152}$$

we have:

$$INT = \mathrm{e}^{\mathrm{i}\mu(M-x/\sigma)}\frac{\sqrt{\theta}}{\theta}\frac{\sqrt{\pi}}{\mathrm{e}^{\mathrm{i}\pi/4}}\mathrm{erf}\left(2\mathrm{i}\theta\right) , \tag{A.153}$$

finally

$$\mathcal{L}_1\left(x,y,z,k_x,k_y\right) = \frac{1}{\pi\sqrt{\left(\kappa'\beta^2+\mathrm{i}\bar{k}_x\right)}}\mathrm{e}^{\mathrm{i}\mu(M-x/\sigma)}\frac{1}{\sqrt{\theta}}\mathrm{e}^{-\mathrm{i}\pi/4}\mathrm{erf}\left(2\mathrm{i}\theta\right) . \tag{A.154}$$

Now to compute the trailing-edge aeroacoustic transfer function we can remember the definition for the transfer function between the airfoil pressure jump and the incoming gust

$$g_2\left(\bar{x},k_x,k_y\right) = \frac{p_2\mathrm{e}^{-\mathrm{i}\omega t}\mathrm{e}^{\mathrm{i}k_y y}}{\pi\rho U w_0} \tag{A.155}$$

To compute $\mathcal{L}_2$ the change of coordination system $X = \bar{x}+1$ is made

$$g_2\left(\bar{x},k_x,k_y\right) = -\frac{\mathrm{e}^{-\left(\kappa'-\mathrm{i}\bar{k}_x^* M^2\right)(\bar{x}+1)}}{\pi\sqrt{2\pi\left(\kappa'\beta^2+\mathrm{i}\bar{k}_x\right)}}\left[1-\mathrm{erf}\left(\sqrt{2\kappa'\left(1-\bar{x}\right)}\right)\right] , \tag{A.156}$$

the aeroacoustic transfer function is computed as

$$\mathcal{L}_2(x,y,z,k_x,k_y) = \int_{-1}^{1} g_2(\xi,k_x,k_y)\mathrm{e}^{-\mathrm{i}\mu(M-x/\sigma)\xi}\mathrm{d}\xi , \tag{A.157}$$

$$= \int_{-1}^{1} -\frac{\mathrm{e}^{-\left(\kappa'-\mathrm{i}\bar{k}_x^* M^2\right)(\xi+1)}}{\pi\sqrt{2\pi\left(\kappa'\beta^2+\mathrm{i}\bar{k}_x\right)}}\left[1-\mathrm{erf}\left(\sqrt{2\kappa'\left(1-\xi\right)}\right)\right]\mathrm{e}^{-\mathrm{i}\mu(M-x/\sigma)\xi}\mathrm{d}\xi , \tag{A.158}$$

remembering that the relation $1 = \mathrm{e}^{-\mathrm{i}\mu(M-x/\sigma)}\mathrm{e}^{\mathrm{i}\mu(M-x/\sigma)}$ is valid

$$\mathcal{L}_2(x,y,z,k_x,k_y) = -\frac{\mathrm{e}^{\mathrm{i}\mu(M-x/\sigma)}}{\pi\sqrt{2\pi\left(\kappa'\beta^2+\mathrm{i}\bar{k}_x\right)}}\int_{-1}^{1}\mathrm{e}^{-\left(\kappa'-i\mu x/\sigma\right)(\xi+1)}\left[1-\mathrm{erf}\left(\sqrt{2\kappa'\left(1-\xi\right)}\right)\right]\mathrm{d}\xi . \tag{A.159}$$

The integral

$$\int_{-1}^{1}\mathrm{e}^{-\left(\kappa'-i\mu x/\sigma\right)(\xi+1)}\left[1-\mathrm{erf}\left(\sqrt{2\kappa'\left(1-\xi\right)}\right)\right]\mathrm{d}\xi , \tag{A.160}$$

should be integrated by parts. Making

$$u = \left[1 - \mathrm{erf}\left(\sqrt{2\kappa'(1-\xi)}\right)\right], \tag{A.161}$$

$$du = -\frac{-\mathrm{e}^{2\kappa'(1-\xi)}}{\sqrt{\pi}} \frac{-2\kappa'}{\sqrt{2\kappa'(1-\xi)}} \mathrm{d}\xi = \frac{2\kappa'}{\sqrt{\pi}} \frac{\mathrm{e}^{-2\kappa'(1-\xi)}}{\sqrt{2\kappa'(1-\xi)}} \mathrm{d}\xi\,, \tag{A.162}$$

$$dv = \mathrm{e}^{-\left(\kappa' - i\mu x/\sigma\right)(\xi+1)} \mathrm{d}\xi\,, \tag{A.163}$$

$$v = -\frac{\mathrm{e}^{-\left(\kappa' - i\mu x/\sigma\right)(\xi+1)}}{(\kappa' - i\mu x/\sigma)}\,, \tag{A.164}$$

and remembering that

$$\mathrm{erf}(x) = \frac{1}{\pi} \int_0^{x^2} \frac{\mathrm{e}^{-t}}{\sqrt{t}} \mathrm{d}t \tag{A.165}$$

$$\frac{\partial(\mathrm{erf}(x))}{\partial x} = \frac{2\mathrm{e}^{-x^2}}{\sqrt{\pi}} \tag{A.166}$$

we have

$$uv = \left[-\left[1 - \mathrm{erf}\left(\sqrt{2\kappa'(1-\xi)}\right)\right] \frac{\mathrm{e}^{-\left(\kappa' - i\mu x/\sigma\right)(\xi+1)}}{(\kappa' - i\mu x/\sigma)}\right]_{-1}^{1} = \tag{A.167}$$

$$-\frac{\mathrm{e}^{-2\left(\kappa' - i\mu x/\sigma\right)}}{(\kappa' - i\mu x/\sigma)} + \frac{\left[1 - \mathrm{erf}\left(\sqrt{4\kappa'}\right)\right]}{(\kappa' - i\mu x/\sigma)}\,, \tag{A.168}$$

and

$$\int_{-1}^{1} v du = \int_{-1}^{1} -\frac{\mathrm{e}^{-\left(\kappa' - i\mu x/\sigma\right)(\xi+1)}}{(\kappa' - i\mu x/\sigma)} \frac{2\kappa'}{\sqrt{\pi}} \frac{\mathrm{e}^{-2\kappa'(1-\xi)}}{\sqrt{2\kappa'(1-\xi)}} \mathrm{d}\xi \tag{A.169}$$

$$= -\sqrt{\frac{2\kappa'}{\pi}} \frac{\mathrm{e}^{-2(\kappa' - i\mu x/\sigma)}}{(\kappa' - i\mu x/\sigma)} \int_{-1}^{1} \frac{\mathrm{e}^{-(\kappa' + i\mu x/\sigma)(1-\xi)}}{\sqrt{1-\xi}} \mathrm{d}\xi \tag{A.170}$$

Making the change of variables

$$t = (\kappa' + i\mu x/\sigma)(1-\xi) \qquad \mathrm{d}t = -(\kappa' + i\mu x/\sigma)\mathrm{d}\xi\,, \tag{A.171}$$

the integral is solved as

$$\int_{-1}^{1} \frac{\mathrm{e}^{-(\kappa'+i\mu x/\sigma)(1-\xi)}}{\sqrt{1-\xi}}\mathrm{d}\xi = \frac{1}{\sqrt{(\kappa'+i\mu x/\sigma)}}\int_{0}^{2(\kappa'+i\mu x/\sigma)} \frac{\mathrm{e}^{-t}}{\sqrt{t}}\mathrm{d}t \tag{A.172}$$

$$= \frac{\sqrt{\pi}}{\sqrt{(\kappa'+i\mu x/\sigma)}}\mathrm{erf}\left(\sqrt{2(\kappa'+i\mu x/\sigma)}\right), \tag{A.173}$$

and in conclusion

$$\mathcal{L}_2(x,y,z,k_x,k_y) = -\frac{\mathrm{e}^{\mathrm{i}\mu(M-x/\sigma)}}{\pi\sqrt{2\pi\left(\kappa'\beta^2+\mathrm{i}\bar{k}_x\right)}}\frac{1}{(\kappa'-i\mu x/\sigma)}$$

$$\left\{\left[1-\mathrm{erf}\left(\sqrt{4\kappa'}\right)\right]-\mathrm{e}^{-2\left(\kappa'-i\mu x/\sigma\right)}+\left(\sqrt{2\kappa'}\frac{\mathrm{e}^{-2(\kappa'-i\mu x/\sigma)}}{\sqrt{(\kappa'+i\mu x/\sigma)}}\mathrm{erf}\left(\sqrt{2(\kappa'+i\mu x/\sigma)}\right)\right)\right\}. \tag{A.174}$$

Figure A.4 compare the directivity patterns for the leading-edge Amiet theory for the subcritical case. This figure compares the amplitude of $\mathcal{L}_1$, $\mathcal{L}_2$ and $\mathcal{L}_1+\mathcal{L}_2$. From this figure it is seen that the trailing-edge back-scattering is more important for the supercritical case than for the subcritical cases. It is seen a very small contribution of the trailing-edge back-scattering for $kc=1$. For higher frequencies the back-scattering is totally negligible. Additionally, for the subcritical case it is seen that the noise scattering has a dipolar directivity pattern independently from the frequency.

A.5 The Schwarzschild theorem

The Schwarzschild theorem was developed to study a problem of the light polarization [60]. The theorem states that the solution for the Helmholtz equation with a set of boundary conditions defined as:

$$\varphi(\bar{x},0) = f(\bar{x}) \qquad \bar{x}\geq 0\,, \tag{A.175}$$

$$\frac{\partial\varphi}{\bar{z}}(\bar{x},0) = 0 \qquad \bar{x}<0\,, \tag{A.176}$$

has solution given by

$$\varphi(\bar{x},0) = \frac{1}{\pi}\int_{0}^{\infty} G(\bar{x},\xi,0)\,f(\xi)\,\mathrm{d}\xi\,, \tag{A.177}$$

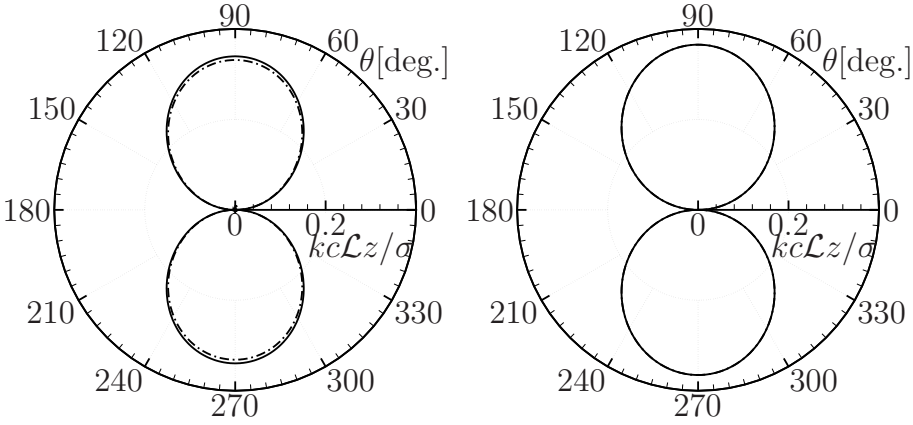

(a) $kc = 1$ (b) $kc = 5$

Figure A.4: Leading-edge Amiet theory aeroacoustic transfer function (ATF) for a subcritical gust. Continous line: $\mathcal{L}_1$; Dash dot line: $\mathcal{L}_1 + \mathcal{L}_2$

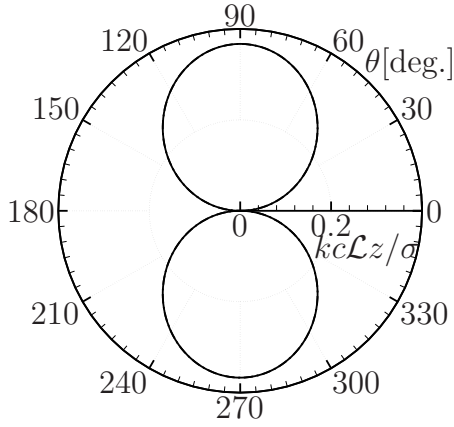

(a) $kc = 10$

Figure A.5: Leading-edge Amiet theory aeroacoustic transfer function (ATF) for a subcritical gust.

where $G(\bar{x}, \xi, 0)$ is the Green's function. The Green's function is defined by the response of the system to an impulsive excitation and, for the present problem, the Green's function for an semi-infinite flat plate is given by:

$$G(\bar{x}, \xi, 0) = \sqrt{\frac{-\bar{x}}{\xi} \frac{\mathrm{e}^{-\mathrm{i}\kappa(\xi-\bar{x})}}{\xi - \bar{x}}} \tag{A.178}$$

A.6 Derivation of complex integrals

On the application of the Schwarzschild theorem the integral below is faced

$$\sqrt{A} \int_0^\infty \frac{1}{\sqrt{x}} \frac{\mathrm{e}^{-\mathrm{i}bx}}{x + A} \mathrm{d}x \,. \tag{A.179}$$

This integral calculation is not straight forward, so this section intends to demonstrate its the derivation from the results presented at the tables of integrals from Gradshteyn and Ryzhik [31]. From Gradshteyn and Ryzhik [31] (ref. pag. 348, item 10) we have

$$\int_0^\infty \frac{x^{\nu-1}\mathrm{e}^{-\mu x}}{x+\beta} dx = \beta^{\nu-1}\mathrm{e}^{\beta\mu}\Gamma(\nu)\Gamma(1-\nu, \beta\mu) \qquad [|arg\beta| < \pi, \quad Re(\mu) > 0, \quad Re(\nu) > 0] \,, \tag{A.180}$$

where arg is the argument (angle) of a complex number and

$$\nu = \frac{1}{2} \qquad \beta = A \qquad \mu = \mathrm{i}b \,. \tag{A.181}$$

Replacing to Eq. A.180 the coefficients corresponding to Eq. A.179 it is obtained

$$\int_0^\infty \frac{x^{-1/2}\mathrm{e}^{-\mathrm{i}bx}}{x + A} = A^{-1/2}\mathrm{e}^{\mathrm{i}A\,b}\Gamma(1/2)\Gamma(1/2, \mathrm{i}A\,b) \tag{A.182}$$

and knowing that $\Gamma(1/2) = \sqrt{\pi}$, according to Gradshteyn and Ryzhik [31] (ref. pag. 899, item 2.11) the incomplete gamma function is written as

$$\Gamma(1/2, iAb) = \int_{\mathrm{i}Ab}^\infty t^{1/2-1}\mathrm{e}^{-t}\mathrm{d}t = \int_{\mathrm{i}Ab}^\infty \frac{e-t}{\sqrt{t}}\mathrm{d}t = \underbrace{\int_0^\infty \frac{\mathrm{e}^{-t}}{\sqrt{t}}}_{\text{Term 1}} - \underbrace{\int_0^{\mathrm{i}Ab} \frac{\mathrm{e}^{-t}}{\sqrt{t}}\mathrm{d}t}_{\text{Term 2}} \tag{A.183}$$

where

Term 1:

$$\int_0^\infty \frac{\mathrm{e}^{-t}}{\sqrt{t}}\mathrm{d}t = \Gamma(1/2) = \sqrt{\pi} \tag{A.184}$$

Term 2:

$$\int_0^{iAb} \frac{\mathrm{e}^{-t_1}}{\sqrt{t_1}} \mathrm{d}t_1 = \int_0^{Ab} \frac{i\mathrm{e}^{-\mathrm{i}t}}{\sqrt{i}\sqrt{t}} \mathrm{d}t = \mathrm{e}^{\mathrm{i}\pi/4} \int_0^{Ab} \frac{\mathrm{e}^{-\mathrm{i}t}}{\sqrt{t}} \mathrm{d}t \tag{A.185}$$

Now replacing the original equation

$$\sqrt{A} \int_0^{\infty} \frac{1}{\sqrt{x}} \frac{\mathrm{e}^{-\mathrm{i}bx}}{x+A} = \sqrt{A} \frac{1}{\sqrt{A}} \mathrm{e}^{\mathrm{i}Ab} \sqrt{\pi} \left(\sqrt{\pi} - \mathrm{e}^{-\mathrm{i}\pi/4} \int_0^{Ab} \frac{\mathrm{e}^{-\mathrm{i}t}}{\sqrt{t}} \right) \tag{A.186}$$

$$= \mathrm{e}^{\mathrm{i}Ab} \pi \left(1 - \frac{\mathrm{e}^{\mathrm{i}\pi/4}}{\sqrt{\pi}} \int_0^{Ab} \frac{\mathrm{e}^{-\mathrm{i}t}}{\sqrt{t}} \mathrm{d}t \right) \tag{A.187}$$

which is directly applicable to the derivation of the Amiet theory.

Appendix B

Experimental facility design

One of the first tasks of this thesis work was the definition of a target experiment. Based on literature survey, it was defined that the most representative testing case that allowed the investigation of a large span of phenomena related to the airfoil noise and was a rod-airfoil configuration. Based on this conclusion, it was decided to design the scaling-down of a testing facility installed at the *École Centrale de Lyon*. This testing facility is extensively described by Casalino [18] and was used for the publication of a rod-airfoil benchmark testing case by Jacob [35].

B.1 Design premises

The first design premise for this project was the test rig localization. Evaluating the available hardware it was defined that the first anechoic chamber built at the *von Kármán Institute for Fluid Dynamics* and described in details by Schram [59] allowed the extensive reuse of previously built parts. For obtaining a maximum flow velocity of 35 m/s, the previous facility demanded the replacement of the original flow generator by a centrifugal fan moved by a 18.5 kW electric engine. The fan replacement also required a new duct to direct the flow from the fan exit into the silencer. The duct system that conducted the flow from the silencer to the anechoic room could be preserved, together with the previous turbulence reduction grids. Finally, it was necessary to design a new jet exit contraction in order to allow the transition from a circular geometry, imposed by previous installations, into a rectangular geometry, desired to this experimental set-up.

Due to the importance of the final contraction geometry to the flow quality more attention to its design was taken. The design procedure was based on analysis of similar solutions present in the literature, followed by application of semi-empirical formulas applicable to the testing case and, finally, CFD RANS analysis of final configurations.

Based on the available fan mass-flow and knowing the pressure drop given by the silencer and duct system, it was defined the basic constraints for the contraction design:

- Jet contraction with rectangular exit measuring $a = 150$ mm by $b = 200$ mm;
- Maximum flow velocity of 35 m/s;
- Design point at 30 m/s;
- Flow with minimum unsteadiness effects at the exit;
- Minimum flow turbulence;
- Maximum velocity uniformity at the exit.

Given the geometric constraint imposed by the 150 mm diameter duct installed downstream the contraction, the final area ratio of 2.35 to 1 was defined to this design.

B.1.1 Baseline profiles

In literature, it exists a limited number of references directly related to a circular-to-rectangular contraction design. In opposition, it exists a reasonable literature regarding the design of circular-to-circular geometries. The literature review showed that the two most successful circular-to-circular contraction profiles are based on the 7^{th} order polynomial and the Lehman polynomial-exponential law [12, 59].

The 7^{th} order polynomial law, applicable for a circular to circular transition is given:

$$\eta(\xi) = \left(-20\xi^3 + 70\xi^2 - 84\xi + 35\right)\xi^4 \tag{B.1}$$

where $\xi = \frac{L-x}{L}$ and $\eta = \frac{y-y_2}{y_1-y_2}$. The Lehman profile is given from the following rule:

$$\frac{D_1}{D_s} = 1 - \frac{D_s - W_s}{D_s} \frac{L_1}{L_1 + L_2} \left(\frac{x_1}{L_1}\right)^3 exp\left[\frac{1}{2}\left(1 - \left(\frac{x_1}{L_1}\right)^2\right)\right] \tag{B.2}$$

$$\frac{D_2}{W_s} = 1 + \frac{D_s - W_s}{W_s} \frac{L_2}{L_1 + L_2} \left(\frac{x_2}{L_2}\right)^3 exp\left[\frac{1}{2}\left(1 - \left(\frac{x_2}{L_2}\right)^2\right)\right] \tag{B.3}$$

where D_s, W_s, L_1, L_2 are defined as indicated in the Fig. B.1:

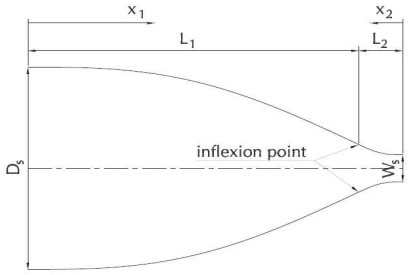

Figure B.1: Lehman polynomial to exponential contraction scheme.

An interesting property of the Lehman profile is the free choice possibility for the profile inflexion point.

Given the limited number of literature references on the design of a rectangular-to-circular transition and the good number references based on the polynomial and Lehman profiles, the initial parametric studies were conducted on circular-to-rectangular transitions with similar contraction area ratio to these profiles.

For the parametric analysis two design parameters was analyzed regarding their impact to the final flow quality: the contraction length and the the inflexion point position. For the contraction length analysis, the 7^{th} order polynomial profile was studied with lengths of $L = 300$ mm, $L = 400$ mm and $L = 500$ mm, where L is the contraction length. The localization of the inflection point analysis was conducted using a $L = 300$ mm length Lehman profile with inflection point localized at 70%, 80% and 90% of its total length.

The contraction area variation from the inlet, $y/L = 0$, to the outlet $y/L = 1$ are presented for the analyzed profiles in Fig. B.2.

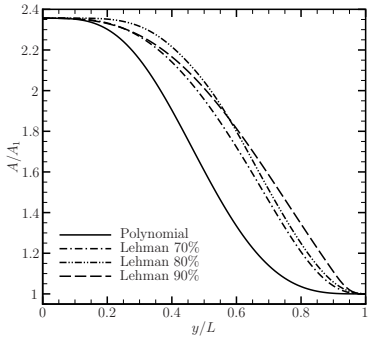

Figure B.2: Contraction profile area variation, where A_1 is the outlet profile area.

From Fig. B.2 it is noticed that the polynomial profile provides a more slow flow acceleration, when compared to the three Lehman profiles analysed here.

B.1.2 Parametric studies

For the parametric studies, a set of RANS simulations was conducted using Fluent. The non-structured mesh was set with resolution enough to guarantee a mean $Y^+ \approx 45$, with boundary layer wall function. The turbulence model chosen was the $k-\epsilon$. The inlet boundary condition was set as a parabolic profile with mass-flow calculated to guarantee average flow velocity at the contraction exit equal to 30 m/s. The inlet turbulence intensity was defined based on measurements results equal to 0.4%. At the outlet, the pressure was defined as the atmospheric pressure.

The outlet flow uniformity

One of the most important flow quality requirements, for contraction profile design, is the velocity uniformity on the exit. Figure B.3 compares the flow profile, measured at contraction exit center line, when the contraction length and the inflection point position is varied.

From Fig. B.3 it is noticed that a longer contraction contributes to reducing the velocity overshoot present at the extremities of the outlet. In addition, it is noticed that localizing the contraction inflection point upstream is advantageous.

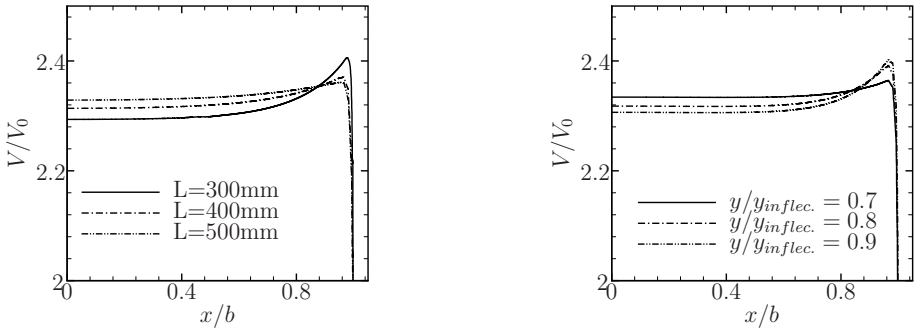

(a) Contraction length (b) Inflection point

Figure B.3: Flow outlet velocity normalized by the inlet velocity.

Intending to quantify the flow non-uniformity (NU) the following relationship was adopted:

$$NU = \frac{u_{max} - u_{CL}}{u_{mean}} \tag{B.4}$$

where u_{max} is the maximum flow velocity, normally localized close to the outlet wall, u_{CL} is the flow velocity of the center of the contraction section and u_{mean} is the mean flow velocity computed along the contraction. Figure B.4 shows the flow non-uniformity metric comparison.

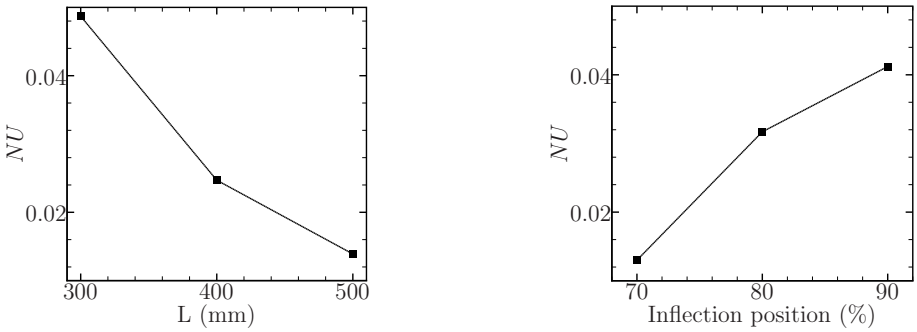

(a) Contraction length (b) Inflection point

Figure B.4: Flow non-uniformity against the contraction length (left) and profile inflection position (right).

From Figs B.3 and B.4 it is noticed that the longer is the contraction, the more time has the flow to accommodate" and the non-uniformity is lower. The same

happen to the inflection point position, the closer is the inflection position to the contraction outlet the higher is the flow non-uniformity.

Boundary layer separation risk

On according to Stratford [62] the turbulent boundary layer separation will occur when the relationship is satisfied:

$$\frac{(n+1)^{(n+1)}(n+2)^{\frac{1}{2}}}{(n-2)^{\frac{n-2}{4}}} C_p^{\frac{n-2}{4}} \left(x \frac{dC_p}{dx} \right)^{\frac{1}{2}} = 11.3217\beta(10^{-6} Re_x)^{\frac{1}{10}} \tag{B.5}$$

where $n = log_{10}Re$ and $\beta = 0.66$ for $d^2C_p/dx^2 < 0$ and 0.73 for $d^2C_p/dx^2 \geq 0$. The distance x represents the curvilinear coordinate along the wall, starting from the constant area section upstream.

It is possible to define the margin of safety as the minimum difference between the left- and right-hand side of Eq. B.5 as [40]:

$$MS = min\{LHS(x) - RHS(x)\} \tag{B.6}$$

where the separation occurs when $MS \leq 0$. Figure B.5 shows the evaluated margin of separation against the contraction length and the inflection point position.

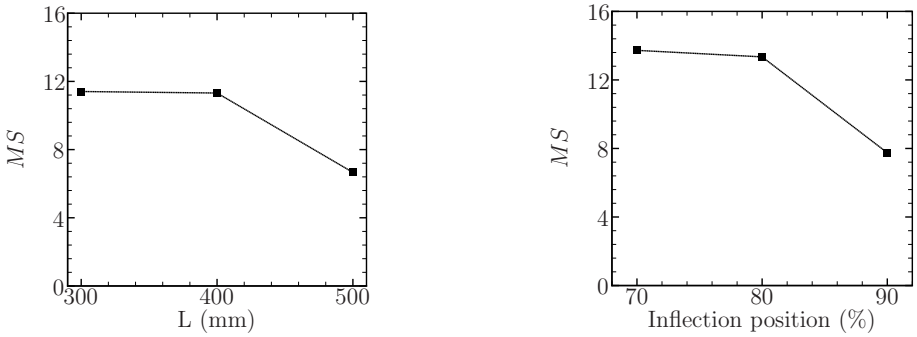

(a) Contraction length

(b) Inflection point

Figure B.5: Margin of separation against the contraction length (left) and against the profile inflection position (right).

From Fig. B.5 it is noticed that the longer is the contraction, the higher is the risk of boundary layer separation. The same trend is present for the inflection

position: the closer is the inflection point from the contraction outlet, the higher is the risk of boundary layer separation.

The boundary layer relaminarization parameter

The positive pressure gradient along the contraction contributes for the flow relaminarization. The boundary layer relaminarization parameter is calculated according the relation [59]:

$$K = \frac{\nu}{U^2}\frac{dU}{dx} \tag{B.7}$$

experimental results shows that the relaminarization occurs when K exceeds 2×10^{-6} [10].

Figure B.6 shows the flow relaminarization parameter evaluated for different contraction lengths and inflection point position locations.

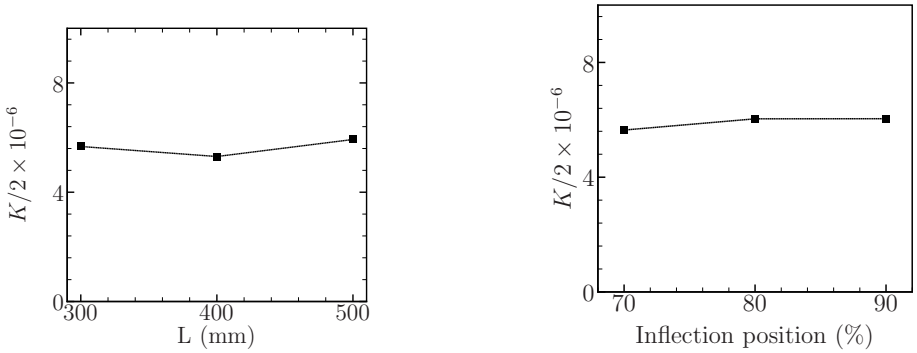

(a) Contraction length

(b) Inflection point

Figure B.6: Relaminarization factor against the contraction length (left) and against the profile inflection position (right).

The boundary layer relaminarization parameter is practically unchanged with the contraction length and the position of the inflection point. This is probably due the fact that the boundary layer relaminarization is more dependent of the inlet to outlet pressure ratio, having small dependence on the pressure gradient evolution along the contraction.

B.1.3 Design optimization phase

The results from the previous parametric analysis served as guidance to a second more complex design phase. During this initial phase, general trends referring the impact of a single parameter change on the metrics adopted to quantify the flow quality was evaluated. In addition, tools able to automatize the mesh generation, RANS computation and data post-processing was developed and served as base for the second design phase.

For the second design phase a multi-disciplinary optimization was conducted using the Matlab Neural Network package together with the software Mode Frontier - a platform essential to handle several independent software (e.g. Matlab, Catia, ICEM, Fluent). In this design phase, the contraction geometry was parametrized in 32 free parameters and this parametrization was implemented in CATIA - tool used for geometry generation and geometrical consistency verification.

Summarizing, the design scheme adopted is present in Fig. B.7:

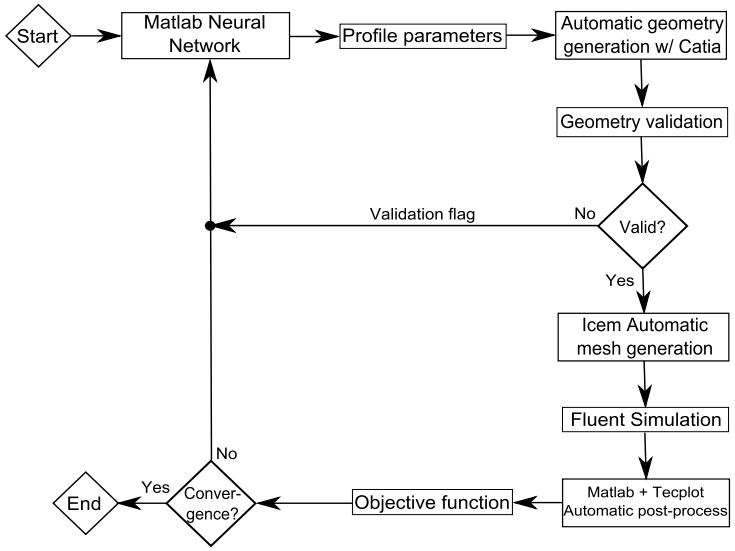

Figure B.7: Multi-disciplinary optimization algorithm used on the contraction profile optimization.

One crucial point for the success of a design optimization is the choice of the objective function. During the implementation of the design algorithm

presented in Fig. B.7 a number of design functions was tested and the final design function found as satisfactory to the present problem was:

$$res = \frac{12}{MS} + \frac{NU}{0.01} + \frac{12 \times 10^{-6}}{K} \tag{B.8}$$

A second imposition found necessary to be imposed during the implementation of the optimization algorithm was the contraction length. During this phase it was found that independently from the contraction length, it was possible to reach a minimum with similar res value. In this way based on construction aspects the length of 300 mm was chosen to the contraction profile.

The optimization algorithm was run for 34 days. After the 31^{th} day of run the solution start to decrease in a rate of less than 1 percentage point per day, after verification, this solution was considered satisfactory and the optimization algorithm was stopped. Finally, the comparison of the flow velocity non-uniformity verified in the designed contraction profile and the baseline testing cases are shown in Fig. B.8.

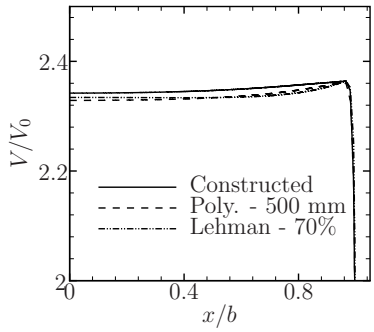

Figure B.8: Flow exit velocity normalized by the inlet flow velocity.

From Fig. B.8 it is noticed that the outlet flow profile is more uniform than the best results of the cases where the length and the inflexion point were tested. In addition, it is noticed that, due the optimization, the final flow velocity is slightly higher than the baseline cases.

Figures B.9 and B.10 compares the parameters adopter for quantification of the outlet flow quality against the baseline cases.

From Fig. B.9 it is remarkable that the optimization algorithm left to an important flow non-uniformity reduction. The optimization also improved the margin of separation, while the relaminarization keeps comparable to

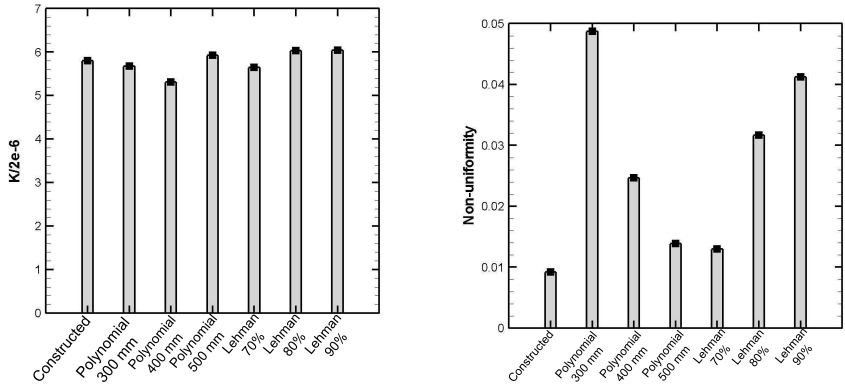

(a) Contraction length (b) Inflection point

Figure B.9: Comparison of the optimized profile against the baseline profiles.

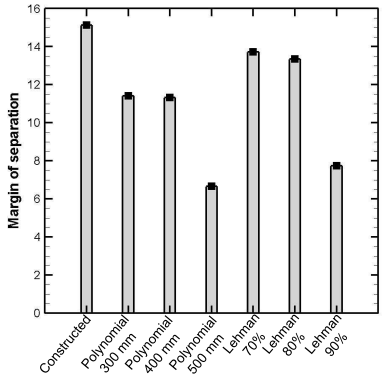

Figure B.10: Comparison of the optimized profile against the baseline profiles.

the reference profiles results. The fact that the relaminarization factor kept comparable to the reference results was already expected since the first design phase showed that this factor is very dependent of the area ratio and but small dependence to the contraction profile was noticed.

Appendix C

Flow velocity measurement procedure and error analysis

The accurate flow velocity measurement is an apparently a simple experimental task which, if not properly treated, leads to meaningful mistakes on further calculations based on this information. Given the importance of the accurate measurement of this flow quantity, this section intends:

1. present the methodology adopted to measure the flow velocity;
2. analyze the uncertainty related to velocity measurements;
3. compare the flow velocity measured by different techniques and verify the accuracy;

C.1 Jet velocity determination procedure

For the mean flow velocity measurement, it is convenient to have a non-intrusive technique to avoid physical interference between the velocity sensor and the testing object. During the development of this research, several solutions have been tested trying to minimize the flow interference, improve the measurements repeatability and robustness to contaminants as PIV seeding, water, dust... The best compromise found was to measure the pressure different across the grid (already used for turbulence reduction) and determine the mean flow velocity through a calibration function. The velocity calibration experimental scheme is shown in Fig. C.1:

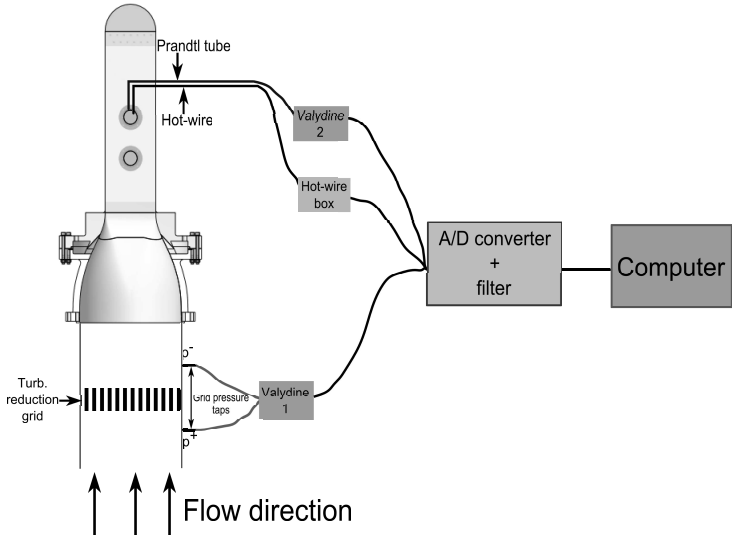

Figure C.1: Experimental scheme adopted for the calibration.

Since the calibration procedure is a boring task, necessary to be systematically repeated (mostly due PIV seeding contamination and environmental variations), a LabVIEW routine was developed to perform this task. In this routine, it is possible to automatically control the rotation of the electric engine that moves the fan, execute data acquisition and post-processing without human interference. Since this procedure is automatized, it is straightforward to calibrate, in-situ, the hot-wire anemometer simultaneously with the determination of the calibration function for the pressure difference across the turbulence reduction grid.

Two different approaches are considered for determining the pressure difference across the grid calibration relation: a first where a non-structured interpolation algorithm is trained with calibration data acquired for the complete envelope of temperature and velocity expected to be present in the actual experiment; a second where a physically inspired model, shown in Eq. C.1, had some parameters calibrated.

$$\begin{aligned} \Delta\, p(U) &= K(U,T)\,\frac{1}{2}\,\rho\, U^2 \\ K(U,T) &= \beta_1\, U^{\beta_2}\, T^{\beta_3} \end{aligned} \tag{C.1}$$

where ρ is the flow density, U_{grid} is the flow velocity at a reference point - for

this work the airfoil leading-edge position, at the center of the jet is chosen as reference point -, T is the flow temperature (in Kelvin) and $\beta_{1,2,3}$ are constants to be obtained by a least-square fit from the calibration. The coefficient K was found to be directly dependent on the flow velocity and temperature. During the experiments, it was noticed that important variations in this coefficient was present after each PIV campaign, due to seeding contamination impossible to be removed. In addition, it was noticed a small, but not negligible, influence of the air humidity due to the rain, dry or snow periods. Due to the physical installation of this testing facility, it is impossible to guarantee dry air supply to the fan. Considering that the derivation of a relationship between the function K and each environmental variable is impractical, it was defined in the experimental procedure to execute a new calibration when important environment changes are noticed. Figure C.2 shows the comparison between the flow velocity measured by the Prandtl tube and the velocity predicted using the formulation of Eq. C.1, the percentage error is given by $100 \times (U_{grid\Delta p} - U_{Prandtl})/U_{Prandtl}$.

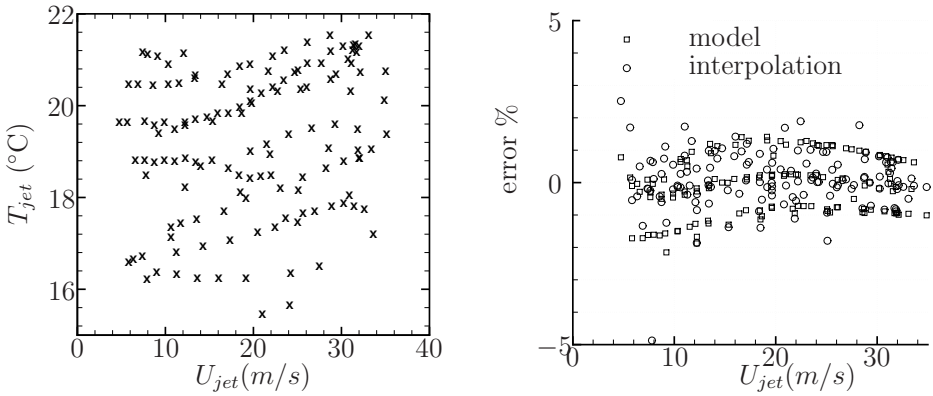

(a) Jet temperature

(b) Calib. error

Figure C.2: Jet calibration function error. Left: jet temperature; Right: calibration error comparison for the cubic non-structured interpolation method and the physicaly inspired model are used to determine the flow velocity.

According to Fig. C.2 the non-structured interpolation gives, in most of the cases, an error smaller than the use of a calibration equation. It is verified that the points where the non-structured interpolation error is larger than the calibration function the algorithm tried to do a data extrapolation. Based on this analysis the routine for flow mean velocity determination used the non-structured interpolation, when enough calibration data was available guarantee

an interpolation otherwise the calibration function was used for the (rare) cases where an interpolation was impossible.

C.1.1 Hot-wire measurement methodology

During the experiments, it was noticed that obtaining repeatable results using hot-wire anemometry is not a straightforward task. In the *von Kármán Institute for Fluid Dynamics* it is usual to adopt in-house hot-wire anemometry systems. There are available systems manufactured in different models and different periods, ranging from 1971 to 1991. For the hot-wire measurements several of these anemometry systems were tested, and some trade-offs had to be made due to system particularities. From the preliminary test campaign it was noticed that the system manufactured in the 70's presented very little electronic noise, being good to measure turbulence spectrum, but they systematically presented a sort of heating problem on the hot-wire temperature compensation system. From the preliminary experimental campaign it was found that the anemometer output voltage was dropping down to zero, after few hours of measurement, independently from the flow velocity, and, after some hours, recovering the previous value if the hot-wire was removed from the flow. This undesirable behavior was verified to 3 systems from this model. While for the anemometer system built in the 90's it was noticed a good measurement repeatability, but with electronic noise high enough to the point to make impossible to measure the turbulence spectrum of laminar flows. Based on this information, it was defined that the measurement of the turbulence spectrum of flows in laminar, or low turbulence, conditions should be made by the anemometer box developed in the 70's, while the anemometer box developed in the 90's was used for measurements of average velocities and turbulence spectrum of flows with velocity fluctuation high enough to guarantee good signal-to-noise-ratio.

A second important issue found in the preliminary test campaign was the temperature drift effect. This testing facility temperature drift was originally considered to be small enough to jeopardize the accuracy of the measurements was shown to be high enough to result in inconsistent results on flow velocity profile measurements. This problem motivated the use of a temperature compensation formulation. A third important issue found during the preliminary testing campaign is related to the traditional hot-wire calibration methodology adopted in the *von Kármán Institute for Fluid Dynamics*. This methodology uses a dedicated calibrator supplied by compressed air. It was noticed that the temperature difference between the calibrator flow and the actual facility flow temperature was, sometimes, higher than 15°C. Given that the control of the calibrator flow temperature is a cumbersome task an in-situ

calibration approach was adopted. For convenience, the hot-wire calibration routine was introduced into the automatic routine for the determination of the pressure difference across the grid, with experimental set-up presented in Fig. C.1.

This work used the temperature compensation model proposed by Bruun [17] (ref. pag. 215) given by equation:

$$E_{w,r} = E_w \left(\frac{T_w - T_a}{T_w - T_{a,r}} \right)^{-0.5} \tag{C.2}$$

where E_w is the Wheatstone bridge imbalance voltage - the anemometer measured voltage, $E_{w,r}$ is the reference imbalanced voltage, T_w is the hot-wire temperature, T_a is the flow temperature and $T_{a,r}$ is the ambient reference temperature. For this experimental campaign, the ambient reference temperature $T_{a,r}$ was chosen as the average value of the flow temperature measured during the calibration procedure.

To evaluate the most adequate calibration model to the available instrumentation, the King's law - given by Eq. C.3 - and a third order polynomial was used to relate the flow velocity and the hot-wire output voltage.

$$E^2(U) = A + BU^n \tag{C.3}$$

The King's law is a physically inspired model for the hot-wire's Wheatstone bridge imbalance voltage E, as a function of the flow velocity. In this model A and B are calibrations constants, U is the flow velocity and n is an exponent, which from the theory, should value 0.5. Bruun [17] analyzes that the coefficient $n = 0.5$ is defined supposing that the hot-wire length is infinite, but, due to the finite length and installation effects, Bruun recommends this constant to be changed to 0.45.

To analyze the error made by using the third order polynomial interpolation formula or the King's law with exponents 0.45 or 0.5, with and without temperature compensation, Fig. C.3 is presented. In this figure the flow velocity was varied up to 10℃– variation higher than the present in a typical experiment –, and the flow velocity measured by the hot-wire was compared with the Prandtl tube reference velocity, and, the relative percent difference $(100 \times (U_{hot-wire} - U_{Prandtl})/U_{Prandtl})$ is compared.

From Fig. C.3 it is noticed, first, that the temperature correction significantly improves the calibration accuracy, and, second, the King's law with $n = 0.45$ best fits to the experimental data. In addition, it is verified that all calibration models, with and without temperature correction, significantly fails to predict small flow velocities. Tests showed that if the velocity range of the calibration

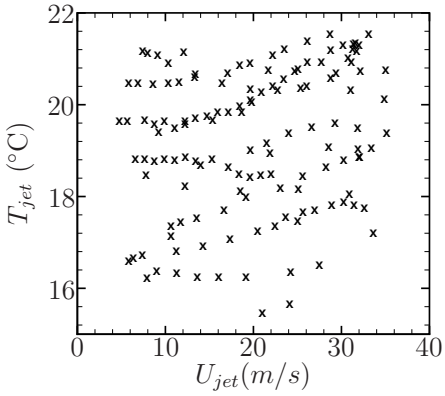

(a) Jet temperature

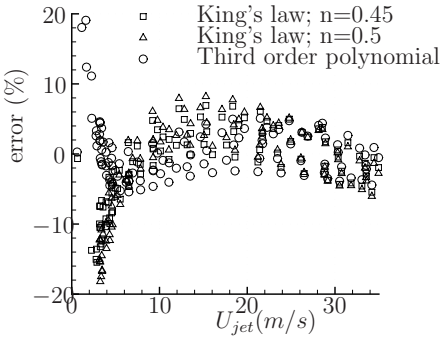

(b) Calib. error – no temp. correction

Figure C.3: Hot-wire calibration error analysis. Left: jet temperature; Right: error when no temperature correction is considered; Right: error when the temperature correction is considered.

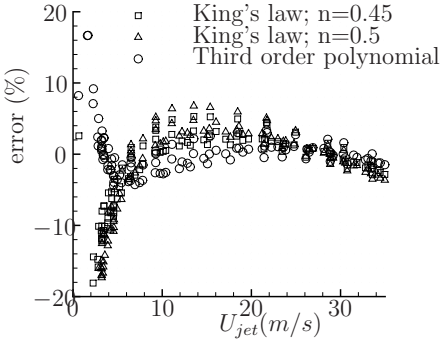

(a) Calib. error - with temp. correction

Figure C.4: Hot-wire calibration error analysis. Error when the temperature correction is considered.

reduces from 0 to 5 m/s, it is possible to find a good agreement between the experimental data and the King's law with $n = 0.45$, but if the velocity calibration ranges from 0 to 35 m/s it is difficult to have a calibration curve that fits well the small and the large velocities. Considering that the present experiment is not interested in such small flow velocities, no further attention was given to this issue.

An additional information obtained from this analysis refers to the cases where the temperature correction was applied. In this analysis, it is obtained the wire temperature of 620 K for King's law with $n = 0.45$, 611 K for King's law with $n = 0.5$ and 630 K to the polynomial calibration. It is important to notice that this temperature does not relate, directly, with the overheating ration. On according to Bruun [17] (ref. pag. 33) the overheating ratio is defined as R_w/R_a, where R_w is the wire resistance after being heated and R_a is the wire resistance at ambient temperature.

C.1.2 Valydine calibration stability

During this experimental campaign, it was noticed that few days after the valydine calibration it was very difficult to measure a velocity (pressure) close to zero. Since low velocity measurements are, in principal, important for the hot-wire and pressure across the grid calibration and considering that the repeated valydine calibration is a cumbersome task, some investigation about how to improve the robustness of the valydine calibration procedure was executed. As schematized in Fig. C.1, during this experimental campaign the 2 valydine type pressure transducer was adopted. This kind of pressure transducer gives a linear relation between the pressure difference imposed to its terminals and the output voltage, expressed as:

$$\Delta p = \alpha_1 V + \alpha_2 \tag{C.4}$$

where $\alpha_{1,2}$ are calibration coefficients, V is the transducer output voltage and Δp is the pressure difference imposed to the valydine terminals - which is normally determined using a water manometer as reference.

From this investigation it was noticed that the valydine has, a daily, fluctuation of the zero coefficient (α_2), while the coefficient α_1 only fluctuated significantly when the valydine box was, for some reason, turned off and on. From this investigation, the present work added to the automatic calibration procedure a routine for obtaining the coefficient α_2, measured at the beginning and the end of each working day. This procedure has been verified at the time and showed to be very robust increasing the precision of the whole calibration procedure. Since this procedure was automatized, it allowed verifying, for a large period,

the variation of the calibration coefficients for the two valydines adopted in this work. Figure C.5 shows the calibration coefficients variation along the period of time with available information.

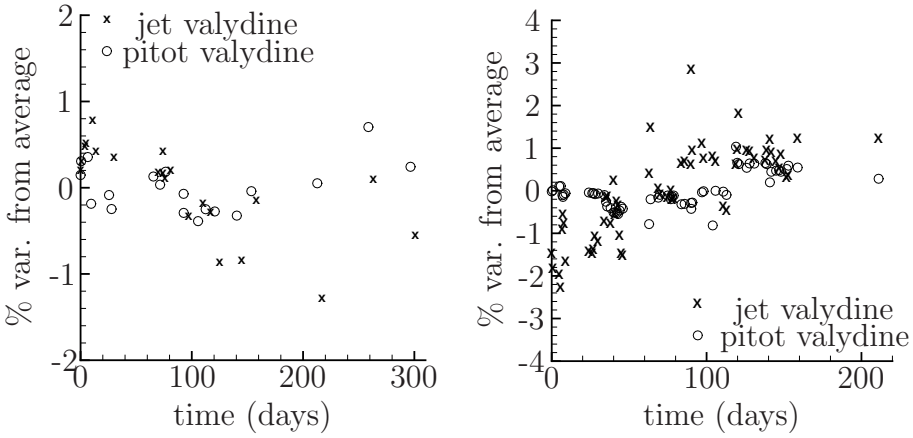

(a) Daily fluctuation for the coefficient α_1.

(b) Daily fluctuation for the coefficientα_2.

Figure C.5: Valydine calibration angular coefficient (α_1) and zero (α_2) fluctuation along the time. The first day with information available for the coefficient α_1 is 06/02/2014 and for the coefficient α_2 is 21/05/2014.

From the Fig. C.5 it is seen that the coefficient α_1 has a variation form the average of less that $\pm 1.5\%$ along a period of approximately 300 days, what can be considered as an excellent performance, and, the coefficient α_2 has a variation, from the average, of approximately $\pm 3\%$. Since this variation some time occurs from one day to the next, some inconsistent measurements, at low flow velocities, may occur.

Appendix D

Rig temperature characterization

D.1 Flow temperature stability

A concern regarding this test rig was the flow temperature stability characteristics. In this facility three main mechanism contribute to the flow temperature raise:

- the air flow compression in the radial fan;
- the flow friction in the acoustic maze;
- the flow friction in the turbulence reduction grids.

Avoid these problems is impractical and since it was noticed that the flow temperature did not raise to unacceptable values, the approach adopted in this work was to measure the temperature variation with time to know for how long should the facility run before starting any experiment. In this verification the electric engine control system was set to keep the fan rotational speed constant and the flow temperature was acquired by a thermocouple. The temperature variation along three hours measurement is shown in Fig. D.1.

From Fig. D.1 it is noticed that the larger temperature variation occurs for the higher flow velocity and that the flow temperature varies approximately 5 ℃reaching a approximately constant value after 90 minutes with the facility

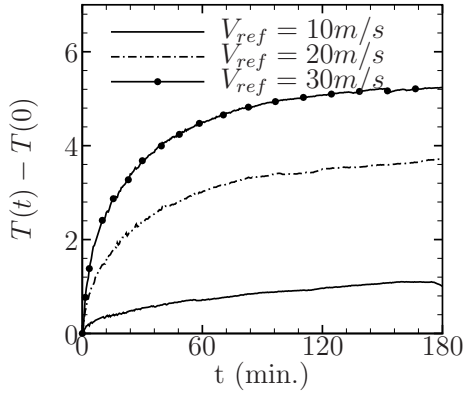

Figure D.1: Flow temperature variation with time.

running. For lower velocities it is seen that the temperature variation is smaller and that the time to reach an stable temperature is smaller. The major conclusion from this study is that, for good accuracy of results, measurements could not be done immediately after starting to run the facility, but some warm-up time should be respected.

In addition to the temperature stability analysis, this test allowed to simultaneously verify the accuracy of the methodology developed to measure the flow velocity (see appendix C). Simultaneously with the temperature measurements the flow velocity was measured by the Pradtl tube, a hot-wire anemometer and by the pressure difference across the turbulence reduction grid. The results comparison are shown in Fig. D.1.

Figure D.2 shows the good agreement of the measured velocity by the three different techniques. As verified, the differences between the measured velocities and the reference values are within the tolerance discussed in Appendix C. In addition, this measurement showed that the recurrent problem presented by the hot-wire anemometer system of voltage decay with time (uncorrelated with the flow velocity) was not present when a more modern system is used.

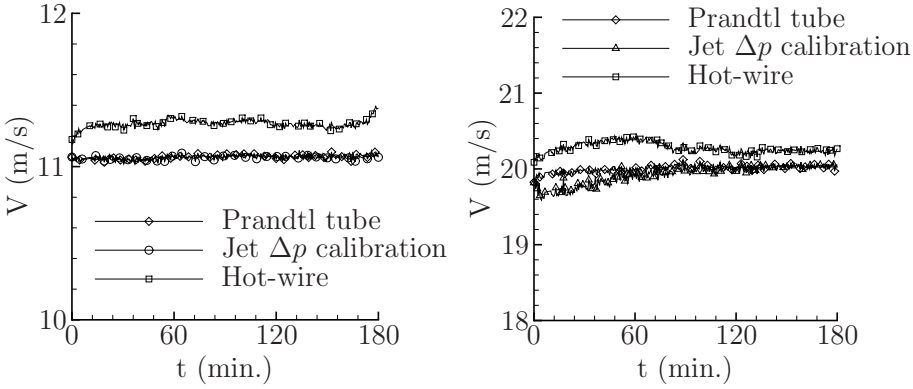

(a) $V_{ref} = 10m/s$ (b) $V_{ref} = 20m/s$

Figure D.2: Velocity fluctuation with time.

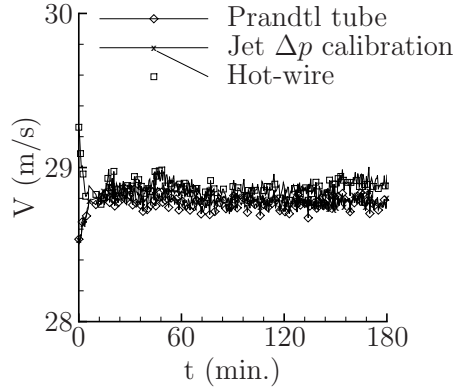

(a) $V_{ref} = 30m/s$

Figure D.3: Velocity fluctuation with time.

Appendix E

Review of the flow correlations for isotropic turbulence

This section reviews the most important definition of flow correlations, turbulence energy spectra and its respective formulas, valid for isotropic turbulence.

Considering a coordinate system where the instantaneous flow velocity (U, V, W) can be decomposed into mean and perturbation component as:

$$(U, V, W) = (\overline{U}, \overline{V}, \overline{W}) + (u, v, w) \tag{E.1}$$

where $(\overline{U}, \overline{V}, \overline{W})$ are time-averaged flow velocity components. It is possible to write the root-mean-square flow velocity fluctuation component as:

$$(u', v', w') = \left(\sqrt{\overline{(u - \overline{u})^2}}, \sqrt{\overline{(v - \overline{v})^2}}, \sqrt{\overline{(w - \overline{w})^2}} \right) \tag{E.2}$$

with this definition it is possible to write the flow longitudinal and traverse space correlation, respectively, $f(x)$ and $g(x)$ as:

$$f(x) = \frac{\overline{u(\xi)u(\xi + x)}}{u'(\xi)u'(\xi + x)} \tag{E.3}$$

$$g(x) = \frac{\overline{v(\xi)v(\xi + x)}}{v'(\xi)v'(\xi + x)} \tag{E.4}$$

and similarly, the time correlation:

$$R_E(t) = \frac{\overline{u(\tau)u(\tau+t)}}{u'(\tau)u'(\tau+t)} \tag{E.5}$$

$$T_E(t) = \frac{\overline{v(\tau)v(\tau+t)}}{v'(\tau)v'(\tau+t)} \tag{E.6}$$

The longitudinal and traverse integral correlation length are defined as:

$$\Lambda_f = \int_0^\infty f(x)\mathrm{d}x \qquad \Lambda_g = \int_0^\infty g(x)\mathrm{d}x \tag{E.7}$$

and, similarly, the integral time correlation scale are defined as:

$$T_E = \int_0^\infty R_E(t)\mathrm{d}t \qquad T_L = \int_0^\infty R_L(t)\mathrm{d}t \tag{E.8}$$

Using a single hot-wire anemometer, it is, generally, only possible to measure time correlations. Considering the flow velocity uniform within the correlation length, the Taylor hypothesis can be applied. In practice, this hypothesis is instrumental to relate time correlation with space correlation, and is given by:

$$\Lambda_f = \overline{U}T_E \qquad \Lambda_g = v'T_L \tag{E.9}$$

According to Hinze [33] (ref. Eq. 3-75), a very important relation exist between Λ_f and Λ_g for isotropic turbulence:

$$\Lambda_f = 2\Lambda_g \tag{E.10}$$

For isotropic turbulence, the two most relevant models for the spatial correlation are the Liepman and the von Kármán models given:

$$f(x) = \mathrm{e}^{(-x/\Lambda_f)} \tag{E.11}$$

$$g(x) = \left(1 - \frac{x}{\Lambda_f}\right)\mathrm{e}^{(-x/\Lambda_f)} \tag{E.12}$$

$$f(x) = \frac{2^{2/3}}{\Gamma(1/3)}(k_e x)^{1/3} K_{1/3}(k_e x) \tag{E.13}$$

$$g(x) = \frac{2^{2/3}}{\Gamma(1/3)}(k_e x)^{1/3}\left[K_{1/3}(k_e x) - \frac{k_e x}{2}K_{-2/3}(k_e x)\right] \tag{E.14}$$

The flow turbulence energy power-spectral density relates with the longitudinal and traverse correlation as:

$$\Phi_{uu}(f) = \frac{4u'}{\overline{U}} \int_0^\infty f(x)\cos(k_x x)\mathrm{d}x = 4u' \int_0^\infty R_E(t)\cos(\omega t)\mathrm{d}t \tag{E.15}$$

$$\Phi_{vv}(f) = \frac{4u'}{\overline{U}} \int_0^\infty g(x)\cos(k_x x)\mathrm{d}x = 4u' \int_0^\infty T_E(t)\cos(\omega t)\mathrm{d}t \tag{E.16}$$

since the flow power spectral density is, generally, defined in terms of k_x the following relation is useful:

$$\Phi_{uu}(k_x) = \frac{\overline{U}}{2\pi}\Phi_{uu}(f) \tag{E.17}$$

$$\Phi_{vv}(k_x) = \frac{\overline{U}}{2\pi}\Phi_{vv}(f) \tag{E.18}$$

According to Hinze [33] (ref. Eq. 3.155) and Paterson and Amiet [49] (ref. Eq. D4 and Figure 6) the longitudinal and traverse turbulence energy spectrum, accordingly to von Kármán, is given by:

$$\Phi_{uu}(k_x) = \frac{2}{\sqrt{\pi}}\frac{\Gamma(5/6)}{\Gamma(1/3)}\frac{\overline{u^2}}{k_e}\left[1+\left(\frac{k_x}{k_e}\right)^2\right]^{-5/6} \tag{E.19}$$

$$\Phi_{ww}(k_x) = \frac{\overline{u^2}\Lambda_f}{2\pi}\frac{1+8/3(k_x/k_e)^2}{\left(1+(k_x/k_e)^2\right)^{11/6}} \tag{E.20}$$

and accordingly to Liepman, these relations are given as:

$$\Phi_{uu}(k_x) = \frac{2}{\sqrt{\pi}}\frac{\Gamma(5/6)}{\Gamma(1/3)}\frac{\overline{u^2}}{k_e}\left(1+\frac{9k_x^2}{16k_e^2}\right)^{-1} \tag{E.21}$$

$$\Phi_{ww}(k_x) = \frac{\overline{u^2}\Lambda_f}{2\pi}\frac{1+27/16(k_x/k_e)^2}{\left(1+9/16(k_x/k_e)^2\right)^2} \tag{E.22}$$

where k_e is the average wavenumber of the energy-containing eddies, given by:

$$k_e = \frac{\sqrt{\pi}}{\Lambda_f}\frac{\Gamma(5/6)}{\Gamma(1/3)} \approx \frac{3}{4}\frac{1}{\Lambda_f} \tag{E.23}$$

Appendix F

Stereo-PIV signal-to-noise ratio

The conclusions regarding the presence of the turbulence distortion, presented in Chapter 4, are only valid if it is possible to guarantee that the data is stereo-PIV data is acquired with enough quality. In chapter 3 an overall presentation of the stereo-PIV acquisition and post-processing parameter has been presented. Here one more detail is observed. One important metric which defines the signal-to-noise-ratio is the proportion between the first and the second highest stereo-PIV correlation window peak. In this work the minimum ratio between those peaks to validate a vector has been set to 1.5. Figure F.1 shows the variation of the peak ratio along the line x at $y = 0$ and Fig. F.2 shows the variation of this quantity along the y line for different x positions.

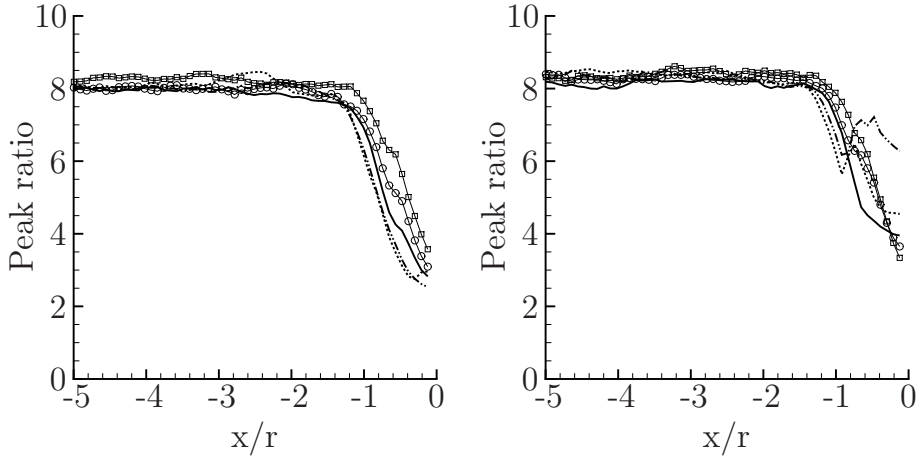

(a) Grid # 1 (b) Grid # 2

Figure F.1: Stereo-PIV signal to noise ratio along the x line at $y = 0$.

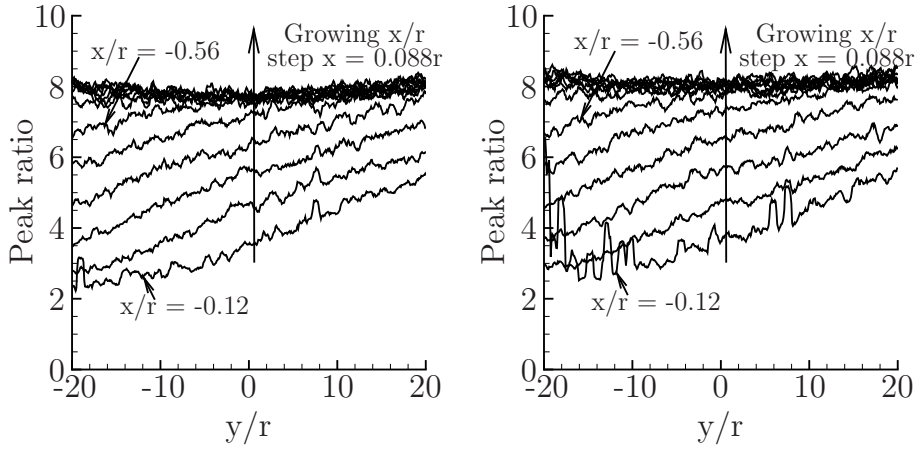

(a) Grid # 1 (b) Grid # 2

Figure F.2: Stereo-PIV signal to noise ratio along the y line for different x positions.

Bibliography

[1] Abramowitz, M., and Stegun, I. A., Eds. *Handbook of Mathematical Functions*, 9^{th} ed. United States Department of Commerce, 1964.

[2] Adamczyk, J. J. The passage of an infinite swept airfoil through an oblique gust. Tech. rep., National Aeronautics And Space Administration, 1974.

[3] Amiet, R. Acoustic radiation from an airfoil in a turbulent stream. *Journal of Sound and Vibration 41*, 4 (1975), 407 – 420.

[4] Amiet, R. Airfoil gust response and the sound produced by airfoil-vortex interaction. *Journal of Sound and Vibration 107*, 3 (1986), 487 – 506.

[5] Amiet, R. K. Compressibility effects in unsteady thin-airfoil theory. *AIAA Journal 12* (1974), 252–255.

[6] Amiet, R. K. High frequency thin-airfoil theory for subsonic flow. *AIAA Journal 14*, 8 (1976), 1076–1082.

[7] Amiet, R. K. Noise due to turbulent flow past a trailing edge. *Journal of Sound and Vibration 47*, 3 (1976), 387 – 393.

[8] Amiet, R. K. Effect of the incident surface pressure field on noise due to turbulent flow past a trailing edge. *Journal of Sound and Vibration 57*, 2 (1978), 305 – 306.

[9] Atassi, H. M. The sears problem for a lifting airfoil revisited - new results. *Journal of Fluid Mechanics 141* (1984), 109–122.

[10] Back, L. H., Cuffel, R. F., Massier, P. F., Mcintyre, T. J., Houwing, A. F. P., Palma, P. C., Rabbath, P. A. B., and Fox, J. S. Laminarization of a turbulent boundary layer in nozzle flow. *AIAA Journal 7* (1969), 730–733.

[11] Batchelor, G. K., and Proudman, I. The effect of rapid distortion of a fluid in turbulent motion. *The Quarterly Journal of Mechanics and Applied Mathematics 7*, 1 (1954), 83–103.

[12] Bottin, B. From subsonic to continuous supersonic wind tunnels: similarity laws, tunnel types and components, design considerations. Tech. rep., von Karman Institute for Fluid Dynamics, 1998.

[13] Brooks, T. Trailing edge noise prediction using Amiet's method. *Journal of Sound and Vibration 77*, 3 (1981), 437 – 439.

[14] Brooks, T., and Hodgson, T. Trailing edge noise prediction from measured surface pressures. *Journal of Sound and Vibration 78*, 1 (1981), 69 – 117.

[15] Brooks, T., and Marcolini, M. Airfoil self noise - effect of scale. In *AlAA 8^{th} Aeroacoustics Conference* (1983).

[16] Brooks, T. F., Pope, S. D., and Marcolini, M. A. Airfoil self-noise and prediction. Tech. rep., NASA - Langley Research Center, 1989.

[17] Bruun, H. H. *Hot-wire anemometry - Principles and Signal Analysis*. Oxford Science Publications, 1995.

[18] Casalino, D. *Analytical And Numerical Methods In Vortex-body Aeroacoustics*. PhD thesis, Politecnico Di Torino And l'Ecole Centrale De Lyon, 2002.

[19] Christophe, J. *Application of Hybrid Methods to High Frequency Aeroacoustics*. PhD thesis, von Karman Institute for Fluid Dynamics, 2011.

[20] Christophe, J., Anthoine, J., and Moreau, S. Amiet's theory in spanwise-varying flow conditions. *AIAA JOURNAL 47*, 3 (March 2009), 788 – 790.

[21] Christophe, J., Anthoine, J., and Moreau, S. Trailing edge noise of a controlled-diffusion airfoil at moderate and high angle of attack. In 15^{th} *AIAA/CEAS Aeroacoustics Conference (*30^{th} *AIAA Aeroacoustics Conference)* (2009).

[22] Christophe, J., Anthoine, J., Rambaud, P., Schram, C., and Moreau, S. Prediction of incoming turbulent noise using a combined numerical / semi-empirical method and experimental validation. In *WEST-EAST HIGH SPEED FLOW FIELD CONFERENCE* (2007).

[23] Curle, N. The influence of solid boundaries upon aerodynamic sound. *Proceedings of the Royal Society of London. Series A, Mathematical and Physical Sciences 231*, 1187 (1955), pp. 505–514.

[24] Devenport, W. J., Staubs, J. K., and Glegg, S. A. Sound radiation from real airfoils in turbulence. *Journal of Sound and Vibration 329*, 17 (2010), 3470 – 3483.

[25] Dobruszkes, F., Decroly, J.-M., and Sotiaux, A. Analyse ex post des nouvelles procédures aériennes mises en service le 6 février 2014 dans la région métropolitaine bruxelloise. Tech. rep., Université Libre de Bruxelles, 2014.

[26] Glegg, S. A., and Devenport, W. Unsteady loading on an airfoil of arbitrary thickness. *Journal of Sound and Vibration 319*, 3-5 (2009), 1252 – 1270.

[27] Glegg, S. A., Devenport, W., and Alexander, N. Broadband rotor noise predictions using a time domain approach. *Journal of Sound and Vibration 335* (2015), 115–124.

[28] Glegg, S. A., and Devenport, W. J. Panel methods for airfoils in turbulent flow. *Journal of Sound and Vibration 329*, 18 (2010), 3709 – 3720.

[29] Goldstein, M. E. *Aeroacoustics*. McGraw-Hill International Book Company, 1976.

[30] Grace, S. M. Unsteady blade response: The bvi model vs. the gust model. In 7^{th} *AIAA/CEAS Aeroacoustics Conference* (2001).

[31] Gradshteyn, I. S., and Ryzhik's, I. M. *Table of Integrals, Series, and Products*, 7^{th} ed. Academic Press, 2007.

[32] Graham, J. M. R. Similarity rules for thin aerofoils in non-stationary subsonic flows. *Journal of Fluid Mechanics 43* (1970), 753–766.

[33] Hinze, J. O. *Turbulence*. McGraw-Hill, 1975.

[34] Hunt, J. C. R. A theory of turbulent flow round two-dimensional bluff bodies. *Journal of Fluid Mechanics 61* (1973), 625 – 706.

[35] Jacob, M. C., Boudet, J., Casalino, D., and Michard, M. A rod-airfoil experiment as a benchmark for broadband noise modeling. *Theoretical and Computational Fluid Dynamics 19* (2005), 171–196. 10.1007/s00162-004-0108-6.

[36] Kucukcoskun, K., Christophe, J., Schram, C., and Anthoine, J. An extension of Amiet's theory for spanwise-varying incident turbulence and broadband noise scattering using a boundary element method. In 16^{th} *AIAA/CEAS Aeroacoustics Conference* (2010).

[37] Lighthill, M. J. On sound generated aerodynamically. i. general theory. *Proceedings of the Royal Society of London. Series A, Mathematical and Physical Sciences 211*, 1107 (1952), pp. 564–587.

[38] Lighthill, M. J. On sound generated aerodynamically. ii. turbulence as a source of sound. *Proceedings of the Royal Society of London. Series A, Mathematical and Physical Sciences 222*, 1148 (1954), pp. 1–32.

[39] Migliore, P., and Oerlemans, S. Wind tunnel aeroacoustic tests of six airfoils for use on small wind turbines. Tech. Rep. NREL/CP-500-35090, National Renewable Energy Laboratory, 2003.

[40] Mikhail, M. N. Optimum design of wind tunnel contractions. *AIAA Journal 17*, 5 (1979), 471–477.

[41] Mish, P. F. *Mean Loading and Turbulence Scale Effects on the Surface Pressure Fluctuations Occurring on a NACA 0015 Airfoil Immersed in Grid Generated Turbulence*. PhD thesis, Virginia Polytechnic Institute and State University, 2001.

[42] Mish, P. F. *An Experimental Investigation Of Unsteady Surface Pressure On An Airfoil In Turbulence*. PhD thesis, Virginia Tech, 2003.

[43] Mish, P. F., and Devenport, W. J. An experimental investigation of unsteady surface pressure on an airfoil in turbulence part 1: Effects of mean loading. *Journal of Sound and Vibration 296*, 3 (2006), 417 – 446.

[44] Mish, P. F., and Devenport, W. J. An experimental investigation of unsteady surface pressure on an airfoil in turbulence part 2: Sources and prediction of mean loading effects. *Journal of Sound and Vibration 296*, 3 (2006), 447 – 460.

[45] Moreau, S., Christophe, J., and Roger, M. LES of the trailing-edge flow and noise of a NACA-0012 airfoil near stall. In *Center for Turbulence Research Proceedings of the Summer Program 2008* (2008).

[46] Moreau, S., and Roger, M. Back-scattering correction and further extensions of amiet's trailing-edge noise model. part II: Application. *Journal of Sound and Vibration 323*, 1-2 (2009), 397 – 425.

[47] Moreau, S., Roger, M., and Jurdic, V. Effect of angle of attack and airfoil shape on turbulence-interaction noise. In 11^{th} *AIAA/CEAS Aeroacoustics Conference (*26^{th} *AIAA Aeroacoustics Conference)* (2005).

[48] Osborne, C. Unsteady thin-airfoil theory for subsonic flow. *AIAA Journal 11* (1973), 205–209.

[49] Paterson, R. W., and Amiet, R. K. Acoustic radiation and surface pressure characteristics of an airfoil due to incident turbulence. Tech. rep., National Aeronautics And Space Administration, 1976.

[50] Paterson, R. W., and Amiet, R. K. Noise and surface pressure response of an airfoil to incident turbulence. *Journal of Aircraft 14*, 8 (1977), 729–136.

[51] Paterson, R. W., and Amiet, R. K. Noise of a model helicopter rotor due to ingestion of turbulence. Tech. rep., NASA, 1979.

[52] Remmler, S., Christophe, J., Anthoine, J., and Moreau, S. Computation of wall pressure spectra from steady flow data for noise prediction. *AIAA Journal 48*, 9 (2010), 1997–2007.

[53] Rienstra, S., and Hirschberg, A. *An Introduction to Acoustics*. Eindhoven University of Technology, 2012.

[54] Roger, M. On broadband jet-ring interaction noise and aerofoil turbulence-interaction noise predictions. *Journal of Fluid Mechanics 653* (2010), 337–364.

[55] Roger, M., and Moreau, S. Back-scattering correction and further extensions of amiet's trailing-edge noise model. part 1: theory. *Journal of Sound and Vibration 286*, 3 (2005), 477 – 506.

[56] Roger, M., and Moreau, S. Extensions and limitations of analytical airfoil broadband noise models. *International Journal of Aeroacoustics, 9* (2010), 273–305.

[57] Roger, M., Schram, C., and Moreau, S. On vortex-airfoil interaction noise including span-end effects, with application to open-rotor aeroacoustics. *Journal of Sound and Vibration 333* (2013), 283–306.

[58] Rozenberg, Y. *Modélisation Analytique du Bruit Aérodynamique à Large Bande des Machines Tournantes: Utilisation de Calculs Moyennés de Mécanique des Fluides*. PhD thesis, École Centrale De Lyon, 2007.

[59] Schram, C. *Aeroacoustics of Subsonic Jets: Prediction of the Sound Produced by Vortex Pairing Based on Particle Image Velocimetry*. PhD thesis, Technische Universiteit Eindhoven, 2003.

[60] Schwarzschild, K. Die Beugung und Polarisation des Lichts durch einen Spalt. I. *Mathematische Annalen 55*, 2 (1901), 177–247.

[61] Sears, W. R. *A systematic presentation of the theory of thin airfoils in non-uniform motion*. PhD thesis, California Institute of Technology, 1938.

[62] Stratford, B. S. The prediction of separation of the turbulent boundary layer. *Journal of Fluid Mechanics 5* (0 1959), 1–16.

[63] von Karman, T., and Sears, W. Airfoil theory for non-uniform motion. *Journal of the Aeronautical Sciences 5*, 10 (1938), 379–390.

[64] Welch, P. D. The use of fast fourier transform for the estimation of power spectra: A method based on time averaging over short, modified periodograms. *Audio and Electroacoustics, IEEE Transactions on 15*, 2 (1967), 70–73.

[65] Winkler, J., Moreau, S., and Carolus, T. Large-eddy simulation and trailing-edge noise prediction of an airfoil with boundary-layer tripping. In 15^{th} *AIAA/CEAS Aeroacoustics Conference* (2009).

List of publications

Journal papers

- **Leandro D. Santana**, Wim De Roeck, Wim Desmet, "Indirect acoustic impedance eduction in presence of flow based on an analytical two-port formulation", Mechanical Systems and Signal Processing, Volume 48, Issues 1-2, 3 October 2014, Pages 388-403
- **Leandro D. Santana**, Christophe Schram, Wim Desmet, "Amiet theory extension for compact airfoil noise prediction", submitted in March 2015 to the Journal of Sound and Vibration

Conference papers

- **Leandro D. Santana**, Christophe Schram, "Amiet theory extension to predict leading-edge generated noise in compact airfoils", Congrès Français de Mécanique, 2015
- **Leandro D. Santana**, Christophe Schram, Wim Desmet, "Airfoil noise prediction from 2D3C PIV data", AIAA/CEAS Aeroacoustics Workshop, 2015
- **Leandro D. Santana**, Christophe Schram, Wim Desmet, "A BEM procedure to compute an airfoil compressible response to turbulence", AIAA/CEAS Aeroacoustics Workshop, 2014
- **Leandro D. Santana**, Christophe Schram, "PIV analysis of airfoil noise reduction by porous materials", Brazilian Congress of Thermal Sciences and Engineering, 2014
- **Leandro D. Santana**, Wim Desmet, Christophe Schram, "Extension of the Amiet theory for compact leading-edge airfoil noise prediction", ISMA, 2014

- **Leandro D. Santana**, Christophe Schram, Wim Desmet, "An extension of Amiet's theory for turbulence-airfoil noise prediction accounting realistic airfoil geometries using BEM", ISROMAC, 2014
- Michel Roger, Christophe Schram, **Leandro D. Santana**, "Reduction of Airfoil Turbulence-Impingement Noise by Means of Leading-Edge Serrations and/or Porous Materials", AIAA/CEAS Aeroacoustics Workshop, 2013
- **Leandro D. Santana**, Christophe Schram, Wim Desmet, "An experimental procedure for the determination of wake-airfoil interaction noise parameters", AIAA/CEAS Aeroacoustics Workshop, 2013
- **Leandro D. Santana**, Christophe Schram, Wim Desmet, "Panel method for turbulence-airfoil interaction noise prediction", AIAA/CEAS Aeroacoustics Workshop, 2012
- **Leandro D. Santana**, Wim De Roeck, Wim Desmet, "Two-Port Indirect Acoustic Impedance eduction in presence of grazing flows", AIAA/CEAS Aeroacoustics Workshop, 2011

FACULTY OF ENGINEERING SCIENCE
DEPARTMENT OF MECHANICAL ENGINEERING
AEROACOUSTICS RESEARCH GROUP
Celestijnenlaan 300B box 2420
B-3001 Heverlee
leandro.deSantanaDantas@kuleuven.be
http://www.mech.kuleuven.be